![USGS logo] USGS
science for a changing world

Stratiform Chromite Deposit Model

Chapter E of
Mineral Deposit Models for Resource Assessment

Scientific Investigations Report 2010–5070–E

U.S. Department of the Interior
U.S. Geological Survey

Stratiform Chromite Deposit Model

By Ruth F. Schulte, Ryan D. Taylor, Nadine M. Piatak, and Robert R. Seal II

Chapter E of
Mineral Deposit Model for Resource Assessment

Scientific Investigations Report 2010–5070–E

U.S. Department of the Interior
U.S. Geological Survey

U.S. Department of the Interior
KEN SALAZAR, Secretary

U.S. Geological Survey
Marcia K. McNutt, Director

U.S. Geological Survey, Reston, Virginia: 2012

Acknowledgments

Contents

Figures

Tables

Conversion Factors

Inch/Pound to SI

Multiply	By	To obtain
Length		
millimeter (mm)	0.03937	inch (in.)
centimeter (cm)	0.3937	inch (in.)
meter (m)	3.281	foot (ft)
meter (m)	1.094	yard (yd)
kilometer (km)	0.6214	mile (mi)
Area		
square centimeter (cm^2)	0.001076	square foot (ft^2)
square centimeter (cm^2)	0.1550	square inch (in^2)
square meter (m^2)	10.76	square foot (ft^2)
square kilometer (km^2)	0.3861	square mile (mi^2)
Volume		
liter (L)	33.82	ounce, fluid (fl. oz)
liter (L)	2.113	pint (pt)
liter (L)	1.057	quart (qt)
liter (L)	0.2642	gallon (gal)
liter (L)	61.02	cubic inch (in^3)
cubic centimeter (cm^3)	0.06102	cubic inch (in^3)
cubic meter (m^3)	35.31	cubic foot (ft^3)
cubic meter (m^3)	264.2	gallon (gal)
cubic meter (m^3)	1.308	cubic yard (yd^3)
Flow rate		
meter per second (m/s)	3.281	foot per second (ft/s)
Mass		
gram (g)	0.03527	ounce, avoirdupois (oz)
milligram (mg)	0.001	gram (g)
Temperature		
degrees Celsius (°C)	°F=(1.8×°C)+32	degrees Fahrenheit (°F)

Abbreviations

avg	average	st dev	standard deviation
b.d.	below detection limit	vol%	volume percent
Cr #	ratio of $Cr/(Cr + Al + Fe^{3+})$	wt%	weight percent
dB/m	decibels per meter	ms	milliseconds
Fo_2	oxygen fugacity	m/µs	meters per microsecond
Ga	billion years old	m/s	meters per second
Ma	million annum or million years old	mGal	milli-Galileo (unit of gravity)
max	maximum	µg/L	micrograms per liter
Mg #	ratio of $Mg/(Mg + Fe^{2+})$ assuming	µs	microsecond
	oxidation ratio R = 90 for $Fe^{2+}/(Fe^{2+}+ e^{3+})$	n.d.	not determined
min	minimum	n.f.	not found
mol	an amount of a substance that contains	nT	nanotesla
	as many elementary entities (for example,	ppb	parts per billion
	atoms, molecules, ions, electrons) as	ppm	parts per million
	there are atoms in 12 grams of pure	>	greater than
	carbon-12	<	less than
ppt	parts per thousand	±	plus or minus

Acronyms

BHR   borehole radar

BSE   back-scattered electron

Bushveld Complex:

     LG   Lower Group

     MG   Main Group

     MSZ   Main Sulfide Zone

     RLS   Rustenberg Layered Suite

     UG   Upper Group

CHUR   chondritic uniform reservoir

COPR   chromite ore-processing residue

HF   high-frequency spectral band

HREE   heavy rare earth element

Ipueria-Medrado Sill:

     LUU   Lower Ultramafic Unit

     UUU   Upper Ultramafic Unit

LREE   light rare earth element

MCL   maximum contaminant limit

MORB   mid-ocean ridge basalt

MSWD   mean square weighted deviation

Niquelândia Complex:

     BGZ   Basal gabbronorite zone

     LGZ   Layered gabbro zone

     LUZ   Layered ultramafic zone

     UA   Upper amphibolite zone

     UGAZ   Upper gabbronorite zone

     US   Upper sequence

NRM   natural remanent magnetization

PEC   preliminary effects concentration

PGE   platinum group element

PGM   platinum group mineral

REE   rare earth element

RF   radio frequencies

Rum intrusion:

     ELS   Eastern Lavered Series

     WLS   Western Layered Series

SCLM   subcontinental lithospheric mantle

TEC   threshold effects concentration

USEPA   United States Environmental Protection Agency

VCDT   Vienna Canyon Diablo Troilite

WHO   World Health Organization

Chemical Symbols

Symbol	Element	Symbol	Element	Symbol	Element
Ac	Actinium	Ge	Germanium	K	Potassium (Kalium)
Al	Aluminum	Au	Gold	Pr	Praseodymium
Am	Americum	Hf	Hafnium	Pm	Promethium
Sb	Antimony (Stibium)	He	Helium	Pa	Palladium
Ar	Argon	Ho	Holmium	Ra	Radium
As	Arsenic	H	Hydrogen	Rn	Radon
At	Astatine	In	Indium	Re	Rhenium
Ba	Barium	I	Iodine	Rh	Rhodium
Bk	Berkelium	Ir	Iridium	Rb	Rubidium
Be	Beryllium	Fe	Iron	Ru	Ruthenium
Bi	Bismuth	Kr	Krypton	Sm	Samarium
B	Boron	La	Lanthanum	Sc	Scandium
Br	Bromine	Lr	Lawrencium	Se	Selenium
Cd	Cadmium	Pb	Lead	Si	Silicon
Cs	Cesium	Li	Lithium	Ag	Silver
Ca	Calcium	Lu	Lutetium	Na	Sodium (Natrium)
Cf	Californium	Mg	Magnesium	Sr	Strontium
C	Carbon	Mn	Manganese	S	Sulfur
Ce	Cerium	Md	Mendelevium	Ta	Tantalum
Cl	Chlorine	Hg	Mercury	Tc	Technetium
Cr	Chromium	Mo	Molybdenum	Te	Tellurium
Co	Cobalt	Nd	Neodymium	Tb	Terbium
Cu	Copper	Ne	Neon	Tl	Thallium
Cm	Curium	Np	Neptunium	W	Tungsten (Wolfram)
Dy	Dysprosium	Ni	Nickel	(Unh)	(Unnihexium)
Es	Eisteinium	Nb	Niobium	(Unp)	(Unnilpentium)
Er	Erbium	N	Nitrogen	(Unq)	(Unnilquadium)
Eu	Europium	No	Nobelium	U	Uranium
Fm	Fermium	Os	Osmium	V	Vanadium
Fm	Fluorine	Os	Oxygen	Xe	Xenon
Fr	Francium	Pd	Palladium	Yb	Ytterbium
Gd	Gadolinium	P	Phosphorus	Y	Yttrium
Ga	Gallium	Pt	Platinum	Zn	Zinc
				Zr	Zirconium

Stratiform Chromite Deposit Model

Ruth F. Schulte, Ryan D. Taylor, Nadine M. Piatak, and Robert R. Seal II

Abstract

A new descriptive stratiform chromite deposit model was prepared which will provide a framework for understanding the characteristics of stratiform chromite deposits worldwide. Previous stratiform chromite deposit models developed by the U.S. Geological Survey (USGS) have been referred to as Bushveld chromium, because the Bushveld Complex in South Africa is the only stratified, mafic-ultramafic intrusion presently mined for chromite and is the most intensely researched. As part of the on-going effort by the USGS Mineral Resources Program to update existing deposit models for the upcoming national mineral resource assessment, this revised stratiform chromite deposit model includes new data on the geological, mineralogical, geophysical, and geochemical attributes of stratiform chromite deposits worldwide. This model will be a valuable tool in future chromite resource and environmental assessments and supplement previously published models used for mineral resource evaluation.

Stratiform chromite deposits are found throughout the world, but the chromitite seams of the Bushveld Complex, South Africa, are the largest and most intensely researched. The chromite ore is located primarily in massive chromitite seams and, less abundantly, in disseminated chromite-bearing layers, both of which occur in the ultramafic section of large, layered mafic-ultramafic stratiform complexes. These mafic-ultramafic intrusions mainly formed in stable cratonic settings or during rift-related events during the Archean or early Proterozoic, although exceptions exist. The chromitite seams are cyclic in nature as well as laterally contiguous throughout the entire intrusion. Gangue minerals include olivine, pyroxenes (orthopyroxene and clinopyroxene), plagioclase, sulfides (pyrite, chalcopyrite, pyrrhotite, pentlandite, bornite), platinum group metals (mainly laurite, cooperite, braggite), and alteration minerals. A few deposits also contain rutile and ilmenite. The alteration phases include serpentine, chlorite, talc, magnetite, kaemmererite, uvarovite, hornblende, and carbonate minerals, such as calcite and dolomite.

Stratiform chromite deposits are primarily hosted by peridotites, harzburgites, dunites, pyroxenites, troctolites, and anorthosites. Although metamorphism may have altered the ultramafic regions of layered intrusions postdeposition, only igneous processes are responsible for formation. From a diagnostic standpoint and for assessment purposes, they have no temporal or spatial relation to sedimentary rocks.

The exact mechanisms responsible for the development of stratiform chromite deposits and the large, layered mafic-ultramafic intrusions where they are found are highly debated. The leading argument postulates that a parent magma mixed with a more primitive magma during magma chamber recharge. The partially differentiated magma could then be forced into the chromite stability field, resulting in the massive chromitite layers found in stratiform complexes. Contamination of the parent magma by localized assimilation of felsic country rock at the roof of the magma chamber has also been proposed as a mechanism of formation. Others suggest that changes in pressure or oxygen fugacity may be responsible for the occurrence of massive chromitite seams in layered mafic, ultramafic intrusions.

The massive chromitite layers contain high levels of chromium and strong associations with platinum group elements. Anomalously high magnesium concentrations as well as low sodium, potassium, and phosphorus concentrations are also important geochemical features of stratiform chromite deposits. The presence of orthopyroxenite in many of the deposits suggests high silica and high magnesium concentrations in the parent magma.

Most environmental concerns associated with the mining and processing of chromite ore focus on the solubility of chromium and its oxidation state. Although trivalent chromium (Cr^{3+}) is an essential micronutrient for humans, hexavalent chromium (Cr^{6+}) is highly toxic. Chromium-bearing solid phases that occur in the chromite ore-processing residue, for example, can effect the geochemical behavior and oxidation state of chromium in the environment.

Introduction

Stratiform chromite deposits are of great economic importance, yet their origin and evolution remain highly debated. Layered igneous intrusions, such as the Bushveld Complex, Great Dyke, Kemi Complex, and Stillwater Complex, provide opportunities for studying magmatic

differentiation processes and assimilation within the crust, as well as related ore-deposit formation processes. Chromitite seams within layered intrusions host the majority of the world's chromium (Cr) reserves and also contain significant platinum group element (PGE) mineralization.

Massive chromitite layers, greater than (>) 90-percent chromite, or seams of disseminated chromite, >60 percent chromite, are usually found in the lower, ultramafic parts of large, repetitively layered mafic-ultramafic intrusions. These intrusions were emplaced in stable cratonic settings or during rift-related events during the Archean or early Proterozoic, although a few younger deposits also exist. In addition, chromitite seams are cyclic in nature as well as laterally contiguous throughout the entire intrusion.

The intrusions are typically funnel-, saucer-, or canoe-shaped, extend anywhere from 2 to 180 kilometers (km) in diameter, and can reach thicknesses of as much as 15 km. In general, the thicknesses of the individual chromitite seams within the intrusions are varied, ranging from less than (<) 1 centimeter (cm) (for example, the Rum intrusion in north-western Scotland; O'Driscoll and others, 2009a) to 5 to 8 meters (m) (for example, the Ipueira-Medrado Sill in Brazil; Marques and Ferreira-Filho, 2003). In some cases, the contained chromite is not economically recoverable, either due to the low grade of the chromite or the limited tonnage of chromite available for mining. Furthermore, the number of exploitable chromite orebodies in a specific layered intrusion can vary from as little as six (Campo Formoso, Brazil; Cawthorn and others, 2005) to as many as 925 (from 20 major chromite mines in the Western and Eastern Bushveld Complex, South Africa; Cawthorn and others, 2005).

Chromite (Mg, Fe^{2+}) (Cr^{3+}, Al, Fe^{3+})$_2$O$_4$ is the only commercial source of chromium. It is a spinel-group mineral with Mg and Fe^{2+} in complete solid solution and Cr^{3+}, Al, and Fe^{3+} in extensive solid solution. The economic potential of chromite deposits depends primarily on the thickness, continuity, and grade of ore. The most important uses of chromium are in stainless steels, nonferrous alloys, and chromium plating. Chemical-grade chromium is widely used in chemicals and pigments. Chromium is also an important component in refractories. Many of the major stratiform chromite deposits, such as the Bushveld Complex, also contain economic levels of platinum, palladium, rhodium, osmium, iridium, and ruthenium, which are referred to as the PGEs. A deposit model for the PGE ores will be covered in another report, as their mineralogy, geochemistry, occurrence within stratiform complexes, and economic importance warrant separate attention.

Chromite has been obtained from four different deposit types: stratiform chromite deposits, podiform chromite deposits, placer chromite deposits, and laterites derived by the weathering of ultramafic rock containing chromite. Most of the world's resources are located in stratiform chromite deposits, such as the Bushveld Complex (South Africa) and the

Great Dyke (Zimbabwe) (Papp and Lipin, 2001; Papp, 2009). Significant podiform chromite deposits occur in Kazakhstan, Turkey, the Phillippines, New Caledonia, and Russia. World production of chromite ores and concentrates is dominated by South Africa, whereas Kazakhstan, India, Russia, and Turkey make up the remaining important producers (Papp, 2009).

Untapped chromite deposits are plentiful, with the highest concentrations in Kazakhstan and southern Africa—principally the Republic of South Africa and Zimbabwe (Papp, 2007). Native chromium metal deposits, on the other hand, are quite rare, although some native chromium metal has been discovered. The Udachnaya Pipe, a diamond-rich kimberlite pipe in Russia, for example, contains traces of the native metal. The reducing environment where the diamonds were created is thought to have facilitated the formation of elemental chromium.

The United States has no primary chromite production and, as such, is import dependent. In 2008, the U.S. consumed about 10 percent of the world chromite production through the import of chromite ore, chromium chemicals, chromium ferroalloys, chromium metal, and stainless steel (Papp, 2009). From 2004 to 2007, chromium was primarily supplied by South Africa (35 percent), Kazakhstan (19 percent), Russia (6 percent), and Zimbabwe (5 percent), with the remainder (35 percent) being supplied by numerous other countries. During 2008, only one company in the U.S. mined chromite ore. Although the Stillwater Complex in Montana hosts the majority of U.S. chromium resources, the mined ore in 2008 originated in Oregon from podiform chromite deposits associated with an ultramafic ophiolitic body (Papp, 2009). Significant production of chromite from the Stillwater Complex has occurred on only two occasions. The first took place during World War II, when the United States government needed domestic sources of chromite. The second period stretched between 1952 and 1962, when the U.S. needed chromite for the Korean War and the subsequent stockpiling program. The Federal Government subsidized the price during both periods of production, and activities abruptly ended each time the Federal subsidy ended.

Although there has been extensive study of large, layered, mafic-ultramafic intrusions where the stratiform chromite deposits are located, little consensus has been reached on the magma chamber processes responsible for chromite segregation and crystallization. Changes in pressure, oxygen fugacity, and country rock assimilation have all been proposed to explain the occurrence of the chromitite seams (see Ulmer, 1969; Irvine, 1975; Cameron, 1980; Lipin, 1993; and references therein); however, some researchers have argued that crystallization of chromite follows magma mixing at the roof of the magma chamber (for example, Alapieti and others, 1989; Spandler and others, 2005). The discovery that thin, subsidiary chromite-bearing seams in the Rum intrusion have different compositions than disseminated chromite from the

surrounding peridotite and troctolite led O'Driscoll and others (2009a) to propose that some of the layering of the intrusion formed by downward infiltration of a picritic melt. According to their model, the infiltrating melt would dissolve and assimilate cumulus olivine and plagioclase from the residual troctolite crystal mush. The most widely accepted explanation for stratiform chromite deposit formation, however, involves the mixing of primitive and fractionated magmas (Lee, 1996; Naslund and McBirney, 1996; Cawthorn and others, 2005; and references therein).

Despite the ongoing controversy surrounding the mechanism(s) responsible for the formation of stratiform chromite deposits within large, layered mafic-ultramafic intrusions, similarities and differences between major deposits, including physical, structural, geochemical, and geophysical attributes, can elucidate aspects that might aide in model refinement, as well as provide guidance for continued research and exploration. The U.S. Geological Survey's Mineral Resources Program therefore has developed a new descriptive stratiform chromite deposit model.

For complementary resources that pertain to stratiform chromite deposits, users of this report may also refer to the following reviews: Hatton and Von Gruenewaldt (1990), Foose (1991), Duke (1995), Naslund and McBirney (1996), Lee (1996), Cawthorn (2005), and Cawthorn and others (2005).

Purpose

The purpose of this report is to describe a model for stratiform chromite deposits. This model was developed as part of an effort by the U.S. Geological Survey's Mineral Resources Program to update existing models and develop new descriptive mineral deposit models. The model supplements previously published models, and can be used for mineral-resource and mineral-environmental assessments. Because of the importance of chromium for the production of stainless- and heat-resisting steel, as well as for matters related to national security, understanding where additional resources might be located is prudent. This model provides a framework for understanding the characteristics of stratiform chromite deposits to aid in future assessment activities. Furthermore, understanding the fundamental characteristics of existing deposits will enhance and expedite new exploration.

Scope

This report focuses on model features that may be common to all stratiform chromite deposits, as a way to gain insight into the processes that gave rise to their emplacement and the significant economic resources contained in them.

The bulk of the material addressed in the assessment covers the Bushveld (South Africa) and Stillwater (Montana, USA) Complexes, as well as major dike-like intrusions, such as the Great Dyke (Zimbabwe); Bird River Sill (Manitoba, Canada); the Muskox (Nunavut, Canada), Kemi (Finland), Burakovsky (Russia), and Rum (Scotland) intrusions; and the Fiskenæsset anorthosite complex (Greenland), because these are the largest, best preserved, and most intensely studied. Additional layered, mafic-ultramafic igneous intrusions with stratiform chromitite layers include the Niquelândia Complex, Campo Formoso Complex, and Ipueria-Medrado Sill in the Jacurici Complex, Brazil. Recently, the Ring of Fire chromite deposit in Ontario, Canada, has attracted attention and appears to be a stratiform complex.

Some controversy exists regarding the classification of the Fiskenæsset anorthosite complex due to evidence suggesting that the Fiskenæsset was emplaced as multiple sills of magma and crystal mush into the oceanic crust (Polat and others, 2009). Although the alternating anorthosite and amphibolite layers could correlate with the A- and U-type magmas (tholeiitic and boninitic, respectively) that are suggested for the Bushveld and Stillwater Complexes, the Fiskenæsset formed in an oceanic arc environment, unlike the Bushveld and Stillwater.

The tectonic environment where the Niquelândia Complex in Brazil formed has also been subject to debate. Structural data, along with different ages and metamorphic patterns, led to the conclusion that the older section of the complex consists of an Archean proto-ophiolitic sequence characterized by granulite facies metamorphism (Danni and Leonardos, 1981; Danni and others, 1982). Subsequent studies have determined, however, that the Niquelândia Complex is a single, layered mafic-ultramafic intrusion that experienced postemplacement deformation and high-grade metamorphism (Ferreira-Filho and others, 1992).

Chromite that occurs in podiform deposits is not considered in this model, because the geotectonic environment is distinctly different. Stratiform chromite deposits are sheet-like accumulations of chromitite that occur in layered mafic-ultramafic igneous intrusions, whereas podiform chromite deposits occur within Alpine peridotite or ophiolite complexes. As such, podiform chromite deposits are originally formed during ocean spreading and subsequently emplaced during continental margin accretionary episodes. For this reason, chromium resources from podiform chromite deposits will be addressed in a separate model. In addition, there is ongoing debate about the classification of chromite deposits that occur in Archean granite-greenstone belts, such as the Nuasahi and Sukinda massifs in the Orissa region of the Singhbhum craton, India, due to their komatiitic affinities and evidence of derivation from subcontinental lithospheric mantle (SCLM) (Mondal and Mathez, 2007). For this reason, these types of deposits have also been excluded from this model.

Deposit Type and Associated Commodities

Name

Stratiform chromite deposit

Synonyms

Alternative terms used in reference to stratiform chromite deposits include massive chromitite, chromite cumulates, stratiform mafic-ultramafic Cr, and Bushveld chromite.

Brief Description

Stratiform chromite deposits exist as massive chromitite bodies or seams of disseminated chromite in large, unmetamorphosed, repetitively layered mafic-ultramafic intrusions that were emplaced in stable cratonic settings or during rift-related events. The chromitite seams are typically found in the lower, ultramafic parts of the layered intrusions. In addition, chromitite seams are cyclic and laterally contiguous throughout the entire intrusion.

Because the amount of chromite varies in the different stratiform chromite deposits, some of the seams are technically not chromitite, because they do not contain >90-percent chromite. However, the use of the term "chromitite seam" in the literature has included seams where chromite is <90 percent of the rock. In these cases, chromite is a predominant mineral present in the rock. For the sake of consistency, this model will also refer to seams where chromite is a predominant mineral as chromitite seams. Modal mineralogy will be provided, where available, so the reader can more readily distinguish a true chromitite seam from a chromite-rich seam.

Associated Deposit Types

Stratiform chromite deposits are associated with magmatic platinum group element (PGE) deposits, or PGE "reefs." For example, the Stillwater-Ni-Cu and Bushveld Merensky Reef PGE deposits are related to the chromitite seams found in each of the respective intrusions. Furthermore, PGE deposits can occur within chromitite seams such as the UG2, which is the main repository mined for PGEs in the Bushveld. In fact, most of the Bushveld chromitites contain significant PGE, although not in mineable amounts (Scoon and Mitchell, 1994; Naldrett and others, 2009). In addition, chromium recovered from PGE-rich placer deposits may originate from stratiform chromite deposits.

Primary Commodities

Chromium is the primary commodity associated with stratiform chromite deposits. The economic potential of chromite deposits depends mainly on the thickness, continuity, and grade of ore. The most important uses of chromium are in stainless steels, nonferrous alloys, and chromium plating. Chemical-grade chromite is widely used in chemicals and pigments. Chromium is also an important component in refractories. Due to technological advances, ferrochrome (FeCr), an alloy of chromium and iron (Fe), can be made from chromite with Cr/Fe >1.5 (Duke, 1995). The Cr/Fe ratios in chromitite layers of the Bushveld Complex (South Africa), for example, vary between 1.42 and 1.61 (Teigler, 1999). As a result, most of the mined chromite can be used in chemical grade applications or in the production of stainless steel. Similarly, the G and H chromitites from the Stillwater Complex (Montana) have chromium/iron (Cr/Fe) ratios that range from 1.0 to 2.1, making them comparable to the Bushveld (Stowe, 1994). Additional data on Cr/Fe ratios between different stratiform chromite deposits are located in table 1 and can provide an initial framework with which to evaluate the economic viability of the various deposits.

Byproduct Commodities

Many of the major stratiform chromite deposits, such as the Bushveld, contain subeconomic levels of platinum (Pt), palladium (Pd), rhodium (Rh), osmium (Os), iridium (Ir), and ruthenium (Ru), which are referred to as the PGEs. Despite their value in the world marketplace, no chromite deposits are currently (2012) being mined from which the PGEs are actively

Table 1.   Reported chromium/iron ratios for select stratiform chromite deposits.

[Max, maximum; avg, average]

Deposits	Chromium/ iron ratio	References
Bushveld Complex (South Africa)	0.95–3.0	1, 2, 4, 10
Stillwater Complex (Montana, USA)	1.0–2.1	1, 3, 6, 10
Great Dyke (Zimbabwe)	2.1–3.9	1, 2, 3, 5, 10
Muskox intrusion (Canada)	1.2 max	1, 3, 11, 12
Burakovsky intrusion (Canada)	0.67–0.80	23
Kemi intrusion (Finland)	2.6 max, 1.53 avg	2, 7, 3
Campo Formoso Complex (Brazil)	1.26–2.43	2, 9, 21
Ipueira-Medrado Sill (Brazil)	1.11–2.64	8, 9
Bird River Sill (Canada)	1.0–1.5	1, 13

1, Stowe (1994) and references therein; 2, Cawthorn and others (2005); 3, Lee (1996); 4, Eales and Cawthorn (1996); 5, Wilson (1996); 6, McCallum (1996); 7, Alapieti and others (1989); 8, Marques and Ferriera Filho (2003); 9, Lord and others (2004); 10, Naldrett (2004) and references therein; 11, Francis (1994); 12, Roach and others (1998); 13, Sharkov and others (1995).

recovered as byproduct commodities. Exploration of the Big Daddy chromite deposit, a potential stratiform chromite deposit located in The Ring of Fire region of northern Canada, however, includes both chromium and PGE as target commodities (*http://www.spiderresources.ca/mineral-exploration-projects/ big-daddy-deposit*). In addition, layered intrusions of Precambrian age are the only deposits that contain PGEs, suggesting that there may have been fundamental differences between the compositions of the mantle during the Archean-Proterozoic and later times (Naldrett and others, 1990).

Example Deposits

The most well known stratiform chromite deposits occur in the Critical Zone of the Bushveld Complex in South Africa. For this reason, stratiform chromite deposits have also been referred to as Bushveld Cr type deposits. Other deposits with features similar to the Bushveld include those hosted by the Great Dyke (Zimbabwe) and Muskox (Nunavut, Canada) intrusions. Additional large, layered igneous intrusions with stratiform chromite deposits include: Stillwater Complex (Montana, USA), Bird River Sill (southeastern Manitoba, Canada), Kemi intrusion (Finland), Burakovsky intrusion (Russia), and Rum intrusion (Scotland). Brazil also hosts several stratiform chromite deposits, specifically the Niquelândia Complex, Campo Formoso Complex, and Ipueria-Medrado Sill. However, with the exception of the Bushveld Complex, none of the stratiform complexes mentioned have been extensively mined for chromite, because the chromitite layers are too thin and do not contain enough tonnage to be considered economic.

For more detailed information regarding each of the example deposits, readers may refer to the references listed in table 2, as they are frequently cited throughout this report.

Historical Evolution of Descriptive and Genetic Concepts

Early studies (Wager, 1929; Hall, 1932) of layered mafic-ultramafic intrusions proposed that they formed via crystal fractionation processes, where layering was produced by a combination of gravity settling and convection of a single parent magma. Subsequent studies refuted this hypothesis, concluding instead that the formation of cumulates involved very little crystal settling. Rather, the fractionated crystals grew in place or were transported to their position at the base of the magma chamber by magmatic density currents (Wager, 1953, 1959; Wager and Brown, 1968; Irvine, 1979, 1980; Huppert and Sparks, 1980), a process subsequently referred to as "bottom growth." For example, Hess (1960) proposed

that each cyclic unit in the Stillwater Complex began with a brief episode of convective overturn followed by a long period of stagnation. Exploration of alternative processes, such as double-diffusive convection, also attempted to deal with the problems associated with gravity settling (McBirney and Noyes, 1979; Irvine, 1980).

In the Muskox intrusion, as well as in the Stillwater, Great Dyke, Bushveld, and Rum intrusions, cyclic layered units have been attributed to repeated influxes of new magma into the chamber (Irvine and Smith, 1967; Jackson, 1970; Campbell, 1977; Dunham and Wadsworth, 1978). The base of each cycle in the Muskox intrusion is thought by some to represent an influx of new primitive magma into the chamber due to the abrupt shift to more primitive mineral and whole-rock compositions (Huppert and Sparks, 1980). In the Bushveld Complex, extremely large volumes of magma were processed in order to produce the thick chromitite layers, due to the high concentration of chromium found in them (Cawthorn, 1995). In addition, early work using strontium (Sr) isotopic ratios suggested the addition of a distinct and different magma at the boundary between the Upper Critical Zone and Main Zone, where ratios change from approximately (~) 0.7064 to ~0.7085, and then again at the level of the Pyroxenite Marker, where the Sr_i is 0.7073 (Kruger and others, 1982; Hatton and others, 1986; Kruger and others, 1987; Kruger, 1990; Cawthorn and others, 1991). Additional Sr isotope work in the Lower and Critical Zones of the Bushveld has since expanded upon the dataset and suggests that the chromitites formed as a result of roof contamination and magma mixing (Kinnaird and others, 2002).

The validity of the episodic magma injection theory has also been refuted by some based on the implausibility that magmas with exactly the required volumes and compositions would regularly intrude into the overlying basement rock. Eales (2000) showed that the amount of chromium present in the Bushveld Complex is in far greater excess than can be accounted for by the solubility of chromium in the parental liquids of the Lower, Critical, Main, and Upper Zones. Furthermore, assuming that the limited solubility of chromium in mafic magmas is correct, adequate volumes of Cr-depleted residue that would represent the original source liquids are missing from the exposed layered sequence (Eales, 2000). Similarly, mass balance calculations for other layered intrusions demonstrate that the amount of magma needed to satisfy the compositional and density requirements are far too large for the sizes of their respective intrusions (Brandeis, 1992).

In response, other mechanisms have been proposed to explain stratiform chromite deposit formation. One such mechanism is precipitation of chromite as a result of decreases in magma temperature and changes in density during fractional crystallization (Huppert and Sparks, 1980). Cooling of basaltic

Table 2.   Key references for 12 major chromite deposits.

Deposit	Chromite mineralogy	Chromite geochemistry	Mineralogy and geochemistry of associated igneous rocks
Bushveld Complex (South Africa)	Cousins, 1964; Cousins and Feringa, 1964; Lee, 1981; Cameron, 1982; Gain, 1985; Eales and Reynolds, 1986; Eales, 1987; Scoon and Teigler, 1996; Shürmann and others, 1998; Mondal and Mathez, 2007; and Voordow and others, 2009	Cousins, 1964; Molyneux, 1974; Cameron, 1978; Lee, 1981; Cameron, 1982; Gain, 1985; Eales and Reynolds, 1986; Eales, 1987; Von Gruenewaldt and others, 1989; Hatton and Von Gruenewaldt, 1990; Teigler, 1990; Teigler and Eales, 1993; Maier and Eales, 1994; Eales and Cawthorn, 1996; Scoon and Teigler, 1996; Cawthorn, 2007; Mondal and Mathez, 2007; and Voordow and others, 2009	Cousins, 1964; Molyneux, 1974; Cameron, 1978; Gain, 1985; Eales and Reynolds, 1986; Von Gruenewaldt and others, 1989; Hatton and Von Gruenewaldt, 1990; Teigler, 1990; Teigler and Eales, 1993; Hoyle, 1993; Maier and Eales, 1994; Eales and Cawthorn, 1996; Crocker and others, 2001; Cawthorn, 2007; Mondal and Mathez, 2007; and Voordow and others, 2009
Stillwater Complex (Montana, USA)	Jackson, 1961; Page, 1972; Page and others, 1976; Campbell and Murk, 1993	Jackson, 1961; Page, 1972; Page and others, 1976; Lambert and Simmons, 1987; Campbell and Murk, 1993; Papike and others, 1995; McCallum, 1996	Jackson, 1961; Page, 1972; Page and others, 1976; Lambert and Simmons, 1987; Campbell and Murk, 1993; Papike and others, 1995; McCallum, 1996
Great Dyke (Zimbabwe)	Prendergast, 1990; Wilson and Tredoux, 1990; Coghill and Wilson, 1993	Naldrett and Wilson, 1990; Prendergast, 1990; Wilson and Tredoux, 1990; Coghill and Wilson, 1993; Fernandes, 1999; Wilson and Prendergast, 2001	Naldrett and Wilson, 1990; Prendergast, 1990; Wilson and Tredoux, 1990; Coghill and Wilson, 1993; Fernandes, 1999; Wilson and Prendergast, 2001
Muskox intrusion (Canada)	Irvine, 1970 and 1980	Irvine, 1970, 1980; Day and others, 2008	Irvine and Smith, 1969; Irvine, 1970 and 1980; Day and others, 2008;
Kemi intrusion (Finland)	Alapieti and others, 1989; Kujanpää, 1989	Alapieti and others, 1989; Kujanpää, 1989	Alapieti and others, 1989; Kujanpää, 1989
Rum intrusion (Scotland)	Butcher and others, 1999; Power and others, 2000	Emeleus and others, 1996; Butcher and others, 1999; Power and others, 2000; O'Driscoll and others, 2009b	Emeleus and others, 1996; Butcher and others, 1999; Power and others, 2000; O'Driscoll and others, 2009b
Burakovsky intrusion (Russia)	Higgins and others, 1997	Higgins and others, 1997	Higgins and others, 1997
Niquelândia Complex (Brazil)	Girardi and others, 1986; Ferreira-Filho and others, 1992; Pimentel and others, 2004; Girardi and others, 2006	Ferreira-Filho and others, 1994; Girardi and others, 2006	Ferrario and Garuti, 1988; Ferreira-Filho and others, 1994; Pimentel and others, 2004; Girardi and others, 2006
Campo Formoso Complex (Brazil)	Girardi and others, 1986; Marques and Ferreira-Filho, 2003; Lord and others, 2004; Girardi and others 2006; Garuti and others 2007	Barbosa de Deus and others, 1991, Barbosa and others, 1996; Girardi and others, 2006; Garuti and others, 2007	Girardi and others, 2006
Ipueira-Medrado Sill (Brazil)	Marques and Ferreira-Filho, 2003	Marques and Ferreira-Filho, 2003	Marques and others, 2003; Marques and Ferreira-Filho, 2003
Fiskenaesset anorthosite complex (Greenland)	Ghisler, 1970; Myers, 1976; Polat and others, 2009	Ghisler, 1970; Myers, 1976; Polat and others, 2009	Ghisler, 1970; Myers, 1976; Myers and Platt, 1977; Polat and others, 2009
Bird River Sill (Canada)	Scoates and others, 1983; Talkington and others, 1983; Ohnenstetter and others, 1986; Theyer and others, 2001	Scoates and others, 1983; Talkington and others, 1983; Ohnenstetter and others, 1986	Scoates and others, 1983; Talkington and others, 1983; Ohnenstetter and others, 1986

liquids will rapidly trigger supersaturation with chromite, inducing chromite precipitation. However, because olivine typically precipitates with chromite, cooling alone would not produce the observed chromitite layers. Instead, another viable mechanism for chromitite formation involves changes in oxygen fugacity (f_{O2}), because increasing f_{O2} within a basaltic liquid would decrease chromite solubility (for example, Ulmer, 1969; Cameron and Desborough, 1969; Cameron, 1977; Ryder, 1984). Changes in total pressure could also lead to formation of the massive chromitite seams (Cameron, 1980). Such variations would operate almost instantaneously throughout the magma, resulting in the formation of laterally extensive chromitite layers, such as those observed in the Bushveld Complex, which can be traced for hundreds of kilometers along strike with little change in thickness or stratigraphic position. However, the likelihood of changes in either f_{O2} or total pressure occurring with adequate repetitiveness to form the numerous chromitite seams found in large, layered mafic-ultramafic intrusions throughout the world is highly questionable.

At present, the most commonly cited explanations for the occurrence of stratiform chromitite layers are magma mixing; for example, Todd and others, 1982; Irvine and others, 1983; Eales, 1987; Naldrett and others, 1987, 1990; Eales and others, 1990) and contamination of the parent magma by localized assimilation of country rock (Irvine, 1975). In the case of magma mixing, a magma precipitating both olivine and chromite would stop crystallizing olivine for a period of time, whereas chromite remains in the liquidus phase (Lipin, 1993). In addition, because the olivine-chromite cotectic in basaltic systems is concave toward the chromite field, mixing of two liquids on different parts of the cotectic would produce a hybrid liquid within the chromite field. On the other hand, contamination of magma with felsic crustal rocks would force the magma off the cotectic and into the chromite stability field, resulting in the formation of massive chromitite layers (Irvine, 1975).

Although significant debate still exists as to how chromitite layers formed in large layered mafic-ultramafic intrusions, continued investigation into the similarities and differences between major deposits, including physical, structural, geochemical, and geophysical attributes, can elucidate those aspects that are critical for refinement of the deposit model.

Regional Environment

Geotectonic Environment

Several varieties of tectonic settings are present where the large, layered mafic-ultramafic intrusions that host the stratiform chromite deposits are found. The variability relates to the origin of the mantle upwelling responsible for the occurrence of the intrusions. Most of the large, layered mafic-ultramafic intrusions formed in stable, mid-continent anorogenic provinces or near their margins. The ~2.05 billion year old (Ga) Bushveld Complex, for example, was emplaced in the stable Kaapvaal craton of the Limpopo province of South Africa (Harmer, 2000). Similarly, the ~2.46 Ga Great Dyke was emplaced in the Zimbabwe craton along the Archean-Proterozoic boundary (Wilson, 1996). Some intrusions formed, however, when magma exploited preexisting discontinuities, such as shears and basement cover unconformities, or were deformed and faulted postcrystallization. The ~2.7 Ga Stillwater Complex in Montana, for instance, lies along a persistent high-gradient gravity zone related to the faulted front of the Beartooth Range, a major block in the Wyoming Archean Province, and the Nye-Bowler structural zone (Foose and others, 1961; Kleinkopf, 1985). The Early Proterozoic (2,449 plus or minus (±) 1.1 million years old (Ma)) Burakovsky intrusion (Russia), on the other hand, is located within an Archean granite-greenstone terrain and is situated on the East Karelian block (fig. 1), a prominent suture zone on the Fennoscandian Shield (Higgins and others, 1997). The 1.27 Ga Muskox intrusion (Canada) is considered to be coeval and possibly cogenetic with the 1.27 Ga MacKenzie Dyke swarm and Coppermine River continental flood basalts on the northwestern Canadian Shield (Fahrig and Jones, 1969; Irvine and Baragar, 1972; Fahrig, 1987; LeCheminant and Heaman, 1989). Some layered mafic-ultramafic intrusions (for example, Burakovsky intrusion and Stillwater Complex) were also subsequently faulted, deformed, or metamorphosed. The Burakovsky intrusion was broken into three blocks by faulting: the Aganozersky, Shalozerksy, and Burakovsky blocks (Higgins and others, 1997). In addition, the intrusion experienced folding and metamorphism during the pre-Jatulian-Seletsky orogenic phase (2,200 to 2,300 Ma; Zonenshain and others, 1990). The Stillwater Complex underwent low-grade regional metamorphism (fig. 2) during the Proterozoic (Wooden and Mueller, 1988). Other postformation events also affected the complex and surrounding rocks, such as uplift, tilting and erosion during the late Proterozic. Laramide deformation during the late Cretaceous-early Tertiary caused another episode of uplifting, tilting, and erosion (McCallum, 1996).

Temporal Relations

Large stratiform chromite deposits are comagmatic with their host intrusions, which are generally Archean or Early Proterozoic (table 3). Deposits with economic grades of chromite typically formed during three main periods: (1) The Stillwater Complex (Montana, USA) (DePaolo and Wasserburg, 1979) and Bird River Sill (southeast Manitoba, Canada) at ~2.7 Ga (Wang, 1993); (2) the Great Dyke (Zimbabwe, Africa) (Hamilton, 1977), Kemi intrusion
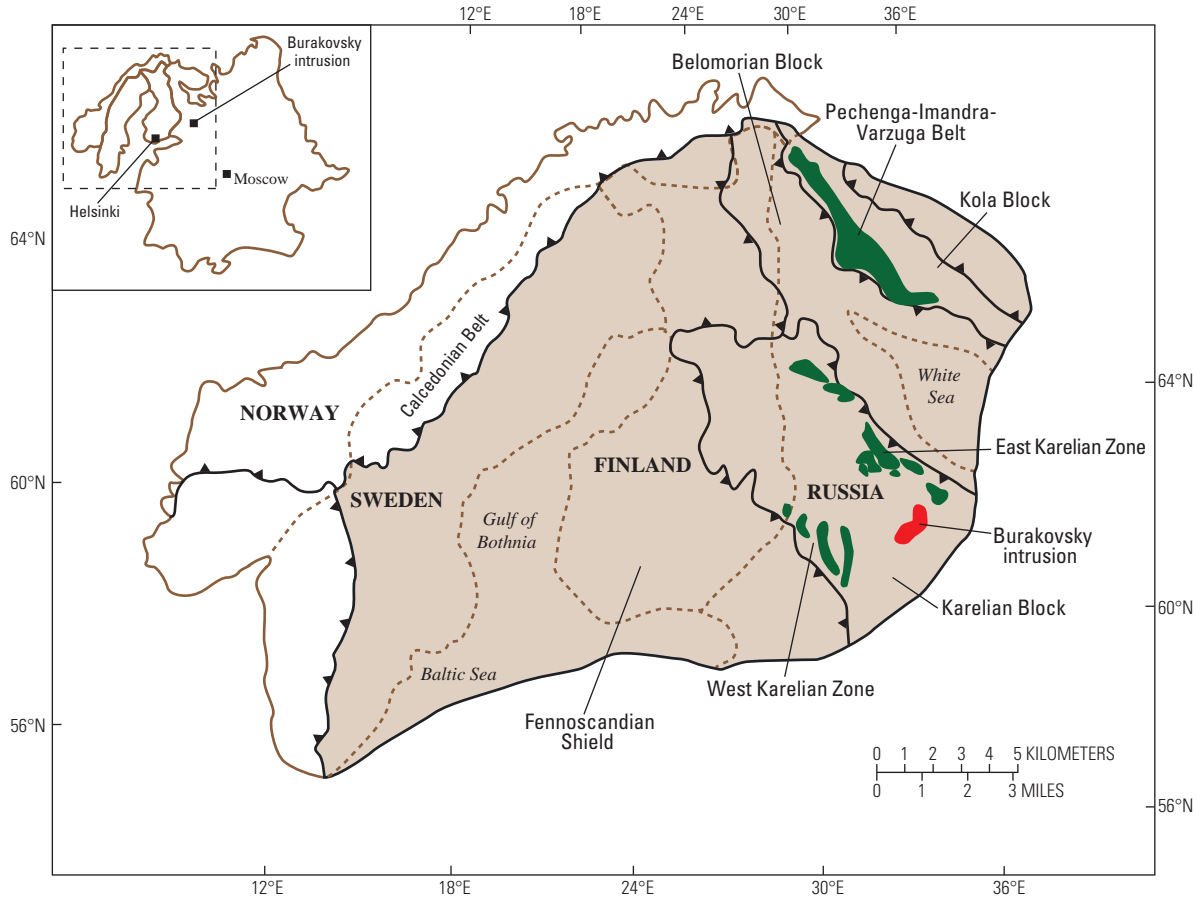
Figure 1.   Simplified tectonic map of the Fennoscandian Shield showing the location of the Burakovsky intrusion. Major tectonic blocks are defined by lines with triangles. Boundaries of countries within the shield are identified by broken lines. The Calcedonian and Pechenga-Imandra-Varzuga supracrustal belts are also shown. Modified from Higgins and others (1997).
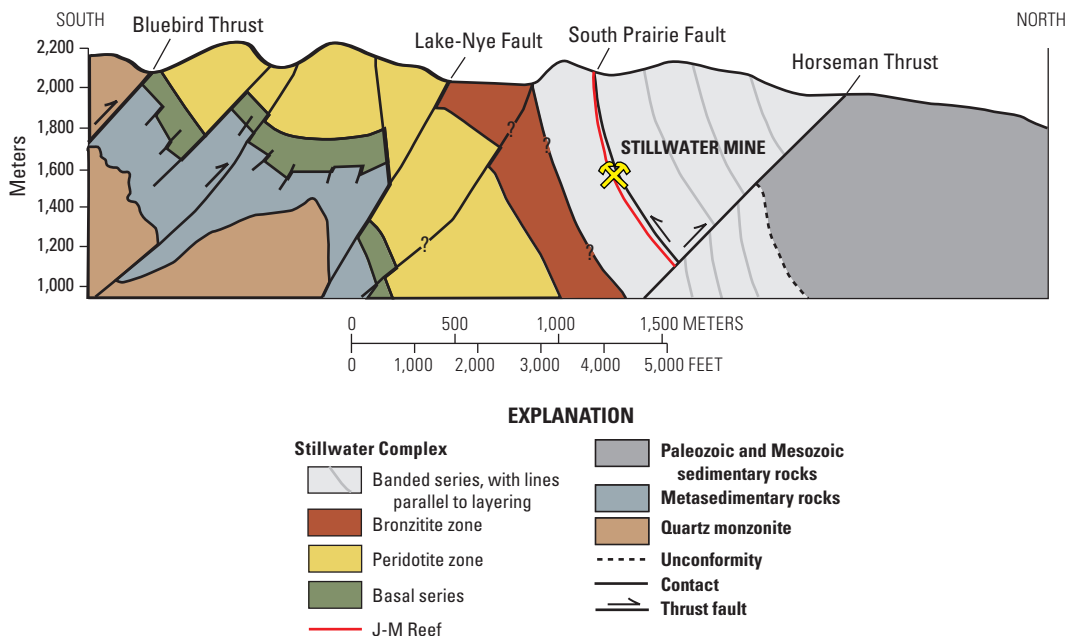
Figure 2.   Structural section through Stillwater Complex in the Mountain View area. Modified from McCallum (1996).

Table 3. Ages for some of the layered mafic-ultramafic complexes covered in this deposit model.

[Analytical method and sample type used to determine the age is shown in italics. Ma, million years old; ±, plus or minus]

Deposits	Age (Ma)	Isotope analytical method	Material	References
Bushveld Complex (South Africa)	2,043 ± 11	Re-Os	Whole rock (*pyroxenites*)	Schoenberg and others (1999)
Stillwater Complex (Montana, USA)	2,701 ± 8	Sm-Nd	Whole rock (*anorthosite, gabbro, pyroxenite*) and separates (*plagioclase, ferroan enstatite, augite*)	DePaolo and Wasserburg (1979)
Great Dyke (Zimbabwe)	2,514 ± 16	Rb-Sr	Whole rock (*various lithologies*) and separates (*plagioclase, clinopyroxene*)	Hamilton (1977)
Muskox intrusion (Canada)	1,270 ± 4	U-Pb	Whole rock (*pyroxenites*)	LeCheminant and Heaman (1989)
Burakovsky intrusion (Canada)	2,431 ± 6	U-Pb	Separates (*zircon*)	Bailly and others (2009)
Niquelândia Complex (Brazil)	1,300–1,250	U-Pb and Sm-Nd	Separates (*zircon*)	Pimentel and others (2004)
Ipueira-Medrado Sill (Brazil)	2,038 ± 19	Pb-Pb	Separates (*zircon*)	Oliveira and Lafon (1995)
Fiskenaesset anorthosite complex (Greenland)	2,835 ± 10	U-Pb	Separates (*zircon*)	Pidgeon and others (1976)
Bird River Sill (Canada)	2,745 ± 5	U-Pb	Separates (*zircon*)	Timmins and others (1985)

(Finland) (Manhès and others, 1980; Patchett and others, 1981), and Burakovsky intrusion (Russia) at ~2.5 Ga (Bailly and others, 2009); and (3) the Bushveld Complex (South Africa) (Harmer, 2000; Schoenberg and others, 1999) and Ipueira-Medrado Sill (Brazil) at ~2.0 Ga (Oliveira and Lafon, 1995).

Other ages characterize some less important deposits. The Muskox intrusion (Canada) and Niquelândia Complex (Brazil) are younger intrusions that were emplaced at 1.27 Ga (LeCheminant and Heaman, 1989) and between 1.3 and 1.25 Ga (Pimentel and others, 2004), respectively. The Rum (also spelled Rhum) intrusion in northwestern Scotland is ~60 Ma (Emeleus and others, 1996). However, the chromitite layers in these younger intrusions are typically very thin. The Fiskenæsset Complex in Greenland is ~2.8 Ga (Alexander and others, 1973; Black and others, 1973; Pidgeon and others, 1976).

Duration of Magmatic-Hydrothermal System and (or) Mineralizing Processes

Studies that have focused on the duration of large, layered mafic-ultramafic intrusions have not addressed the timeframe where the chromitite seams formed, only the intrusion as a whole. Due to the difficulty in assessing the full extent of chromium contained in the layered intrusions, as well as debates over how the layered intrusions formed, consistent estimates regarding the duration of the magmatic activity and mineralizing processes have proven challenging. The amount of time required for the formation of the Rustenburg Layered Suite of the Bushveld Complex, where the chromitite seams are located, has been reported to range from 1 to 3 million years (Harmer, 2000; Letts and others, 2009). However, using thermal modeling, Cawthorn and Walraven (1998) calculated the emplacement of the injected magmas occurred over a period of 75,000 years and crystallization took 200,000 years.

Relations to Igneous Rocks

Stratiform chromite deposits occur as chromitite seams within large, layered mafic-ultramafic igneous intrusions. They occur in the lower part of the Ultramafic Series, usually as cyclic units that are laterally continuous throughout the intrusion.

Relations to Sedimentary Rocks

From a diagnostic standpoint, stratiform chromite deposits are not related to sedimentary rocks. The layered mafic-ultramafic intrusions where the chromitite seams are located may have been emplaced into or been overlain by sedimentary rocks, but the presence of sedimentary rocks alone does not predict that an intruded mafic-ultramafic sequence exists nearby.

Relations to Metamorphic Rocks

During emplacement of the stratiform chromite deposit host intrusions, contact metamorphism occurs. In addition, some deposits, such as the Kemi intrusion (Finland) and Stillwater Complex (Montana), have undergone metamorphism subsequent to formation, but the cores of the chromite grains are well-preserved.

Physical Description of Deposit

Dimensions in Plan View

Plan views of layered mafic-ultramafic intrusions that contain stratiform chromite deposits typically exhibit shapes that are akin to a saucer or funnel with sill- or dike-like geometry. Plan dimensions of the chromitite seams themselves are difficult to ascertain, as much of the rock is inaccessible at the surface. Some examples of dimensions of chromite-bearing layered intrusions include:

1. The Bushveld Complex in South Africa has been reported to be 60,000 to 65,000 km^2 (Harmer, 2000).

2. The original areal extent of the Stillwater Complex in Montana is not known, but gravity data suggest that the exposed rocks represent only a small fraction of the original layered intrusion (Foose, 1991). The strike-length of the complex is about 47 to 55 km, with a width of 5.5 to 8 km (Czamanske and Zientek, 1985; Naldrett, 1989; Hatton and von Gruenwaldt, 1990; Foose, 1991).

3. The Great Dyke extends for 550 km north-northeast across the Zimbabwe craton. The width of the intrusion varies from 4 to 11 km (Wilson and Tredoux, 1990).

4. The Kemi chromite deposit in Finland is lenticular in shape and about 15-km long, with widths that range from 0.2 to 2 km (Alapieti and others, 1990).

5. The Burakovsky Layered intrusion (Russia) occupies an area of more than 700 km^2, with a thickness that measures between 4 and 6 km (Higgins and others, 1997).

6. In Brazil, the Campo Formoso Complex, located in the northern part of the São Francisco Craton in the State of Bahia (also spelled Baía), is about 40-km long and 1-km wide (Giuliani and others, 1994; Girardi and others, 2006). The nearby Niquelândia Complex, which is part of the Goiás Massif, is 50 by 25 km (Ferreira-Filho and others, 1992).

Table 4 also contains information on the physical descriptions of the various stratiform chromite deposits used for this model.

Size of Magmatic System Relative to Extent of Economically Mineralized Rock

Estimates for the amount of magma involved in the formation of the layered mafic-ultramafic intrusions relative to the ore bodies have proven difficult due to the limited exposure of the intrusions as well as the contained chromitite seams. As a result, the type of data provided in the literature is inconsistent from one deposit to another. In some cases, volumes are given; in other cases, only the thickness of the magma chamber is provided. Cawthorn and Walraven (1998), for example, calculated that the volume of magma required to produce the Bushveld Complex exceeded 100,000 km^3. No estimates to date have been reported for the chromitite seams. For the Stillwater Complex, Campbell and Murck (1993) determined that 2,000 to 4,000 m of magma would have been required to crystallize a 1-m-thick massive chromitite layer. An estimate by Lipin (1993) suggests that a magma thickness of at least 931 m was required to form the 2.6-m-thick G chromitite seam in the Stillwater Complex. In the Ipueira-Medrado mafic-ultramafic sill of Brazil, mass balance calculations estimate an enormous amount of melt (>10,000 m) was associated with the formation of the Main Chromitite layer (Marques and Ferreira-Filho, 2003).

Vertical Extent

On average, the layered mafic-ultramafic intrusions that host stratiform chromite deposits are at least 2-km thick. In some deposits, the original vertical extent of the intrusion is not known due to erosion or post-ore deformation. The actual chromitite layers within the layered intrusions are thin relative to the size of the overall magmatic system. For example, in the Bushveld Complex, the thickness of the layered mafic-ultramafic Rustenberg Layered Suite (RLS) is estimated to be about 5 km, with a maximum composite thickness of 9 km (Von Gruenwaldt and others, 1988; Harmer, 2000). The Critical Zone within the RLS, which hosts the bulk of the chromitite layers as well as cyclic units of pyroxenite, norite, and anorthosite, is 1,500- to 1,700-m-thick. However, even the thickest chromitite seam, the LG6 chromitite layer, in the Critical Zone ranges only from 0.5- to 1.05-m thick (Schürmann and others, 1998). The other main chromitite seams that are mined for chromite include the MG1 and MG4; the thicknesses of these seams range from 0.31 to 1.58 m and 0.86 to 2.23 m, respectively (Cameron, 1964; Cousins and Feringa, 1964). Estimates for the thickness of the UG2 chromitite layer, which is mined for its PGE contents, vary from 40 to 120 cm (Cawthorn, 2005), although other estimates indicate the thickness is the same as the LG6 seam (Schürmann and others, 1998).

The entire vertical extent of the Stillwater Complex ranges from 5.5 to 6.5 km. Chromitite layers found in the Stillwater Complex, however, range from <4-cm thick to 8-m thick. The thickest seams are found in the G (1 to 8 m), H (about 1.3 m), B (3 layers, each 20 cm to 1 m), A (0.3 m), and K seams (2 layers, each 2 to 4 cm). The other chromitite layers are <4-cm thick (Jackson, 1968).

The ultramafic zone of the Burakovsky intrusion is ~3-km thick, but the chromite-rich layers, with 50- to 75-percent chromite, within the ultramafic zone only range from 0.5 to 4 m (Higgins and others, 1997). For the Kemi intrusion, the entire vertical extent is estimated to be about 2 km based on geophysical data, with the individual chromitite seams varying from 0.5 to 90 m (Alapieti and others, 1989; Kujanpää, 1989). The Ipueira-Medrado Sill, on the other hand, is <300-m thick, whereas the massive chromitite layers range from 5- to 8-m thick, making this deposit unique because of its relatively thick ore layer (Marques and Ferreira-Filho, 2003). See table 4 for additional deposit dimensions.

Table 4. Physical dimensions of selected stratiform chromite deposits.

[km², square kilometer; km, kilometer; m, meter; cm, centimeter; ~, approximate]

Deposit	Shape	Areal extent	Volume	Intrusion thickness	Chromitite seam thickness	References
Bushveld Complex (South Africa)	Funnel-shaped; four peripheral limbs that may connect at depth (fifth limb hidden under sediment cover)	~65,000 km²		7–9 km	Tens of centimeters to ~2 m	1, 2, 3
Stillwater Complex (Montana, USA)	Truncated top; upper parts lost to exhumation and erosion	180 km²; maximum dimensions of 47 km × 8 km		Maximum exposed thickness of 6.5 km	More than 10 seams ranging centimeters to 8 m	3, 4, 17
Great Dyke (Zimbabwe)	Highly elongate linear body; Y-shaped in cross section	550 km × 4–11 km		>3 km	Up to 1.8 m in upper pyroxenite; 10–20 cm in lower ultramafic part	3, 11
Kemi intrusion (Finland)	Originally funnel-shaped, later tilted to current lenticular-shaped	15 km × 0.2–2 km		Extends downward at least 2 km	Main layer is 20 m, locally up to 90 m; as thin as 0.5 m	6
Rum intrusion (Scotland)	Mushroom-like; circular in plan view	10 km diameter ~700 km²;	700–1,000 km³	n.d.	Millimeters to <2 cm	7, 8, 14
Burakovsky intrusion (Russia)	Lopolithic or funnel-shaped; irregular oval in plan view; majority of intrusion is covered by glacial sediments	50 km × 13–17 km		4–6 km	0.5–4 m	5, 6
Niquelândia Complex (Brazil)	Fault-bounded on all sides	1,800 km²		10–15 km	Two horizons, 5–30 cm, locally reaching 1 m	9, 15
Campo Formoso Complex (Brazil)	Tabular, arch-shaped	40 km × 0.1–1.1 km		Unknown due to extensive erosion	At least seven layers, few centimeters to several meters; maximum 12 m	10, 15
Ipuera-Medrado Sill (Brazil)	Sill-shaped	7-km long		300 m	Main seam 5–8 m; others 0.3–1.1 m	13
Bird River Sill (Canada)	Sill-shaped	700-km long		700 m	Five 5–10 cm seams in lower series; three chromite members in 3.1-m-thick group in upper series	12, 16

References: 1, Eales and others (1993); 2, Eales and Cawthorn (1996); 3, Cawthorn and others (2005); 4, McCallum (1996); 5. Higgins and others (1997); 6, Alapieti and others (1990); 7, Tepley III and Davidson (2003); 8, Emeleus and others (1996); 9, Ferreira Filho and others (1995); 10, Garuti and others (2005); 11, Wilson (1996); 12, Ohnenstetter and others (1986); 13, Marques and Ferreira Filho (2003); 14, Power and others (2000); 15, Girardi and others (2006); 16, Theyer (1991); 17, Jackson (1968).

Form/Shape

Chromitite seams are laterally contiguous throughout a layered mafic-ultramafic intrusion and generally conform to the overall shape of the layered intrusion where they are located. Typically, the layered mafic-ultramafic intrusions where stratiform chromite deposits are found have a sill geometry and commonly display a saucer- or funnel-shape (for example, Irvine, 1975; Cawthorn and Walraven, 1998). However, several of the deposits are described as being shaped like a dike—most notably the Great Dyke in Zimbabwe. Additional details regarding the various forms the different layered intrusions possess are as follows:

1. The Bushveld Complex takes the form of a funnel or saucer-shaped intrusion, with mostly undeformed rocks that generally dip <20 degrees toward the center of the hosting basin, giving cross sections a synclinal appearance (Duke, 1995; Eales and Cawthorn, 1996).

2. The Stillwater Complex is an exposed 48-km-long, layered, mafic-ultramafic wedge with a truncated top (Hess, 1960; Jackson, 1961). Trending approximately east-west and dipping 40 to 60 degrees to the north, the wedge-shaped complex is considered to be the upturned edge of a sill-like lopolith centered to the northeast of the complex beneath a cover of sedimentary rocks. In addition, the rocks are bounded to the east and west by Laramide-age (80 to 35 Ma) faults (Jones and others, 1960; Foose, 1991; McCallum, 1996). Magnetic and gravity data indicate that the complex has a synformal shape and continues over an area of more than 2,500 km² to the northeast of its present outcrop position (Kleinkopf, 1985). The presence of numerous Stillwater-type cumulate xenoliths in Late Cretaceous dacitic intrusions situated roughly 8 to 12 km to the north also support this assertion (Brozdowski, 1985).

3. The Muskox intrusion has the overall structure of a giant funnel-shaped dike that is ~125-km long, 11-km wide in the north, and 0.1-km wide in the south (Day and others, 2008). The intrusion merges into a vertical dike extending to the south, referred to as the Keel feeder dike. Aeromagnetic and gravity anomalies indicate the intrusion extends northward for at least 250 km under younger cover (Day and others, 2008).

4. The Kemi intrusion originally had a funnel shape, although the present form has been described as lenticular. Due to tectonic movements during the Svecokarelidic orogeny (1,900 to 1,800 Ma), the Kemi intrusion was tilted to form a body dipping about 70 degrees to the northwest that extends downward at least 2 km (Alapieti and others, 1989).

5. The Great Dyke is shaped like a dike with gently inward dipping layers of ultramafic rocks in its lower part and gabbroic rocks in the upper part (Cawthorn, 2005). The shape of the Great Dyke intrusion has also been referred to as canoe-like. However, whereas the Great Dyke has the outward form of a dike, the intrusion developed as a series of isolated chambers that became linked at progressively higher levels during magma filling (Wilson, 1996). In addition, gravity studies indicate the presence of a deep structure with a Y-shaped transverse section, making the inner form of the Great Dyke funnel-like (Podmore, 1982, 1985; Podmore and Wilson, 1987).

6. The Burakovsky intrusion has been broken into three distinct blocks due to faulting: the Aganozersky, Shalozersky, and Burakovsky blocks (Higgins and others, 1997). Due to the thickness of the overlying Quarternary glacial sediments, much of the data about the extent, composition, and internal structure of the intrusion have been obtained by geophysical methods and from shallow (200 to 500 m) drill cores (Sharkov and others, 1995). These data suggest that the Shalozersky and Burakovsky blocks are shaped like lopoliths, whereas the Aganozersky block in the eastern part of the intrusion is shaped like a funnel, slightly tilted to the west, and sheared by submeridional faults.

Host Rocks

Host rocks may include alternating layers of norite, gabbronorite, dunite, harzburgite, lherzolite, pyroxenite, troctolite, anorthosite, orthopyroxenite, and gabbro, although not all will be found in each layered intrusion (table 5). There is considerable lithological variability between the different stratiform chromite deposits, as well as within the different regions of the same layered intrusion. The main host rocks where the chromite is located are generally cumulate pyroxenites, such as feldspathic pyroxenite in the Bushveld Complex, or harzburgites (olivine cumulates), evidenced in the Stillwater Complex and Muskox intrusion. Typically, a layered mafic-ultramafic intrusion consists of two main sections: an Ultramafic Series and a Mafic Series. The majority of chromitite seams are found in the lower, ultramafic parts of the layered intrusions.

Table 5.   Rock associations of select stratiform chromite deposits.

[Ma, million years ago]

Deposit	Age	Rock types contained within the intrusion	Main host rocks	Country rocks	References
Bushveld Complex (South Africa)	2,060 Ma	Dunite, pyroxenite, anorthosite, harzburgite, norite, gabbro, gabbronorite, orthopyroxenite, troctolite, ferrodiorite, oxide layers	Pyroxenite, Melanorite	Transvaal Supergroup (quartzite, dolomitic and banded ironstone, shales, volcanics)	1, 2, 17
Stillwater Complex (Montana, USA)	2,700 Ma	Peridotite, anorthosite, orthopyroxenite, harzburgite, norite, gabbro, gabbronorite, troctolite, olivine gabbro	Peridotite	Archean metasedimentary rocks of the Beartooth Range	5
Great Dyke (Zimbabwe)	2,514 ± 16 Ma	Pyroxenite, harzburgite, dunite, gabbronorite, norite, websterite	Pyroxenite, dunite	Granitoids and greenstones of the Archean Zimbabwe Craton	13,21
Muskox intrusion (Canada)	1,269 ± 1 Ma	Diabase, gabbro, peridotite, websterite, orthopyroxenite, olivine-clinopyroxene, dunite, gabbronorite, granophyre, picrite	Orthopyroxenite, peridotite	Coppermine Homocline consisting of para- and orthogneiss, metavolcanics and metasediments	3, 4, 18
Kemi intrusion (Finland)	2,440 Ma	Peridotite, websterite, orthopyroxenite, gabbro, gabbronorite, anorthosite	Peridotite	Late Archean granitoids and supracrustal mafic volcanic and clastic sedimentary rocks	7
Rum intrusion (Scotland)	58–61 Ma	Peridotite, allivolite, gabbro, dunite, troctolite, olivine gabbro	Olivine, bronzite-olivine, and bronzite cumulates		8, 23
Burakovsky intrusion (Russia)	2,449 ± 1.1 Ma	Pyroxenite, gabbronorite, gabbrodiorite, dunite, peridotite, websterite, norite, anorthosite	peridotite	Archean granite-greenstone terrane	6, 19
Niquelândia Complex (Brazil)	799 ± 6 Ma	Gabbro, anorthosite, gabbronorite, websterite, norite, dunite, harzburgite, pyroxenite, troctolite, lherzolite	Dunite, peridotite	Metamorphic volcanic and sedimentary rocks	9, 10, 11, 23
Campo Formoso Complex (Brazil)	Controversial	Peridotite, pyroxenite, gabbro, norite	Serpentinized peridotite	Archean granulites of the Caraíba Group	11, 12
Ipueira-Medrado Sill (Brazil)	2,038 ± 19 Ma	Dunite, harzburgite, pyroxenite, norite, gabbro, orthopyroxenite	Harzburgite	Archean granulites of the Caraíba Group	16, 22
Bird River Sill (Canada)	2,745 ±5 Ma	Dunite, lherzolite, peridotite, gabbro, anorthosite	Serpentinized peridotite	Archean greenstone	14, 15

References: 1, Eales and others (1993); 2, Eales and Cawthorn (1996); 3, Day and others (2008); 4, Irvine and Smith (1967); 5, McCallum (1996); 6, Higgins and others (1997); 7, Alapieti and others (1990); 8, Emeleus and others (1996); 9, Ferreira Filho and others (1992); 10, Girardi and others (1986); 11, Garuti and others (2005); 12, Girardi and others (2006); 13, Wilson (1996); 14, Timmins and others (1985); 15, Talkington and others (1983); 16, Marques and Ferreira Filho (2003); 17, Walraven and others (1990); 18, French and others (2002); 19, Amelin and others (1995); 20, Pimentel and others (2006); 21, Hamilton (1977); 22, Oliveira and Lafon (1995); 23, Butcher and others (1999).

Bushveld Complex

The Bushveld Complex of South Africa transgressively intruded the epicrustal felsic lavas of the Rooiberg Group and sedimentary rocks of the Transvaal Supergroup (Eales and Cawthorn, 1996). Exposure occurs in four main regions: the Far Western, Western, Eastern, and Potgietersrus (Northern) limbs (fig. 3). The Southern or Bethal Limb is known only from borehole cores. This large, layered mafic-ultramafic intrusion is subdivided into the Marginal, Lower, Critical, Main, and Upper Zones, referred to collectively as the Rustenberg Layered Suite (RLS). The Upper Critical Subzone and Lower Critical Subzone host the main strati-form chromitite layers (fig. 4). The chromitites are grouped together into the Lower, Middle, and Upper Groups depending on their stratigraphic position (Cousins and Feringa, 1964). Chromitite seams of the Lower Group (LG) are contained within the Lower Critical Subzone. The LG contains seven chromitite layers, LG1 through LG7, that are hosted in feldspathic pyroxenite, with the LG6 layer being the thickest

chromitite seam in the Bushveld and the most economically exploitable. The Main Group (MG), situated above the LG chromitite layers, consists of four chromitite seams, MG1 through MG4. These layers straddle the boundary between the Lower and Upper Critical Zone. Overlying the MG chromitite layers are the Upper Group (UG) chromitite seams, which occur in norite and anorthosite sequences in the Upper Critical Subzone and include the UG1, UG2, UG3, and UG3A (Gain, 1985; Eales and Cawthorn, 1996). The UG3 and UG3A chromitite seams are only locally developed throughout the Bushveld.

As many as 25 individual chromitite layers are present in the Critical Zone in some localities (Fourie, 1959; Cousins and Feringa, 1964; Schürmann and others, 1998), and considerable lateral variation occurs between the different sectors of the complex such that not all seams are present in all areas (Hatton and Von Gruenewaldt, 1990). A total of 14 layers have been identified as major chromitite seams. Scoon and Teigler (1994) also recognized that the chromitite layers can also be divided into four categories. Type I chromitite seams occur
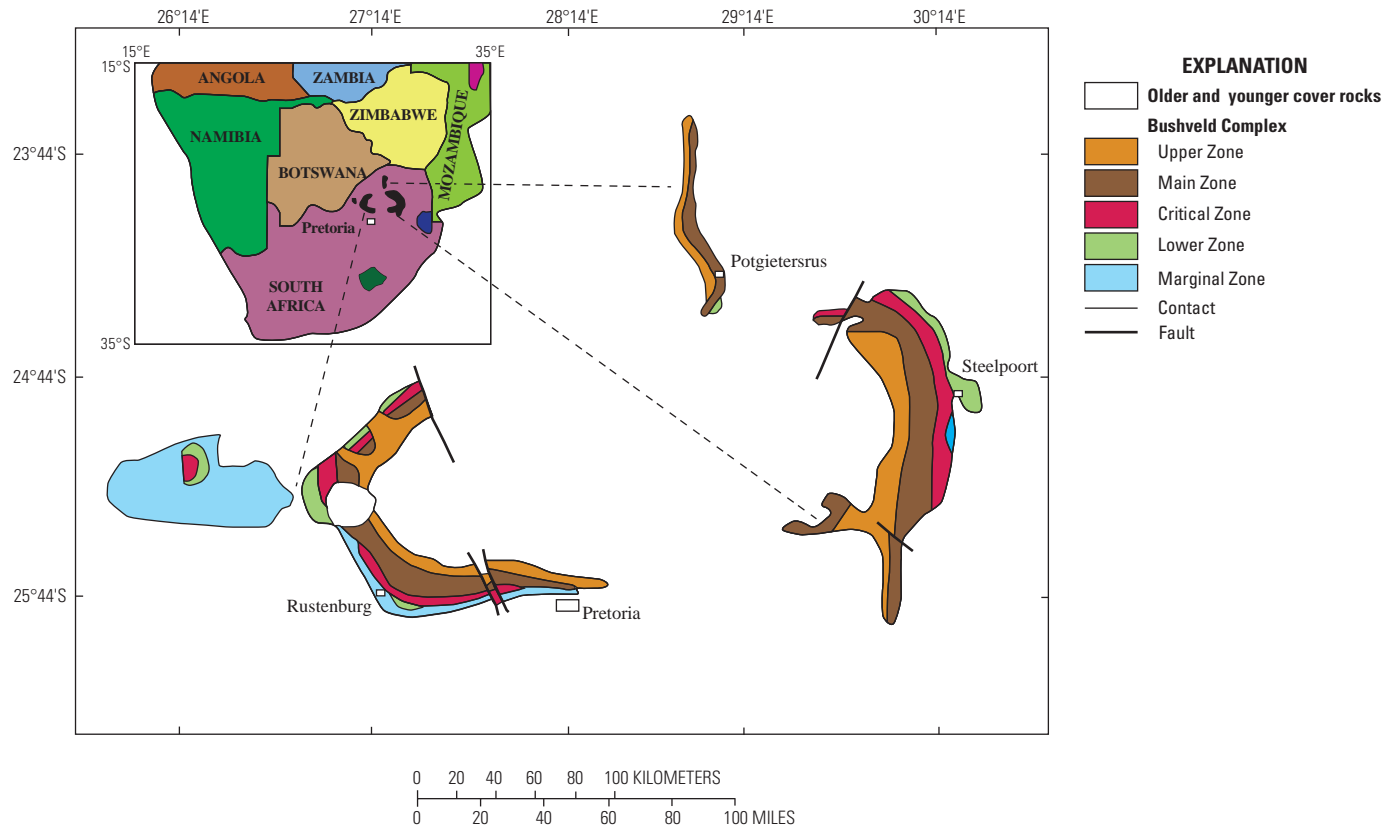
Figure 3.   Simplified geological map of the Bushveld Complex. Modified from Cawthorn (2007). Inset map shows locations of enlarged bodies. City names shown for orientation.
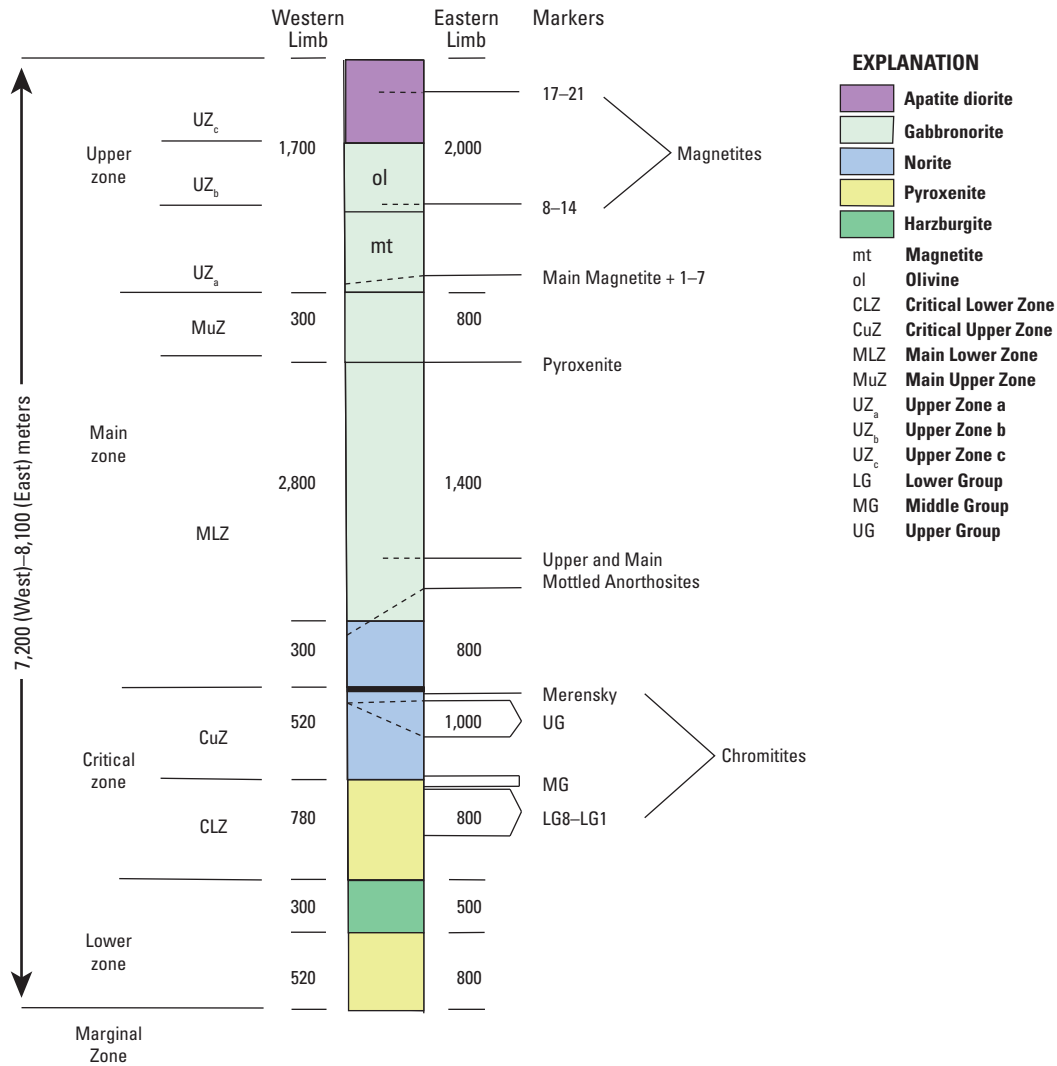
Figure 4. Generalized stratigraphic sections of the Rustenburg Layered Suite through the Western and Eastern limbs of the Bushveld Complex. Modified from Eales and Cawthorn (1996). Maximum thicknesses of the zones in different parts of each limb are shown. Some of the major marker horizons are identified, although these may not appear in both limbs, and are thus shown as incomplete dashed lines. Clustered magnetite layers are indicated by numbers 1–7, 8–14, and 17–21.

at the bases of cycles in the Lower Critical Zone, type II at the bases of cycles in the Upper Critical Zone, type III are thin layers that occur in the intermediate parts of cycles, and type IV are stringers associated with orthopyroxene pegmatoids. Based on lithostratigraphy, chromite and PGE chemistry, and sulfide content, Scoon and Teigler (1994) further categorized chromitite seams that occur at the bases of cycles into types Ia (LG1 through LG4), Ib (LG5 through MG1), IIa (MG2 through UG1), and IIb (UG2 and above). The main mined chromitite seams are the LG6, MG1, and MG4, which are presently exploited using trackless and conventional

underground mining methods (Schürmann and others, 1998; Naldrett and others, 2009). The UG2 chromitite seam is mined for PGEs.

Lithologically, the Lower Critical Subzone generally contains orthopyroxenite (bronzitite), with subordinate dunites, harzburgites, and chromitites (Cameron, 1982; Teigler and Eales, 1996). The Upper Critical Subzone mainly consists of interbedded anorthosite, norite, and orthopyroxenite (Mondal and Mathez, 2007). Chromitites and chromite-silicate rocks only occur at widely separated intervals in this zone (Cameron, 1982).

Stillwater Complex

In the Stillwater Complex, Montana, three series define the mineral deposit types: (1) the Basal Series, with low-grade copper-nickel sulfides, (2) the Ultramafic Series, where the chromite is located, and (3) the Banded Series, which has PGE-bearing sulfides (figs. 5 and 6; McCallum, 1996). The Basal Series consists of two zones. The lower, Basal Norite Zone, contains multiphase cumulates primarily made up of bronzite, olivine, and plagioclase. Minor amounts of chromite and inverted pigeonite are present. This zone grades upward into the Basal Bronzite Zone, where bronzite cumulates domi-nate the lithology. Sulfides are most abundant toward the base of the series, although they are also present in lesser amounts throughout the two basal zones.

The Peridotite Zone of the Ultramafic Series consists mainly of a series of cyclic units, and about 20 are present in the thickest part. An ideal cyclic unit (fig. 7) consists of, from bottom to top, an olivine cumulate layer with oiko-crysts of bronzite (poikilitic harzburgite of Jackson, 1968), an olivine-bronzite cumulate with interstitial plagioclase (granu-lar harzburgite of Jackson, 1968), and a bronzite cumulate with interstitial plagioclase and clinopyroxene (bronzitite of Jackson, 1968) (Zientek and others, 1985; McCallum, 1996).

Chromite-bearing seams with chromite from <50 percent (chromite-bearing) to nearly 100 percent (chromitite) almost always occur in the olivine cumulate layer, but never at the very base of that layer (Loferski and others, 1990). The thickest chromite-bearing seams have sharp basal contacts and grade upwards from massive chromitite at the base, into disseminated chromite with olivine, and into typical olivine cumulates with about 2-percent chromite.

The base of the Ultramafic Series is defined by the first appearance of laterally continuous cumulus olivine and gener-ally overlies the Basal Series rock. In localized areas, the Basal Series is absent, such that the Ultramafic Series rests directly on the footwall rocks. Chromite is pervasive in each cyclic unit and averages about 2 percent in the olivine cumu-lates, about 1 percent in the olivine-bronzite cumulates, and a trace amount in the bronzite cumulates (McCallum, 1996). Some olivine cumulates contain economically significant chromite-bearing layers.

The Banded Series has been divided into three sections: the Lower, Middle, and Upper Banded Series. Norite and gabbronorite make up the Lower and Upper Banded Series, whereas the Middle Banded Series contains anorthosite, troc-tolite, and olivine gabbro. The PGE-rich sulfide zone, known as the J-M Reef, is located in the Lower Banded Series.
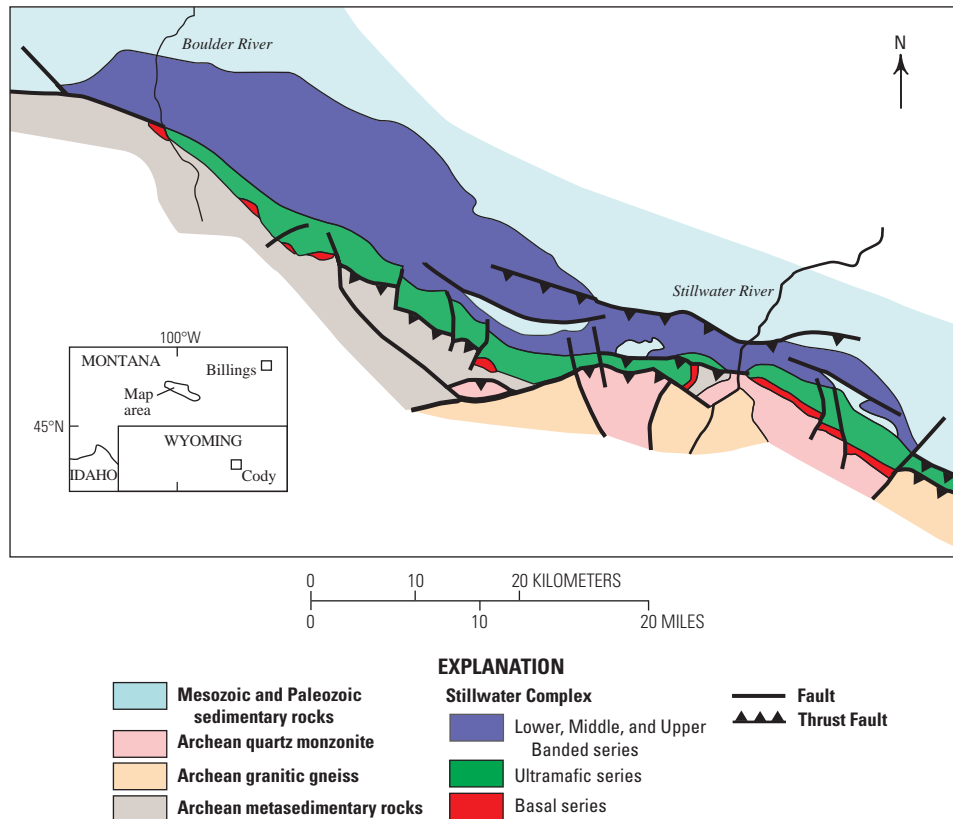
Figure 5. Generalized geologic map of the Stillwater Complex, Montana. Modified from Campbell and Murck (1993).
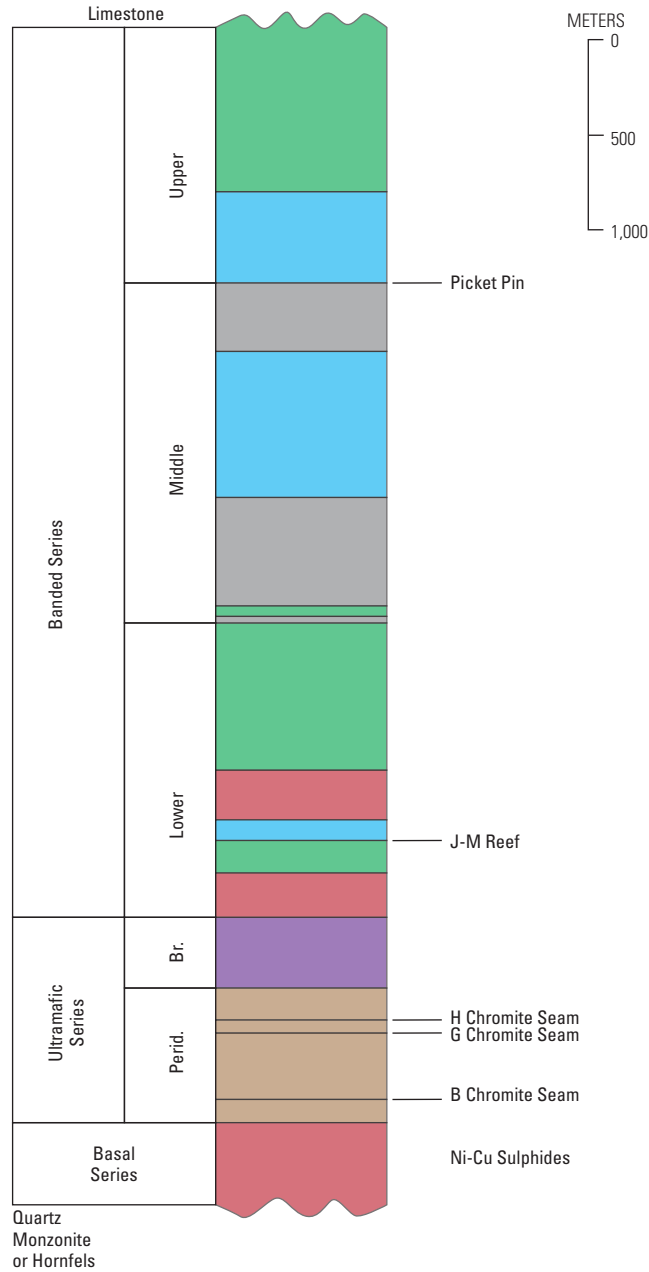
Figure 6.   Generalized stratigraphic section of the Stillwater Complex with the main chromite-bearing seams identified. Modified from Campbell and Murck (1993).
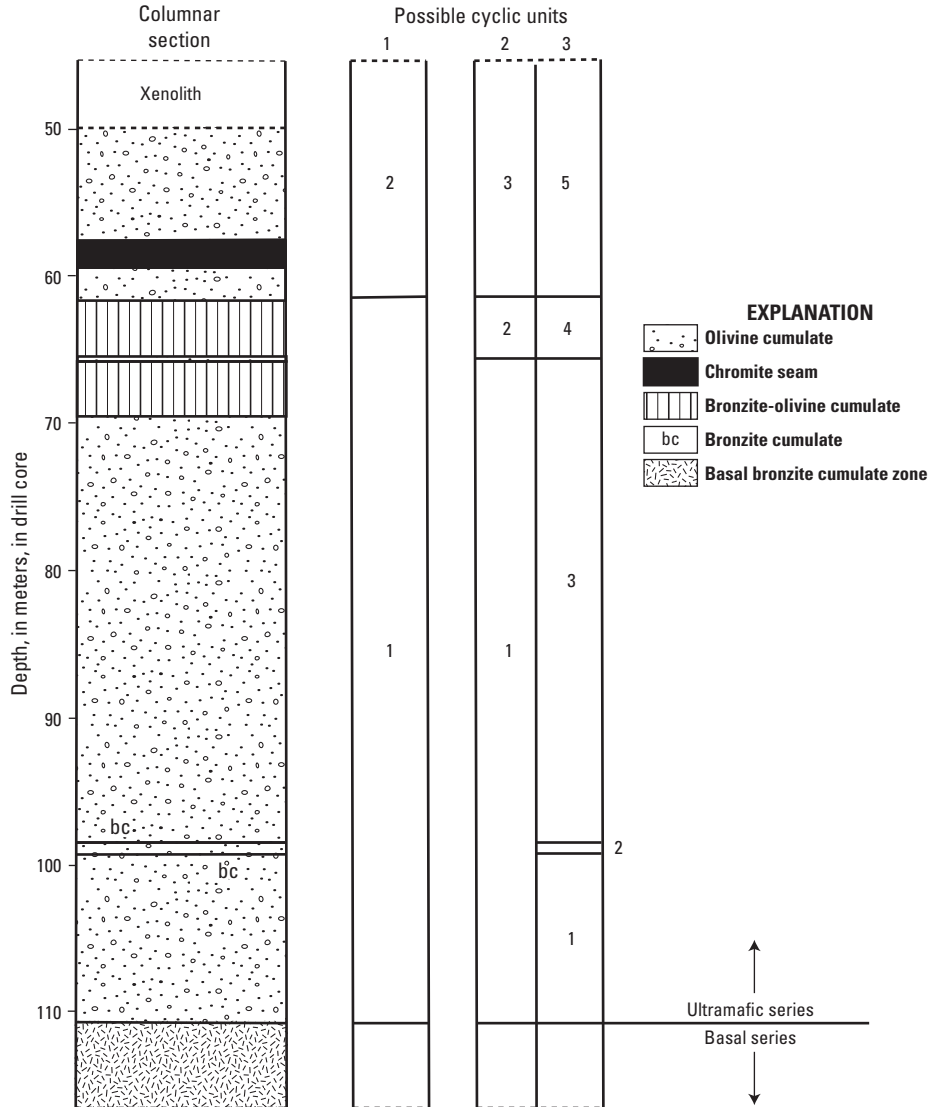
Figure 7.   Stratigraphic section of the M-16 drill core in the Stillwater Complex with three possible subdivisions of the Ultramafic Series into cyclic units. Modified from Loferski and others (1990).

Great Dyke

The Great Dyke is a layered mafic-ultramafic intrusion that intruded into the granites and greenstone belts of the Zimbabwean craton (fig. 8; Wilson and Tredoux, 1990). The intrusion has been subdivided longitudinally into two large magma chambers: North and South chambers, with a possible third, small chamber (Mvuradona chamber) in the extreme north. Several subchambers make up the North and South chambers. For the North chamber, from north to south, there are the Musengezi, Darwendale, and Sebakwe subchambers (Wilson and Prendergast, 1987). The Selukwe and Wedza subchambers make up the South chamber. These subdivisions are based on stratigraphic correlation, thicknesses, character-istics of cyclic units, and gravity studies. Satellite dikes and craton-wide fractures are also associated with and parallel to

the Great Dyke. Quartz gabbro satellite dikes occur along the eastern and western sides, whereas the southern satellite dike complex contains ultramafic rocks (Wilson, 1996).

The Great Dyke is subdivided into a lower Ultramafic Sequence and an upper Mafic Sequence (fig. 9; Wilson, 1982). The Mafic Sequence is extensively eroded such that the roof of the uppermost layered rocks is not preserved (Wilson and Tredoux, 1990). Broadly, the Ultramafic Sequence consists of cyclic units with a lower dunite or harzburgite layer and an upper pyroxenite (classified as bronzitite by some) layer. As a result, the Ultramafic Sequence has been subdivided into the Dunite Succession and the Pyroxenite Succession, which is similar to the subdivision of the Stillwater Complex into a lower Peridotite Member and an upper Pyroxenite Member (Jackson, 1961). In the Dunite Succession, pyroxenite is entirely absent and chromitite layers define the base of the
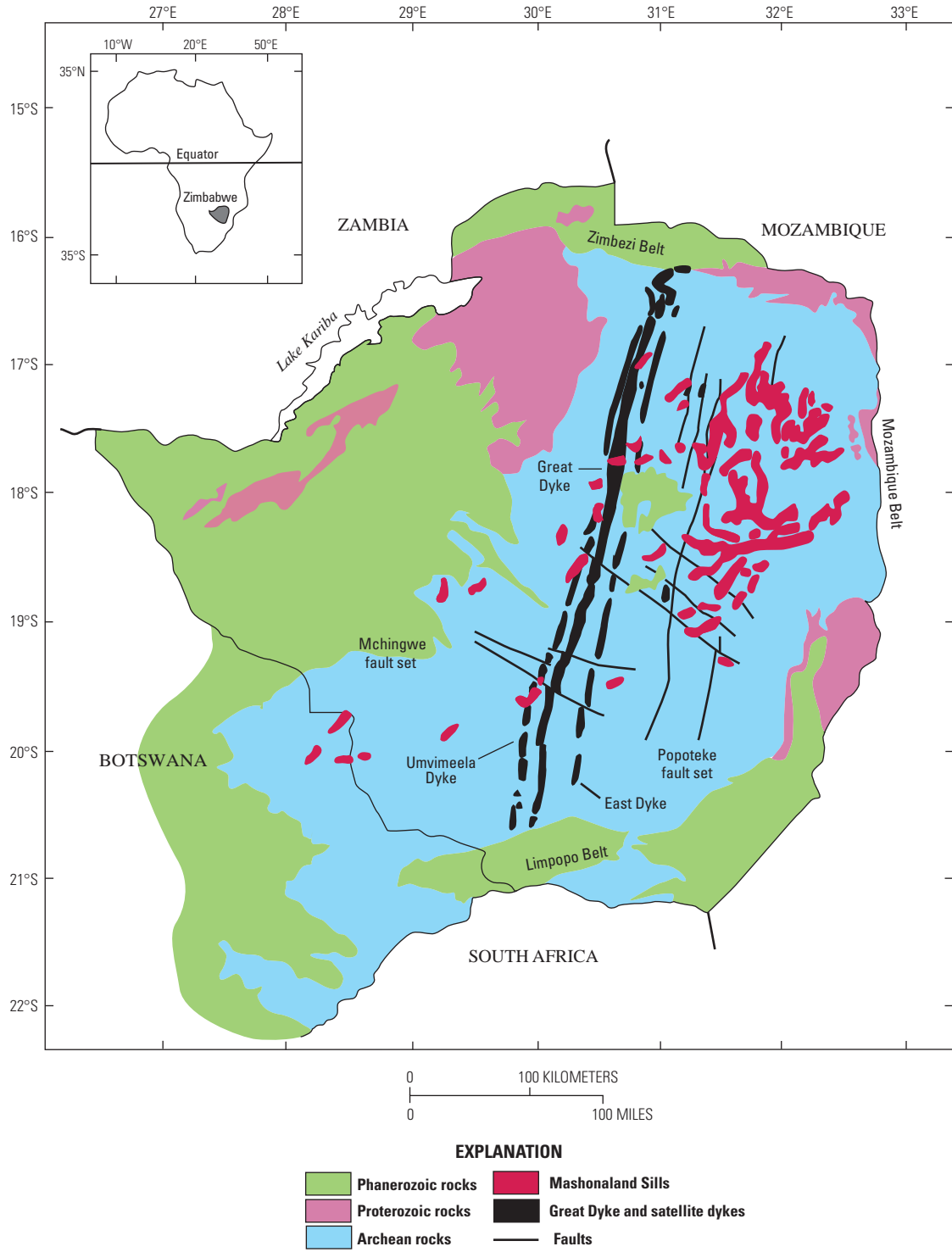
Figure 8.   Geologic map of Zimbabwe showing the extent of the Great Dyke and surrounding satellite dikes, faults, and sills. Modified from Stubbs and others (1999).
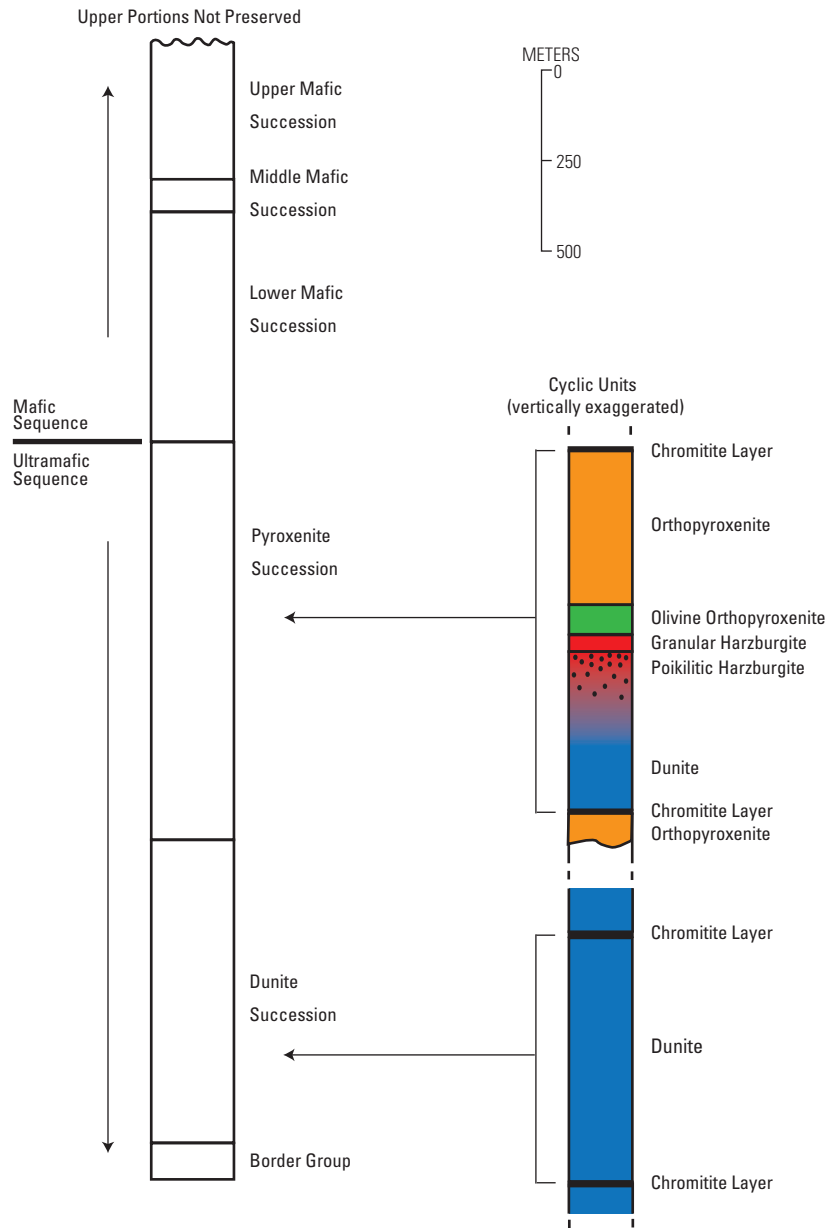
Figure 9. Generalized stratigraphic column of the Great Dyke. Modified from Wilson (1996).

cyclic units. Contacts of the chromitite layers with dunite are generally sharp with disseminated upper and lower contacts observed infrequently. Massive chromitite layers, measuring 10- to 15-cm thick, are located in the Dunite Succession (fig. 9) of the Darwendale Subchamber (Wilson, 1996).

The Pyroxenite Succession, on the other hand, contains cyclic units that start with dunite layers at the base and grade upward through harzburgite into olivine bronzitite and finally a major bronzitite layer at the top (fig. 9). In most cases, the Pyroxenite Succession has a basal chromitite layer that is generally less well developed than those that occur in the Dunite Succession. Only Cyclic Unit 5 contains chromitite layers that are well developed in the lower part of the succession and has been mined for chromite (Wilson, 1996). Six chromitite layers also have been identified at the top of the Ultramafic Sequence, but only two, C1c and C1d, are economically viable and extensively mined (Wilson and Prendergast, 1987).

Of note, the dunite in the Great Dyke is not preserved in surface outcrops due to total replacement by serpentine. However, the degree of serpentinization decreases with depth, such that unaltered dunites occur at depths of about 300 m (Wilson, 1996).

Muskox Intrusion

The country rocks surrounding the Muskox intrusion (Canada) consist of paragneisses and orthogneisses (fig. 10) related to the 1,900 Ma Wopmay orogeny (Hoffman, 1984). Geologic, petrogenetic, paleomagnetic, and geochronological studies suggest that the Muskox intrusion is coeval and possibly cogenetic with the Coppermine flood basalts and MacKenzie dike swarm (Fahrig and Jones, 1969; Irvine and Baragar, 1972; Fahrig, 1987; LeCheminant and Heaman, 1989). The intrusion itself has been divided into five zones: the keel dike, the east and the west marginal zones, the layered series, and the granophyre zone (Irvine, 1980; Barnes and Francis, 1995). The keel dike consists of gabbronorites at the margins, and olivine gabbronorites and picrites in the center. The marginal zone is similar lithologically to the keel dike, containing gabbronorites followed by olivine gabbronorites and picrites. However, there is more orthopyroxene in the gabbronorites and olivine gabbronorites of the marginal zone than in the keel dike. In some cases, the rocks of the marginal zone could be classified as norites.

Irvine (1970) divided the layered series into 25 cyclic units consisting of alternating layers of dunite, peridotite, pyroxenite and gabbro. Each of the cyclic units can be grouped into four megacycles. Ideal cyclic units in layered series of the Muskox intrusion have basal dunite with 1 to 2-percent chromite, overlain by harzburgite with about 1-percent chromite, and an uppermost orthopyroxenite with only trace amounts of chromite. The main chromitite seams occur within the dunite of the cyclic units and are thin (<10 cm) (Day and others, 2008).
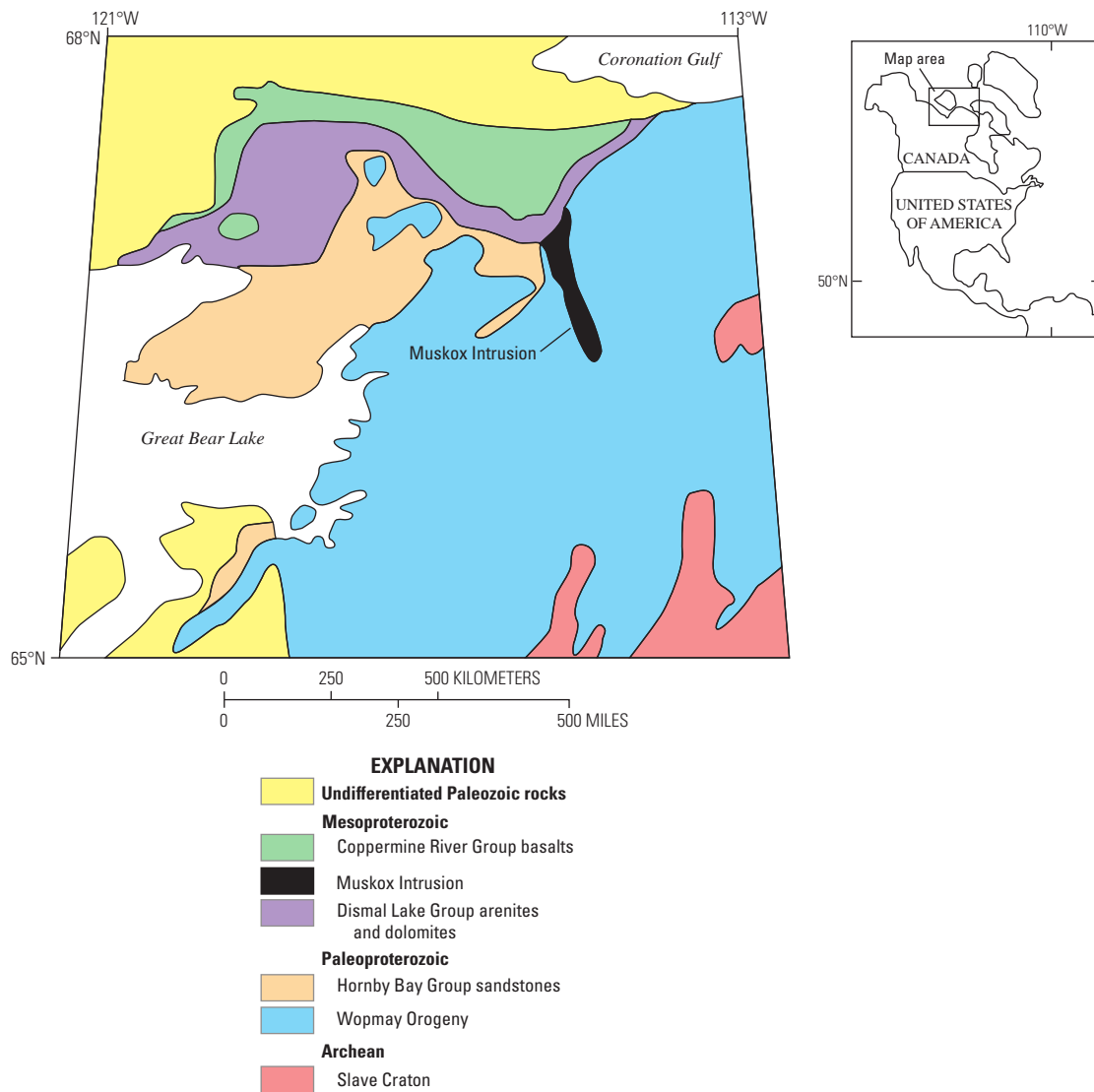
Figure 10.   Location of the Muskox intrusion and surrounding geology. Modified from Barnes and Francis (1995).

Kemi Intrusion

The Kemi intrusion (Finland) strikes northeastward along the Svecokarelidic Peräpohja schist belt on the northern Fennoscandian Shield (fig. 11). The footwall of the layered intrusion consists of Archean granitoids. Either younger mafic volcanic or subvolcanic sills that are 2.15 Ga in age (Sakko, 1971) or a polymict conglomerate of unknown age make up the hangingwall rocks (Alapieti and others, 1989). Albite diabase feeder dikes associated with the subvolcanic sills cut the intrusion. The estimated downdip extension of the intrusion is 2 km, with a downdip angle of 70 degrees (Alapieti and others, 1989). Due to poor surface exposure, little has been reported on the overall thickness.

At the base of the intrusion are ultramafic rocks where the silicate minerals have been completely recrystallized. However, the chromite in this layer, accounting for 15 volume percent (vol%) of the whole rock, has been preserved (Alapieti and others, 1989). The ultramafic layer is below the main chromitite layer, which is overlain by intensely altered peridotitic cumulates that once hosted olivine, chromite, and occasional bronzite as cumulus minerals. Alteration minerals include talc and carbonate, with tremolite found in the upper contact between the main chromitite layer and the peridotitic sequence. The peridotitic sequence is interlayered with 15 chromite-rich seams that vary in thickness from 5 cm to 2.5 m, with the uppermost seam being about 370 m above the main chromitite layer (Alapieti and others, 1989). Pyroxenite occurs as interlayers surrounding the core of the peridotitic sequence, and is also altered. At the top of the intrusion, leucogabbros and anorthosites are the dominant lithologies.
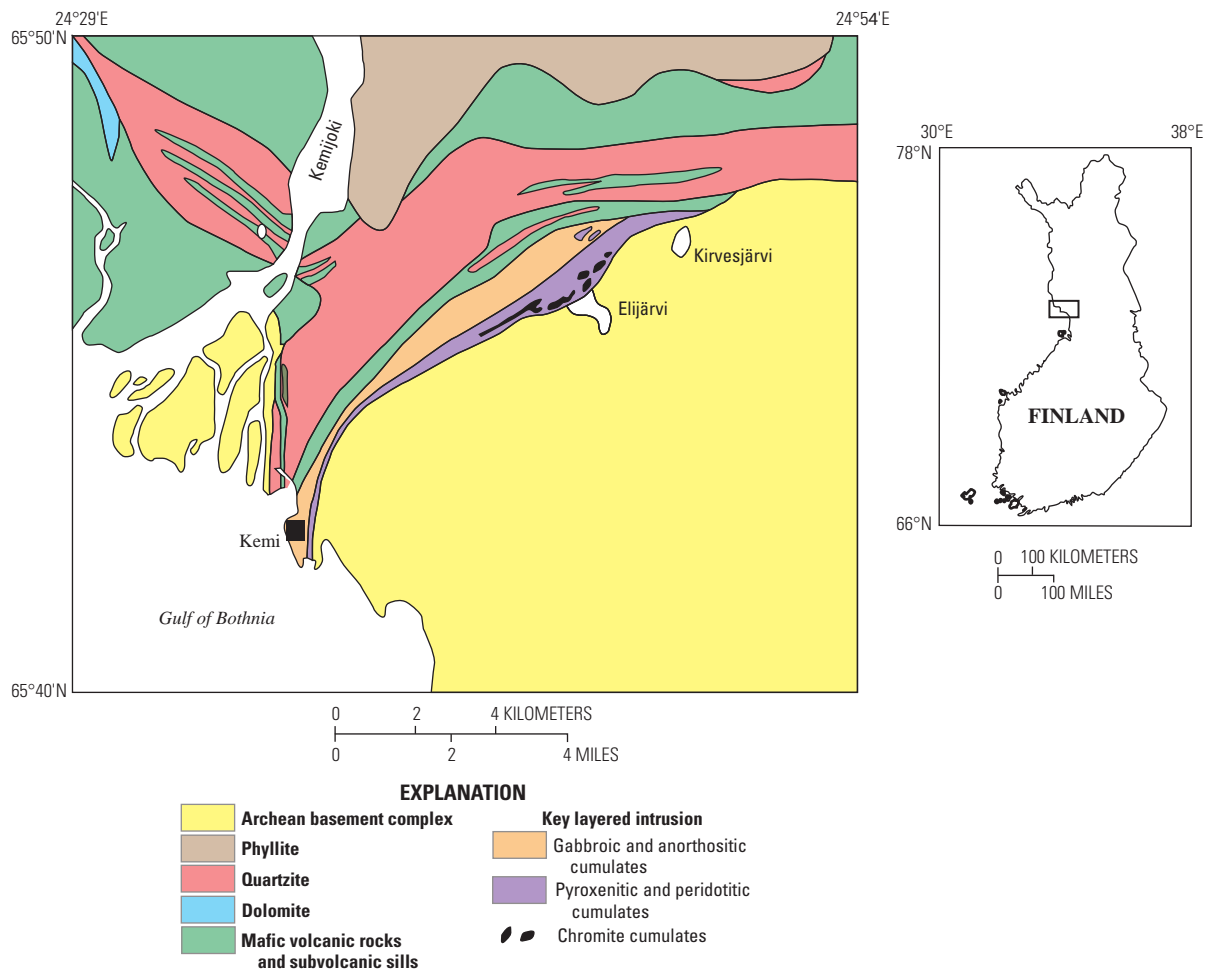
Figure 11.   Geologic map of the region surrounding the Kemi intrusion. Modified from Alapieti and others (1989).

Rum Intrusion

The Rum layered intrusion (Scotland) consists of three divisions: the Eastern Layered Series (ELS), Western Layered Series (WLS), and Central Series (CS) (fig. 12; Power and others, 2000). The ELS contains at least 15 megacyclic units of alternating peridotite (olivine-rich cumulate) and allivalite (plagioclase-rich cumulate or troctolite) that generally dip 10 to 30 degrees toward the center of the intrusion (Butcher and others, 1999). Thin (2 to 5 mm), laterally continuous (>1 km) chromitite seams (chromite >60-percent modal) occur along intercyclic unit contacts (Power and others, 2000; O'Driscoll and others, 2009b). Chromitite seams rarely occur within the ultramafic components of the individual units. However, disseminated chromite occurs throughout the ELS, and is typically found at the junctions of some of the major cycle units.

Discordant bodies of intrusive gabbro are also locally present (Butcher and others, 1999). The chilled margin of the ELS peridotite layer is picritic in composition and, based on textural evidence, the peridotite layers formed from an olivine tholeiite magma rich in olivine (Greenwood and others, 1990).

The WLS and CS contain thin (<20 mm) chromitite seams interlayered with olivine cumulates. The olivine cumulates can be classified as dunites or peridotites, and often exhibit harrisitic or dendritic, skeletal textures (Butcher and others, 1999; O'Driscoll and others, 2006). Disseminated chromium spinel is abundant in these regions as well. The Central Series is formed by peridotites and troctolites, some of which are well-layered, whereas others are highly slumped, brecciated, and veined (Emeleus and others, 1996; Butcher and others, 1999).
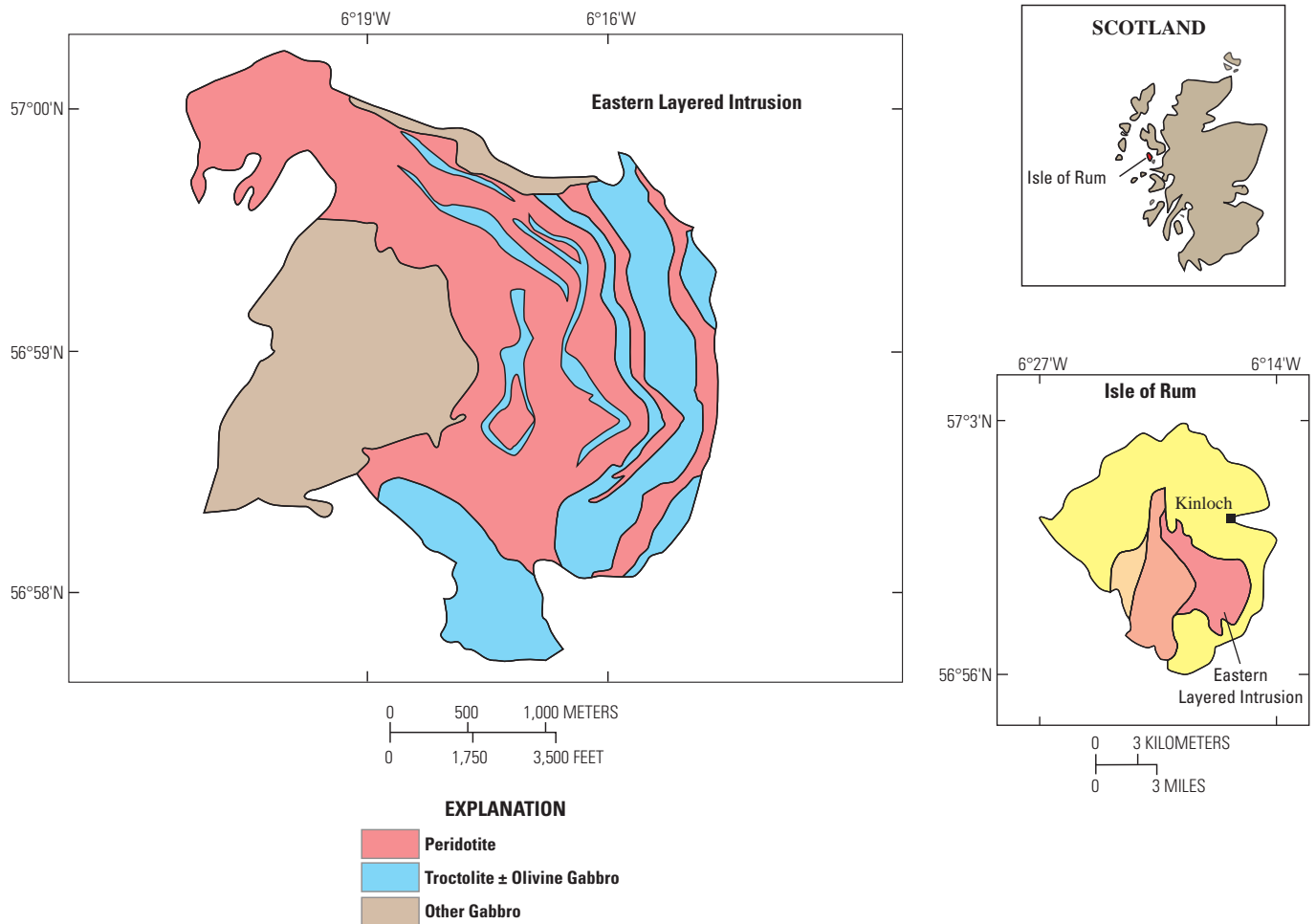
Figure 12. Generalized map of the Rum intrusion with the location of cumulates in the Eastern Layered Series identified. Modified from O'Driscoll and others (2009a).

Burakovsky Intrusion

The Burakovsky intrusion in southern Karelia, Russia, is a mafic pluton in the Fennoscandian Shield. The complex is a layered igneous body containing an Ultramafic Series (85 percent dunite) and a Mafic Series (mostly gabbros) (Higgins and others, 1997). The Ultramafic Series forms the lowest part of the layered intrusion (3- to 3.5-km thick; Sharkov and others, 1995) and is divided into two subzones: a lower dunite sequence (olivine ± chromite), and an upper peridotite sequence (olivine + clinopyroxene ± chromite and rare chromite cumulates) (fig. 13). The dunite rocks have been described as mesocumulates or orthocumulates, with the primary cumulus phases being olivine and chromite. The largest chromitite seam, the Main Chromite Horizon, is 3- to 4-m thick and situated at the top of the peridotite subzone. The pyroxenite zone, 0.2-km thick, is located above the ultramafic zone and contains orthopyroxene ± chromite and orthopyroxene ± clinopyroxene ± chromite ± olivine (Sharkov and others, 1995). Overlying the pyroxenite zone are the gabbronite zone, pigeonite-gabbronorite zone, and magnetite-gabbronorite zone. The gabbronorite zone, ~1.1-km thick, consists of banded cumulates (orthopyroxene, orthopyroxene + clinopyroxene ± chromite, plagioclase + orthopyroxene ± clinopyroxene) in the lower section and massive cumulates (plagioclase + orthopyroxene + clinopyroxene, plagioclase) in the upper section. The pigeonite-gabbronorite zone, 1.2-km thick, hosts plagioclase + inverted pigeonite, pigeonite-augite, and plagioclase cumulates. The magnetite-gabbronorite zone is 0.8-km thick and contains plagioclase + inverted pigeonite and clinopyroxene and titanomagnetite mineral assemblages.

Niquelândia Complex

The Niquelândia Complex in Brazil is part of the Goiás Massif, and consists of two main sequences: the lower unit (LS) and the upper unit (US) (figs. 14 and 15; Girardi and others, 1986). The LS occurs in the eastern part of the body and includes a basal gabbro zone (BGZ), a basal peridotite zone (BPZ), a layered ultramafic zone (LUZ), and a layered gabbro zone (LGZ). The BGZ contains predominantly gabbronorite with minor pyroxenite, whereas the LUZ hosts dunite, minor harzburgite, and pyroxenite (Pimentel and others, 2004). Dunite has been partially serpentinized and contains relicts of olivine and minor orthopyroxene in a matrix of lizardite, chrysolite, and talc (Girardi and others, 2006). The LGZ is dominated by gabbronorite.

The US is located in the western part of the body and consists of an upper gabbronorite zone (UGAZ) and an upper amphibolite zone (UA). Rocks within these zones include leuco-troctolites, anorthosites, and minor pyroxenites (Pimentel and others, 2004). The chromitites occur in two horizons, at the boundary between the BPZ and LUZ and in the LUZ (Girardi and others, 1986). The thicknesses of the chromitite seams vary from 5 to 30 cm and can reach as much as 1 m locally (Girardi and others, 2006).
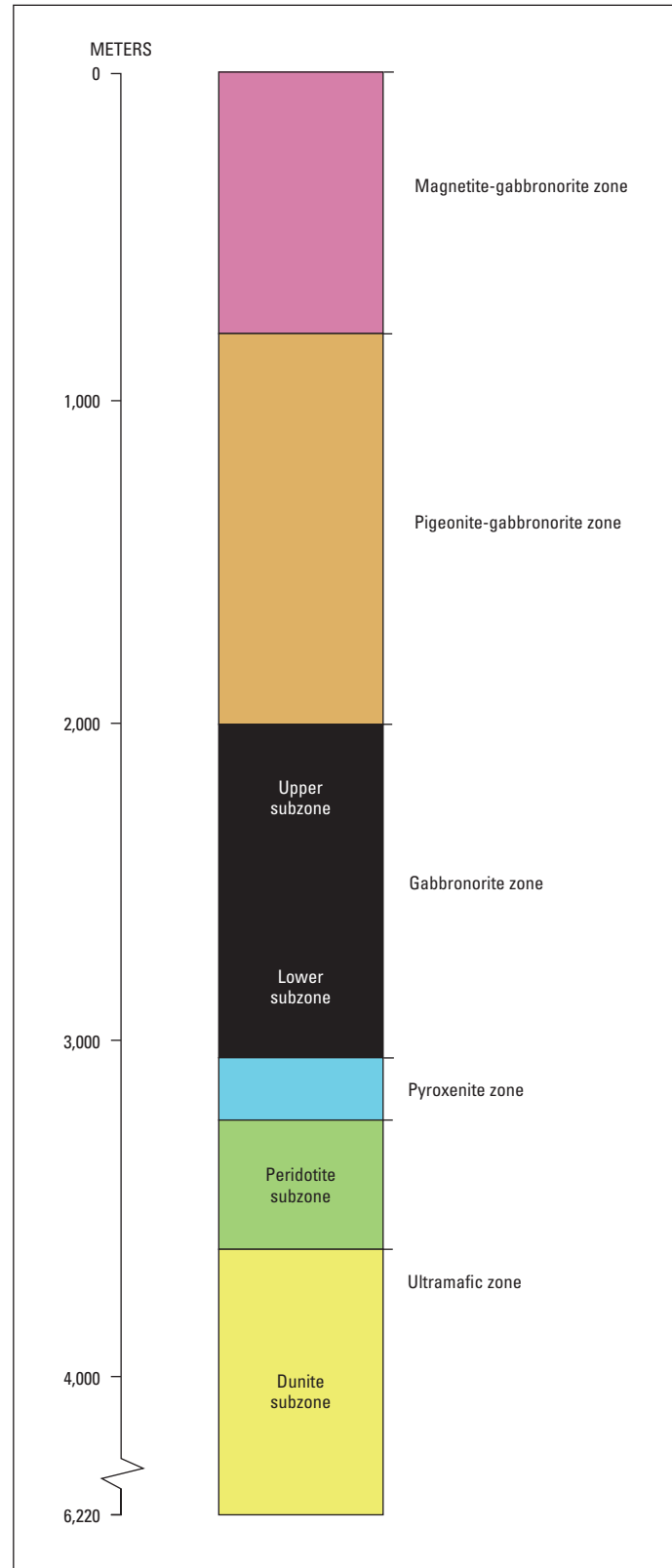
Figure 13. Stratigraphic profile of the layered series in the Burakovsky intrusion. Modified from Higgins and others (1997). The entirety of the ultramafic zone, ~3,000-meters thick, is not shown.
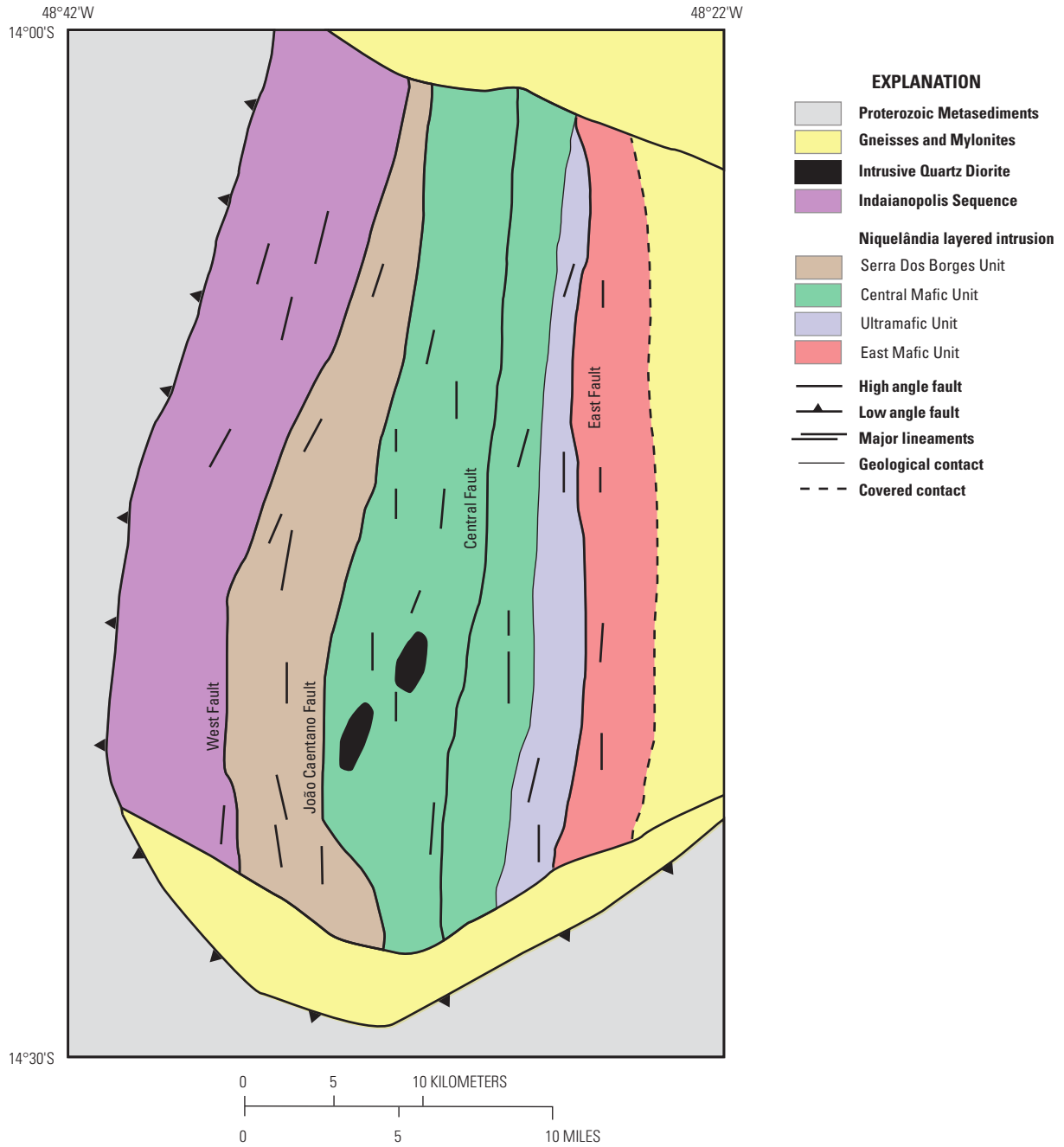
Figure 14. Simplified map of the Niquelândia Complex. Modified from Ferreira-Filho and others (1992).
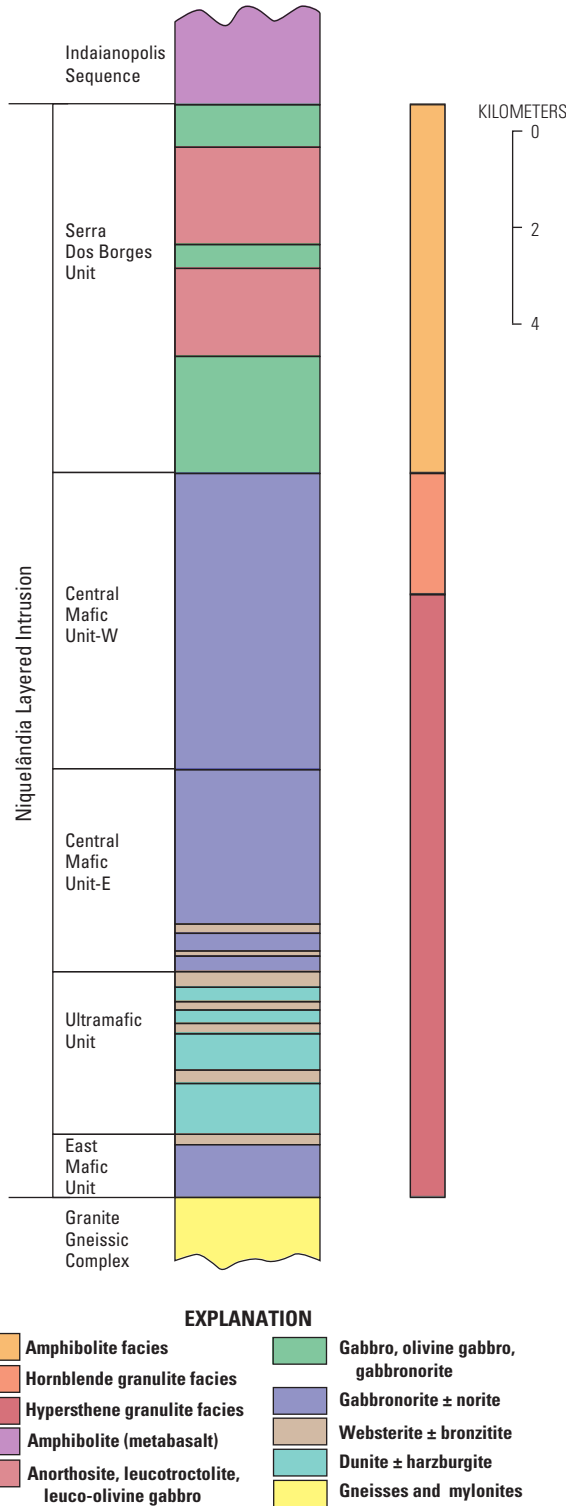
Figure 15.   Stratigraphic profile of the Niquelândia Complex. Modified from Ferreira-Filho and others (1992).

Ipueira-Medrado Sill

The Ipueira-Medrado Sill in the Bahia State of Brazil is part of the Jacurici complex, a north-south trending swarm of chromite-mineralized, mafic-ultramafic bodies (fig. 16) located in the northeast segment of the São Francisco cration and thought to be emplaced in granulite-gneiss terranes of the Caraíba granulite complex (Barbosa and others, 1996; Marques and Ferreira-Filho, 2003). The sill is divided into three zones (fig. 17): Marginal, Ultramafic, and Mafic (Marques and Ferreira-Filho, 2003). The Ultramafic zone consists of a Lower Ultramafic, Main Chromitite, and Upper Ultramafic layers. The Lower Ultramafic Unit contains interlayered dunites, minor harzburgites, and chain-textured chromitite. Chain-textured chromitite is characterized by fine-grained aggregates of chromite surrounding larger orthopyroxene crystals, and massive chromitites The Main Chromitite layer is 5- to 8-m thick and consists of chain-textured chromitite. The Main Chromitite layer has three sublayers: the lowest sublayer, chain-textured layer, and upper massive chromitite sublayer. The lowest sublayer consists of massive or "lumpy" ore that sticks together and is 0.5- to 1-m thick (Marques and Ferreira-Filho, 2003). The chain-textured sublayer is 0.3- to 0.6-m thick. The upper sublayer also consists of massive chromitite (lumpy ore) that is 4- to 6-m thick and continuous throughout the sill. The Upper Ultramafic Unit consists mainly of harzburgite with minor chain-textured chromitite and dunite. In the Upper Ultramafic Unit, the abundance of pyroxene progressively increases until the dominant rock type at the top is an orthopyroxenite. At this level, magmatic intercumulus amphibole is as abundant as 20 vol% (Marques and Ferreira-Filho, 2003). The marginal zone contains highly sheared gabbro and pyroxene-rich harzburgite. In the Mafic zone, leuconorites and melanorites dominate, and are partially metamorphosed under amphibolite facies conditions.
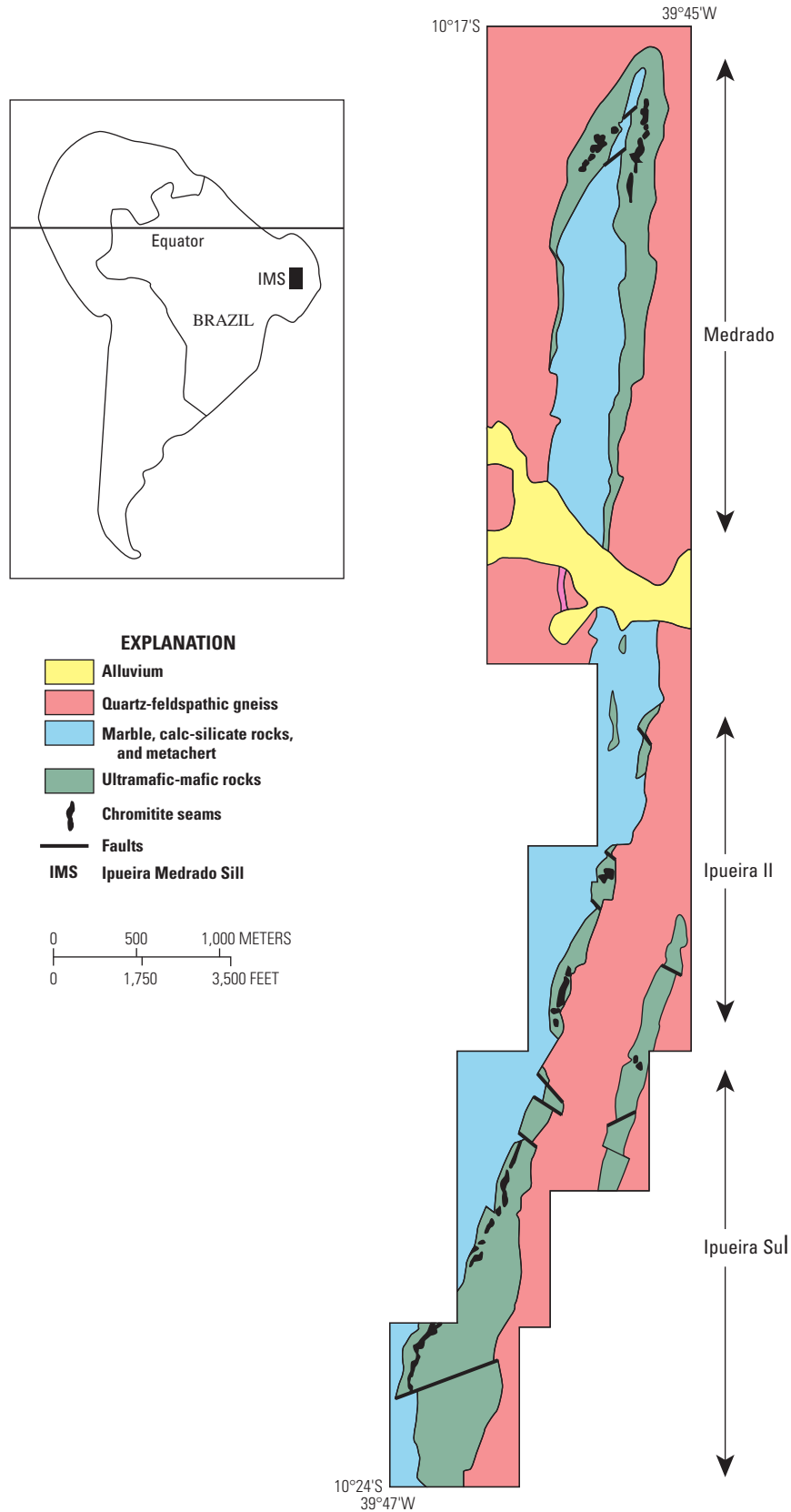
Figure 16.   Simplified geologic map of the Ipueria-Medrado Sill. Modified from Marques and Ferreira-Filho (2003) after unpublished data from the Geology Division of the Mineração Vale do Jacurici, South America.

Mafic Zone
<40 meters

Upper
Ultramafic Unit
<50 meters

Harzburgite with
minor Dunite

Main Chromitite Layer
5–8 meters

Ultramafic Zone
<250 meters

Lower
Ultramafic Unit

100–180 meters

Dunite interlayered
with Harzburgite

Marginal Zone
5–20 meters

EXPLANATION

Norite

Gabbro

Chain-textured chromitite

Chromitite (Lumpy ore)

Pyroxene-rich harzburgite

Harzburgite

Dunite

Figure 17.   Generalized stratigraphic column of the Ipueira-Medrado Sill.
Modified from Marques and Ferreira-Filho (2003).

Campo Formoso Complex

The Campo Formoso Complex in Brazil is located in the northern part of the São Francisco craton, roughly 50 km west of the Ipueira-Medrado Sill (Marques and Ferreira-Filho, 2003). The basement rocks consist of gneisses and migmatites (fig. 18). The chromitite seams are interlayered with serpentinized and chloritized peridotites, and vary in thickness from a few centimeters to 15 m (Girardi and others, 1986; Garuti and others, 2007). Pyroxenite, gabbro, and norite occur in some outcrops.

The variety of ores found in the open-pit mines in the southwestern tip of the ultramafic belt include lumpy (massive ore that sticks together), stratified (layered), disseminated, and net-textured types (Lord and others, 2004). Evidence of lateral variation is suggested between the seven economic chromite seams, which vary from 5- to 15-m thick and dip approximately 50-degrees east. However, due to low-grade regional metamorphism, later granitic intrusion, and strong hydrothermal alteration, almost no primary igneous lithology has been preserved. Furthermore, reconstruction of the original stratigraphy is problematic due to faulting and deformation. Relict grains of olivine, chromite, clinopyroxene, and orthopyroxene are rare (Girardi and others, 2006). Hydrothermal minerals include serpentine, talc, calcite, dolomite, tremolite, and magnetite. Interpretation of bulk-rock geochemistry by Lord and others (2004) suggests that the currently exposed cross section originally contained 400 to 500 m of peridotite overlain by pyroxenite.
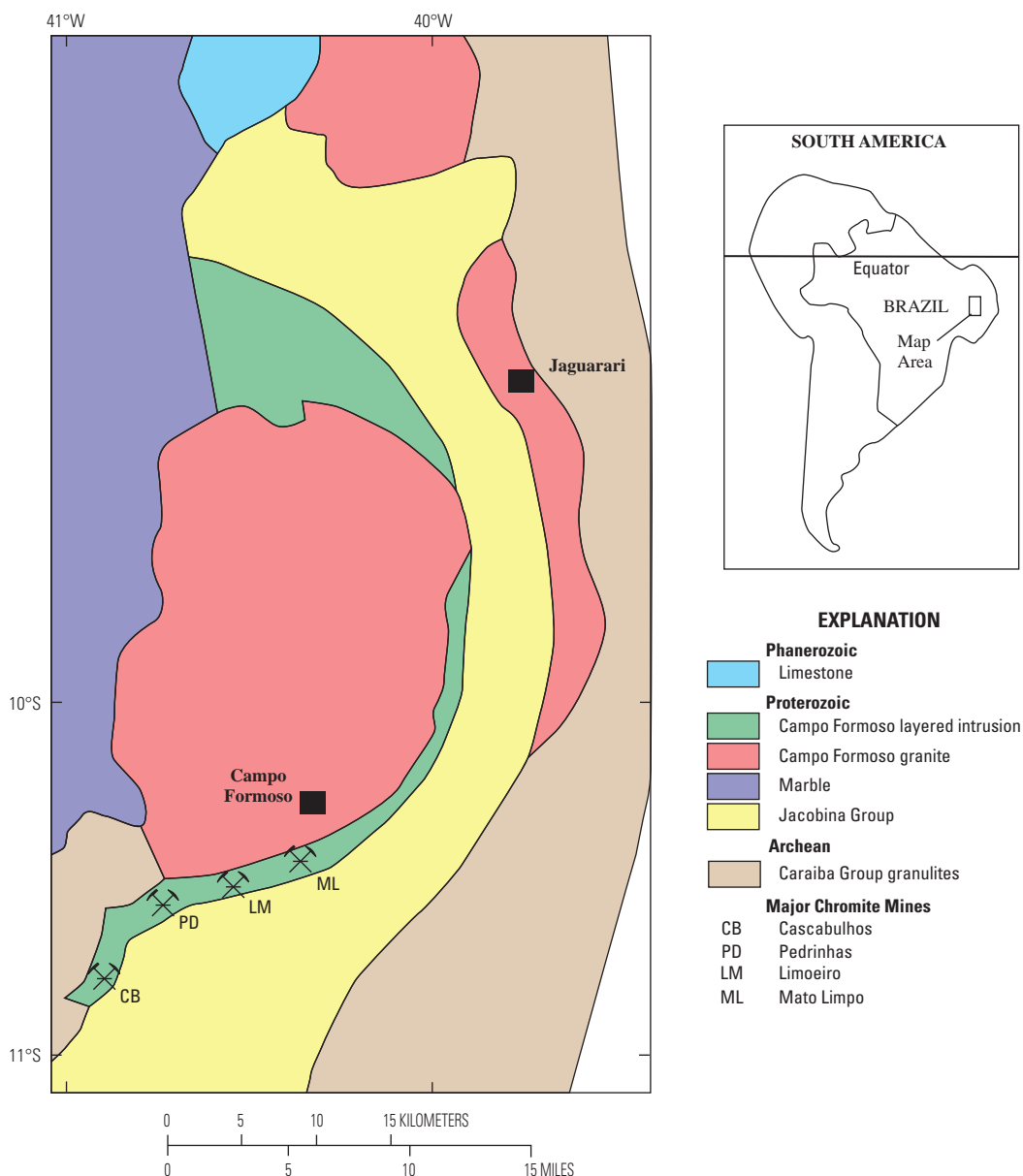
Figure 18. Location of Campo Formoso Complex and surrounding geology. Modified from Garuti and others (2007) after de Deus and others (1982).

Fiskenæsset Anorthosite Complex

The Fiskenæsset anorthosite complex in West Greenland is a layered sheet of anorthosite, leucogabbro, gabbro, peridotite, dunite, and chromitite, located ~20 km southeast of the Isua Greenstone Belt (Appel and others, 2002). The complex occurs within a terrane of amphibolite and granulite facies gneisses that have been folded several times. As a result, most of the rocks have been partly or completely recrystallized or deformed during metamorphic and tectonic events (Myers, 1976). However, most of the magmatic features are still recognizable. Chromitite layers are found within nearly all anorthosite horizons and, in rare cases, in smaller ultramafic units of the complex (Ghisler, 1976). Anorthosite is the dominant rock of the complex and is intercalated with pyribolite and amphibolite layers on all scales (Ghisler, 1970). The gneisses of the Fiskenæsset region are plagioclase-rich and locally contain abundant plagioclase feldspar. The main stratigraphic units, from top to bottom, are: Lower Gabbro, Ultramafic, Lower Leucogabbro, Middle Gabbro, Upper Leucogabbro, Anorthosite, and Upper Gabbro (fig. 19; Polat and others, 2009). The main chromitite layers, as much as 20-m thick, predominantly occur in the Anorthosite unit at the top of the Upper Leucogabbro unit.
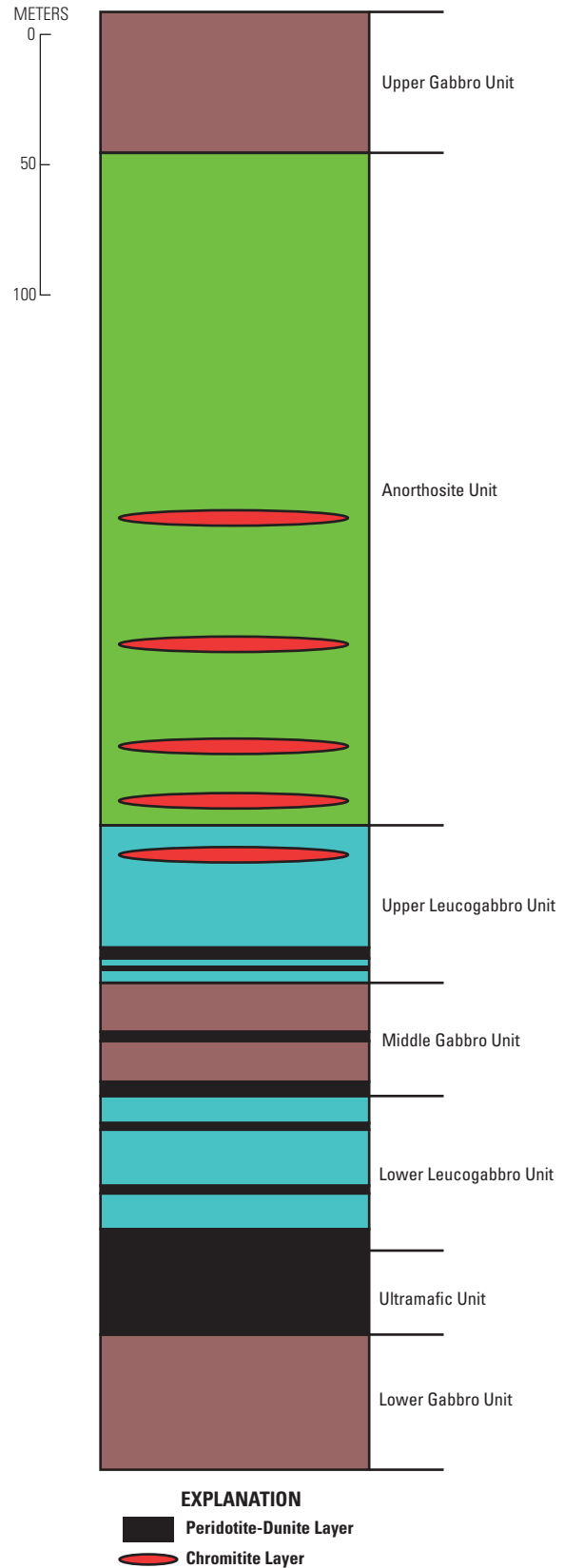
Figure 19. Simplified stratigraphic profile of the Fiskenæsset anorthosite complex. Modified from Myers (1985) after Polat and others (2009).

Bird River Sill

The Bird River Sill is a mafic-ultramafic layered body that intruded the Archean supracrustal rocks of the Bird River greenstone belt in the Superior Province of Manitoba, Canada (fig. 20). This synvolcanic intrusion is ~700-m thick, extends for more than 20 km, and has been weakly deformed and metamorphosed to a lower amphibolite facies (Coates and others, 1979; Talkington and others, 1983; Ohnenstetter and others, 1986). The Bird River Sill has been divided into a basal sulfide zone, a layered ultramafic sequence, and an upper gabbro zone.

The ultramafic sequence is ~200-m thick and includes dunite, peridotite, chromitite, and pyroxenite (Talkington and others, 1983; Theyer and others, 2001). Trueman (1971) subdivided the ultramafic sequence into 19 layers of serpentized dunite and lherzolite, with 18 layers of interbanded chromite-bearing peridotite and serpentized peridotite. Disseminated chromite is generally ubiquitous throughout the ultramafic sequence, whereas the chromitite seams (>80-percent chromite) are located in the upper section of the ultramafic sequence.

The chromitite seams have been identified as Lower Main, Banded Diffuse, Upper Main, and Upper Paired (Scoates and others, 1989; Theyer and others, 2001). A Lower Group chromitite layer and a Disrupted Chromitite layer have also been identified within the Bird River Sill (Scoates and others, 1989). On the Page property, chromitite pebbles are evident in the Disrupted Chromitite Layer. In addition, chromitite units located on the Page property (fig. 20) show a complex array of chromitite fragments that are the result of tectonically disrupted chromitite layers. The chromitite fragments are offset by faults and vary from 1 cm to several meters in length (Theyer and others, 2001). Similar stratigraphy has been noted at the Chrome property (Scoates and others, 1989).

The gabbro zone consists of anorthositic gabbro, which is in places glomeroporphyritic, hornblende gabbro, and anorthosite. Primary magmatic sulfides are confined to the basal sulfide zone and include pyrrhotite, pentlandite, chalcopyrite, and pyrite (Talkington and others, 1983).
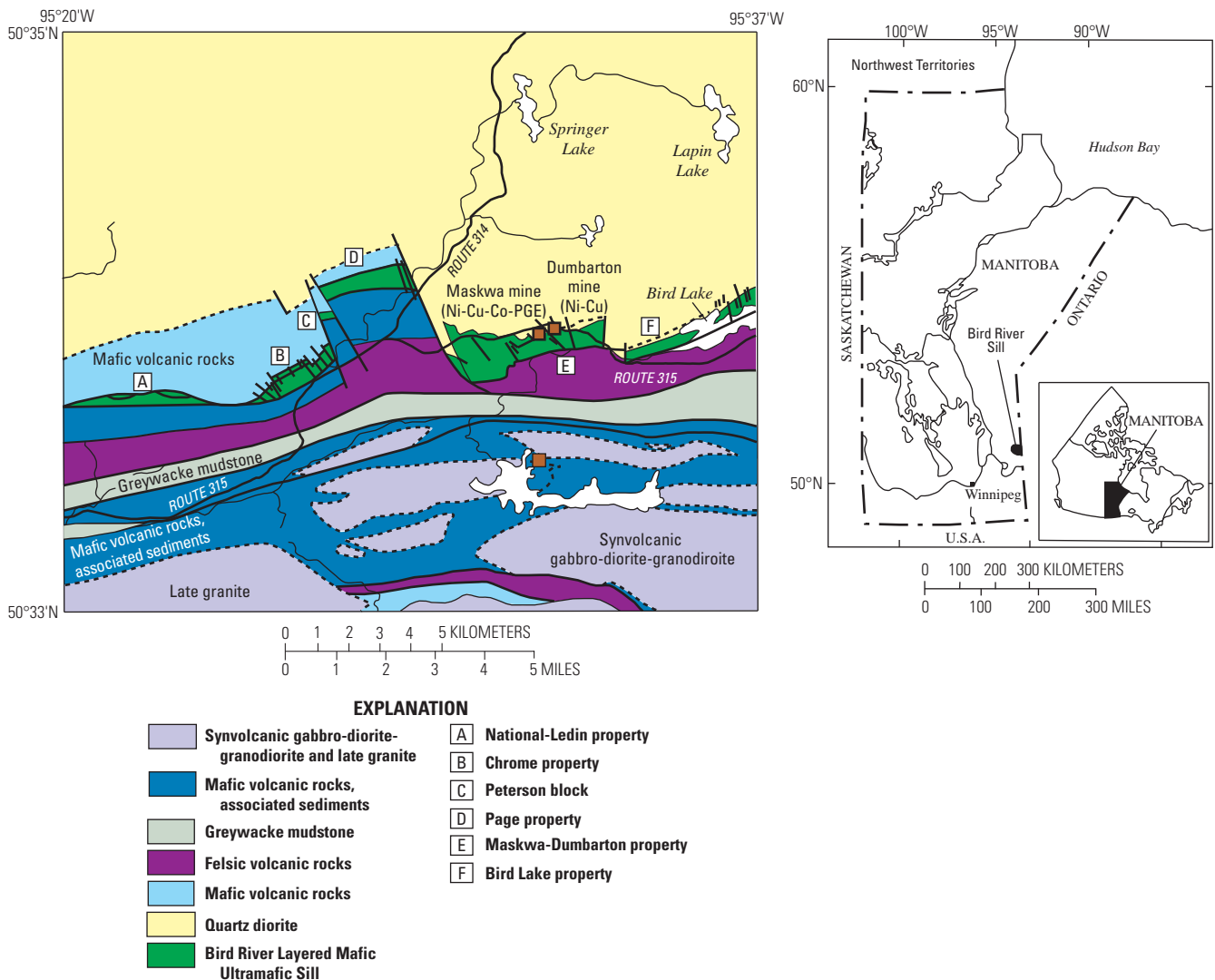
Figure 20.   Location of the Bird River Sill. Modified from Theyer and others (2001).

Structural Settings and Controls

Large stratiform chromite deposits, such as those found in the Bushveld Complex, typically formed in mid-continent anorogenic provinces during the Archean and Proterozoic. However, there is considerable debate regarding the structural control of stratiform chromite deposits, because several intrusions (for example, the Muskox, Great Dyke, Kemi, and Burakovsky) record evidence that rifting may have been involved in their formation. In these cases, an upwelling magma or mantle plume exploited preexisting discontinuities, such as shears in the Muskox intrusion and uncomformities in the Kemi intrusion. Advanced rifting may have lead to the eruption of continental flood basalts.

To explain the formation of the Great Dyke, several tectonic controls have been proposed, including wrench tectonics from an aborted rift system, failed greenstone belt formation, and vertical tectonics due to crustal flexure (Wilson and Prendergaast, 1987, and references therein). A pure shear model has also been suggested, such that the Great Dyke would have been emplaced during a period of crustal extension (Wilson, 1987). On a broader scale, emplacement of stratiform intrusions, such as the Great Dyke, may be related to rifting associated with major orogenic cycles that result from plate-tectonic processes (Hatton and Von Gruenewaldt, 1990).

Geophysical Characteristics

Magnetic Signature

The magnetic signature of large, layered mafic-ultramafic intrusions mainly arises due to the proportion of magnetite seams or other secondary magnetite-bearing lithologies such as peridotites (where magnetite forms during serpentinization of olivine), which are low in chromite. Furthermore, when present, chromite does not substantially contribute to rock magnetic properties, because its intrinsic magnetic susceptibility (the degree of magnetization in response to an applied magnetic field) is significantly lower than magnetite (table 6). As a result, investigations into the magnetic characteristics of layered intrusions have focused on the contained magnetite or the magnetic properties of the intrusion as a whole, not the chromite or individual chromitite seams. Other minerals besides magnetite that may add to the magnetic signature of rocks in layered complexes include titanomagnetite (also referred to as magnetite-ulvöspinel), pyrrhotite, paramagnetic mafic silicates, such as olivine and pyroxenes, and diamagnetic plagioclase (Ferré and others, 2009). However, like chromite, their contribution is largely insignificant compared to magnetite (table 6).

Table 6. Intrinsic magnetic susceptibilities of common minerals found in mafic-ultramafic layered intrusions.

[K equals the induced magnetization (M), in amperes per meter (A/m) divided by the applied field (H, in A/m) such that K is dimensionless in the International System (SI)]

Minerals	Magnetic susceptibility $K_{intr} 10^6$ [SI]	References
Olivine (FO_{70})	1,088	Ferre and others (2009)
Olivine (FO_{80})	722	Ferre and others (2009)
Olivine (FO_{85})	539	Ferre and others (2009)
Orthopyroxene	1,898	Ferre and others (2009)
Clinopyroxene	1,219	Ferre and others (2009)
Magnetite	2,500,000	Heider and others (1996)
Ilmenite	1,900	Clark (1997)
Chromite	1,770	Ferre and others (2009)
Pyrrhotite	300,000	Dekkers (1990)
Plagioclase	−14	Borradaile and others (1987)

Rock magnetic data for rocks of the Banded Series in the Stillwater Complex reveal that magnetite inclusions within plagioclase crystals are the main source of primary natural remanent magnetization (NRM) (Saxton and Geissman, 1985; Geissman and Harlan, 1986). However, secondary magnetite that formed during alteration of olivine to serpentine is more significant to aeromagnetic data analyses, because the intensity of NRM and the magnetic susceptibility of secondary magnetite is greater than primary magnetite (Blakely and Zientek, 1985). This can be seen in the magnetic susceptibilities of samples that contain olivine, as they are generally several orders of magnitude greater than samples without olivine (table 7). Consequently, aeromagnetic anomalies, such as those mapped in 1978 by the Anaconda Minerals Company (fig. 21), show banding that is approximately coincident with the olivine-bearing zones of the Stillwater Complex and surrounding area.

Provided sufficient concentrations of magnetic minerals are present, aeromagnetic data can be used to identify magnetic anomalies in layered mafic-ultramafic intrusions. The distribution of the magnetic minerals within the layered complexes, as well as the relationships between the intrusions and surrounding terranes, can then be assessed. Furthermore, by transforming the aeromagnetic anomalies into pseudogravity anomalies using Poisson's relation (Baranov, 1957) and differentiating in the direction of maximum horizontal gradient, magnetic boundaries of layered complexes can be mapped if the boundaries are assumed to be abrupt and vertical (Cordell and Grauch, 1982; Blakely and Zientek, 1985; Blakely and Simpson, 1986).

For example, aeromagnetic anomalies mapped over the mafic and ultramafic rocks of the Stillwater Complex range from 50 to 300 nanotesla (nT) and are generally parallel to

Table 7.   Magnetic properties of rock samples from the Stillwater Complex.

[From Blakely and Zientek, 1985; emu, electromagnetic unit]

Sample	Susceptibility (x10⁻⁶ emu)	Lithology
Banded Series[a]		
83MAP4	44	Plagioclase-bronzite cumulate
83MAP4a	42	Plagioclase-bronzite cumulate
83MAM13	22	Plagioclase-bronzite cumulate
83MAP48	18	Plagioclase-bronzite cumulate
83MAP48a	18	Plagioclase-bronzite cumulate
83MAP26	16	Plagioclase-bronzite cumulate
83MAP26a	12	Plagioclase-bronzite cumulate
83MAP26b	14	Plagioclase-bronzite cumulate
83MAP22	26	Plagioclase-augite-bronzite cumulate
83MAP56	30	Plagioclase-augite-bronzite cumulate
83MAM26	2,528	Plagioclase-olivine cumulate
83MAM26a	2,462	Plagioclase-olivine cumulate
83MAM28	8	Plagioclase cumulate containing pyroxene
83MAM29	64	Plagioclase cumulate containing pyroxene
83MAM29a	88	Plagioclase cumulate containing pyroxene
Ultramafic Series[b]		
80MVL9	1,202	Olivine cumulate (fresh)
80MVL9a	430	Olivine cumulate (fresh)
81MVL109	212	Bronzite cumulate (fresh)
81MVL109a	180	Bronzite cumulate (fresh)
81MVL137	462	Bronzite-olivine cumulate (fresh)
81WFL16	122	Bronzite cumulate (serpentinized)
81WFL20	1,578	Olivine cumulate (serpentinized)
81WFL20a	2,328	Olivine cumulate (serpentinized)
81WFL23	120	Bronzite-olivine cumulate (serpentinized)
81WFL23a	102	Bronzite-olivine cumulate (serpentinized)

[a]Hosts the platinum-group element-bearing sulfides.

[b]Hosts the chromite-bearing seams.

the layering of the intrusion (fig. 21; Blakely and Zientek, 1985). Using gradient analyses techniques discussed by Cordell and Grauch (1982) and streamlined by Blakely and Simpson (1986), the location of the edges of magnetic bodies of the Stillwater Complex and vicinity were then approximated (fig. 22; Blakely and Zientek, 1985). However, gradient analysis does not account for the amplitude of the magnetic anomalies, because the calculated magnetic boundaries represent both intensely magnetized rocks and less magnetic boundaries. As a result, Blakely and Zientek (1985) compared the calculated magnetic boundaries with the original aeromagnetic survey to identify boundaries between magnetic rocks which are more and less magnetic (figs. 21 and 22). With significant magnetic contacts established, the geologic significance of the magnetic boundaries using appropriately scaled geologic maps could be subsequently determined (fig. 23). In addition to defining the location of magnetic boundaries, major disruptions in aeromagnetic anomaly patterns that strike across the Stillwater Complex provide insight into the potential presence of fault zones (fig. 23).

Although aeromagnetic data are useful in defining boundaries of magnetite-bearing stratiform complexes, the presence of iron formations or other highly magnetic rock units that are not genetically related to the layered intrusions can obscure magnetic anomalies within the layered sections (fig. 23). Proximity to the banded iron formation makes it difficult to isolate magnetic anomalies caused by the lowest layers of the Stillwater Complex (Blakely and Zientek, 1985). Only in the Mountain View area are the positions of the anomalies correlated with the Peridotite zone of the Ultramafic Series (figs. 21–23).

Overall, layered mafic and ultramafic intrusions contain magnetic minerals in sufficient concentrations, allowing aeromagnetic data to record significant anomalies. These anomalies provide constraints on the distribution of magnetic minerals in the intrusions as well as the relation of these intrusions to the surrounding terrane. Magnetic boundaries of layered mafic-ultramafic intrusions can also be defined when aeromagnetic anomaly data are transformed using gradient analyses techniques and interpreted in conjunction with structural and petrologic fieldwork. For these reasons, aeromagnetic surveys may prove useful when investigating the geologic and structural aspects of a layered mafic-ultramafic intrusion, its tectonic history, and mineralogical composition.

Gravity Signature

No studies address the gravity properties of individual chromitite seams within large, layered mafic-ultramafic intrusions. Gravity data on the layered complexes as a whole can be useful in assessment purposes, however, in that they may provide limits on the extent of the buried sections of the intrusions. As such, a brief review of key gravity studies on some of the major stratiform complexes follows.

Early gravity studies of the Bushveld Complex revealed that the Bushveld Complex is not a pure lopolith (Cousins, 1959; Smit and others, 1962). Instead, the complex consists of four lobes: a western, northern, eastern, and southeastern section. Subsequent gravimetric and magnetic modeling (Molyneux and Klinkert, 1978; De Beer and others, 1987), as well as geoelectrical and seismic reflectance studies (Odgers and others, 1993), indicate that the rocks of the Rustenburg Layered Suite dip 10 and 25 degrees toward the center of the complex (Cawthorn and Webb, 2001). Gravity estimates indicate that the granite's thickness in the eastern Bushveld Complex is between 2.5 and 6 km (Molyneux and Klinkert, 1978; Hattingh, 1980). For the layered mafic sequence in the eastern lobe, gravity data suggest the maximum thickness is about 5 km. However, these estimates are complicated by the complex regional geological setting. In particular, the Travsvaal basin has an unknown thickness with rock units that record different densities (De Beer and others, 1987).
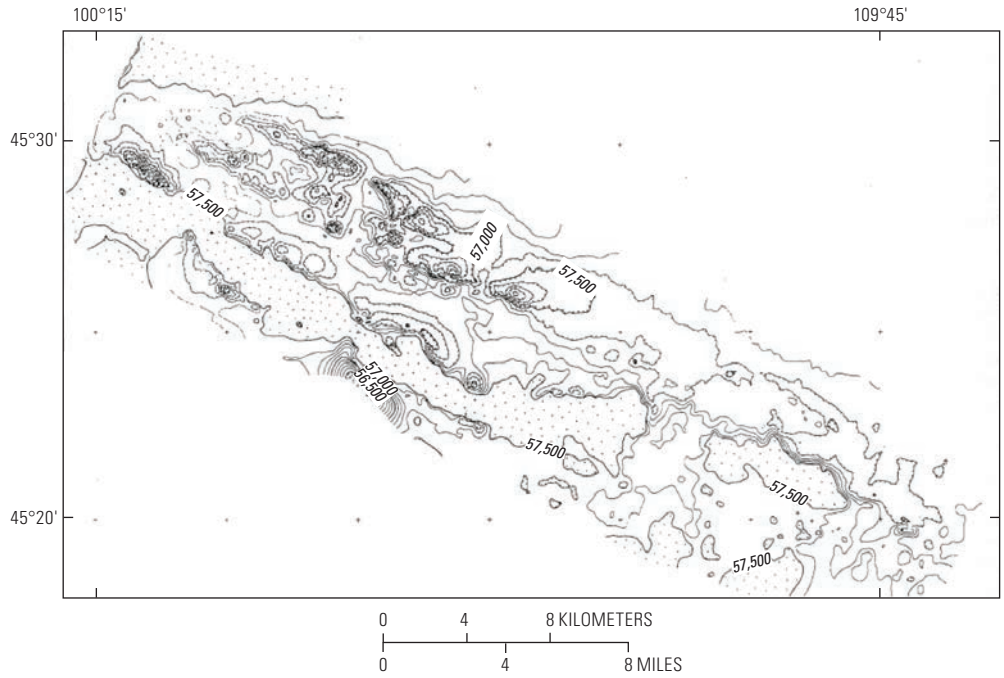
Figure 21. Aeromagnetic data over the Stillwater Complex (Mountain View area), recorded by Anaconda Minerals Company in 1978. Contour interval 100 nanotesla (nT) for magnetic intensities less than 57,500 nT. Stipple areas without contours denote magnetic intensities greater than 57,500 nT. Gradient lines indicate closed lows. From Blakely and Zientek (1985, fig. 3).
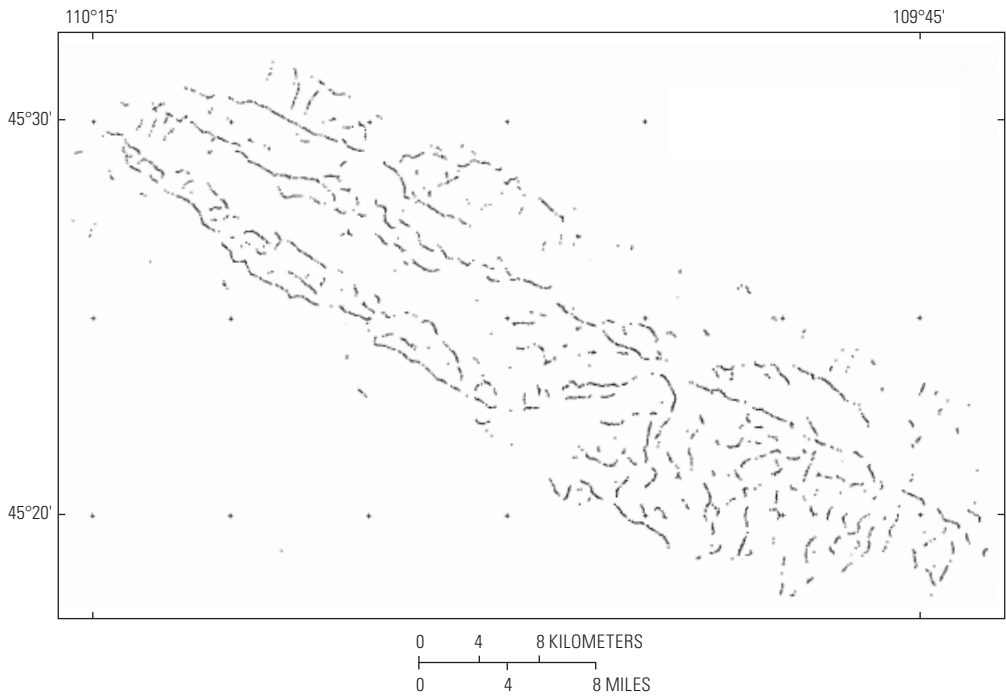
Figure 22. Locations of magnetic boundaries within the Stillwater Complex and adjacent rocks, calculated from aeromagnetic data. Boundaries assumed to be abrupt and vertical. From Blakely and Zientek (1985, fig. 3).
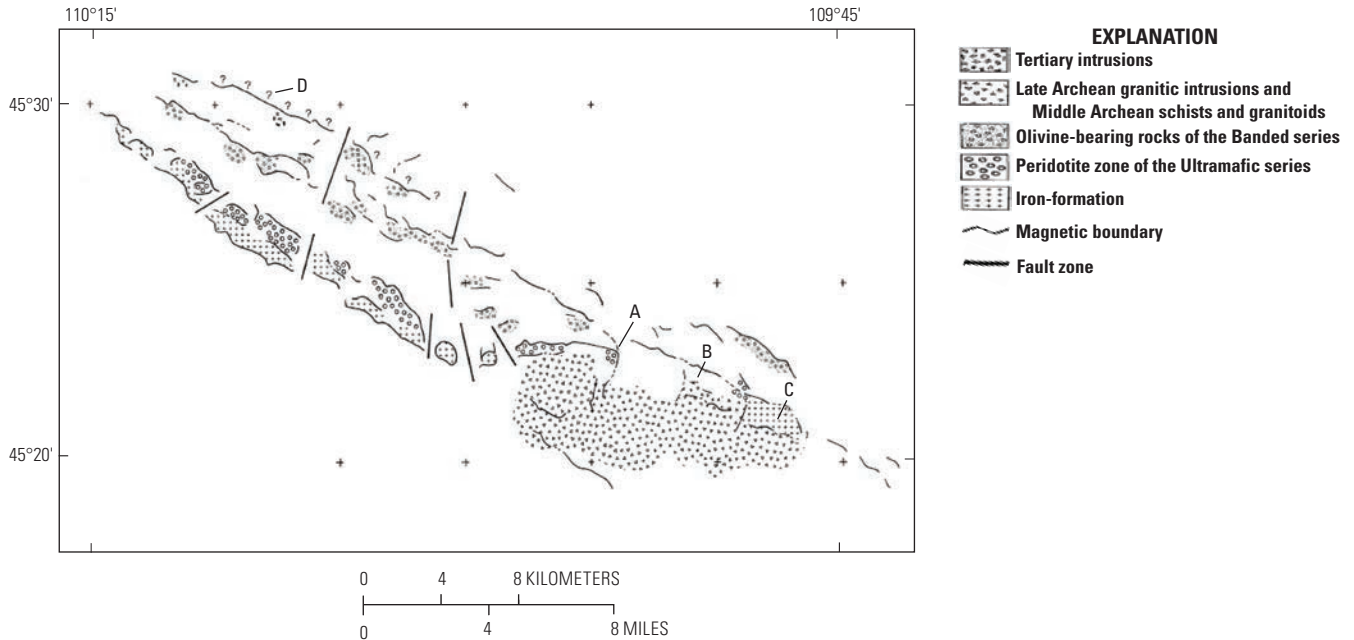
Figure 23. Geologic map extrapolated from the aeromagnetic anomalies and magnetic boundaries shown in figures 21 and 22, respectively. A, B, C, and D represent magnetic anomalies caused by the lowest layers of the Stillwater Complex. From Blakely and Zientek (1985, fig. 4).

Even so, the thicknesses for layers of the eastern lobe are distinctly thinner than the geologically determined average thicknesses for the western and northern mafic sequences, which each measure ~8 km (Vermaak and Lee, 1981).

Because of numerous similarities between the eastern and western limbs of the Bushveld Complex, in terms of stratigraphic successions and layering sequences, it was originally assumed that these two bodies were physically connected at depth (Hall, 1932). However, studies later revealed an absence of a positive gravity anomaly in the central area, suggesting that the mafic rocks were not continuous at depth (Cousins, 1959). Further studies confirmed this hypothesis, concluding that the eastern and western limbs dipped inwardly, became thinner toward the center, and terminated at depth (Van der Merwe, 1976; Molyneux and Klinkert, 1978; Meyer and De Beer, 1987; Du Pleiss and Kleywegt, 1987). However, these Bouguer gravity models failed to consider the isostatic response of the crust to emplacement of the 65,000 km² complex (Cawthorn and Webb, 2001).

Adjusting for isostasy, as well as considering the size of the complex, would result in depression of the crust by as much as 6 km. According to the revised model, mafic rocks of the Bushveld have a well-defined Bouguer gravity anomaly at 60 to 70 milli-Galileo (mGal) at the margins, relative to a regional background of –140 mGal (Cawthorn and Webb, 2001). This gravity anomaly disappears in the central part of the complex, however, due to the isostatic response of the crust, which closely matches the observed gravity profile recorded from the western to eastern Bushveld. As a result,

connectivity between the western and eastern limbs of the Bushveld at depth becomes fairly plausible, at least as a first-order approximation.

Combining the Bouguer gravity model by Cawthorn and Webb (2001) with published Vibroseis (a seismic vibrator) results and seismic velocity modeling of the crust from the Southern African Seismic Experiment, Webb and others (2004) determined new crustal thicknesses using the receiver function method for Bushveld Complex stations and thereby confirmed the connected model of the Bushveld. Webb and others (2010) also established continuity between the eastern and western Bushveld Complex based on xenoliths from the Cretaceous Palmietgat kimberlite pipe, which is located halfway between the exposed regions of the eastern and western lobes. The xenoliths from this kimberlite pipe are chromite-bearing feldspathic pyroxenites with petrologic and mineral compositions equivalent to those of the Critical Zone of the Bushveld Complex. Similarities in lithologies and textures also suggest that the pyroxenitic xenoliths are fragments from the layered cumulate rocks of the Bushveld Complex.

The Stillwater Complex lies along a persistent high-gradient gravity gradient, defined by roughly –175 to –155 mGal contours (Kleinkopf, 1985). This gravity zone is thought to be related to the faulted front of the Beartooth Mountains and the Nye-Bowler structural zone, which extends east to southeastward from the Beartooth Mountains (Foose and others, 1961). Three gravity highs are superimposed along the broad gravity high associated with the Stillwater Complex, suggesting an unusual thickness of high density rocks, most likely the Basal and Ultramafic Series, in the near-surface.

The positive gravity anomalies over the Stillwater reach an intensity of –145 mGal along the southwestern flank of a major west- to northwest-trending gravity ridge, ~10 km northeast of the Stillwater Complex outcrops (Kleinkopf, 1985). The likely source of this gravity high is buried ultramafic rocks, which could be an extension of the Stillwater Complex or a separate mass. Xenoliths from the Tertiary Lodgepole intrusion, about 8 km to the north, provide petrologic evidence for the continuation of the complex (Brozdowski and others, 1982; Brozdowski, 1985). Using a northeast-southwest oriented gravity profile across the Stillwater Complex and surrounding area, along with density measurements on the major rock types of the Stillwater Complex, Kleinkopf (1985) developed a gravity model where the complex extends about 25 km to the northeast of the Beartooth Mountains front. His data also suggest that the complex is 2- to 7-km thick and synformal in shape.

Electrical Signature

Electrical resistivity is also known as resistivity, specific electrical resistance, or volume resistivity and is a measure of how strongly a material (such as a rock or rock unit) opposes the flow of electric current. A material with a low resistivity, for example, easily allows an electrical charge to move through it. By knowing the electrical resistivities of identified lithologic units within a layered stratiform chromite deposit, the ability to determine the composition of the buried sections becomes plausible. This may assist in identifying potential mining targets.

For example, Rütschlin and others (2007) determined the dielectric properties of rocks in the UG1 and UG2 units of the Bushveld Complex using radio frequencies (RF) at 25 megahertz. The UG1 and UG2 chromitite layers exhibit significant velocity contrast, making them good radar reflectors. Furthermore, the UG chromitite layers are hosted in rocks (pyroxenite, norite, and anorthosite) that are translucent in the high frequency spectral band, such that the ability to predict the location of potholes (depressions caused by the overlying footwall horizon descending to touch another footwall horizon; Davison and Chunnett, 1999) and other obstructive features in the UG1 and UG2 is possible. Where potholes form a regional-scale reef, such as the Merensky Footwall unit and Pseudoreef (which underlie the Merensky Reef), they represent potentially significant mining targets. Therefore, one of the main objectives in seismic studies is to detect such areas of relief. In addition, because the host rocks of other lithologic units, such as the Merensky Reef, and layered mafic-ultramafic intrusions are similar to the UG2, with pyroxenite, norite, and anorthosite zones, these electrical techniques may be applied to exploration elsewhere.

Specifically, the average permittivity (e_r; a measure of the ability of a material, such as a rock layer, to transmit an electric field) of Bushveld chromitite layers from the UG1 and UG2 ranges from 11.67 to 12.16, and loss of tangent (tan δ; a dielectric parameter that quantifies the dissipation of electromagnetic energy in a material) from 0.09 to 0.11, which differ from the properties of the pyroxenite, norite, and anorthosite host rocks (table 8; Rütschlin and others, 2007). Melanorite is an exception to this, with a mean loss of tangent of about 0.08, slightly lower than that of chromite. Chromite also has a fairly high attenuation constant that varies between about 0.7 and 0.9 decibels per meter (dB/m). The UG2 host rocks, on the other hand, have RF attenuation values <0.5 dB/m, such that the host rocks, excluding melanorite, have favorable propagation conditions for borehole radars (BHR). With respect to propagation velocities, the UG2 pyroxenites, norites, and anorthosites vary from about 105 meters per microsecond (m/ms) to 110 m/ms, whereas the propagation velocities of chromitite are about 87 m/ms. This marked velocity contrast enables radar reflectivity, which bolsters the planning, processing, and interpretation of BHR surveys in the Bushveld Complex, and, as a result, may be useful in assessing BHR surveys in other stratiform complexes.

Table 8.   Average material properties of rock types from the Upper Group 2.

[From Rütschlin and others (2007, table 3). Abbreviations: ε_r, electrical permittivity; $CV\varepsilon r$, coefficient of variation of electrical permittivity; δ, loss tangent; $CVtan\delta$, coefficient of variation of loss tangent; α, attenuation; dB/m, decibels per meter; $CV\alpha$, coefficient of variation of attenuation; v, velocity in meters per microsecond; CVv, coefficient of variation of velocity; PFP, pegmatoidal feldspathic pyroxenite]

Material (measured at 25 megahertz)	Sample	Permittivity		Loss tangent		Attenuation		Velocity	
		ε_r	$CV^*\varepsilon_r$	tan δ	$CV_{tan\,\delta}$	α	CV_α	v	CV_v
Anorthosite	1	7.43	3.20	0.05	9.09	0.33	10.42	109.98	1.61
Feldspathic pyroxenite	2	8.26	2.08	0.06	7.76	0.42	8.66	104.30	1.03
	3	8.31	2.06	0.05	5.01	0.33	5.44	104.00	1.03
	4	8.21	5.38	0.05	11.65	0.33	14.20	104.70	2.65
	5	8.00	3.49	0.05	12.37	0.34	13.63	105.98	1.75
	9	7.75	2.24	0.04	10.60	0.27	11.51	107.70	1.13
Chromitite	3	12.16	2.92	0.10	5.95	0.83	7.00	85.88	1.49
	6, 7	11.67	2.57	0.11	5.03	0.86	5.51	87.65	1.29
	9	11.70	4.36	0.09	4.93	0.72	6.76	87.62	2.23
PFP	10	8.28	5.89	0.06	29.69	0.38	32.21	104.29	2.76
Melanorite	11	8.19	1.23	0.08	4.27	0.52	4.67	104.68	0.62

*The coefficient of variation (CV) is the percentage ratio of standard deviation to the mean of a particular.

Seismic Data

Early investigation into the seismic properties of the Merensky Reef, UG2 chromitite, and associated structures such as seismic lines (Maccelari and others, 1991a,b) in the Bushveld Complex focused on identifying the entire Rustenberg Layered Suite, where the main chromitite layers, or deeper structures such as the Moho, are located (Odgers and Du Plessis, 1993).

Using vibrators with sweeps of as much as 250 hertz, high resolution seismic lines identified a major acoustic boundary at the Bastard pyroxenite, located ~10 m above the Merensky Reef (Davison and Chunnett, 1999). The seismic data also indicated the presence of a "Reef Zone," which extends from the Bastard Reef through the Merensky Reef, Merensky Footwall unit, Pseudoreef, and down to the UG2 and UG1 chromitite layers. This "Reef Zone" can be followed with confidence to as much as 50 milliseconds (ms), or ~130 m in depth. With the aid of borehole control, the reflection can be followed to as shallow as 30 ms, or ~65 m. In addition, the high resolution dataset permits identification of fault throws as small as ~10 m, which can assist in evaluating the structure of potential mining targets.

On a seismic data section, the Merensky Reef is interpreted as a negative wavelet, which is based on the estimated interval sonic velocities for the hanging wall rocks at ~6,500 meters per second (m/s) (Davison and Chunnett, 1999). Similarly, the seismic data of the UG2 chromitite layer also appears as a negative wavelet. As a result, if the Merensky Reef and the UG2 chromitite are approximately one wavelength apart (12 ms), then they are each seismically recognizable (Davison and Chunnett, 1999). When the two layers are stratigraphically closer to each other, however, destructive interference signals prevent clear imaging. In this case, only the "Merensky" reflection appears. Using high resolution frequency input also enables identification of possible potholes in the Merensky Reef. Changes in the reflection character in the seismic wave, particularly amplitude and wavelength, produce clear imaging of pothole areas. Although the potholes imaged by Davison and Chunnett (1999) have not been confirmed by drilling, their study demonstrates that significant ore bodies may be located using seismic data, particularly in areas where the potential potholes appear extensive.

Hypogene Ore Characteristics

Mineralogy

The mineralogy of the hypogene ore primarily includes the following: chromite ± magnetite ± pyrrhotite ± pentlandite ± chalcopyrite ± platinum group minerals (dominantly laurite, cooperite, and braggite).

Chromite

Chromium (Cr) is a shiny, steely gray, hard metal with a high melting point that withstands high polishing. It is also odorless, tasteless, and malleable. The name of the element originates from the Greek word chroma (χρωμα), meaning color, since many of its compounds are intensely colored. Chromium metal rarely occurs naturally on Earth. However, chromium is found in a wide variety of oxide and silicate minerals in the Earth's crust. The first identification of chromium in a mineral occurred in 1797 by Nicolas Vauquelin in the mineral crocoite (lead chromate). The most important of the chromium-bearing minerals, however, is chromite, because it is the only known economically viable chromium ore.

Chromite is a mineral in the spinel family with the general chemical formula XY_2O_4. Figure 24 shows the spinel minerals in a prism with the end member compositions at each corner. Because of complete or extensive solid solution at high temperatures between most of the spinel end member compositions, chromite compositions fall within the prism. The end member compositions and names are as follows:

$$MgAl_2O_4 = \text{spinel}$$
$$FeAl_2O_4 = \text{hercynite}$$
$$FeCr_2O_4 = \text{chromite}$$
$$MgCr_2O_4 = \text{picrochromite}$$
$$MgFe_2O_4 = \text{magnesioferrite}$$
$$Fe_3O_4 = \text{Magnetite or } Fe_2TiO_4 = \text{ulvospinel}$$
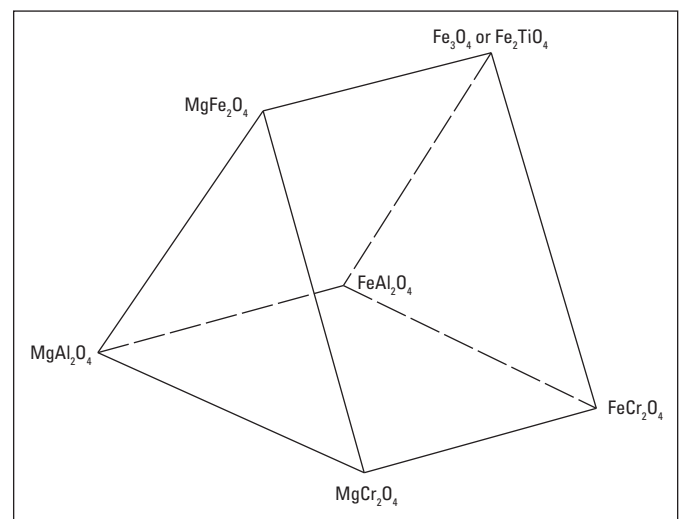
Figure 24. Spinel tetrahedron with end members shown at corners.

Thus, the base of the prism consists of aluminum- and chromium-bearing spinels with no trivalent iron (or titanium). The higher they are in the prism, the richer in trivalent iron and poorer in divalent iron the compositions become. The nomenclature is a bit confusing due to the fact that one of the end members of the spinel group of minerals is also called spinel ($MgAl_2O_4$). In addition, another end member is called chromite ($FeCr_2O_4$). Most geologists, however, call any

spinel with a substantial chromium content, typically more than about 15 percent, chromite. This is probably because chromium-bearing spinels are by far the most economically important of the spinel-group minerals.

The ions in spinel-group minerals form a cubic close packed, face-centered lattice, which imparts a relatively high density compared to many other minerals. Thus, the typical range of specific gravity of commercial chromite is 4.5 to 4.8 gm/cm^3. Chromite is black with a metallic to dull luster and yields a dark-brown streak. This streak distinguishes chromite from other black spinel-group minerals, such as magnetite, that typically have a white streak.

Chromite is opaque to slightly translucent in thin section, depending on the amount of trivalent iron in the chromite. If it has very little Fe^{3+}, then the mineral will be slightly translucent, but opaque if it contains more that a few percent Fe^{3+}. Trivalent iron also has an effect on the magnetic properties of chromite. Chromite with very low amounts of trivalent iron, less than a few percent, is almost non-magnetic; higher amounts of trivalent iron add a substantial magnetite component to the chromite and it becomes weakly magnetic. The hardness, using the Mohs hardness scale, is typically 5.5 to 6.5. Chromite does not show cleavage, but does exhibit conchoidal to uneven fracture.

Bushveld Complex

For the most part chromite is a cumulus mineral in the Bushveld Complex. Chromite may be a postcumulus mineral, however, where it occurs as a trace mineral (Cameron, 1977). As sparse, discrete grains, chromite is spatially isolated by intercumulus minerals, such as bronzite or plagioclase, or embedded in silicate grains (Eales and Reynolds, 1986), and ranges from 0.05 to 0.3 mm in diameter (fig. 25). Clusters of grains lead to chromite masses 10 to 50 times larger. In some of the chromites, intergrain triple junctions, a reduction of interstitial silicate matrix, and near-planar boundaries between subgrains of aggregates, including the cuspate forms, suggest significant annealing and recrystallization (Eales and Reynolds, 1986; Eales, 1987).

Chromite grains in the LG6 chromitite layer are coarse-grained cumulates, comprising 97 percent of the rock (fig. 26); orthopyroxene, clinopyroxene, plagioclase, and other minor
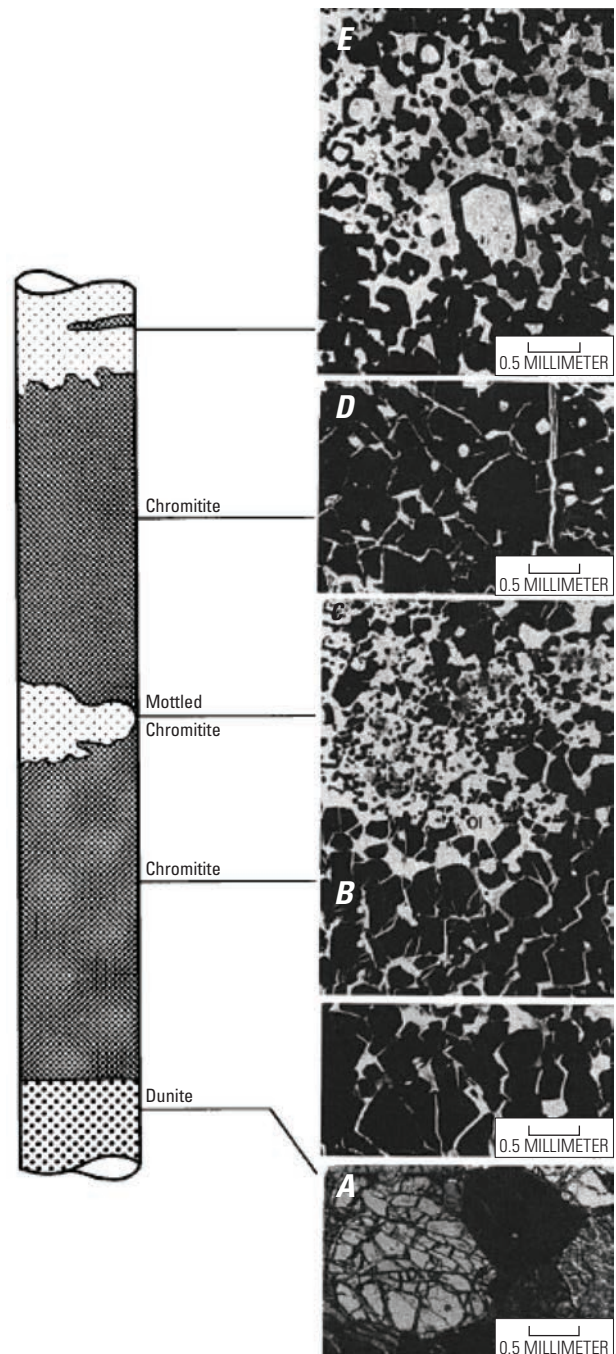
Figure 25. Photomicrographs showing textural characteristics of the lower chromitite layer at the G66, 6 level, Grasvally chrome mine, with idealized columnar section on the left (approximately 50-centimeters vertically). From Hulbert and Von Gruenewaldt (1985, fig. 4). *A,* footwall dunite found in association with the lower chromitite layer; *B,* coarse, massive hard lumpy chromitite (90 percent chromite) with large polygonal chromite grains; *C,* mottled chromitite with 50 to 60 percent chromite where grains are 50 to 100 times smaller than over- and underlying massive chromitite; *D,* coarse, massive chromitite with large polygonal chromites that typically contain spherical olivine inclusions; *E,* large, irregular chromite grains occur with serpentinized olivine grains surrounded by chromite mantles.

accessory minerals, such as biotite, sulfides, quartz, talc, chlorite, and carbonates, make up the remaining 3 percent (Shürmann and others, 1998) The size of the chromite grains range from 53 to 2 mm and they are generally friable in nature, with some patches of hard lumpy ore in sections of the eastern Bushveld. Very fine-grained chromite grains are enclosed by pyroxene and (or) plagioclase crystals, giving the LG6 a poikilitic texture where the oikocrysts vary in size from 5 to 20 mm in diameter (Shürmann and others, 1998). Chromites from the MG1 layer are euhedral cumulates that are evenly distributed with a fine, dense, granular texture (Meadon, 1995). Grain size varies between 0.25 and 2.0 mm. Chromite constitutes 70 to 88 percent of the MG1 chromitite, whereas plagioclase, orthopyroxene, and accessory minerals, such as biotite, chlorite, phlogopite, quartz, talc, and carbonates, make up the remainder. Similar to the LG6, oikocrysts occur throughout the MG1, although to a lesser extent, and they are generally oval shaped and range in size from 3 to 15 mm (Shürmann and others, 1998).

Stillwater Complex

The chromite grains found in the massive chromitite layers of the Stillwater Complex are coarse and blocky (fig. 27), characteristically with recrystallized, polygonal grain boundaries (Campbell and Murck, 1993). Cumulus chromite grains from the main G chromite seam are 1 to 2 mm in diameter and set in a matrix of foliated serpentine (fig. 28). Chromite can also occur in pods, lenses, strings, and chains (fig. 29). "Reverse" grading is observed where grains are size-graded, such that the finest grained olivine and chromite crystals are at the bottoms of the chromitite layers (Jackson, 1961). In addition, chromite-olivine and olivine-chromite cumulates in the Stillwater Complex have an occluded silicate texture (Jackson, 1961; Campbell and Murck, 1993). In this case, cumulus chromite grains outline the original boundaries of cumulus olivine grains, some of which have subsequently been replaced by bronzite and resemble textures found in the Bushveld chromitites.

Figure 26.   Outcropping of the Bushveld Lower Group 6 (LG6) chromitite seam. Photograph courtesy of Klaus J. Schulz, U.S. Geological Survey.

Figure 27.   Typical chromite-bearing rock from the Stillwater Complex. Photograph courtesy of Bruce Lipin, U.S. Geological Survey.
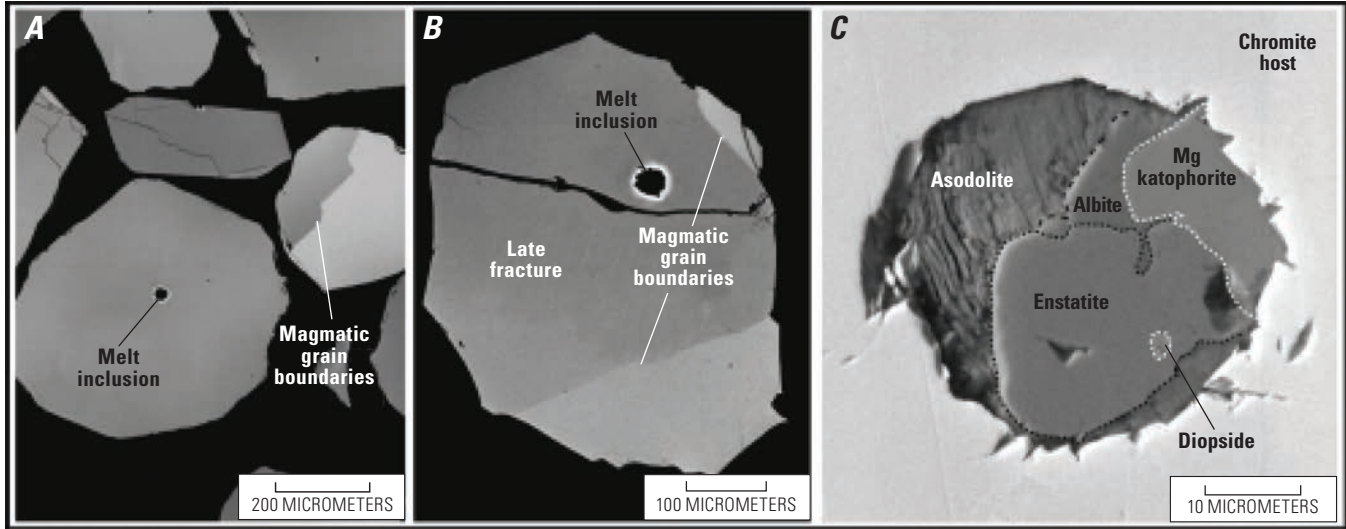
Figure 28.   High-resolution, back-scattered electron (BSE) images of typical chromite grains (*A–B*) and inclusions (*C*) from the main G chromitite seam located above the Benbow Mine head frame. Original magmatic grain boundaries and melt inclusions clearly visible (*A–B*). Image *C* is a melt inclusion within a chromite grain prior to rehomogenization. From Spandler and others (2005, fig. 1).
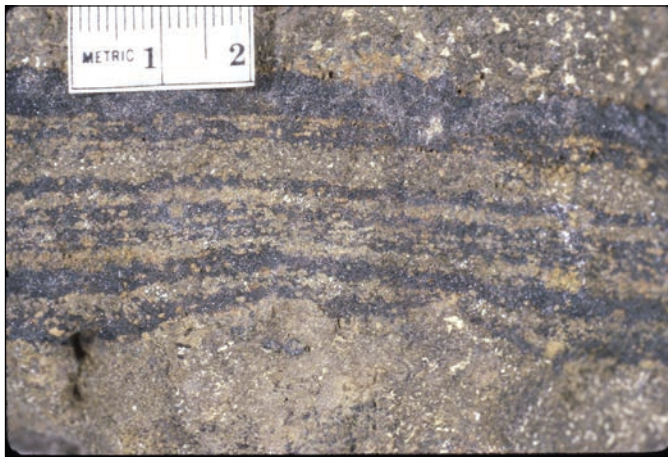
Figure 29.   Thin chromite-bearing seams (black) located in the Stillwater Complex. Photograph courtesy of Michael Zientek, U.S. Geological Survey.

Great Dyke

Massive chromitite layers occur in the Dunite Succession of the Darwendale Subchamber of the Great Dyke, and are coarse-grained with little or no primary silicate material. Magnesite, talc, and secondary serpentine minerals occur only in fractures. These chromitite layers are referred to as the lower group chromitites and mark boundaries between the cyclic units in the Dunite Succession (Prendergast and Wilson, 1989). Minor chromitite layers may also be found. Generally, the chromitite layers have sharp contacts with the dunite, although disseminated upper and lower contacts are also noted (Wilson, 1996).

Overall, the massive chromitites contain polygonal chromite grains with planar crystal boundaries (fig. 30) and mean grain sizes that range from 0.5 to 10 mm (Prendergast and Wilson, 1987). However, as olivine increases in proportion, the chromitites grade from massive to semi-massive, and then into disseminated olivine chromitite and chromite dunite (fig. 31). In the latter case, chromite occurs as clusters on the margins and along triple junctions of olivine grains (Wilson, 1996). Some of the disseminated olivine chromitites and olivine dunites exhibit millimeter-scale layering that arises from alternating layers of olivine and chromite (Prendergast and Wilson, 1989).

Muskox Intrusion

With the exception of two concentrated layers of massive chromitite, most of the chromite in the Muskox intrusion is disseminated throughout olivine cumulates, such as dunite, peridotite, feldspathic peridotite, or picrite, and makes up only 1 to 3 percent of the rock (Irvine and Smith, 1969; Irvine, 1975). Typically, the chromite is octahedral or subhedral and 0.05 to 0.15 mm in diameter. In addition, chromite is commonly present as isolated grains or within small clusters between larger cumulus olivine grains. Locally, small euhedral chromite crystals occur as inclusions within olivine. Chromite from the massive chromitite layers is similar to the disseminated chromite in habit, but recrystallization has occurred such that the chromite crystals are coarser grained and situated in close contact with one another. Although disseminated chromite is uniformly distributed in the olivine-rich cumulates (Irvine and Smith, 1969), it is not economic.
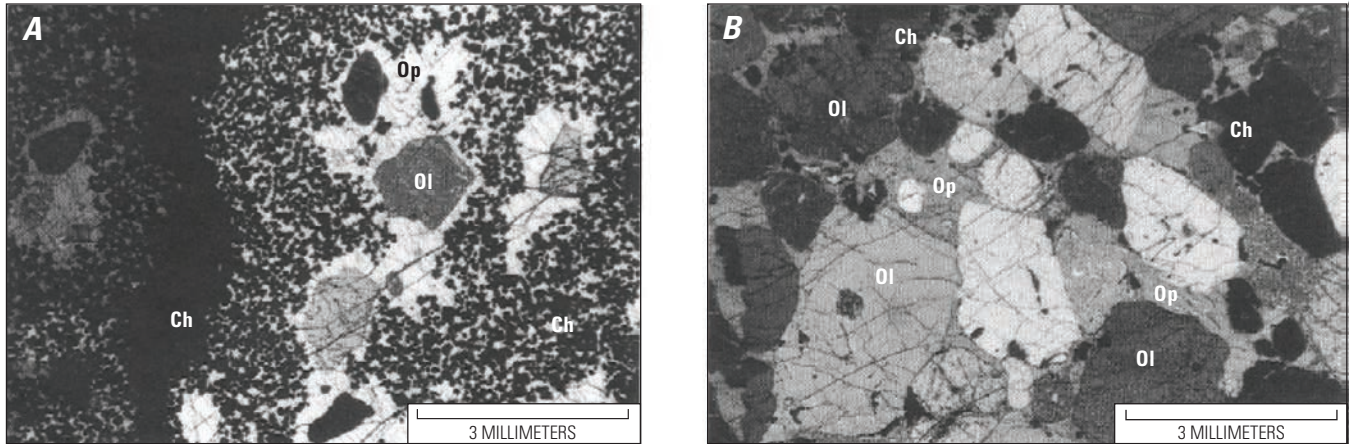
Figure 30. Photomicrographs of chromite-bearing rocks from the Ultramafic Sequence of the Great Dyke. *A,* Disseminated chromitite C1c with fine-grained, polygonal chromite; olivine and orthopyroxene in reaction relationship. *B,* Fine-grained chromite in dunite; chromite grains located at the edges of cumulus olivine and within the orthopyroxene. From Wilson (1996, fig. 13). Abbreviations: Ol, olivine; Op, orthopyroxene; Ch, chromite
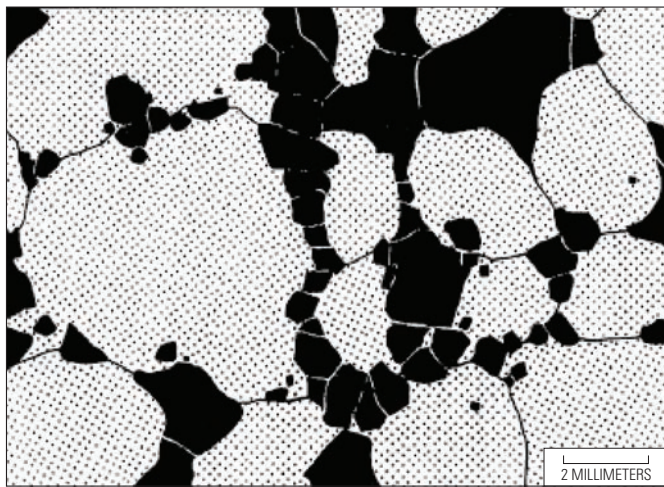
Figure 31. Artistic rendering of chromite dunite photomicrograph from the Great Dyke, showing chromite (black) occurring as clusters at the margins of olivine (dots) and at triple junctions between olivine grains. From Prendergast and Wilson (1989, fig. 4).

Kemi Intrusion

In the Kemi intrusion, chromite occurs as euhedral phenocrysts that vary from a few tens of microns to more than 1 mm in diameter (fig. 32). Chromite grains contain abundant spherical silicate inclusions (fig. 32*B*) that vary from 5 to 100 µm in diameter (Alapieti and others, 1989). Due to lower amphibolite facies metamorphism, some of the chromite grains may be broken and altered (fig. 32*D*) along margins and cracks (Alapieti and others, 1989; Kujanpää, 1989). Where altered at the rims, the external shell is commonly magnetite, and between the core and the outermost rim, there is typically a thin zone of ferran chromite (fig. 32*G*). Serpentine locally replaces chromite, such that the chromite grains show corroded external surfaces (fig. 32*H–I*).
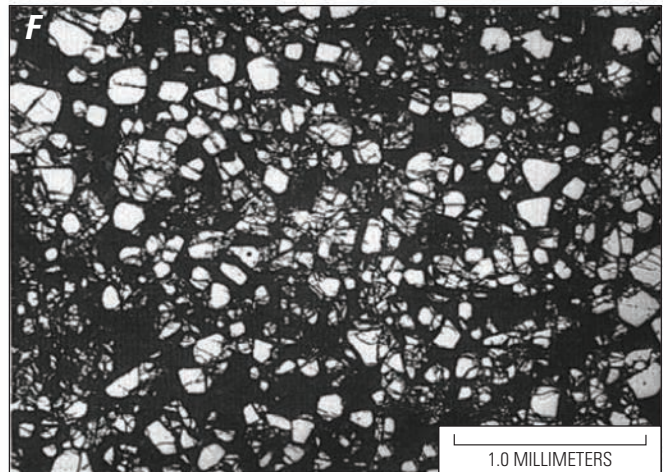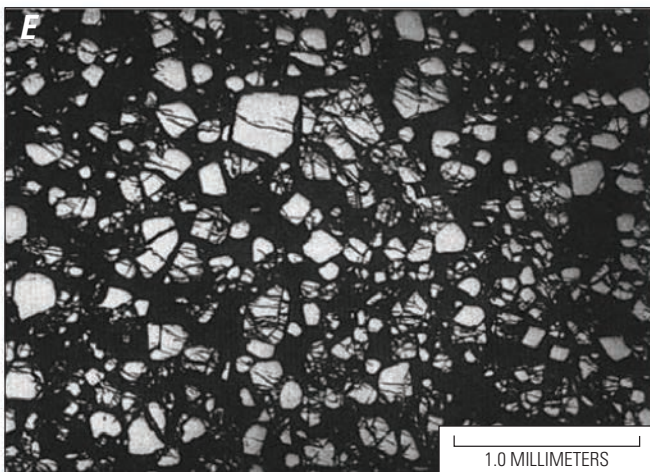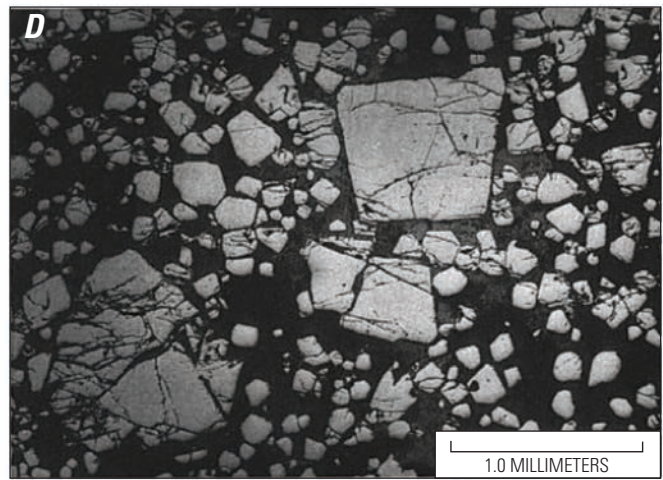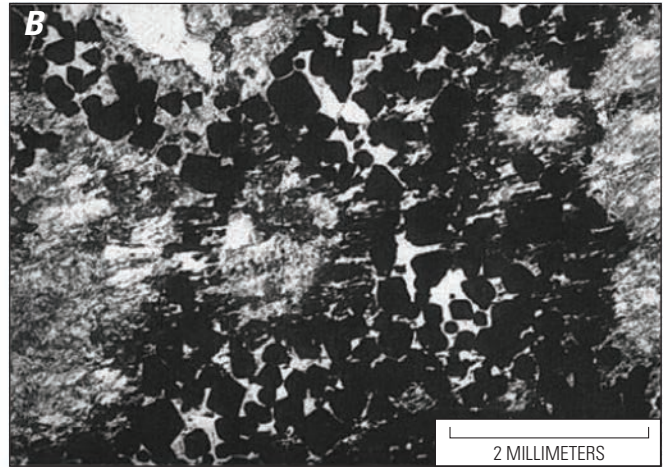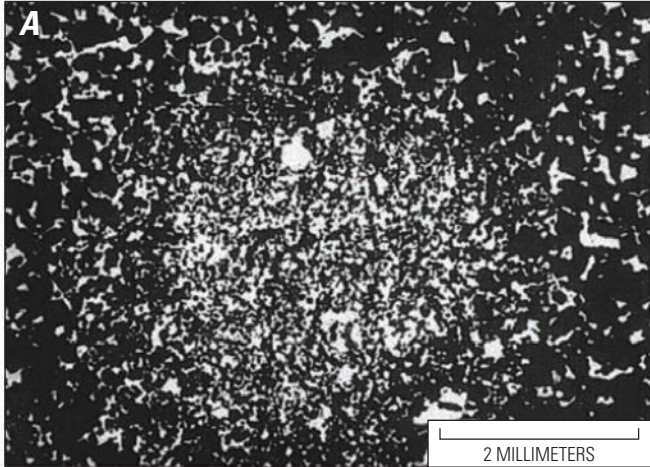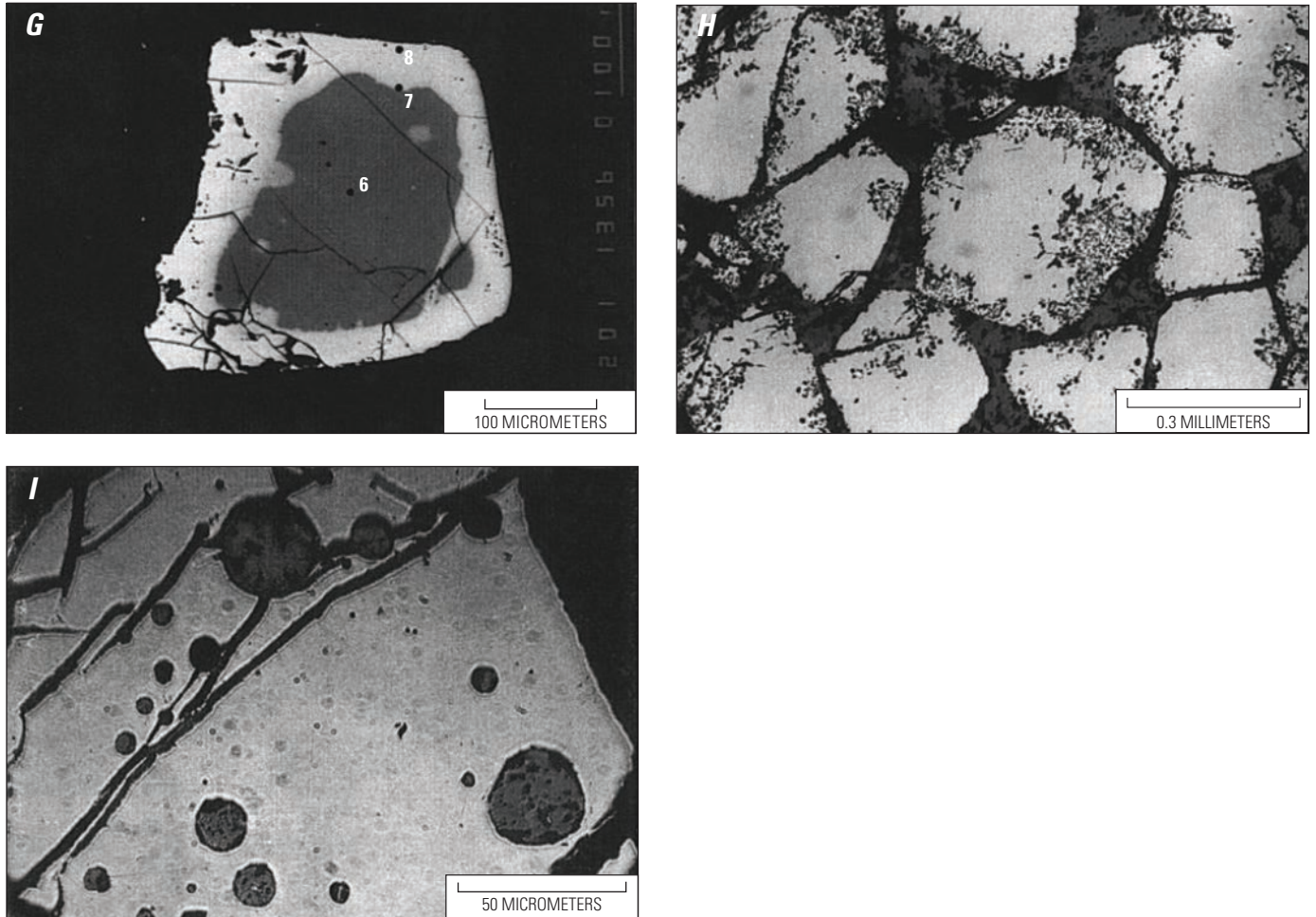
Figure 32. (above and facing page).   Photomicrographs of Kemi chromite ores. From Alapieti and others (1989, fig. 5). *A,* Fine-grained chromite. *B,* Coarse-grained chromite ore with carbonate and olivine inclusions. *C,* Typical chromite ore showing wide variation in chromite grain size. Serpentinized olivine inclusions in chromite grains. *D,* Medium-grained chromite ore with fractured and altered chromite grains. *E,* Chromite grains with abundant cracking. (*F*) Highly fractured chromite grains close to the fault zone. *G,* Back-scattered electron image of a rimmed chromite grain. *H,* Iron-rich regions of chromite grains replaced by serpentine. *I,* Chromite grain with serpentinized olivine inclusion.

Rum Intrusion

The Eastern Layered Series (ELS) of the Rum intrusion contains thin (2 to 5 mm), laterally continuous (>1 km) chromitite seams (chromite >60-percent modal) along unit boundaries (Power and others, 2000). The chromitite seams generally do not occur within the ultramafic components of the individual units. Instead, they are found at the junctions of some of the major cycle units.

Chromite also occurs disseminated throughout the ELS, and is euhedral or enclosed in olivine (fig. 33*A–D*; Emeleus and others, 1996). Rarely will chromite grains form within clinopyroxene oikocrysts (fig. 33*H*). The Western Layered Series and Central Series contain thin (<20 mm) chromitite seams interlayered with olivine cumulates. Disseminated chromite is also abundant in these regions.

Subsidiary chromite-bearing seams are found several tens of centimeters below the main unit junctions (O'Driscoll and others, 2009a). The subsidiary seams are thinner (1 to 2 mm) than the main chromitite seam, have a significantly higher proportion of spinel to silicate, and are laterally discontinuous on the scale of tens of meters. Modally, the subsidiary chromitite seams contain 50- to 60-percent chromite and ~30-percent intercumulus olivine, with intercumulus plagioclase and minor amounts (~1 percent) of sulfides comprising the remainder (O'Driscoll and others, 2009a).

Ipueira-Medrado Sill

The lowest sublayer in the Main Chromitite layer of the Ipueira-Medrado Sill contains massive chromitite and is 0.5- to 1.0-m thick (Marques and Ferreira-Filho, 2003). Chromite crystals in this sublayer are typically small (0.1 to 0.2 mm), euhedral to subhedral, and homogeneous (fig. 34*F*). Although chromite is present in >90 vol% of the rock, orthopyroxene occurs as a postcumulus mineral. As a result, chromite is locally enclosed in poikilitic oikocrysts, as much as 1.5 cm in diameter, of orthopyroxene. The orthopyroxene oikocrysts are, in turn, typically surrounded by massive bands of larger annealed chromite crystals that range from 0.5 to 0.8 mm in diameter. Whereas alteration of chromite grains is rare, a few highly fractured and serpentinized zones contain chromite grains with very thin Ti-rich exsolution lamellae.

A 0.3- to 0.6-m-thick chain-textured chromitite sublayer also occurs in the Main Chromitite layer (fig. 34*G* and 34*H*). The chain-like texture is characterized by olivine pseudomorphs, resembling orthopyroxene grains, that are surrounded by ovoid chromite crystals, which represent the relict cumulus texture. Close to silicate margins, the chromite is fine-grained, but grades to coarse-grained where aggregated.
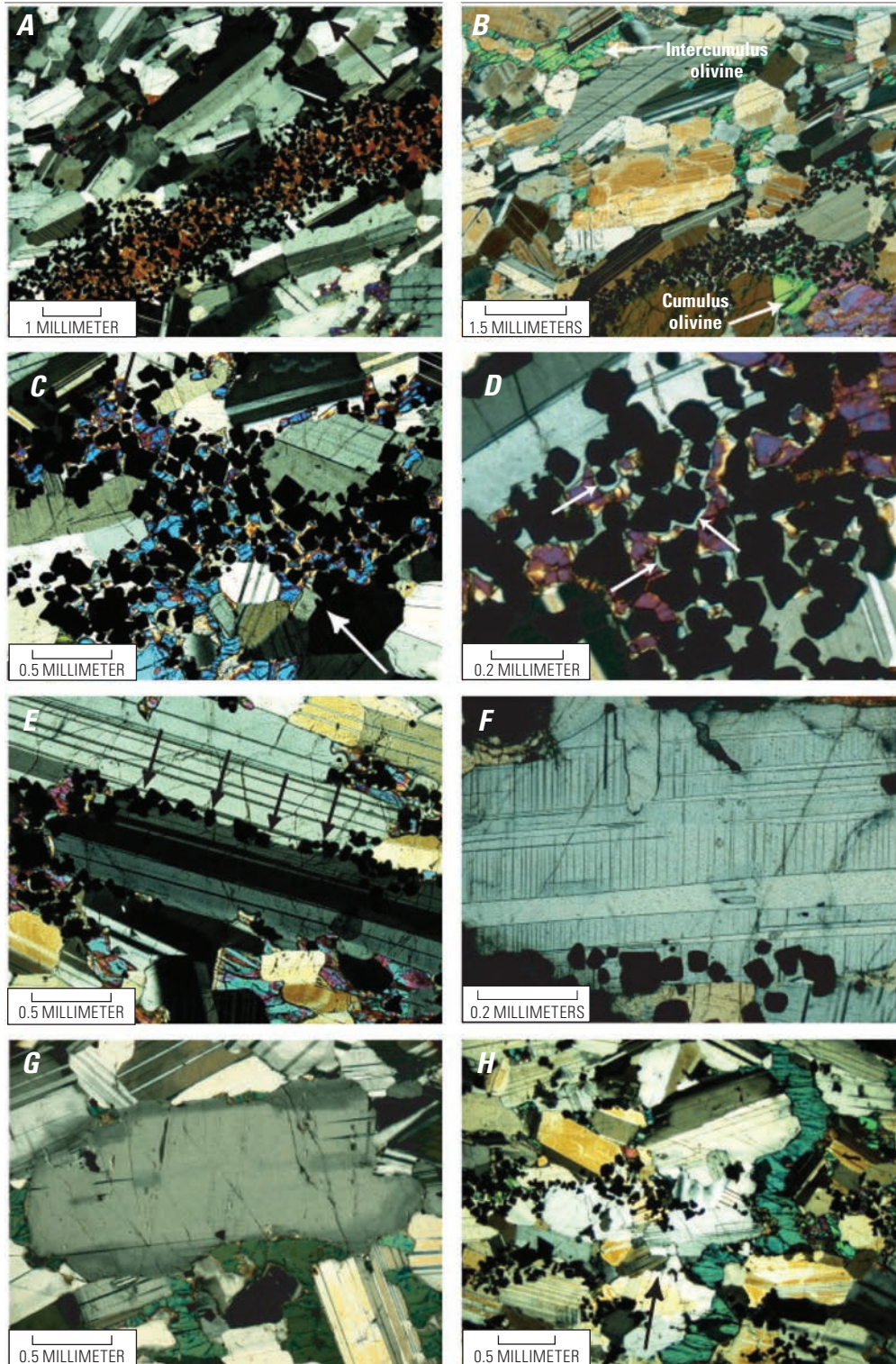
Figure 33. Photomicrographs of chromite-bearing rocks in the Rum intrusion. From O'Driscoll and others (2009a, fig. 3). *A,* Laminated anorthosite with subsidiary chromite-bearing seam. Chromite grains are embedded in optically continuous olivine oikocrysts. Arrow indicates upward direction. *B,* Cumulus olivine in troctolite is optically continuous with olivine oikocrysts in the subsidiary seam and in the anorthosite. *C,* Chromite occurring in anorthosite and occurs with intercumulus olivine and at plagioclase grain boundaries. Arrow indicates upward direction. *D,* Chromite in indentations and embayment structures (arrowed) of olivine. *E,* Chromite within anorthosite crystallize along plagioclase grain boundaries (arrowed). *F,* Chromite alongside edge of twinned plagioclase grain boundaries. *G,* Zoned plagioclase typical of anorthosite and troctolite rocks. *H,* Clinopyroxene vein cross-cutting subsidiary chromite seam in anorthosite host. Arrow indicates upward direction.
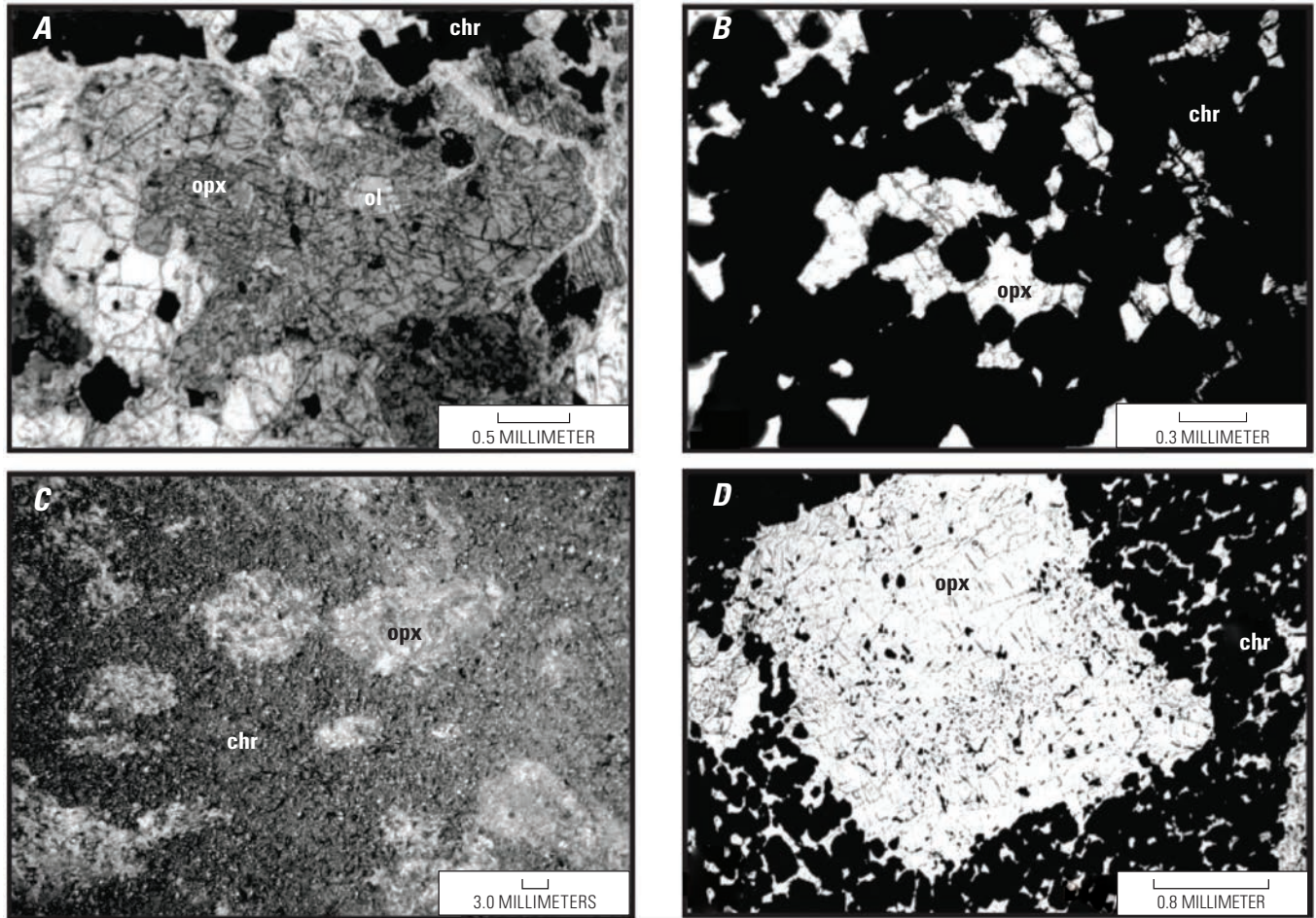
Figure 34. Photomicrographs of ultramafic rocks from the Ipueria-Medrado Sill illustrating textural characteristics. From Marques and Ferreira-Filho (2003, fig. 8*e-h*). *A,* Cumulus olivine in orthopyroxenite that has almost been completely resorbed by orthopyroxene. *B,* Fine-grained massive chromitite from the Main Chromitite layer. Plane-polarized light. *C,* Chromitite from Main Chromitite layer with chain-textured chromitite. Drill core surface. *D,* Chain-textured chromitite from Main Chromitite layer in plane-polarized light. Abbreviations: ol, olivine; chr, chromite; opx, orthopyroxene

Fiskenæsset Anorthosite Complex

Nearly all the chromite in the Fiskenæsset Complex is associated with the Anorthosite unit, except for a few minor chromitite layers in the Ultramafic sequence. The chromitite seams generally contain between 50- and 75-percent chromite in a silicate matrix of hornblende, with minor biotite and plagioclase (Ghisler, 1970). Rutile, ilmenite, magnetite, and base metal sulfides are also accessory phases (fig. 35). The chromite itself is characteristically euhedral to subhedral with rounded corners. However, in places where the chromite grains are packed tightly, they are more anhedral in shape.

The grain size ranges between 0.05 and 0.7 mm, with 0.3 mm as typical (Ghisler, 1970; Appel and others, 2002). In a few cases, single octahedral crystals are as much as 3 mm in diameter (Appel and others, 2002). The chromite grains occur as elongate aggregates that are 2- to 5-mm long and parallel to layering (Ghisler, 1970). In places, the aggregates show chain structures. Inclusions of silicate minerals, ~0.02 mm in diameter, are common either as irregular grains or as regular outlines congruent to the crystallographic direction of the chromite (fig. 35). Fracturing of chromite grains appears to be only a local feature.
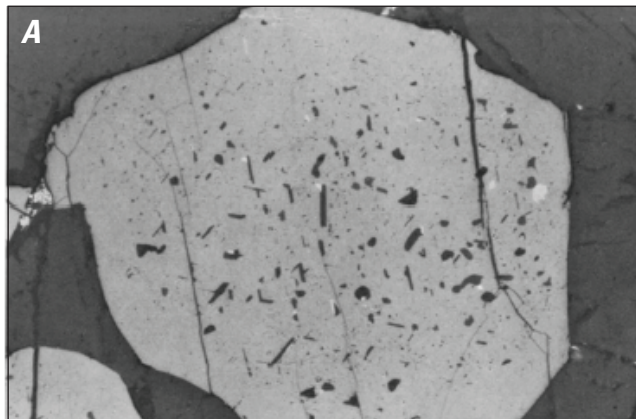
150 x
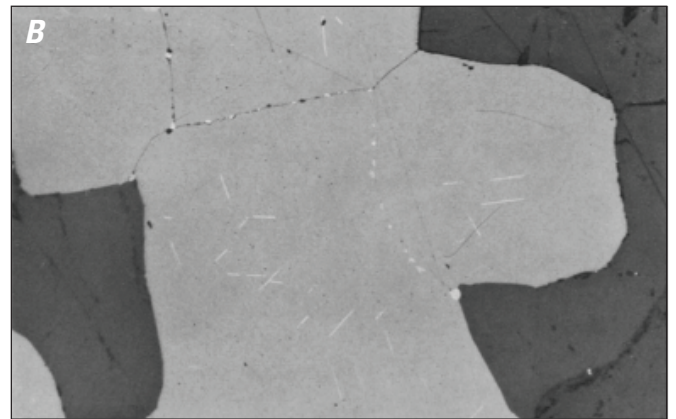
150 x
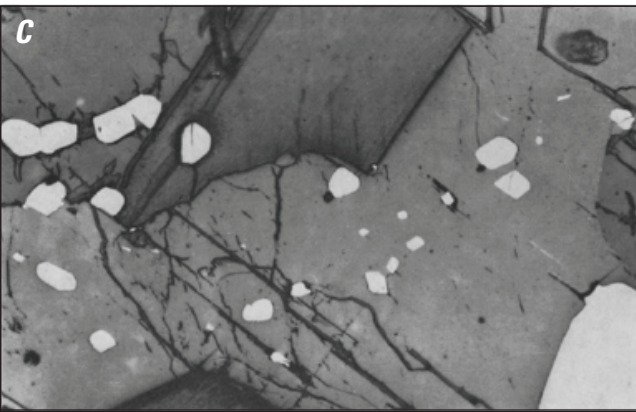
150 x

Figure 35.   Reflected light photomicrographs (150x) of chromite grains from the Fiskenæsset anorthosite complex. From Ghisler (1970, figs. 10*a*, 11*b*, 12*c*). *A,* Silicate inclusions and exsolutions of rutile within chromite grain. *B,* Chromite containing exsolutions of rutile within and along chromite grain boundaries. *C,* Chromite surrounded by recrystallized hornblende and biotite (upper part).

Sulfide-PGE Mineralization

The most common sulfides found in many of the chromitite seams are pyrrhotite (Fe_{1-x} S, x = 0–0.2), pentlandite [$(Fe, Ni)_9 S_8$], pyrite (FeS_2), and chalcopyrite ($CuFeS_2$). There are strong geochemical interrelationships between the sulfides and platinum group elements (PGE), suggesting close association of PGE with sulfide fractionation. The dominant platinum group minerals (PGM) in stratiform chromite deposits include laurite (RuS_2), cooperite (PtS), and braggite [(Pt, Pd)S], and these are frequently encapsulated in silicates.

The sulfides associated with the UG2 chromitite layer on the Maandagshoek Farm in the eastern section of the Bushveld Complex include pentlandite, chalcopyrite, pyrrhotite, and bornite (Gain, 1985). Minor amounts of covellite and millerite are also present. Tellurides, bismuthides, stibnides, and arsenides are also associated with the PGE in this layer. Chemical analyses on six borehole intersections in the UG2 layer show that the PGE are enriched at the top and bottom of the main chromitite layer, though the concentration at the base is generally greater (Gain, 1985).

In the Ultramafic Series of the Stillwater Complex, the chromitite, chromite-olivine, and bronzite cumulates contain small blebs (>185 mm) of pyrrhotite-pentlandite-chalcopyrite. At the base of the G chromite-bearing zone, located in the Ultramafic Series, massive pyrrhotite-pentlandite-chalcopyrite pods are conformable to the layering.

Pyrrhotite, pentlandite, cubanite, and chalcopyrite are the main sulfide minerals found in the ultramafic layers of the Muskox intrusion. The chromite-rich peridotites and orthopyroxenites contain 1- to 7-percent disseminated sulfide minerals and locally form irregular patches, 1 mm to 1 cm in diameter, between chromite and silicate grains (Irvine and Smith, 1969; Barnes and Francis, 1995). In the thickest chromitite layer, the sulfides may occur as ellipsoidal globules.

Platinum group minerals have also been found in the Unit 6–Unit 7, Unit 7–8, and Unit 11–12 chromitites in the Eastern Layered Series of the Rum intrusion (Butcher and others, 1999). The PGM identified in these units include Pd-Cu alloys, Fe-Pt alloys, native Pt, laurite, Pd and Pt tellurides and varieties of bismuthides, such as moncheite and sperrylite (Butcher and others, 1999). Less common grains include Pt-Cu alloys, Pt-Ir alloys, Pd-Sb arsenides, and irarsite.

The PGM in the Rum intrusion are mostly 0.2 to 2 mm in diameter, although some grains reach as much as 10 mm. Overall, the PGM are anhedral, inequant, and occur at sulfide-silicate grain boundaries or enclosed within pentlandite, chalcocite, chalcopyrite, bornite, magnetite, or plagioclase. Less frequently, these minerals are present as inclusions in clinopyroxene and olivine. In addition, PGM may occur at silicate-silicate, chromite-silicate, and magnetite-plagioclase grain boundaries (Butcher and others, 1999). At the Unit 7–Unit 8 contact in the Eastern Layered series, sulfides include pentlandite, bornite, chalocite, chalcopyrite,

magnetite, and ilmenite. Consistently enclosed by or intergrown with plagioclase and (or) olivine, the sulfides are anhedral, 10 to 60 mm in diameter, and occur interstitially to chromite.

Chromite grains from the Campo Formoso layered intrusion contain discrete inclusions of PGM, such as laurite and Os-Ir-Ru alloys (Garuti and others, 2007). Laurite, erlichmanite, Ir-Ru-Rh sulfarsenides (irarsite, ruarsite, hollingworthite), and Pt-Pd compounds with antimony (Sb), bismuth (Bi), and tellurium (Te), such as sudburyite, can also occur interstitially to chromite. In addition, these PGM are commonly intergrown with low-temperature Ni-sulfides. Typically, PGM grains are <10 mm in size and rarely exceed 20 mm, with habits that are anhedral to euhedral. Laurite is locally associated with rutile and (or) pentlandite. In some cases, small chlorite lamellae are present in the laurite inclusions.

In the Bird River Sill, PGM inclusions have been identified in chromite (Talkington and others, 1983). The primary PGM include laurite and ruteniridosmine, an Os,- Ir-, and Ru-bearing alloy. Talkington and others (1983) did not detect platinum or rhodium in chromite inclusions, although one PGE alloy contained 0.96 wt% rhodium. Generally, the proportion of laurite inclusions initially increases and then decreases with height in the ultramafic zone. The size of the PGM grains averages 10 mm, although laurite grains are typically larger than the alloys and can be as large as 20 mm. The PGM inclusions are usually polyhedral, with rounded grains being rare. Twinning is also evident in several of the laurite inclusions.

Mineral Assemblages

The most common mineral assemblages in the chromitite seams are olivine + chromite, chromite ± bronzite + plagioclase, chromite + plagioclase, and chromite + clinopyroxene (augite). However, most of the chromitite seams in the Bushveld Complex, which contains the bulk of the world's stratiform chromite, are associated with either bronzite and (or) plagioclase.

Paragenesis

Petrogenesis of the monomineralic layers of stratiform chromite deposits remains a highly debated topic. As such, a clear paragenetic sequence model is not applicable to all the stratiform chromite deposits. However, during magmatic differentiation, chromite is considered an early cumulus mineral that does not form immiscible liquids in silicate melts (Cameron and Emerson, 1959). In addition, the solubility of chromium is low in silicate melts (Roedder and Reynolds, 1991). As a result, chromite generally crystallizes as a minor, but significant cumulus phase during olivine cumulate layer formation. The amount of cumulus chromite decreases sharply

when cumulus olivine is replaced with cumulus Ca-poor pyroxene. This change has little effect on the total Cr content of the rocks, however, insofar as the melting relationship between Cr-rich pyroxene and chromite is incongruent (Dickey and others, 1971; Campbell, 1976). In addition, during orthocumulate crystallization, chromites are highly reactive with the intercumulus liquid, such that the release of Cr is absorbed by the crystallization of intercumulus pyroxene.

With respect to the various magma chambers of the Great Dyke, the crystallization sequence is based on the cumulus assemblage and proceeds as follows: chromite, olivine, orthopyroxene, clinopyroxene, plagioclase, pigeonite, and magnetite (Wilson, 1996). The textures and abundances of minerals in the Peridotite Zone of the Stillwater Complex, where the bulk of the chromitite seams are located, suggest a crystallization sequence beginning with olivine (± chromite), followed by orthopyroxene, plagioclase, clinopyroxene, phlogopite, and finally amphibole (McCallum, 1996). Reaction relationships between olivine and orthopyroxene, orthopyroxene and clinopyroxene, and clinopyroxene and amphibole are also evident. Similarly, the ore paragenesis in the Main Chromite Horizon of the Burakovsky intrusion is olivine + chromite, followed by intercumulus clinopyroxene and minor amounts of orthopyroxene, plagioclase, phlogopite, amphibole, and sulfides (Sharkov and others, 1995).

Zoning Patterns

If metamorphism has occurred, such as evidenced in the Kemi intrusion and Stillwater Complex, chromite grains may be broken and altered along margins and cracks. In this case, the external shell consists of magnetite and, between the core and the outermost rim, there is typically a thin zone of ferroan chromite (fig. 32*G*). However, the chromite cores remain intact and are chemically unaltered. In some places, the chromite grains show corroded external surfaces due to replacement by serpentine. Chromite-ferrian zoning is also observed in chromite from the Campo Formoso layered intrusion, with polyphase, penetrative hydrothermal metasomatism as the likely cause (Garuti and others, 2007). The ferrian chromite rims are porous and commonly intergrown with chromian clinochlore and carbonates. Locally, hydroxycarbonate stichtite is present along the rim of the chromite grains due to replacement.

Textures and Structures

Chromitite rocks occur in massive to disseminated layers, most frequently with cumulus texture. In stratiform chromite deposits, the chromite grains tend to be larger than those found in podiform chromite deposits. They are frequently subhedral to euhedral in shape. Chromite may also occur as sparse, discrete grains that are spatially isolated by intercumulus minerals, such as bronzite or plagioclase, or embedded in and

intergrown with silicate grains, although this type of chromite is of subeconomic importance and not contained within the chromitite seams.

The massive chromitite of the Campo Formoso Complex, for example, contains chromite that is intergrown with primary silicates, such as olivine, clinopyroxene, orthopyroxene, and, more frequently, with secondary minerals, such as serpentine, chlorite, talc, tremolite-actinolite amphibole, kaemmererite, and smectites (Garuti and others, 2007). In the Ipueira-Medrado Sill of the Jacurici complex, the chromitite seams are either chain-textured or massive (figs. 34*G* and 34*H*; Marques and Ferreira-Filho, 2003). The chain-textured chromitite in the lower part of the Main Chromitite layer is characterized by fine-grained aggregates of chromite surrounding large orthopyroxene crystals. The upper chromitite sublayer is massive, homogeneous, and continuous throughout the sill. Overall, the massive chromitite is fine-grained and consists mainly of chromite crystals (>90 vol%), with poikilitic oikocrysts of orthopyroxene enclosing small grains in some areas.

Dunitic rocks of the Ipueira-Medrado Sill contain fine-grained (<0.2 mm), subhedral, and disseminated chromite crystals, which occur as intercumulus minerals between larger olivine crystals (0.4 to 0.8 mm) (fig. 36). Larger clumps of chromite, as much as 0.8 mm in diameter, are present as well as, probably due to annealing or coalescence of small grains. Disseminated chromite occurs in the harzburgite rocks and is as large as 0.5 mm in diameter. Accessory chromite can be found in the gabbroic rocks of the marginal zone (<1 vol%), pyroxene-rich harzburgites, and orthopyroxenites from the upper part of the Upper Ultramafic Unit, generally at 3 to 5 vol%, but as much as 10 vol% in orthopyroxenites. Rarely, norites contain as much as 3 vol% (Marques and Ferreira-Filho, 2003).
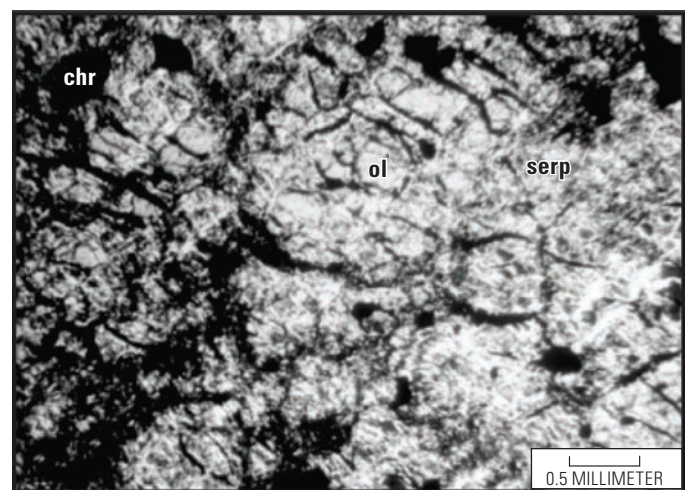
Figure 36. Photomicrograph of a serpentinized dunite with olivine relicts (ol) and chromite (chr) from the Lower Ultramafic Unit of the Ipueria-Medrado Sill. From Marques and Ferreira-Filho (2003, fig. 8*a*).

Most chromite grains in the LG6 chromitite seam of the Bushveld Complex are accumulate types and coarse granular, with sizes that range from 53 mm to >2 mm (Schürmann and others, 1998; Kinnaird and others, 2002). In the eastern Bushveld Complex, the LG6 chromitite is generally friable, with hard lumpy patches, and has a poikilitic texture due to pyroxene and (or) plagioclase grains enclosing very fine-grained chromite grains. The oikocrysts range from 5 to 20 mm in diameter (Schürmann and others, 1998). The MG1 chromitite seam consists of cumulus chromite that has a fine, dense, and granular texture. The chromite grains are mostly euhedral and evenly distributed throughout the layer, varying in size from 0.25 and 2.0 mm (Schürmann and others, 1998). Oikocrysts occur throughout the MG1 and are oval shaped,

ranging in size from 3 to 15 mm, but their occurrence is less pronounced than in the LG6. A disseminated zone of chromite has formed about 20 cm above the upper contact of the MG1.

Although not mined for chromite, the UG1 and UG2 from the Dwars River area of the Bushveld Complex have chromite grains with subspherical forms. However, their sizes and abundances change in an unpredictable and patchy manner on mm- to cm-scales (Voordouw and others, 2009). Intergrain triple junctions, a reduction of interstitial silicate matrix, and near-planar boundaries between subgrains of aggregates, including the cuspate forms, in some of the chromites in the Bushveld Complex suggest that significant annealing and recrystallization may have taken place (fig. 37; Eales and Reynolds, 1986; Eales, 1987). Small grains of chromite may
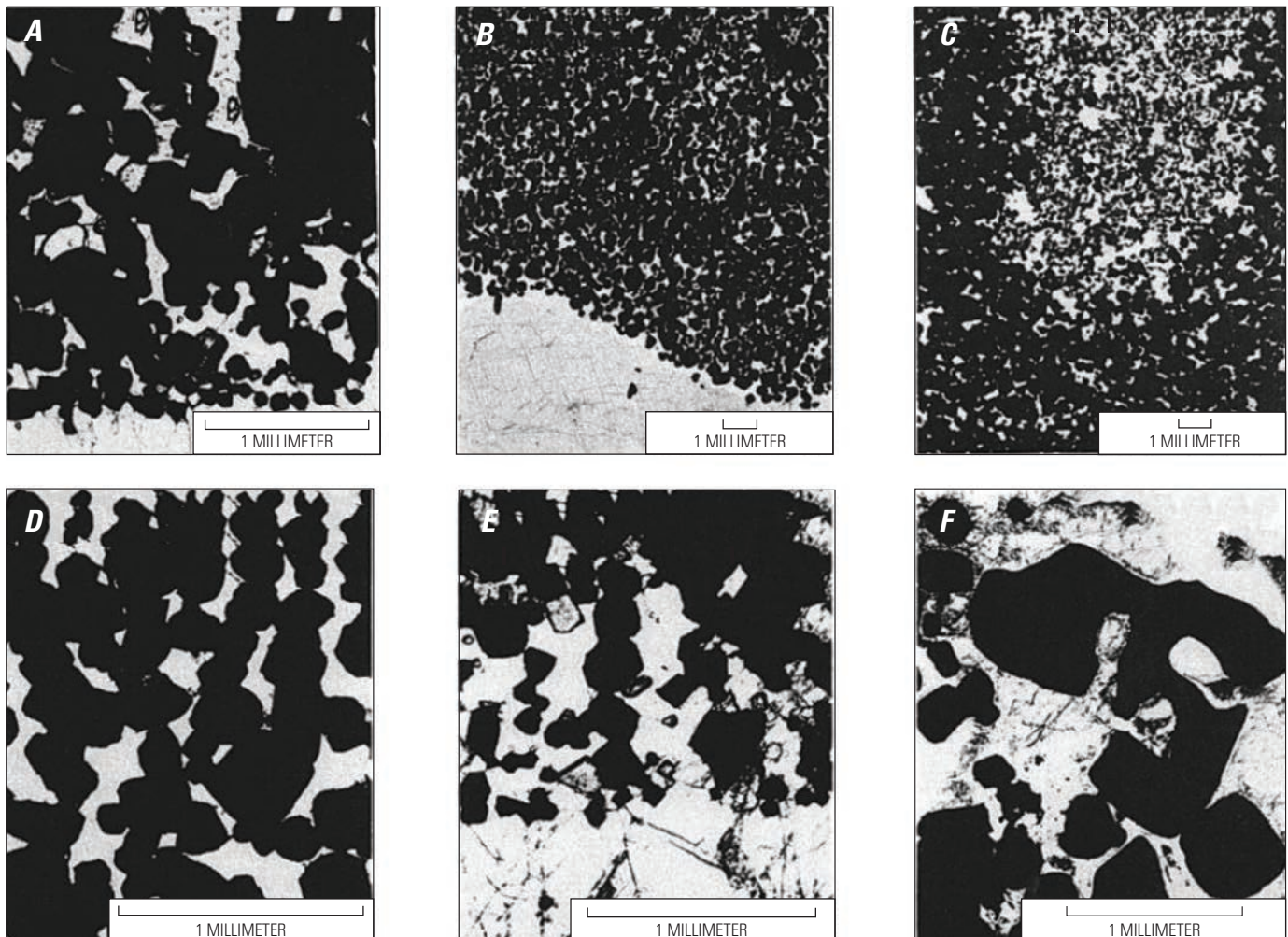
Figure 37.   Photomicrographs of typical Bushveld chromite grains illustrating textural features. From Eales and Reynolds (1986, fig. 2). *A,* Transition from fine-grained to coarse-grained chromite. *B,* Chromitite layer with little evidence of annealing. *C,* Coarse, massive chromitite with poikilitic pyroxene enclosing small ovoid chromite grains. *D,* Chromite grains oriented in vertical columns within poikilitic pyroxene. Failed annealing. *E,* Vertical columns of chromite grains. *F,* Cuspate, lobate forms of chromite from the Pseudoreef, Merensky Reef, and Bastard Reef.

also be found in abundance with poikilitic, pale green chrome diopside oikocrysts. In these cases, their small size is attributable to their being spatially separated by intervening septa of silicate host oikocrysts, which has inhibited the process of annealing, because individual chromite grains are not in intimate physical contact. This texture is, therefore, a clear indication of the generally limited size of the chromite granules in the earlier stages of accumulation, before annealing. In the Dwars River area, as well as at the Maandagshoek Farm, the UG1 and UG2 chromitite seams have anastomized vein-like structures, host xenoliths, and bifurcate structures and textures in host silicates (fig. 38; Gain, 1984; Voordouw and others, 2009). The chromitite seams in these units have also been described as braided.

The chromitite horizons in the Fiskenæsset Complex can be followed laterally for 4 km, but they are disrupted, boudinaged, and faulted due to metamorphic and tectonic events (fig. 39). Folds are common on both minor and major scales, along with tectonic thinning and thickening, which creates considerable local variation in thickness (fig. 39E). Shearing is evident in many places, both along and within the chromitite horizons. This results in the appearance of "pseudo-crossbedding" structures (Ghisler, 1970).

The main chromite-bearing seams in the Rum intrusion occur at the boundary of Unit 7–8 and Unit 11–12 (O'Driscoll and others, 2010). Downward-pointing "cone structures" occur at the Unit 7 (anorthosite) and Unit 8 (peridotite) boundary (fig. 40B). Small packages of detached chromitite are also observed below the main seam (fig. 40B). When hosted in peridotite, the chromite grains occupy embayment structures in the cumulus olivine, with thin rims of plagioclase providing separation from the cumulus olivine (see fig. 33D). Occasionally, chromite and olivine directly contact one another. Locally, olivine crystals may contain chromite inclusions. When intercumulus plagioclase grains enclose chromite grains, most of the chromite is euhedral. On the other hand, chromite grains are rounded and subhedral where embedded within clinopyroxene and olivine (O'Driscoll and others, 2010). Above the main chromite-bearing seam at the Unit 7–8 boundary chromite grains concentrate around the margins of olivine grains creating a "chain-texture" (fig. 41C).

"Subsidiary" chromitite seams are also observed in the Rum intrusion and are thinner (1 to 2 mm) than the main chromitite seams (fig. 40D). Typically the subsidiary chromitite seams occur along the boundary between troctolite, where olivine is a cumulus mineral, and anorthosite, where olivine is only an intercumulus mineral. This boundary cuts the deformation structures, such asperidotite schlieren and anorthosite pods, which are observed in the upper 2 m of the troctolite. In addition, the subsidiary seams are laterally discontinuous on the scale of tens to hundreds of meters (O'Driscoll and others, 2009a; O'Driscoll and others, 2010).

The use of the term "cumulate" is sometimes debated when referenced to chromitite layers found in stratiform chromite deposits. McBirney and Hunter (1995) argue that subsolidus transformations may have influenced final rock textures, such that the term "cumulate" is inaccurate. The recognized role of metasomatism in the alteration of the chromium ore lends support to this criticism. However, for the sake of consistency and in deference to the numerous articles published using the cumulate nomenclature, the prefix "meta" will be regarded as implicit in this model.
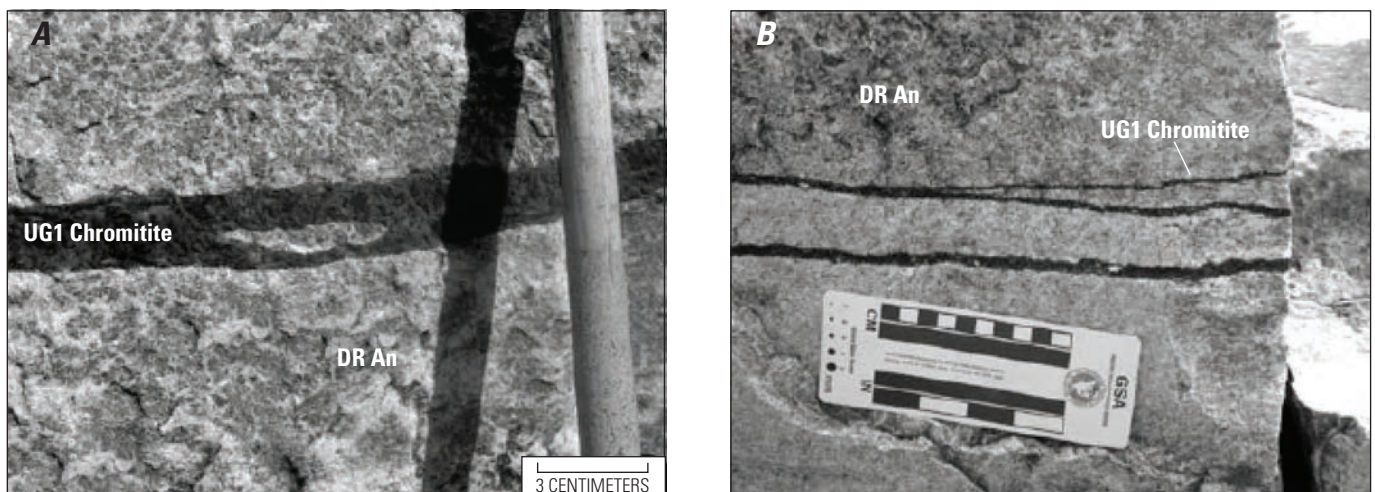
Figure 38.   Photographs of the Upper Group (UG) chromitite seams in the Dwars River area of the Bushveld Complex. A, UG1 chromitite seam, taken at Dwars River Monument, containing an anorthosite (DR An) xenolith. From Voordouw and others (2009, fig. 5e). B, Branching of UG1 chromitite seam in Dwars River area. From Voordouw and others (2009, fig. 6).
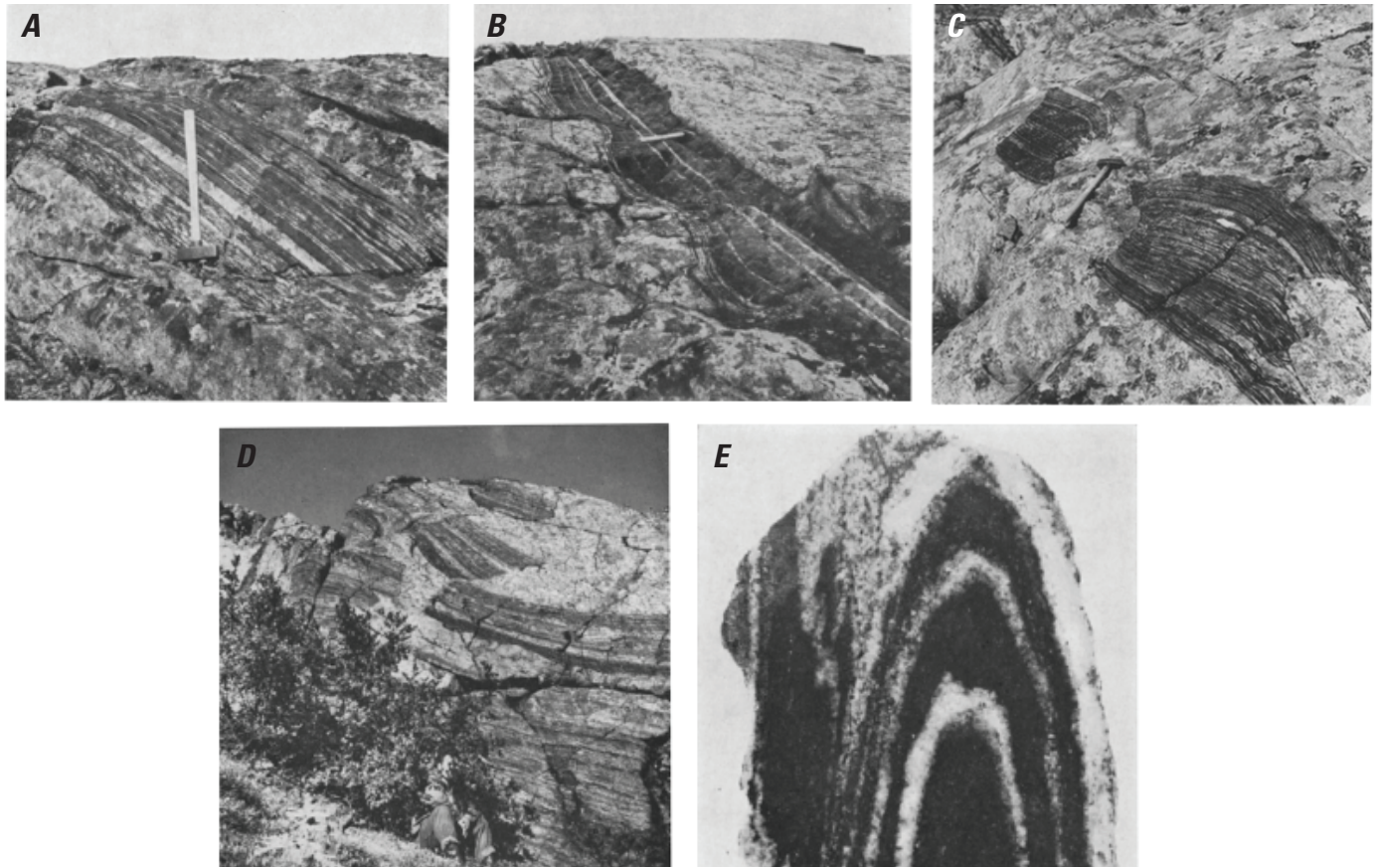
Figure 39.   Outcroppings of the chromitite horizon in the Fiskenæsset anorthosite complex. *A,* Alternating layers of chromitite and anorthosite. Hammer shaft measures 60 centimeters. From Ghisler (1970, fig. 2). *B,* Basin-like structures. From Ghisler (1970, fig. 3). (*C*) Boudinage relics. From Ghisler (1970, fig. 6). *D,* Disrupted chromite horizon in anorthosite. From Ghisler (1970, fig. 7). *E,* Chromitite with small-scale fold (4.5 cm across), interlayered with anorthosite. From Ghisler (1970, fig. 8).
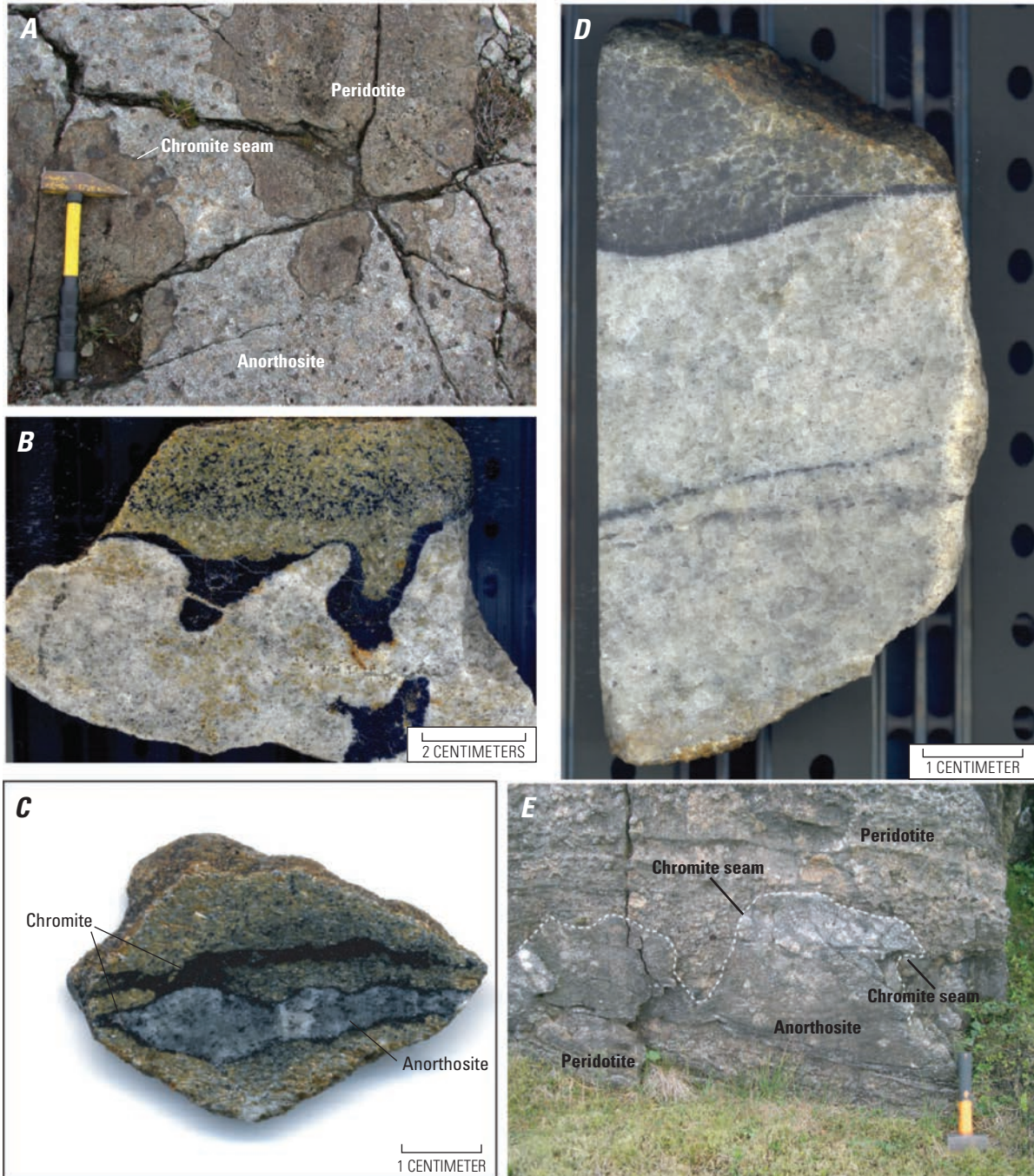
Figure 40. Photographs of chromite-bearing seams from the Rum intrusion. From O'Driscoll and others (2010, fig. 2). *A,* Field photo in plan view of the Unit 7 (anorthosite) and Unit 8 (peridotite) boundary. Main chromite-bearing seam extends around the margins of the dimpled peridotite. Identified. Hammer shaft is ~30 centimeters (cm). *B,* Polished hand specimen from the Unit 7–8 boundary illustrating the "cone-structure" found in the main seam. Small package of chromitite is detached in the underlying anorthosite. Image is oriented in the upward direction. *C,* Hand specimen of peridotite at the Unit 7–8 boundary showing anorthosite lens surrounded by chromitite. Rock is oriented in the upward direction. *D,* Typical lithological relationship between peridotite and underlying anorthosite with chromite-bearing seam at the boundary (Unit 11–12). Main chromite-bearing seam undulates at boundary. Two subsidiary chromite-bearing seams are visible about 3 cm below the unit boundary. *E,* Boundary of peridotite and anorthosite at Unit 11–12 showing undulatory nature of contact. The main chromite-bearing seam forms a "rind" along the boundary. The length of the hammer shaft is ~25 cm.
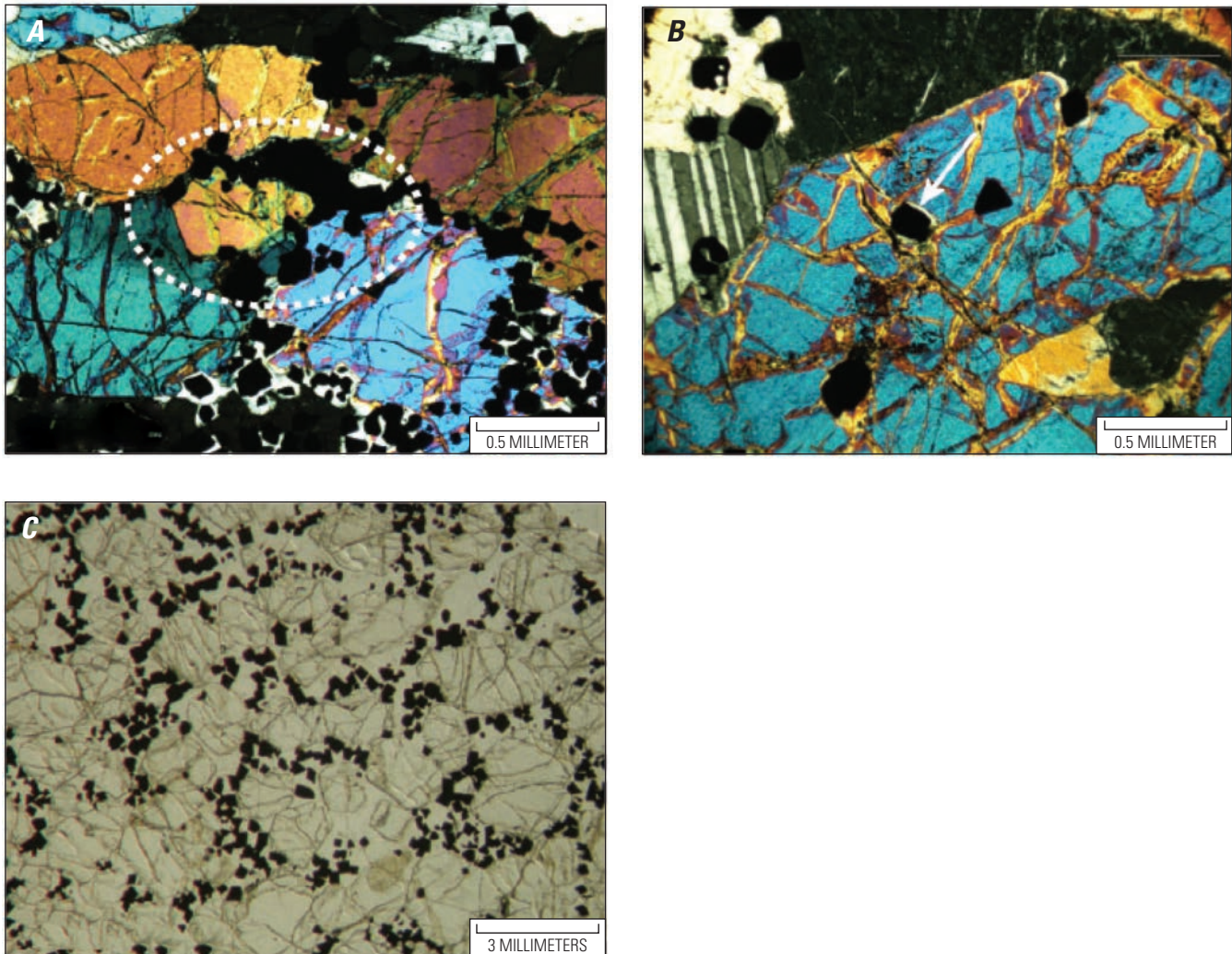
Figure 41.   Photomicrographs of chromite located in the Rum intrusions. From O'Driscoll and others (2010, figs. 4*c,e,g*). *A*, Olivine crystals in direct contact with chromite above the Unit 7–8 chromite-bearing seam. Chromite is concentrated at triple junctions and around grain boundaries (circled in white). *B*, Cumulus olivine crystals located in the Unit 12 peridotite that contain chromite. Thin rims of plagioclase surround the chromite (white arrow). *C*, Example of "chain-texture" chromite where chromite concentrates around the edges of the olivine grains. Plane-polarized light.

Grain Size

Typical chromite grains can range from a few tens of microns (for example, Kemi) to as large as several centimeters (for example, Campo Formoso) in diameter, with the average size being ~0.1 mm. The average size of UG1 and UG2 chromite grains in the Bushveld Complex is, for example, ~0.1 mm (Voordouw and others, 2009). The main chromitite layer at the Unit 7–Unit 8 contact in the ELS of the Rum intrusion also consists of discrete euhedral to subhedral chromite grains that are typically 0.1 mm in diameter (Butcher and others, 1999). Grain size distribution of chromite is uniform throughout the various massive chromitite seams.

Hypogene Gangue Characteristics

Mineralogy

The predominant mineralogy of the stratiform chromite gangue is olivine ± orthopyroxene ± clinopyroxene ± plagioclase (table 9). Rutile and ilmenite are also found in a few deposits. In many cases, the primary silicates have been altered to serpentine, chlorite, and talc. Other alteration phases include magnetite, kaemmererite, uvarovite, hornblende, and carbonate minerals, such as calcite and dolomite.

Olivine-bearing layers within the chromitite zone of the Stillwater Complex contain, in addition to the chromite, intercumulus bronzite and minor clinopyroxene. In the massive

Table 9. Mineralogical comparison between selected stratiform chromite deposits.

Deposits	Chromite mineral assemblage	Gangue minerals	Major base metal sulfides	Minor base metal sulfides	Platinum group minerals	Producing metals	Occurring metals	References
Bushveld Complex (South Africa)	chr ± ol + plag + opx + cpx + phl	opx, plag, mic, cpx, ol	po, cp, pn, py	gn, cub, sph	lrt, spe, coo, brg, i, mer, iso, ele, al	Pt, Pd, Cr, Fe, V	Au, Ag, Cu, Ni, Co, S, Ti, Rh, Ru	1, 2, 5
Stillwater Complex (Montana, USA)	chr + lrt + ol + opx ± plag ± phl	ol, opx, cpx, plag	po, cp, pn	py, ml, cub, vi, mon, kot, coo, brg, mo	lrt, mon, spe, coo, brg, vsk, kot, mer, stw, paa, sbp	Pt, Pd, Cu, Ni, Cr	Ru, Os, Ir, Au, Rh	2, 4, 5, 6, 7
Great Dyke (Zimbabwe)	chr ± lrt ± mgs ± tlc ± ol ± opx	opx, cpx, ol, plag	po, pn, cp, py	gn, bn, apy	spe, ele, brg, coo, lrt, mon, msl, mich, kot, pol, hgw	Pt, Pd, Cr	Cu, Ni, Au, Rh	2, 3
Muskox intrusion (Canada)	chr + cpx + opx + plag + ser ± cpy ± mt ± bt ± po ± pn ± ol	cpx, opx, plag, ol	po, pn, cub, cp, py	gn, sph			Pt, Pd, Cu, Ni, Cr, Fe	2, 8, 9
Kemi intrusion (Canada)	chr + ol ± opx ± cpx ± amp ± plag ± ml	ol, opx, cpx, carb, chl, tlc, srp	po, pn, cp	gn, sph	lrt	Cr	Pt, Pd	2, 11
Rum intrusion (Scotland)	chr ± plag ± ol ± cpx ± sulfides		cp, po, pn	cc, bn	Pd-Cu al, Fe-Pt al, Pt-Cu al, Pt-Ir al, lrt, Pd-Pt tlr, Pd-Pt bis, Pd-Sb ars, i, spe, pl, mich		Cr	12
Campo Formoso Complex (Brazil)	chr + Cr-clc ± tlc ± carb	Cr-clc, tlc, carb	pn	gn, ml, hz, py, cp, bn, pd, vi	lrt, erl, Os-Ir-Ru al, i, hgw, ras, sud	Cr		15, 16
Ipueira-Medrado Sill (Brazil)	chr + opx ± rt ± ol	srp, chl, tlc, carb, opx, ol, rt	no major occurrences		not significant		Cr	19
Burakovsky intrusion (Russia)	chr + ol + cpx ± opx ± plag ± phl ± amp ± sulfides	ol	py, pn, cp, po	cub, ml, bn	lrt, erl, Os- Ir- Rh- sulfides, mon, mer, fr, sob, kot, spe, brg, mich, ele, gev, mln, ngg, pl, hgw, I, coo		Cr, Ni, Ti, V, PGE	10, 20
Niquelândia Complex (Brazil)	chr + ol ± opx	ol, opx, amp, kln, smc, hem, goe, amorphous Fe-hydroxides, amorphous silica	cp, pn	ml, hz, sph, mo, ac, bta	lrt, erl,i, Os-Ir al, Pt-Fe al		Ni, Cr, Pt, Pd, Rh, Ru, Au, Ag	2, 13, 14
Bird River Sill (Canada)	chr + ol + numerous inclusions		po, pn, cp, py	sph, vi, br, smt	lrt, rti, PGE alloys		Cr, Ni, Cu, Pt, Pd, Ag, Au	17, 18

Mineral abbreviations: ac, acanthite; al, alloys; amp, amphibole; apy, arsenopyrite; ars, arsenides; bis, bismuthides; bn, bornite; br, bravoite; brg, braggite; bt, biotite; bta, breithaupite; carb, carbonates; cc, chalcocite; chl, chlorite; chr, chromite; coo, cooperite; cp, chalcopyrite; cpx, clinopyroxene; Cr-clc, chromium clinoclore; cub, cubanite; ele, electrum; erl, erlichmanite; fr, froodite; gev, geversite; gn, galena, goe, goethite; hem, hematite; hgw, hollingwothite; hz, heazlewoodite; i, irarsite; iso, isoferroplatinum; kln, kaolinite; kot, kotulskite; lrt, laurite; mer, merenskyite; mgs, magnesite; mic, mica; mich, michenerite; ml, millerite; mln, malanite; mo, molybdenite; mon, moncheite; msl, maslovite; mt, magnetite; ngg, niggliite; ol, olivine; opx, orthopyroxene; paa, palladoarsenide; pd, polydymite; phl, phlogopite; pl, platarsite; plag, plagioclase; pn, pentlandite; po, pyrrhotite; pol, polarite; py, pyrite; ras, ruarsite; rt, rutile; rti, rutheniridosmine; sbp, stibiopalladinite; ser, sericite; sig, sigenite; smc, smectite; smt, smithite; sob, sobolevskite; spe, sperrylite; sph, sphalerite; srp, serpentine; stw, stillwaterite; sud, sudburyite; tlc, talc; tlr, tellurides; vi, violarite; vsk, vysotskite.

Metal abbreviations: Ag, silver; Au, gold; Co, cobalt; Cr, chromium; Cu, copper; Fe, iron; Ir, iridium; Ni, nickel; Os, osmium; Pd, palladium; Pt, platinum; Rh, rhodium; Ru, ruthenium; S, sulfur; Ti, titanium; V, vanadium.

References: 1, Von Gruenewaldt and others (1986); 2, Lee (1996); 3, Wilson (1996); 4, McCallum (1996); 5, Cawthorn and others (2005); 6, Page and others (1976); 7, Marcantonio and others (1993); 8, Chamberlain (1967); 9, Day and others (2008); 10, Mazzucchelli and Robbins (1973); 11, Sharkov and others (1995); 12, Alapieti and others (1989); 13, Butcher and others (1999); 14, Rudashevsky and others (2002); 15, Girardi and others (2006); 16, Garuti and others (2005); 17, Garuti and others (2007); 18, Talkington and others (1983); 19, Scott and Gasparrini (1973); 20, Marques and Ferreira Filho (2003); 21, Grishaenko (2007).

chromite-rich layers, cumulus minerals include mostly clino-pyroxene and minor plagioclase (Campbell and Murck, 1993). Postcumulus bronzite crystals in the chromite-bearing seams of the Stillwater Complex enclose many olivine grains, giving the olivine grains a net-like appearance. However, in some locations, bronzite occurs both as typical cumulus crystals and as postcumulus oikocrysts. Chromite in the LG6 in the Lower Critical Zone of the eastern Bushveld Complex accounts for 97 percent of the rock, with the remaining 3 percent being made up of orthopyroxene, clinopyroxene, plagioclase, and other minor accessory minerals, such as biotite, sulfides, quartz, talc, chlorite, and carbonates (Schürmann and others, 1998). In the lower MG chromitite seams of the Lower Critical Zone in the eastern Bushveld, chromite makes up 70 to 88 percent of the rock, whereas plagioclase and orthopyroxene make up the major gangue mineralogy (Schürmann and others, 1998; Kinnaird and others, 2002). Accessory minerals include biotite, chlorite, phlogopite, quartz, talc, and carbonates. The chromitite layers of the Upper Critical Zone, which hosts the MG3, MG4, UG1, and UG2 seams, are richer in feldspar gangue than the Lower Critical Zone and also contain minor orthopyroxene (Kinnaird and others, 2002; Kruger, 2005). In the Dwars River region of the Bushveld Complex, the UG chromitite seams contain sili-cate phases that make up ~35 to 40 vol% of the modal mineral-ogy (Voordouw and others, 2009). Alteration minerals in these seams include amphibole, chlorite, clinozoisite-epidote, talc, serpentine, quartz, and carbonates. Although these secondary minerals occur in both the UG chromitite seams, they are much more abundant in the UG2 chromitite, comprising as much as ~50 vol% of the silicate minerals (Voordouw and others, 2009).

Clinopyroxene and orthopyroxene crystals in the Burakovsky intrusion also occur as cumulus phases within an intercumulus matrix, and are subhedral to euhedral and contain apparent parallel exsolution lamellae that are 10 to 20 mm in width (Higgins and others, 1997). In the Ipueira-Medrado Sill, the main gangue mineral is also orthopyroxene, which has commonly been altered to serpentine, chlorite, talc, and minor carbonate (Marques and Ferreira-Filho, 2003). Primary igneous orthopyroxene crystals in the massive chromitites of the Ipueira-Medrado Sill are poikilitic oikocrysts, as much as 1.5 cm in diameter, that enclose dozens of small chromite crystals (0.1 to 0.2 mm) (fig. 34*H*; Marques and Ferreira-Filho, 2003). These orthopyroxene oikocrysts are also surrounded by massive bands of larger annealed chromite crystals that range from 0.5 to 0.8 mm. The orthopyroxene crystals are only preserved in areas of serpentinization in the Main Chromitite layer.

In the case of the Campo Formoso layered intrusion, chro-mitite zones underwent several episodes of metamorphism, such that chromian chlinochlore is the main gangue mineral. How-ever, subordinate amounts of lizardite, chrysotile, magnetite, chlorite, antigorite, magnesite, talc, dolomite, calcite, and quartz are also present in the gangue mineralogy (Garuti and others, 2007). Monazite, apatite, galena, bismuthinite, antimony, and unknown Pb-Sb compounds have been identified in chromitite samples, and may have also been added metasomatically.

Roughly 5 to 10 percent of the gangue minerals in the Kemi intrusion are carbonates, with dolomite being the most common variety identified (Kujanpää, 1989). In addition, due to alteration, talc and chlorite make the Kemi chromite ore quite friable. Magnetite and chlorite are other common gangue minerals found in Kemi, with chlorite often taking the form of the chrome-bearing mineral kaemmererite. The rarer mineral uvarovite, a chrome-silicate, occurs in places as a gangue mineral, and is typically found close to the upper contact of the orebody.

Hornblende is the dominant silicate mineral of the chro-mitites in the Fiskenæsset Complex, and is generally associ-ated with minor biotite. The grain sizes of hornblende and biotite are similar to that of the chromite, although chromite is locally embedded in a more coarse-grained matrix, such that the texture is described as pseudo-poikilitic (Ghisler, 1970). Pyroxene grains are observed in only a few localities, and relicts of hornblende exist along faults and shear zones. The remaining matrix consists of chlorite and fuchsite, both of which have slightly altered chromite grain boundaries and give a deep green color to the rocks. Where plagioclase occurs, the mineral is equidimensional and generally 2 mm to 2 cm in diameter.

Magnetite is also an important gangue mineral, although it may be present only in minor amounts in some deposits. As inclusions, magnetite may be regular and rounded, varying from a few microns to 0.015 mm in size, for example, in the Fiskenæsset Complex. Magnetite is often widely distributed throughout the chromite grains in the Fiskenæsset Complex, with the smallest magnetite grains arranged along crystal-lographic directions. In general, the size of the magnetite inclusions decreases from the center to the outer edges of the chromite (Ghisler, 1970).

Zoning Patterns

Little evidence appears to support the occurrence of major zoning in the main gangue minerals from chromitite seams.

Textures and Structures

Gangue minerals typically occur as intercumulus grains, although they can also occur as oikocrysts in poikilitic textures (table 9). Postcumulus bronzite crystals in the chromite-rich seams of the Stillwater Complex, for example enclose many olivine grains, which gives the olivines a net-like appearance. However, bronzite can occur both as typical cumulus crystals and as post-cumulus oikocrysts. For additional information on the types of textures and structures found in the gangue minerals associated with stratiform chromite deposits, readers are referred to the previous section on the hypogene gangue mineralogy.

Geochemical Characteristics

Major and Trace Elements

Chromitites from layered mafic-ultramafic igneous intrusions contain high levels of chromium and demonstrate strong associations with PGE. The rocks are also characterized by anomalously high magnesium (Mg) contents and low sodium (Na), potassium (K), and phosphorus (P) compositions. Variations in overall composition are attributed to competition between chromite and orthopyroxene for aluminum (Al), iron (Fe), and Mg during coprecipitation and subsolidus reequilibration.

In particular, there is an inverse correlation between Fe^{2+} and Mg^{2+} in chromite. The Mg # $[Mg^{2+}/(Mg^{2+} + Fe^{2+})]$ or Mg ratio, generally decreases upward stratigraphically in most stratiform chromite complexes due to the diminishing availability of Mg^{2+} in the residual melt fraction. As a result, the Mg # is often used to indicate the degree of crystal fractionation. Variations in temperature, pressure, or effective f_{O2}, or the cocrystallization of Fe-Mg silicate mineral phases, can also cause cyclic fluctuations in the Mg ratio. In addition, the maximum Cr/Fe ratios generally diminish with stratigraphic height of successive layers, whereas Fe, titanium (Ti), and vanadium (V) increase.

Aluminum is an important geochemical parameter in that it substitutes freely for chromium in the spinel structure, such that there is a slight upward decrease in the chrome ratio $[Cr^{3+}/(Cr^{3+}+Al^{3+}+Fe^{3+})]$, or Cr #, through a layered sequence. This phenomenon is usually attributed to the depletion of Cr in the melt fraction (Irvine, 1977; Hulbert and Von Gruenewaldt, 1985). However, if cocumulus Al silicate phases are crystallizing, the use of the Cr ratio is inappropriate, insofar as Al^{3+} will partition preferentially into the Al silicates (Eales and Marsh, 1983). Studies by Irvine (1967) and Dick and Bullen (1984) highlighted the ability to use the Cr # as a petrogenetic indicator. They found that a Cr ratio >0.70 indicates that the deposit formed in an arc-related setting, whereas a value between 0.30 and 0.70 suggests mid-ocean ridge origins.

Manganese (Mn) also has the potential to enter the chromite crystal lattice, but if olivine is present, Mn will mainly partition into olivine due to its large ionic radius. Although the Mn content in chromite can be highly variable, it generally stays within the range of 0.15 to 0.25 cation units (Stowe, 1994). Along with Mg #, the Mn content of stratiform chromite deposits decreases upward through the layered sequence. Both nickel (Ni) and cobalt (Co) behave similarly to Mn in that they have large ionic radii and low concentrations. Zinc (Zn) can also substitute into the chromite lattice, but few studies examine the Zn content of chromite ores.

A brief summary of the major and trace element characteristics of important stratiform chromite deposits is included in table 10. For more details on those complexes not covered in the following summary, readers may refer to the references cited at the bottom of table 10.

Bushveld Complex

The amount of total Cr in the chromite layers and pyroxenes of the Critical Zone in the eastern Bushveld varies between 6,000 and 13,000 parts per million (ppm) (Cameron, 1982). The LG6 chromitite layer has Cr_2O_3 contents between 46 and 48 wt%, with a Cr/Fe ratio that varies from 1.56 to 1.6 (Schürmann and others, 1998). Teigler (1999) reports Cr/Fe values, where the ratio includes total Fe, for the LG6 chromitite layer between 1.52 and 1.61, but the Cr/Fe values fall below 1.42 in the orthopyroxenite footwall and hangingwall. Chromite mined in the Nietverdiend area, 60 km north of Zeerust, is more refractory-grade, with Cr_2O_3 contents that range between 47.6 and 51.7 wt% and Cr/Fe ratios that vary between 1.88 and 2.06 (Engelbrecht, 1987).

In general, the Cr content of the chromitite in the Lower Critical Zone declines between the lowest and highest layers, whereas Al initially increases through this section and then remains constant with the appearance of cumulus plagioclase (Teigler and Eales, 1993). The TiO_2 contents rise irregularly from 0.65 wt% at the base of the Lower Critical Zone to 1.8 wt% at higher levels, with no visible patterns in the profile. The MG chromitite seams that are thick enough to allow mining have Cr_2O_3 contents between 44 and 46 wt% and Cr/Fe ratios between 1.35 and 1.50 (Schürmann and others, 1998). High Cr/Fe ratios (2.13 to 2.83) in the chromitite layers of the Upper and Lower Critical Zone are found in the Grasvally area south of Potgietersrus.

Chromite grains from the chromitite layers of the Critical Zone contain the highest PGE compositions (717 to 945 parts per billion (ppb) total PGE), whereas chromite from adjacent chromitiferous orthopyroxenite layers record lower values (304 ppb total PGE) (Teigler, 1999). At the Union Section mine, in the northern limb of the western sector of the Bushveld Complex, the average Cr_2O_3 contents are 42.4 to 44.3 wt% for the UG1 unit, 37.2 to 43.8 wt% for the UG2, and <41.3 wt% for the remaining upper layers (Eales and Reynolds, 1986) (table 10). Schürmann and others (1998) report the average chrome content of the UG2 chromitite as 43.5 wt% Cr_2O_3, with Cr/Fe ratios that vary between 1.26 and 1.4. Mitchell and Scoon (2007) have demonstrated an inverse correlation in the Merensky Reef at Winnaarshoek in the eastern Bushveld between the Cr/Fe ratio and the ratio of low-temperature (Pt+Pd+Rh) to high-temperature (Ru+Os+Ir) PGEs within the layers. Successive chromitite layers reveal Cr/Fe ratios that decline upward stratigraphically from 2.2 to 1.3 (Eales and Cawthorn, 1996). However, the chromite produced as a by-product from the mining of PGEs in the UG2 currently has no market, despite the fact that the UG2 is the world's largest PGE resource.

Table 10.   Geochemical attributes of selected stratiform chromite deposits.

[max, maximum; avg, average; wt%, weight percent; Mg_{chr} #, magnesium ratio [Mg/(Mg+Fe)] of chromite; Mg_{opx} #, magnesium ratio [Mg/(Mg+Fe)] of orthopyroxene; tot, total; g/t, gram/tonne; ppm, parts per million; <, less than; >, greater than; ~, approximate]

Deposits	Bushveld Complex (South Africa)	Stillwater Complex (Montana, USA)	Great Dyke (Zimbabwe)	Muskox intrusion (Canada)	Burakovsky intrusion (Canada)	Kemi intrusion (Finland)	Rum intrusion (Scotland)	Niquelandia complex (Brazil)	Campo Formoso Complex (Brazil)	Ipueira-Medrado Sill (Brazil)	Fiskenaesset anorthosite complex (Greenland)	Bird River Sill (Canada)
Cr/Fe	0.95–3.0	1.0–2.1	2.1–3.9	1.2 max	0.67–0.80	2.6 max, 1.53 avg			1.26–2.43	1.11–2.64		1.0–1.5
Cr/(Cr+Al)	0.60–0.75	0.60–0.66	0.70–0.80	0.681 avg		0.60–0.97; mostly 0.6–0.7			0.59–0.77	0.48–0.63		0.57–0.64; 0.57–0.69
Ore Cr_2O_3 (wt%)	40–50	35–47	40		49–52	26.6	21–45	35.99–46.12	30–57	30–40	34.48	
Al_2O_3 (wt%)			9.96–10.09				10–40	20.96–28.98	10.64–20.46		24.02	
MgO (wt%)			12.17–12.32				5–15	11.08–15.75	2.97–14.58		6.20	
Mg_{chr} #	0.24–0.58	0.39–0.57	0.36–0.67	0.338 avg		0.01–0.54	0.55–0.70		0.24–0.43	0.40–0.61		0.13–0.43; 0.08–0.44
Mg_{opx} #	30–89	60–85	48–91	0.74–0.86		0.83						
FeO (wt%)			14.41–14.82								25.23	
Fe_2O_3 (wt%)			0.98–3.73								6.48	
FeO_{tot} (wt%)					24			14.83–22.20	14.22–36.12			
TiO_2 (wt%)	0.65–1.8		0.27–0.33		1.2–1.4			0.19–0.52	0.13–0.452		0.44	
V_2O_5											0.27	
PGE conc.	5.67 g/t	24.91 g/t	5.42g/t						<1 g/t			
Ore Pt/Pd	variable, typically ≥1	0.35	1.65	0.28		~1			<1	>1		<1
Cu (wt%)	0.06	0.02	0.14	0.32					Cu/Ni <1	Cu/Ni <1		
Ni (wt%)	0.13	0.05	0.21	0.25	up to 0.33	0.10–0.14						630–1,030 ppm
MnO (wt%)						0.3–0.6					0.28	
ZnO (wt%)						3.4						
References	1, 2, 4, 18	1, 3, 7, 18	1, 2, 3, 5, 18	1, 3, 19, 20	23	2, 11, 3	22	21	2, 9, 15, 21	13, 15	24	1, 23

References: 1, Stowe (1994) and references therein; 2, Cawthorn and others (2005); 3, Lee (1996); 4, Eales and Cawthorn (1996); 5, Wilson (1996); 6, Emeleus and others (1996); 7, McCallum (1996); 9, Garuti and others (2007); 11, Alapieti and others (1989); 12, Perron (1995); 13, Marques and Ferriera Filho (2003); 15, Lord and others (2004); 16, Marathon PGM Corp. (2008); 18, Naldrett (2004) and references therein; 19, Francis (1992); 20, Roach and others (1998); 21, Girardi and others (2006); 22, O'Driscoll and others (2009a); 23, Sharkov and others (1995); 24, Ghisler (1970); 25, Ohmenstetter and others (1986).

Stillwater Complex

The highest concentrations of chromite occur in the peridotite member of each cyclic unit within the Ultramafic Series of the Stillwater Complex. Within the chromite-rich zones of the peridotite member, the chromite Cr content strongly correlates with its stratigraphic position, with Cr generally higher at the base of each massive chromite-bearing layer and decreasing upward (Jackson, 1969; Campbell and Murck, 1993). Overall, the Cr_2O_3 values of the chromite vary from 35 to 47 wt%, and the Cr/Fe ratio spans 1.0 to 2.1 (Stowe, 1994;

Naldrett, 2004). There is a correlation between decreasing $Fe^{+3}/(Cr+Al+Fe^{+3})$ and $Fe^{+2}/(Mg+Fe^{+2})$ in the H chromite-bearing seam, with an increase in volume percent of sulfide minerals (fig. 42; Page, 1971). The primary compositions of the chromites are preserved in the massive chromite-bearing seams, but subsolidus exchange with silicates has occurred in the disseminated chromites. Minor amounts of chromite are also present in harzburgites, bronzitites, and in olivine-bearing rocks of the J-M Reef (McCallum, 1996). However, the chromites are more Fe-rich in the J-M Reef than in the Ultramafic Series.
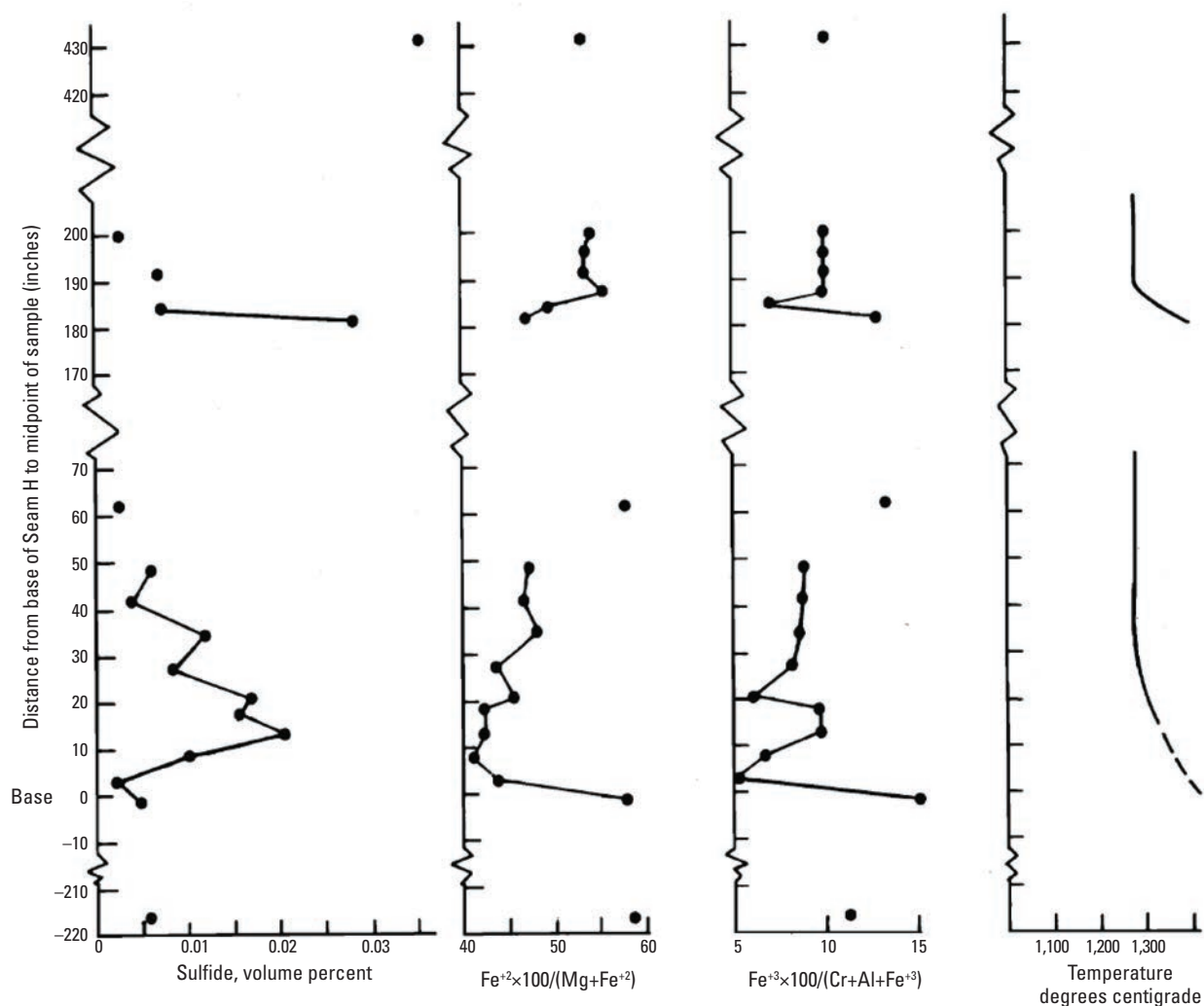
Figure 42.   Graphs illustrating the changes in volume percent of sulfides with decreasing $Fe^{+3}/(Cr+Al+Fe^{+3})$ and $Fe^{+2}/(Mg+Fe^{+2})$ in the H chromite-bearing seam. Liquidus temperature trends of olivine-chromite crystallization shown in relation to stratigraphic position in the H seam.

Great Dyke

Chromite ore in the Great Dyke contains 40 wt% Cr_2O_3 and is characterized by Cr/Fe ratios that vary from 2.1 to 3.9 (Stowe, 1994). In the Darwendale Subchamber, the chromite in chromitite seams of the Ultramafic Sequence shows a trend of increasing MgO and Cr_2O_3 with stratigraphic height (Wilson, 1996). Sheared chromite grains differ slightly in composition from the primary euhedral chromite crystals. For example, an unsheared chromitite has 57.40 wt% Cr_2O_3 whereas a sheared chromitite has 60.16 wt% Cr_2O_3 (Fernandes, 1999). Minor differences are also observed in TiO_2 contents (0.33 wt% versus 0.27 wt%), Al_2O_3 (10.09 wt% versus 9.96 wt%), FeO (14.82 wt% versus 14.41 wt%), and MgO (12.17 wt% versus 12.32 wt%). The Cr/Fe ratio is also markedly different. For the unsheared chromitite the Cr/Fe ratio is 2.78, whereas the sheared chromitite has a Cr/Fe ratio of 3.46 (Fernandes, 1999). The most pronounced difference between the two types of chromitites, however, occurs in the Fe_2O_3 contents, with the unsheared chromitites at 3.73 wt% and the sheared chromitites at 0.98 wt%.

Muskox Intrusion

In the Muskox intrusion, the chromite contains 35 to 44 wt% Cr_2O_3 and Cr/Fe ratios range from 0.9 to 1.2 (Irvine and Smith, 1969). The Mg # and compatible element contents, such as Cr and Ni, increase progressively upward in the lower 100 m of the intrusion (Mg #: 64.9 to 85.5 ppm, Cr: 15.3 to 4,843 ppm, Ni: 5.71 to 3,338 ppm; Day and others, 2008). In addition, at the juncture of the Main Chromitite Horizon with the roof rocks, a sharp decrease in MgO content occurs and SiO_2 content increases. Rare earth element (REE) profiles vary greatly in the intrusion, with concentrations in the ultramafic rocks lower relative to the granophyric roof and gabbronoritic and picritic marginal zone rocks (fig. 43; Irvine, 1980; Day and others, 2008). The main chromitite layer exhibits Ti anomalies, due to the presence of Ti-rich chromite, as well as niobium (Nb), tantalum (Ta), and lead (Pb) anomalies. Unlike chromitite reefs in other large, layered mafic-ultramafic intrusions, the elevated Ti content (up to 0.86 wt% TiO_2) of the Muskox chromites correlates with
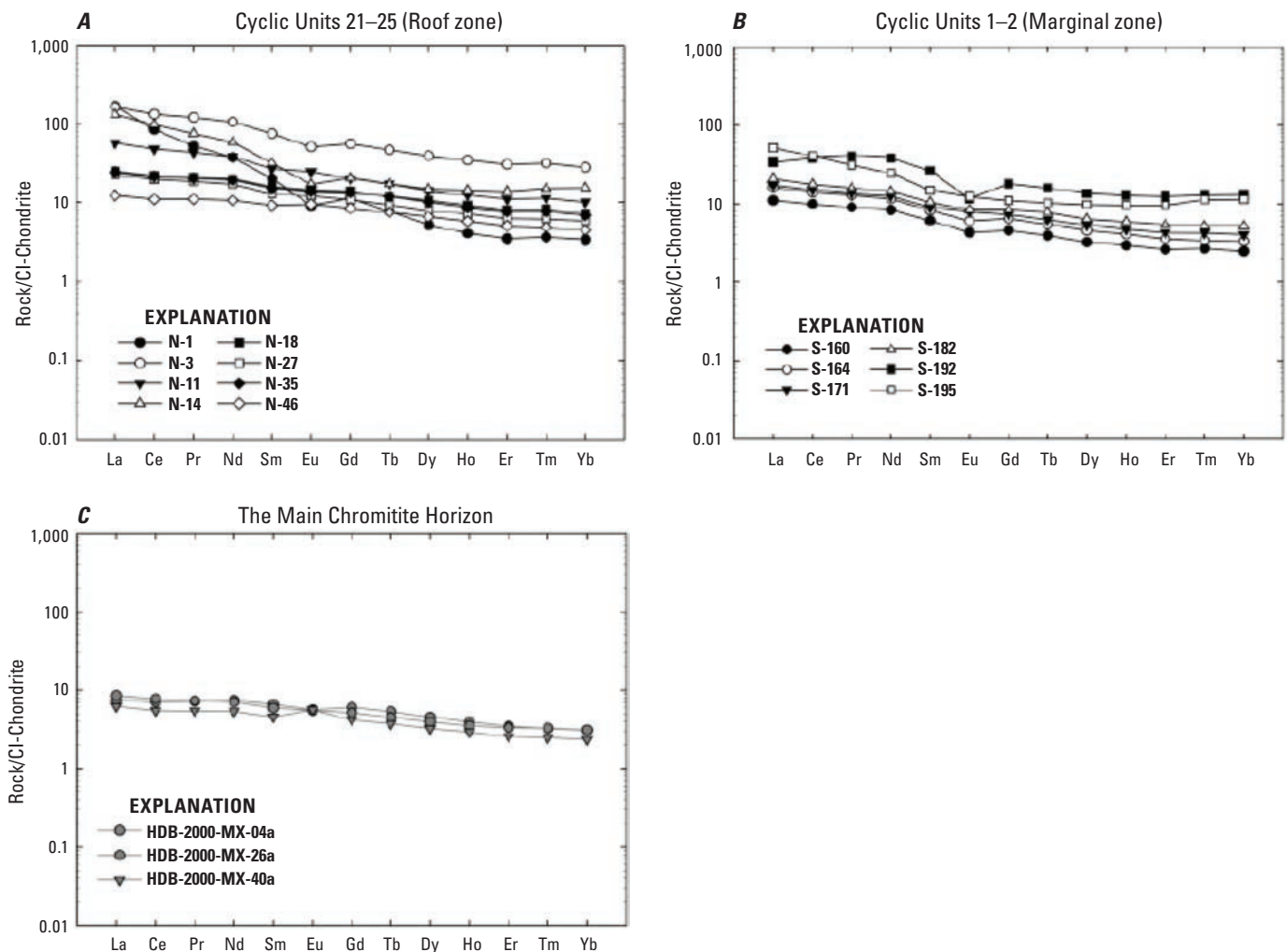
Figure 43. Rare earth element profiles for the *A*, roof rocks; *B*, marginal rocks; and *C*, Main Chromitite Horizon. From Day and others (2008, figs. 5*a,f,h*). Chondrite normalization values based on the work of McDonough and Sun (1995).

greater Fe^{3+} contents, as well as higher $Fe^{2+}/(Fe^{2+} + Mg)$ ratios. This difference may be due to the formation of chromitite higher in the stratigraphic section than elsewhere. In addition, the abundance of the more siderophile elements, such as Re, Pt, and Os, is highly variable throughout the mafic and ultramafic rocks (Re = 0.02 – 105 ppb; Pt = 0.23 – 115 ppb; Os = 0.02 to >200 ppb; Day and others, 2008).

Kemi Intrusion

The proportion of chromite in the chromitite seams of the Kemi intrusion varies irregularly from 50 to 88 percent by mode, whereas the Cr content averages 34 percent (Cawthorn and others, 2005). Although Cr/Fe values of the chromitite are typically about 1.5, the chromite grains have Cr/Fe ratios >2. Due to metamorphism, the chromite grains are frequently altered at the rims, showing a sharp drop in Al from the core of the grain outward. The drop in Al contents corresponds to replacement by ferric iron. However, the Cr content does not decline significantly in an outward direction, making the Cr composition rather constant. The difference in the Cr_2O_3 content between the core and the outer rim is only 3.5 wt%, compared to a 16 wt% decrease in Al content (Alapieti and others, 1989). The Mg content, like Al, also declines abruptly from core to rim. Nickel content, however, increases toward the rim, probably due to the absorption of Ni by chromite from the surrounding mafic magma during alteration. The MnO content in the Kemi chromite is constant, ranging from 0.3 to 0.6 wt%, with the exception of one Cr-rich layer below the main chromitite seam that exceeds 2 wt% (Alapieti and others, 1989). Chromite grains from the ultramafic rocks at the basal contact of the intrusion have anomalously high ZnO contents, averaging 3.4 wt%, compared to typically ~0.11 wt% ZnO in chromite elsewhere in the intrusion (Alapieti and others, 1989). The highest Cr values occur in the main chromitite seam, with decreasing concentrations in the overlying stratigraphic layers. Concentrations of Fe^{+3} Ti, and V increase from the main chromitite upward: Fe^{+3} increased from 3.926 to 7.190 ppm; Ti from 0.078 to 0.851 ppm; and V from 0.023 to 0.119 ppm (Alapieti and others, 1989).

Rum Intrusion

The composition of chromite in the Rum intrusion is variable. The MgO content of chromite in the main chromitite seams ranges from 5 to 15 percent, Al_2O_3 from 10 to 40 percent and Cr_2O_3 from 21 to 45 percent (Emeleus and others, 1996). Chromites from the subsidiary seams are rich in Mg and Al, whereas disseminated chromites in the adjacent anorthosites and troctolites are rich in Fe and Cr (O'Driscoll and others, 2009a). The Mg #s for chromite grains in the subsidiary seam range from about 0.55 to 0.70, and 0.15 to 0.35 for the anorthosite and troctolite. Corresponding Cr #s vary between 0.3 and 0.5 in the subsidiary chromitite seams, and 0.5 and 0.9 in the anorthosite and troctolite. With respect to Fe_2O_3, electron microprobe results reveal that the ferric iron

content of chromites within the subsidiary seams is lower than those outside the seams (O'Driscoll and others, 2009a). Correspondingly, Ni content decreases in chromite grains outside the seam compared to grains within the seam.

Stable Isotope Geochemistry

Oxygen

In layered mafic intrusions, oxygen isotopes are commonly used to determine parental magma sources and extent of crustal contamination. Rarely, oxygen isotopes are used as a geothermometer. Whereas most oxygen isotope studies have not analyzed chromite, a review of oxygen isotopes for other minerals from large, layered stratiform complexes can provide a more complete understanding of the processes involved in formation of the complexes and perhaps shed light on mechanisms related to layering. The same can be said for whole rock analyses.

Progressive upward variations throughout a mafic intrusion have been interpreted to indicate crystal fractionation and (or) hydrothermal alteration during cooling (Taylor, 1968; Dunn, 1986). Due to the temperature-dependant fractionation of oxygen, isotopic equilibrium must be verified to support interpretations of magmatic conditions and is indicated by near constant per mil differences between mineral phases crystallized at magmatic temperatures. If isotopic disequilibrium is established outside of the magmatic range, then it is likely the result of a later hydrothermal alteration event, such that the data cannot be interpreted as tracing the various end-member melt components.

Mantle derived basaltic magma is expected to have a $\delta^{18}O$ value of +5.7 per mil (‰) using the standard meteoric ocean water (SMOW) standard (Ito and others, 1987). The Great Dyke has an average $\delta^{18}O$ of 6.14 ‰, 6.90 ‰, and 6.91 ‰ for orthopyroxene, plagioclase, and clinopyroxene (table 11), respectively, whereas the Bushveld has average mineral values of ~7.1 ‰ (Chaumba and Wilson, 1997; Harris and others, 2005). Isotopic equilibrium between mineral phases for both the Great Dyke and Bushveld suggest that the heavy $\delta^{18}O$ signatures are not the result of hydrothermal alteration, but instead the result of the crustal assimilation in the magma components. Day and others (2008) analyzed chromite, olivine, and clinopyroxene from the Muskox intrusion and found a range of 4.25 to 7.14‰ (table 11), which straddles the range of what would be expected from mantle-derived magmas and suggests localized hydrothermal alteration and limited amounts of crustal contamination. A heavier isotopic signature for many intrusions should not be entirely unexpected, because extraordinary volumes of hot mafic magma injected into the crust will undoubtedly cause some crustal contamination.

The Rum intrusion has $\delta^{18}O$ whole-rock values that range from as depleted as −5.1 ‰ in granophyre to as enriched as +6.8 ‰ in felsite (table 11; Forester and Harmon, 1983; Greenwood and others, 1992). Although some variance between

Table 11.   Oxygen isotopes of selected stratiform chromite deposits.

[wr, whole rock; plag, plagioclase; pyx, pyroxene; opx, orthopyroxene; cpx, clinopyroxene; ol, olivine; n.d., not determined]

Lithology	Stratigraphic zone	$\delta^{18}O$ (‰) wr	$\delta^{18}O$ (‰) plag	$\delta^{18}O$ (‰) pyx	$\delta^{18}O$ (‰) opx	$\delta^{18}O$ (‰) cpx	$\delta^{18}O$ (‰) ol	References
Bushveld Complex (South Africa)								
Pyroxenite and harzburgite	Lower Zone		7.12	6.59			6.23	1
Pyroxenite and norite	Critical Zone		6.88	6.32			n.d.	
Norite/gabbronorite	Main Zone		7.08	6.33			n.d.	
Gabbronorite and apatite diorite	Upper Zone		7.52	6.22			n.d.	
Norite and pyroxenite	Marginal Zone		7.65	6.83			n.d.	
Muskox intrusion (Canada)								
Chromitite	Chromite horizon						5.41	2
Clinopyroxenite, websterite, dunite	Cyclic units						6.07	
Gabbronorite	Keel dyke						6.14	
Stillwater Complex (Montana, USA)								
Peridotite	Peridotite zone		5.9 to 7.1	5.7				3
Orthopyroxenite	Bronzitite zone		4.8	n.d.				
Olivine-bearing troctolite	Lower Banded Series		5.1 to 6.7	5.7 to 6.0				
Gabbronorite/norite	Lower Banded Series		6.2 to 6.4	5.8 to 6.3				
Anorthosite	Middle Banded Series		7.7 to 6.0	n.d.				
Rum intrusion (Scotland)								
Peridotite		1.8 to 4.7	−2.3					4, 5
Gabbro		−2.8 to 3.4	−1.5					
Felsite		−1.8 to 6.8	n.d.					
Granophyre		−5.1 to 3.1	n.d.					
Granite		1.7 to 10	n.d.					
Great Dyke (Zimbabwe)								
Gabbro, websterite, and gabbronorite	Lower Mafic succession		6.9		6.14	6.91		6

1. Harris and others (2005); 2. Day and others (2008); 3. Dunn (1986); 4. Greenwood and others (1992); 5. Taylor (1968); 6. Chaumba and Wilson (1997).

samples can be attributed to modal mineral abundance differences between the analyzed rock samples, the large spread is mainly a function of heated meteoric water interacting with parts of the cooling intrusion complex at various water/rock ratios.

Oxygen isotope geothermometry is primarily utilized at lower temperatures than those that characterize stratiform chromite deposits. At magmatic temperatures, calculations have a greater amount of uncertainty, but can nevertheless be used to determine if multiple injections of magmas occurred at varying temperatures. For example, Dunn (1986) calculated $\Delta^{18}O_{plag–pyx}$ isotopic temperatures of the Stillwater magma using the empirical plagioclase-pyroxene thermometer of Kyser and others (1981) to suggest that the Stillwater Complex was emplaced by the injection of two distinct magmas, each with different temperatures. However, because of the relatively high temperatures of magmatic systems, exchange of oxygen occurs readily. Thus, the isotopic temperature represents the closure temperature of the minerals involved, which is dependent on factors such as cooling rate and grain size. The larger errors associated with high temperature oxygen isotope geothermometry should cause concern to anyone intent on quantitatively characterizing chromite deposit temperatures via this method.

Sulfur

Although sulfide minerals are ubiquitous within stratiform chromite deposits, the source of the sulfur (S) may not be identical in all deposits. Mass balance calculations using total S indicate that many deposits containing abundant sulfide minerals require the addition of sulfur from the surrounding country rocks. Sulfur isotope ratios $[\delta^{34}S; \delta^{34}S = ((^{34}S/^{32}S)_{sample}/(^{34}S/^{32}S)_{VCDT}) − 1$, where VCDT is the standard Vienna Canyon Diablo Troilite, expressed in per mil (‰)$]$ that are dissimilar to mantle values (0 ± 2 ‰ $\delta^{34}S$ VCDT) are likely to have incorporated crustal sulfur, assuming local crustal sulfur composition differs from the parent mantle values. A complicated scenario arises, however, in the interpretation of Archean intrusions (for example, Fiskenæsset) with mantle-like sulfur isotope values, because many Archean country rocks have mantle-like values ($\delta^{34}S = $ ~0 ‰; (Ripley, 1999).

Deposits, such as the Bushveld Complex (Penniston-Dorland and others, 2008) and Great Dyke (Li and others, 2008), record sulfur isotope ratios that suggest a predominantly magmatic sulfur source for sulfide minerals (table 12). The $\delta^{34}S$ values of different size fractions (<125 mm and 125 to 250 mm) of pyrite, pyrrhotite, and chalcopyrite in the Main Sulfide Zone (MSZ) of the Great Dyke ($\delta^{34}S = 0.1$ to 1.0 ‰), for example, are consistent with the argument that the sulfide-bearing layers derived sulfur from a mantle source (Li and others, 2008). To rule out the role of Archean sedimentary sulfides in the formation of the MSZ of the Great Dyke, secondary pyrite was analyzed. The limited range in sulfur isotope values ($\delta^{34}S = 0.4$ to 1 ‰) for secondary pyrite in the MSZ indicates that the pyrite formed in a reduced, H_2S-bearing fluid, which is consistent with an origin from a magmatic source.

In the Bushveld Complex, Penniston-Dorland and others (2008) examined the relationship between the pyroxenitic rocks of the Platreef with the underlying metapelite and metacarbonate footwall rocks and showed that the Bushveld magma at the level of the Platreef was saturated in magmatic sulfur: $\delta^{34}S$ = 1.3 to 3.2 ‰ and $\Delta^{33}S$ = 0.11 to 0.21 ‰, where $\Delta^{33}S = \delta^{33}S - 1{,}000 \times (1 + \delta^{34}S/1000)^{0.515} - 1$. Although the pyroxenites in the upper portions of the Platreef record low $\Delta^{33}S$ values (average = 0.15 ‰), the most distant metapelite and metacarbonate footwall rocks have high $\Delta^{33}S$ values, up to 5.1 ‰. Between the two end members, the $\Delta^{33}S$ profile is variably smooth (fig. 44). As a result, the displacement of the $\Delta^{33}S$ values suggests that sulfur migrated via fluid transport into the footwall country rocks while back diffusion of the S isotope tracer ($\delta^{34}S$) into the Platreef occurred, such that during the formation of the Platreef ore horizon sulfur was lost to the footwall country rocks.

Table 12. Sulfur isotopes for selected stratiform chromite deposits.

[‰, per mil; VCDT, Vienna Canyon Diablo Troilite standard]

Deposits	Type	Lithology	Stratigraphic zone	$\delta^{34}S$ (‰ VCDT)	$\Delta^{33}S$ (‰)	References
Bushveld Complex (South Africa)	Whole rock	Pyroxenite	Platreef	1.3 to 3.2	0.11 to 0.21	1
	Mineral separate (sulfide)	Pyroxenite	Platreef	2.7 to 11.4	0.03 to 0.55	1
	Mineral separate (sulfide)	Pyroxenite	Platreef	–0.7 to 10		1, 2, 3
	Whole rock	Metapelite and metacarbonate	Platreef footwall	–14.5 to 29	0.03 to 5.04	1, 2
Stillwater Complex (Montana, USA)	Mineral separate (sulfide)	Metashale and metagraywacke	Country rock	1.0 to 6.0		4
	Mineral separate (sulfide)	Iron-formation	Iron-formation	–2.6 to 0.0		4
	Mineral separate (sulfide)	Diabase, norite and massive sulfide	Associated sills and dikes	–3.8 to 2.4		4
	Mineral separate (sulfide)	Pyroxenite	Basal series	–2.1 to 3.0		4
	Mineral separate (sulfide)	Peridotite	Peridotite zone	–1.2 to 6.7		4
	Mineral separate (sulfide)	Troctolite, anorthosite	J-M reef, Lower Banded series	–1.0 to 3.7		4
	Mineral separate (disseminated sulfide)	Anorthosite and plagioclase cumulate	Picket Pin, Middle Banded series	–3.0 to 7.3		4
Great Dyke (Zimbabwe)	Mineral separate (sulfide)	Orthopyroxenite	Main Sulfide Zone	0.1 to 1.0		5

1. Penniston-Dorland and others (2008); 2. Buchanan and others (1981); 3. Holwell and others (2007); 4. Zientek and Ripley (1990); 5. Li and others (2008).
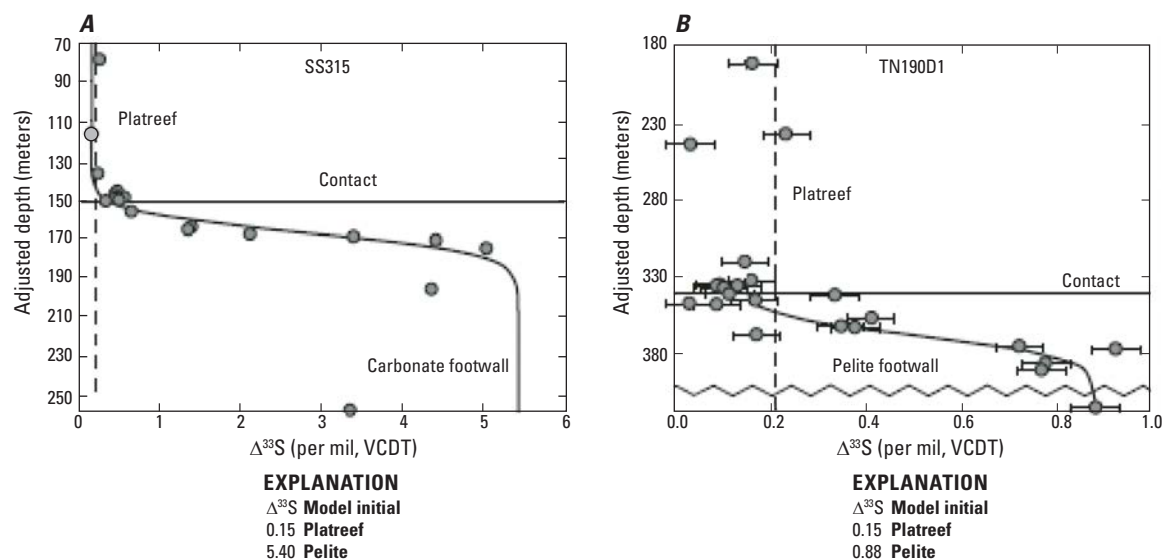
Figure 44. The $\Delta^{33}S$ profiles for two cores (SS315 and TN190D1) taken through the Platreef horizon into the underlying footwall. From Penniston-Dorland and others (2008, figs. 2, 3). A, Cores SS315 and B, N190D1 showing sulfur isotope compositions with depth. Note the smooth, variable profile in $\Delta^{33}S$ with depth between the upper Platreef samples and the distal footwall rocks. Displacement of $\Delta^{33}S$ values across the contact is also evident. Dark solid line represents best fit to data. Dashed line shows upper limit of $\Delta^{33}S$ values for unaltered pyroxenites of the Platreef. Abbreviation: VCDT, Vienna Canyon Diablo Troilite

In contrast, the Stillwater Complex ($\delta^{34}S$ = –3.8 to 7.3 ‰; Zientek and Ripley, 1990) obtained a significant quantity of its sulfur species from assimilation of metashale and metagraywacke ($\delta^{34}S$ = 1.0 to 6.0 ‰) country rock and the nearby ironformation ($\delta^{34}S$ = –2.6 to 0.0 ‰) (Zientek and Ripley, 1990; Ripley and Li, 2003) . Mantle sulfur may account for the formation of the basal sulfide ores due to the fact that many of the $\delta^{34}S$ values at this level are near zero, although exceptions exist ($\delta^{34}S$ values range from –2.1 to 3.0 ‰) (table 12; Zientek and Ripley, 1990; Ripley and Li, 2003).

Radiogenic Isotope Geochemistry

Rb-Sr Isotopes

The rubidium-strontium (Rb-Sr) isotope system is useful in assessing geochronological and geochemical information. In particular, the parent-daughter ratios can provide insight into the sources of igneous rocks, including the role of the mantle and of crustal contamination. However, Rb-Sr isotope studies rarely address just the chromitite seams or chromite minerals found in the layered stratiform complexes. Instead, the focus has been whole rock analyses and mineral separates from the entire layered intrusion. Despite this, Rb-Sr studies are useful in the understanding of this deposit type, insofar as understanding the process of formation for the entire intrusion can elucidate further insight into formation of the chromitite seams.

The Bushveld Complex displays a wide range of initial Sr isotope ratios (Sr_i) between ~0.703 in the chilled rocks marginal to the lowermost zones, and >0.709 in the Main Zone (table 13; Sharpe, 1985; Kruger, 1994; Kinnaird and others, 2002). The changes in isotope ratios may also be distinct through relatively short stratigraphic intervals, suggesting several episodes of magma addition took place. For example, the contrasting Sr isotopic compositions of the Lower, Critical, and Lower Main Zones of the Bushveld Complex, along with concomitant mixing, crystallization, and deposition of cumulates, indicate formation in an open system, referred to as the 'Integration stage' (Kruger, 1994, 2005; Kinnaird and others, 2002). Specifically, the initial $^{87}Sr/^{86}Sr$ ratio changes from ~0.705 in the harzburgite of the Lower Zone, to ~0.7064 in orthopyroxenite from the Lower Critical Zone and norite and anorthosite in the Upper Critical Zone, and then finally to ~0.7064 to 0.709 in norite and gabbronorite in the Lower Main Zone (Molyneux, 1974; Cameron, 1978; 1982; Kruger, 1994; Kinnaird and others, 2002). Within solely the LG chromitites, the initial Sr ratio of the interstitial plagioclase varies from 0.7066 to 0.7070 (Kinnaird and others, 2002). The highest initial Sr ratio ($^{87}Sr/^{86}Sr$ = 0.7080) for the chromitite seams occurs in the MG3 package. Furthermore, the extremely abrupt increases in the Sr isotope ratio throughout the major chromitite layers in the Bushveld Complex suggest that the intruding parent melt experienced massive contamination upon contact with the roof of the chamber, which caused

incorporation of the floating granophyric liquid, forcing the precipitation of chromite (Kruger 1999; Kinnaird and others, 2002).

A closed system where there were no major magma influxes occurred in the Upper Main Zone (initial $^{87}Sr/^{86}Sr$ = 0.7084) and Upper Zone (initial $^{87}Sr/^{86}Sr$ = 0.7072), and has been referred to as the "Differentiation stage" (Kinnaird and others, 2002; Kruger, 2005). As a result, the thick magma layers found at this level of the Bushveld Complex formed by fractional crystallization. One exception is a single, very large, and final magma addition that occurred at the level near the Pyroxenite Marker, a distinctive orthopyroxenite layer in a relatively uniform succession of gabbronorites at the base of the Upper Zone (Kruger and others, 1987; Cawthorn and others, 1991). Both the significant increase in Sr_i ($^{87}Sr/^{86}Sr$ = 0.7064–0.7086) at the basal contact of the Merensky Reef, which overlies the Critical Zone and marks the beginning of the Main Zone, followed by a sharp decline in Sr_i ($^{87}Sr/^{86}Sr$ = 0.7073) close to the level of the Pyroxenite Marker, which is a prominent orthopyroxenite layer occurring at or near the Main Zone-Upper Zone boundary, suggests the introduction of a different magma composition at this level (Hamilton, 1977; Kruger and Marsh, 1982).

In the Stillwater Complex, the Rb-Sr ratios are inhomogeneous, indicating postcrystallization remobilization of Rb and (or) Sr. In particular, the initial Sr isotopic ratios, reported as $\varepsilon_{Sr(2701)}$, range from +1.4 to +31.3 (table 13; Simmons and Lambert, 1982). Stewart and DePaolo (1987) determined that $\varepsilon_{Sr(2701)}$ varies from –2.0 to +25. In both cases, the ranges are larger than expected for a homogeneous magmatic system. For a more in-depth discussion, see Fenton and Faure (1969), Kistler and others (1969), DePaolo and Wasserburg (1979), and Lambert and others (1989).

The Great Dyke records Sr isotopic ratios similar to values reported for the Stillwater (~0.7024; DePaolo and Wasserburg, 1979) and Bushveld (0.703 to 0.708; Sharpe, 1985). However, unlike the Bushveld and Stillwater Complexes, the initial Sr values for minerals and whole rocks of the Great Dyke are basically constant ($^{87}Sr/^{86}Sr$ = 0.70327 to 0.72940; table 13), even for samples located in vastly different parts of the stratigraphic column and in different subchambers (Hamilton, 1977). At the same time, the initial $^{87}S/^{86}Sr$ averages 0.70261 ± 4, indicating that the initial magma was primitive and not crustally contaminated (Hamilton, 1977).

The $^{87}Sr/^{86}Sr$ of the Rum intrusion for Units 8–14 in the Eastern Layered Series vary from 0.7034 to 0.7065 (table 13; Palacz, 1985). In the overlying feldspathic peridotites, the $^{87}Sr/^{86}Sr$ ranges from 0.7049 to 0.7053, and, the $^{87}Sr/^{86}Sr$ in the allivalite is ~0.706. Together with Sm-Nd isotopic data (below), these sets of values and their respective positions within the intrusion also suggest that the Eastern Layered Series formed from uncontaminated batches of picritic magma that were injected into a magma chamber containing crustally contaminated and relatively evolved basaltic magma.

Table 13. Sulfur isotopes for selected stratiform chromite deposits.

[Values in parentheses are averages; ‰, per mil; VCDT, Vienna Canyon Diablo Troilite standard]

Stratigraphic location	Zone or seam	Lithology	$^{87}Sr/^{86}Sr_i$	$^{143}Nd/^{144}Nd$	ε_{Nd}	$^{187}Os/^{188}Os_i$	γOs	References
Bushveld Complex (South Africa)								
Lower Zone		Pyroxenite and harzburgite	(0.705)	0.511393 to 0.511549	–6.0 to –5.4		+10 ± 34	1, 2, 3, 4, 5, 6, 7, 8, 9, 10, 11, 12, 13, 26, 27
Lower Critical Zone	Lower Group chromitite	Orthopyroxenite	0.7048 to 0.707		–6 to –5.3			
		Chromitite	0.7066 to 0.7070			0.1151 to 0.1400	+23.0 +12.7	
Critical Zone	Main Group chromitite	Pyroxenite		0.511462 to 0.511513				
		Chromitite	0.7080			0.129 to 0.1422		
Upper Critical Zone		Chromitite, norite and anorthosite	(0.7064)	0.5111000 to 0.511428	–7.6 to –6.3	0.13632 to 0.1530 0.1773	+22.4 ± 35.8	
	Upper Group chromitite Merensky Reef	Chromitite Pyroxenite, harzburgite, dunite	0.7064 to 0.7086					
Lower Main Zone		Norite and gabbronorite	0.7064 to 0.7090	0.511604 to 0.511792	–7.9 to –6.4			
Upper Main Zone		Gabbronorite	(0.7084)					
Main Zone-Upper Zone boundary	Pyroxenite Marker	Orthopyroxenite	(0.7073)					
Upper Zone		Gabbronorite	0.7075 to 0.709					
Marginal Zone		Norite and pyroxenite	(0.703)					
Muskox intrusion (Canada)								
Chromite horizon		Chromitite	0.705 to 0.709			0.1338 to 0.1502		14
Cyclic units		Clinopyroxenite, websterite, dunite		0.511330 to 0.512945	–11.4 to –0.1	0.1228 to 0.2539	+1.8 ± 87.6	
Keel dyke		Gabbronorite		0.512290		0.13661 to 0.15401		
Marginal Zone		Bronzite gabbro				0.13626 to 2.93012		
Stillwater Complex (Montana, USA)								
Ultramafic series	Peridotite zone	Peridotite and chromitite	(0.7024)	0.511714 to 0.513422	–5.6 ± 1.7	0.11174 to 0.19794	+2 ± 34	15, 16, 17, 18, 19

Table 13.   Sulfur isotopes for selected stratiform chromite deposits.—Continued

[Values in parentheses are averages; ‰, per mil; VCDT, Vienna Canyon Diablo Troilite standard]

Stratigraphic location	Zone or seam	Lithology	$^{87}Sr/^{86}Sri$	$^{143}Nd/^{144}Nd$	ε_{Nd}	$^{187}Os/^{188}Osi$	γOs	References
Rum intrusion (Scotland)								
	Units 8 -15	Peridotite, troctolite, gabbro	0.7036-0.706	0.51281-0.5123	2.2 ± 3.9	0.1305 to 0.1349	+3.4 ± 35.7	20, 21
	Undefined cyclic units	Feldspathic peridotites	0.7019 - 0.7053	0.51271 - 0.51253				
		Allavite	(0.706)	0.51249 - 0.5123				
Great Dyke (Zimbabwe)								
Entire intrusion	Chromitite seams in layered series	Chromitite	0.70327 - 0.72940	0.511068 - 0.514724	+0.4 ± 5.0	0.1025 to 0.1150 0.1106 to 0.1126	-6.9 ± 4.4	6, 7
Ipueria-Medrado sill (Brazil)								
Ultramafic Zone	Lower Ultramafic Unit	Chromitite		0.510930 to 0.511553	-3.9 to -6.7	0.11038 0.14013 to 0.17910	-3.25 18 ± 50	22
		Harzburgite						
	Main Chromitite Layer	Chromitite				0.10890 to 0.11406	-4.6 to -0.27	
	Upper Ultramafic Unit	Amphibole-rich harzburgite		0.511314 to 0.511772	-6.3 to -6.8 (-6.5)	0.23430 to 0.43650	+37 ± 235	
		Chromitite				0.11621 to 0.11899	+1.4 ± 3.3	
		Amphibole-free harzburgite			-4.7			
Niquelândia Complex (Brazil)								
Lower sequence		Peridotite, pyroxenite, gabbronorite, chromitite	0.70650 to 0.73366	0.511874 to 0.513730	-10.83 to 6.48 (-5.8)	0.12598 to 0.12777	+2.9 ± 10	23, 24, 25
Upper sequence		Gabbro, anorthosite, amphibolite	0.70262 to 0.70647	0.512439 to 0.513618	-0.27 to 7.67			
Lower sequence		Crustal xenoliths	0.75029 to 0.75625	0.511396 to 0.511469	-12.5			

References: 1. Molyneux (1974); 2. Cameron (1978); 3. Cameron (1982); 4. Kruger (1994); 5. Kinnaird and others (2002); 6. Schoenberg and others (1999); 7 Hamilton (1977); 8 Harmer and Sharpe, (1985); 9. Sharpe (1985); 10. Hatton and others (1986); 11. Kruger and Marsh (1982); 12. Kruger (2005); 13. von Gruenewaldt (1972); 14. Day and others (2008); 15. Horan and others (2001); 16. Lambert and others (1994); 17. DePaolo and Wasserburg (1979); 18. Simmons and Lambert (1982); 19. Steward and DePaolo (1987); 20. Palacz (1985); 21. O'Driscoll and others (2009b); 22 Marques and others, (2003); 23. Rivalenti and others (2008); 24. Girardi and others (2006); 25. Pimentel and others (2004); 26. McCandless and others (1999); 27. Maier and others (2000); 28. Mukasa and others (1998)

Sm-Nd Isotopes

Due to the greater resistance of the rare-earth elements (REEs) to metamorphic and hydrothermal redistribution, samarium-neodymium (Sm-Nd) studies can evaluate the role of crustal contamination in the formation or alteration of large, layered mafic-ultramafic intrusions where stratiform chromite deposits are found. For this reason, Sm-Nd studies rarely address just the chromitite seams; rather, their primary objective is to understand how large, layered mafic-ultramafic complexes formed. As with Rb-Sr investigations, a review of the major Sm-Nd isotope analyses for the layered intrusions where chromitite seams are located subsequently follows.

The work by Maier and others (2000) in the Sm-Nd system, on the Lower and Lower Critical Zone rocks of the Bushveld Complex, returned chondritic uniform reservoir (CHUR) values within the range –6.0 to –5.3 , and –7.9 to –6.4 in Main Zone rocks (table 13). These data, in conjunction with higher ratios of incompatible/compatible trace elements recorded in the Lower Zone and Lower Critical Zone than in the Main Zone, with $^{87}Sr/^{86}Sr$ initial ratios that are lower, led Maier and others (2000) to conclude that there had been a higher degree of crustal contamination of the Main Zone rocks than of the Lower and Critical Zones.

In the case of the Stillwater Complex, Sm-Nd studies prove enigmatic. Five whole rocks, from several stratigraphic levels throughout the Ultramafic and Banded Series of the complex, lie within analytical uncertainty of the mineral isochron from a Banded Series gabbro (DePaolo and Wasserburg, 1969). Furthermore, these five whole rocks record identical initial ratios. However, heterogeneous Sm-Nd results, with ε_{Nd} (where $\varepsilon_{Nd}(t) = \left[^{143}Nd/^{144}Nd_{sample}(t) - ^{143}Nd/^{144}Nd_{chond\ avg}(t) \right] \times 10^4$; t, time; chond avg, average chondritic composition) from –5.6 to +1.7, attained from whole rocks throughout the Stillwater Complex (table 13) suggest crustal assimilation played an important role in the formation of the Stillwater magma (Lambert and others, 1989).

Evidence for crustal assimilation is also evident beginning at the Main Chromitite layer of the Ipueira-Medrado Sill. Although the Sm-Nd isotopic compositions of the ultramafic rocks show considerable scatter surrounding an isochron, there is a reasonable trend (fig. 45) for the amphibole-rich harzburgites from the Upper Ultramafic Unit that yields an initial ε_{Nd} of –6.5 (mean square weighted deviation [MSWD] = 0.67) (table 13; Marques and others, 2003). The amphibole-free harzburgites record a higher initial ε_{Nd} at –4.7

(MSWD = 0.25). Both the strongly negative initial ε_{Nd} values and high volume of amphibole in some rocks suggests that the magma may have experienced crustal contamination.

Similarly, the initial ε_{Nd} of whole rocks from the layered series of the Muskox intrusion averages –4.5 ± 5.5 (table 13; Day and others, 2008). In addition, the apparent age of the layered series is 1,400 ± 260 Ma, whereas the older roof and marginal zone rocks are ~1,900 Ma. Taken together, they suggest that mixing between magmatic and local country rock may have occurred.

In the Niquelândia Complex, Rivalenti and others (2008) report positive ε_{Nd} (+3.12 to +7.67, with one exception where ε_{Nd} is –0.27) and slightly negative ε_{Sr} (–27.18 to –1.81) values (table 13) for gabbros, anorthosites, and amphibolites in the upper, smaller sequence (US). In US samples that record lower ε_{Nd} (–0.27) and higher ε_{Sr}, the REE patterns within each unit vary from LREE-depleted to LREE-enriched, suggesting a depleted mantle source that mixed with a residual, crustal component (fig. 46). Ultramafic rock and gabbro layers in the larger, lower sequence (LS) are characterized by negative ε_{Nd} (–10.83 to –0.87 with two outliers, where ε_{Nd} = +2.22 and +6.48; Rivalenti and others, 2008) and positive ε_{Sr} (+26.08 to +269.40) values. Crustal xenoliths, which are abundant in the LS, are very high at ε_{Sr} >300, with negative ε_{Nd} values at –12.5 (table 13). Based on these trends, the LS gabbroic rocks describe an array that indicates the melt first originated from a depleted mantle source that then mixed with residual, contaminated melt in the lower unit during crystallization (fig. 47). As such, the geochemistry of both the LS and US can be explained to result from the interaction of the same depleted magma source with the same crustal component, provided that different environmental conditions are assumed for the two sequences. In addition, plagioclase and clinopyroxene concentrates from the lower part of the eastern part of the Niquelândia Complex indicate ε_{Nd} of –5.8, which also suggests heavy contamination with older crustal material in that part of the intrusion (Pimentel and others, 2004).

With respect to the Rum intrusion, the $^{143}Nd/^{144}Nd$ of rocks in Units 8 through 15 averages 0.51281 at ~60 Ma (table 13; Palacz, 1995). In the overlying peridotites, $^{143}Nd/^{144}Nd$ varies from 0.51271 to 0.51253. The allivalite has $^{143}Nd/^{144}Nd$ compositions that range between 0.51249 and 0.5123. Together with the Sr isotopic data, these values indicate that the Eastern Layered Series may have crystallized from uncontaminated batches of picritic magma that were subsequently injected into a magma chamber containing a crustally contaminated and relatively evolved basaltic magma.
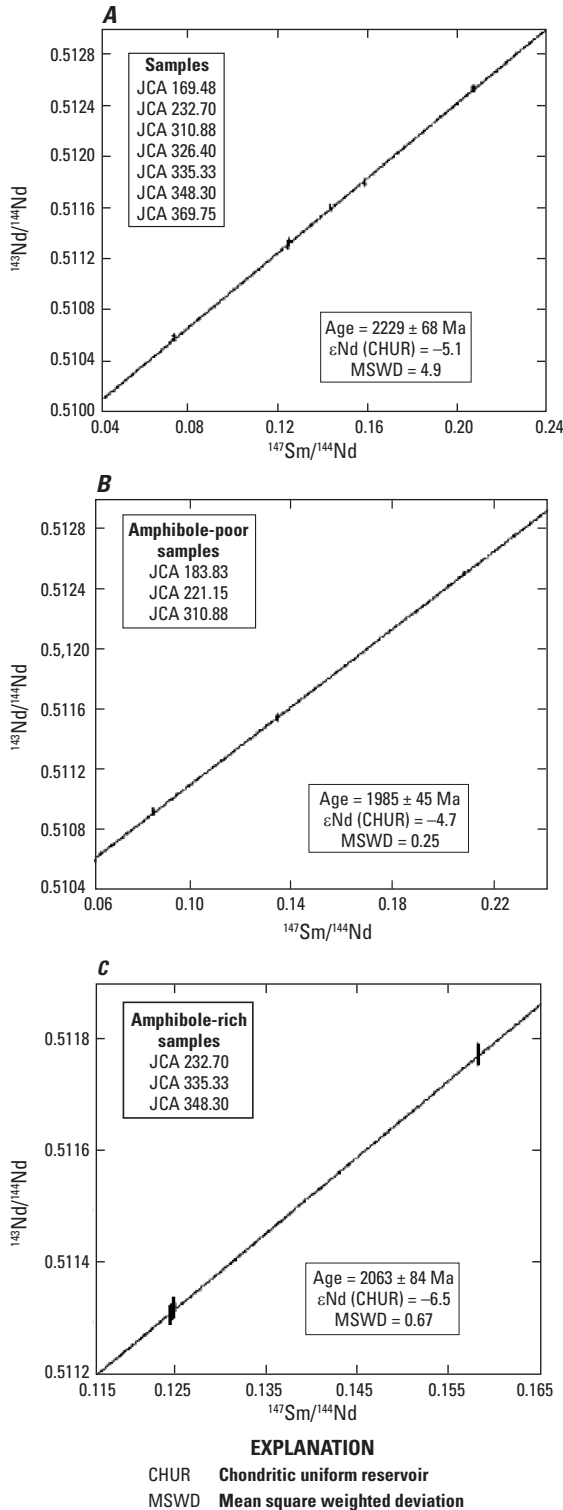
Figure 45. Plot of samarium-neodymium (Sm-Nd) isochrons for harzburgite samples from the Lower Ultramafic Unit and Upper Ultramafic Unit of the Ipueria-Medrado Sill. From Marques and others (2003, fig. 7). *A,* Best fit line using seven samples from both units. *B,* Isochron of harzburgite samples lacking abundant amphibole. *C,* Isochron for amphibole-rich harzburgites. Abbreviations: Ma, million years; CHUR, chondritic uniform reservoir; MSWD, mean square weighted deviation
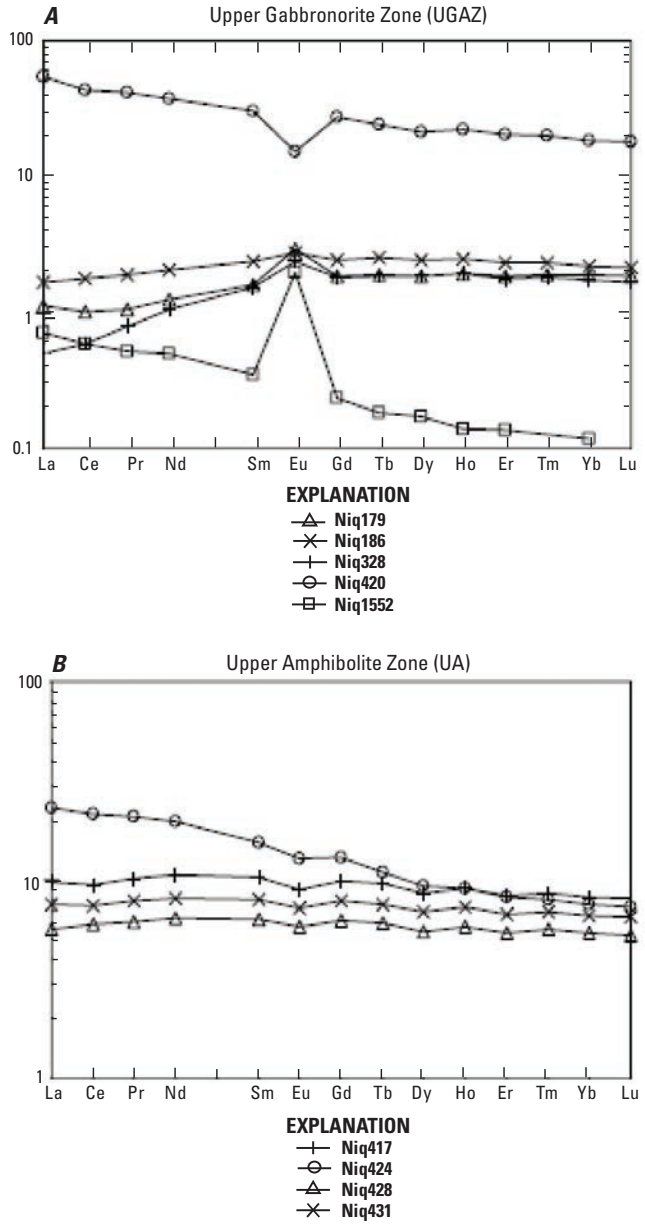
Figure 46. Rare earth element patterns of gabbros, anorthosites, and amphibolites in samples from the upper sequence of the Niquelândia Complex. *A,* In the upper gabbronorite zone (UGAZ). *B,* In the upper amphibolite zone (UA). From Rivalenti and others (2008, fig. 3). See chemical elements table in front of report for abbreviations.
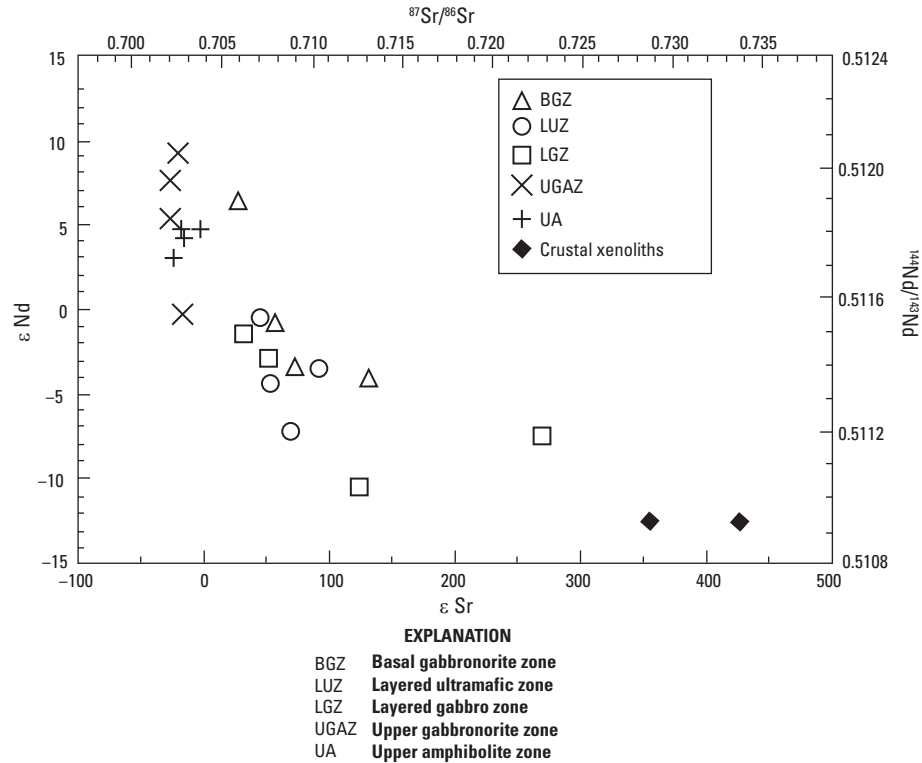
Figure 47. The $^{87}Sr/^{86}Sr$ – $^{144}Nd/^{143}Nd$ isotopic array for the Niquelândia Complex. From Rivalenti and others (2008, fig. 2). The lower sequence of rocks include gabbronorites, pyroxenites, and peridotites and are identified by the abbreviations BGZ, LUZ, and LGZ. Rocks from the upper sequence include gabbro, amphibolites, and anorthosite and correspond to the abbreviations UGAZ and UA. Crustal xenoliths found in the lower sequence are also represented.

Re-Os Isotopes

The rhenium-osmium (Re–Os) isotope system ($^{187}Re \rightarrow {}^{187}Os + \beta^-$; $\lambda = 1.67 \times 10^{-11}$ yr^{-1}; Smoliar and others, 1996) has proven valuable in the study of the chemical evolution of the mantle, because Re is incompatible and Os is highly compatible during mantle melting. As such, removal of melt will lead to a reduction in Re/Os and inhibit the growth of $^{187}Os/^{188}Os$ in the residue relative to ambient, fertile mantle (Allègre and Luck, 1980; Walker and others, 1989). Because chromite forms as a mineral in the mantle residue, it concentrates Os, but not Re. As a result, analysis of chromite using Re-Os isotopic analyses has proven very useful in assessing the geochemical characteristics of the parental magma, potential contamination sources, and hydrothermal events, as well as the potential mechanisms involved with chromite crystallization (Lambert and others, 1989; Schoenberg and others, 1999; Horan and others, 2001; Day and others, 2008).

Radiogenic osmium isotopic signatures from the Stillwater (Martin, 1989; Lambert and others, 1989) and Bushveld (Hart and Kinloch, 1989; McCandless and Ruiz, 1991) Complexes have been used to argue for a significant crustal component in the formation of the ores. The γ_{Os} values (where γ_{Os} is the percentage difference between the Os isotopic composition of

a sample and the average chondritic composition at that time (t = $\{[({}^{187}Os/^{188}Os)_{sample} \times t/({}^{187}Os/^{188}Os)_{chond\ avg}]-1\}$) of the Bushveld vary from +10 to +55 (table 13) (Schoenberg and others, 1999), whereas for the Stillwater the range is +12 to +34 (Lambert and others, 1994; Horan and others, 2001). The supra-chondritic γ_{Os} values in both the Bushveld and Stillwater argue for assimilation and mixing of crustally contaminated melts with mantle-derived magmas. Furthermore, the variable radiogenic osmium isotope ratios in the Stillwater Complex could suggest assimilation or mixing of a crustal component with one or two mantle-derived magmas, such as U- and A-type magmas (Irvine and Sharpe, 1982; Irvine and others, 1983). In the case of the two magma types, the "U" magma is defined as crystallizing olivine and orthopyroxene first, whereas the "A" magma is more evolved and crystallizes plagioclase first. The presence of molybendite in the G-chromite seam of the Stillwater Complex, however, suggests hydrothermal fluids mobilized Re, and perhaps Os, shortly after crystallization (Marcantonio and others, 1993). As such, the recorded Re-Os systematics could be explained solely by hydrothermal processes rather than assimilation of continental crust. The initial osmium isotopic ratios would then indicate derivation from a mantle-derived magma with little to no interaction with the continental crust prior to crystallization.

Suprachondritic γ_{Os} values (2.9 to 10.2) recorded in the 0.79 Ga lower unit (LS) (table 13) of the Niquelândia Complex (Girardi and others, 2006) suggest either assimilation of crustal rocks by parental magma or presence of hydrothermal fluids during late-stage crystallization or post-magmatic reequilibration (for example, Lambert and others, 1989; Horan and others, 2001). Another possibility is that the parental magma was derived from an enriched mantle source (for example, Schiano and others, 1997; Tsuru and others, 2000). Crustal assimilation may also be involved in the formation of some chromitite seams of the Ipueira-Medrado Sill, at the beginning of the Main Chromitite Layer. In particular, the Lower Ultramafic Unit chromitite and lower part of the Main Chromitite Layer have chromite separates with negative γ_{Os} (–4.6 to –0.27), whereas the Upper Ultramafic Unit has chromites with positive γ_{Os} (+1.4 to +3.3) (table 13; Marques and others, 2003). Alternately, the negative γ_{Os} values could be derived from the depleted continental lithosphere, which would drive the composition of the magma to subchondritic Os isotopic compositions (O'Driscoll and others, 2009b). In the Muskox intrusion, the most radiogenic Os compositions

($^{187}Os/^{188}Os$ up to 2.93) occur in the bronzite gabbros of the marginal zone (table 13) whereas the rocks of the layered series (clinopyroxenite, websterite, and dunite) have both subchondritic to suprachondritic $^{187}Os/^{188}Os$ values (0.1228 to 0.2539) (Day and others, 2008). However, the chromitite horizons record a limited range of suprachondritic $^{187}Os/^{188}Os$ compositions (0.1338 to 0.1502) (table 13). In addition, the initial Os isotope compositions (γ_{Os}) of the layered series peridotites are suprachondritic, though with a large range from +1.8 to +87.6 (Day and others, 2008). The γ_{Os} values become progressively more positive moving up the layered series section. However, the negative γ_{Os} values recorded in the marginal and roof rocks (table 13) suggest that their non-isochronous relations may result from mobilization of Re in the intrusion during post-magmatic hydrothermal processes. Furthermore, these rocks demonstrate considerable scatter on a Re-Os isochron plot (fig. 48), which can also be explained by a postcrystallization disturbance, such as hydrothermal activity. In addition, there are no obvious correlations between Os* (Os content that has been corrected for radiogenic growth of Os) and initial γ_{Os} in the Muskox intrusive rock suite.
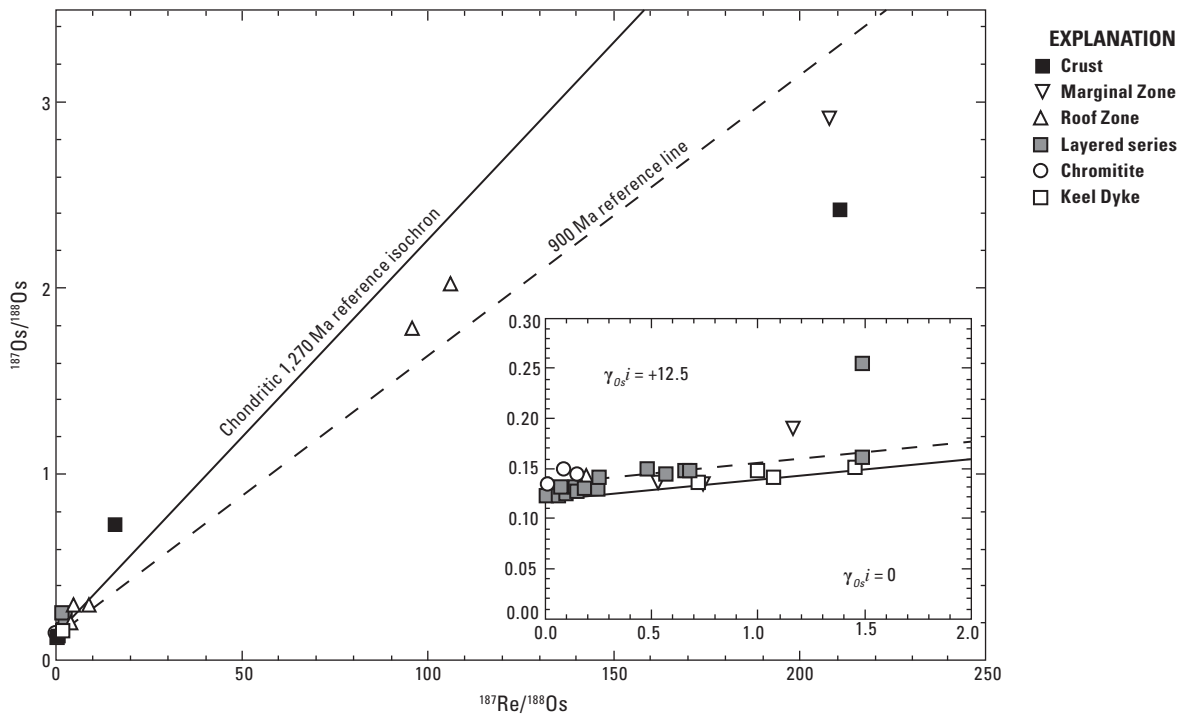
Figure 48.   Plot of $^{187}Re/^{188}Os$ for the Muskox intrusion marginal and roof zones, layered series, chromitite seams, and Keel Dyke. Crustal samples are shown for comparison. The best-fit reference line at 900 million years (Ma) is indicated by the dashed black line for the roof and marginal zone rocks; a chondritic reference isochron at 1,270 Ma is represented by the solid black line. Inset map shows low Re/Os samples. γ_{Os} *i* signifies percentage difference between the initial Os isotopic composition of a sample and the average chondritic composition at that time.

Initial $^{187}Os/^{188}Os$ for rocks from the Rum intrusion range from 0.1305 to 0.1349, which is atypical of values for the convecting upper mantle (O'Driscoll and others, 2009b). However, this range falls within the scope reported for recently erupted picrites and basalts from Iceland ($^{187}Os/^{188}Os$ = 0.1269–0.1369; Skovgaard and others, 2001) and Paleogene picrites and basalts from Baffin Island and West Greenland ($^{187}Os/^{188}Os$ = 0.1267–0.1322; Dale and others, 2009). Individual units within three stratigraphic levels of the Rum intrusion preserve a range of initial $^{187}Os/^{188}Os$ values, with γ_{Os} values from +3.4 to +35.7. With respect to the chromitite seams alone, the γ_{Os} values are also suprachondritic (γ_{Os} = +5.5 to +7.5). Unlike the Stillwater Complex, where γ_{Os} and Os isotopic heterogeneity decrease within increasing stratigraphic height, the highest γ_{Os} values in the study by O'Driscoll and others (2009b) occur at an intermediate level. Due to the observed isotopic heterogeneity, the Re-Os data do not define an isochron in the suite of rocks examined nor within the various units. Rather, the heterogeneity suggests that the composition of the magmas replenishing the original magma chamber may have been heterogeneous in nature and (or) that crustal assimilation may have been involved.

Schoenberg and others (2003) examined the Re-Os isotopic systematics of the Great Dyke and reported initial $^{187}Os/^{188}Os$ ratios for chromite separates in ten of the massive chromitite seams, with a narrow range from 0.1106 to 0.1126. This range is only slightly higher than expected for the value of coeval primitive upper mantle (0.1107), making them chondritic to very modestly suprachondritic, and far above estimates for the subcontinental lithospheric mantle (SCLM) at that time. As a result, crustal contamination of the Great Dyke magma would be minimal, at 0 to 33 percent. To explain this, a reservoir with a somewhat higher than average Re/Os ratio relative to the primitive upper mantle and within a heterogeneous mantle would have served as the parent magma of the Great Dyke. To account for the lack of contamination by continental crust or SCLM, the mantle upwelling, or "plume," would have formed in a failed rift setting and escaped by vertical volume or propagation in conduits already used by previous intrusions.

Petrology of Associated Igneous Rocks

Chromitite seams form within large layered mafic-ultramafic intrusions. Nevertheless, the lower, ultramafic parts of the layered complexes are those that typically host the main chromitite or chromite-bearing seams. This is due to the fact that chromite is one of the first phases to crystallize in mafic and ultramafic magmas (Barnes and Roeder, 2001).

Rock Names

Intrusions where the chromitite is located may include norite, gabbronorite, dunite, harzburgite, peridotite, pyroxenite, troctolite, anorthosite, leucogabbro, and gabbro. However, because the chromitite seams are associated with the ultramafic sections of large, layered stratiform complexes, the most common host rocks for the chromite ore are pyroxenite and orthopyroxenite (for example, the Bushveld Complex, Stillwater Complex, Great Dyke, and Burakovsky layered intrusion); peridotite (for example, the Stillwater Complex, Kemi intrusion, Rum intrusion, Burakovsky layered intrusion, Niquelândia Complex, Campo Formoso Complex, and Bird River Sill); dunite (for example, the Great Dyke, Muskox intrusion, Rum intrusion, Niquelândia Complex, and Bird River Sill); and harzburgite (for example, the Ipueira-Medrado Sill). In the Upper Critical Zone of the Bushveld Complex anorthosite and norite are the main chromitite host rocks, although the chromite ore at this level is not recoverable from an economic standpoint (Schürmann and others, 1998). The chromitite seams of the Fiskenæsset anorthosite complex are found in association with nearly all the anorthosite horizons (Ghisler, 1970). In the Eastern Layered Series of the Rum intrusion, allavite (a plagioclase-rich troctolite) also hosts the chromite-bearing layers (Power and others, 2000; O'Driscoll and others, 2009a).

Forms of Igneous Rocks and Rock Associations

Troctolite

Troctolites in layered intrusions associated with stratiform chromite deposits contain variable amounts of olivine, calcic plagioclase, and minor pyroxene. As such, troctolite is sometimes considered to be a pyroxene-depleted gabbro. More traditionally, troctolite is a mafic rock and typically occurs in the upper parts of layered mafic-ultramafic intrusions. Troctolites from the Eastern Layered Series of the Rum intrusion are generally homogeneous and contain olivine and plagioclase, with <7-percent modal pyroxene (Bédard and others, 1988), and are commonly referred to as allivalite. Chromite is also a common accessory mineral. The troctolites are either massive equigranular, massive laminated, or strongly layered. Deformation is supported by the presence of sheared-out and folded schlieren of peridotite (fig. 49) within the top 2 m of the troctolite in Unit 7 of the intrusion, which is below the chromitite seam at the Unit 7–8 boundary (O'Driscoll and others, 2009a). In addition, the deformed troctolite contains elongated pods of anorthosite that are as much as 0.5 m in length, which are typically parallel to the strike of the layering (fig. 50). However, the anorthosite pods are not, like the peridotite, folded.

Figure 49.   Field photograph of troctolite with deformed peridotite schlieren. Located below the main chromite-bearing seam at the Unit 7–8 boundary of the Rum intrusion. From O'Driscoll and others (2009a, fig. 2a).

Anorthosite

Anorthositic rocks found in large, layered mafic-ultramafic igneous complexes are, by definition, mainly made up of plagioclase feldspar with only minor amounts of cumulus pyroxene, olivine, amphibole, and other phases, such as chromite or garnet. Where altered, the anorthosite may contain calcite, epidote, chlorite, and quartz.

Cyclic units in the Upper Critical Zone of the Bushveld, such as the PGE-bearing UG2 and Merensky Reef frequently include anorthosite (fig. 39 and 51) and norite; although, the chromitite seams in the Upper Critical Zone are not presently mined for chromite ore. The anorthosites in these layers have a number of different textural features, including "spotted" and "mottled" textures (Seabrook and others, 2005). Spotted anorthosites contain abundant isolated cumulus orthopyroxene grains, surrounded by cumulus and interstitial plagioclase, whereas mottled anorthosites contain cumulus plagioclase and poikilitic orthopyroxene grains. Plagioclase accounts for about 90 percent of the mottled anorthosites, whereas interstitial and optically continuous orthopyroxene and (or) clinopyroxene account for the remaining 10 percent,
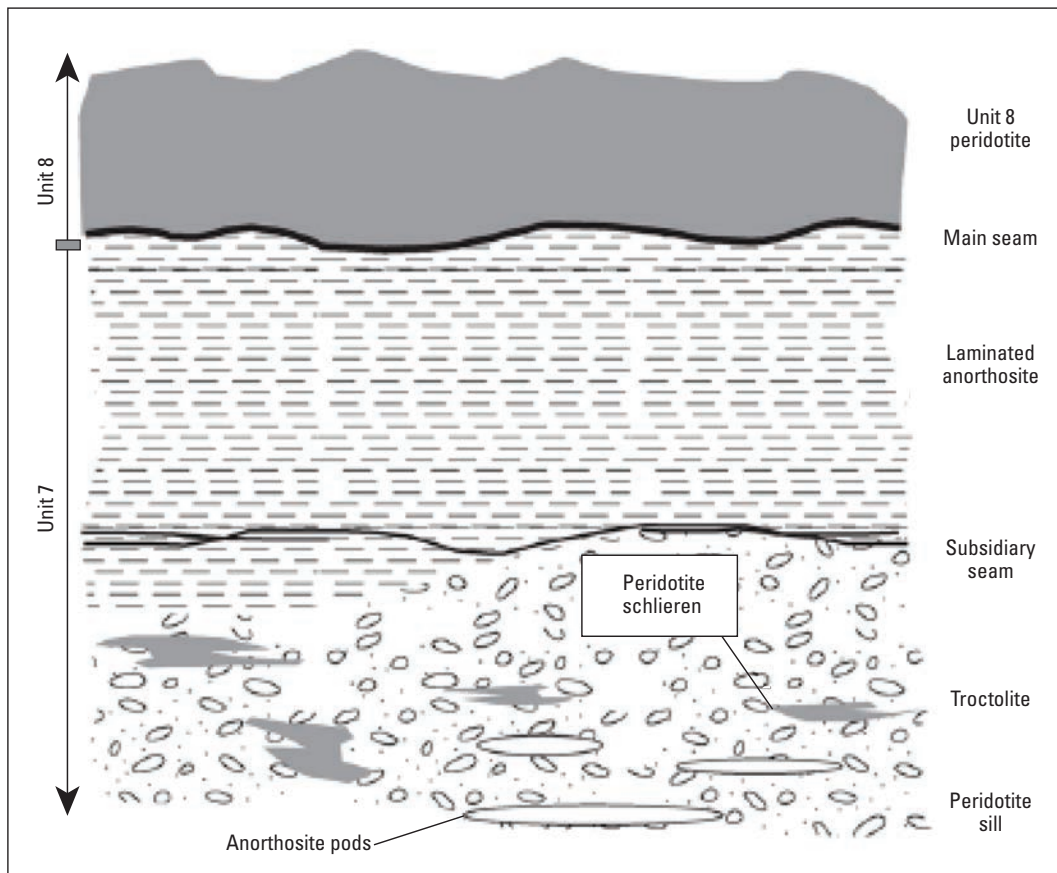
Figure 50.   Schematic showing the relationship of the peridotite schlieren and elongated anorthosite pods within the troctolite below the chromitite seam at the Unit 7–8 boundary of the Rum intrusion. From O'Driscoll and others (2009a, fig. 2d).

Figure 51.   Chromitite above anorthosite at the Lower Critical Zone-Upper Critical Zone boundary of the Bushveld Complex. Note the anorthosite stringers in the chromitite. Pen for scale. Photograph courtesy of Klaus Schulz, U.S. Geological Survey.

which gives rise to the observed mottled texture (Seabrook and others, 2005). The poikilitic grains range from 0.5 to 1.5 cm in smaller mottles, Plagioclase inclusions are smaller than the poikilitic grains, generally <1 mm, when enclosed in orthopyroxene and mostly euhedral in shape. These plagioclase chadacrysts also occur without preferred orientation.

The main chromitite seams of the Fiskenæsset Complex are located in the Anorthosite unit and the top of the Upper Leucogabbro unit (fig. 19). The anorthosites contain abundant plagioclase (90 to 95 percent), with amphibole (5 to 10 percent), clinopyroxene (0 to 5 percent), and orthopyroxene (0 to 3 percent) as minor phases (Polat and others, 2009). Accessory minerals, such as garnet and chromite, make up <3 percent of the rock. In some cases, plagioclase encloses rounded clinopyroxene inclusions (fig. 52A), whereas elsewhere clinopyroxene

occurs as inclusions within amphibole; clinopyroxene may also be interstitial (intercumulus) between plagioclase. Many samples show that the contacts between amphibole and clinopyroxene inclusions are frequently sharp and rounded (fig. 52A and B). The intercumulus clinopyroxene, however, is altered to amphibole along cleavage planes and often displays a thin reaction rim of amphibole (fig. 52A). Within recrystallized plagioclase grains, chains of small amphibole crystals have been observed to occur along twin planes. Some of the anorthosites have 1- to 2-cm-thick layers or lenses of chromite (fig. 52C). Amphibole is typically associated with these layers. Hydrothermal alteration in areas has resulted in irregular domains of calcite, epidote, chlorite, and minor quartz (fig. 52D). As a result, these recrystallized and deformed domains do not exhibit cumulus textures.
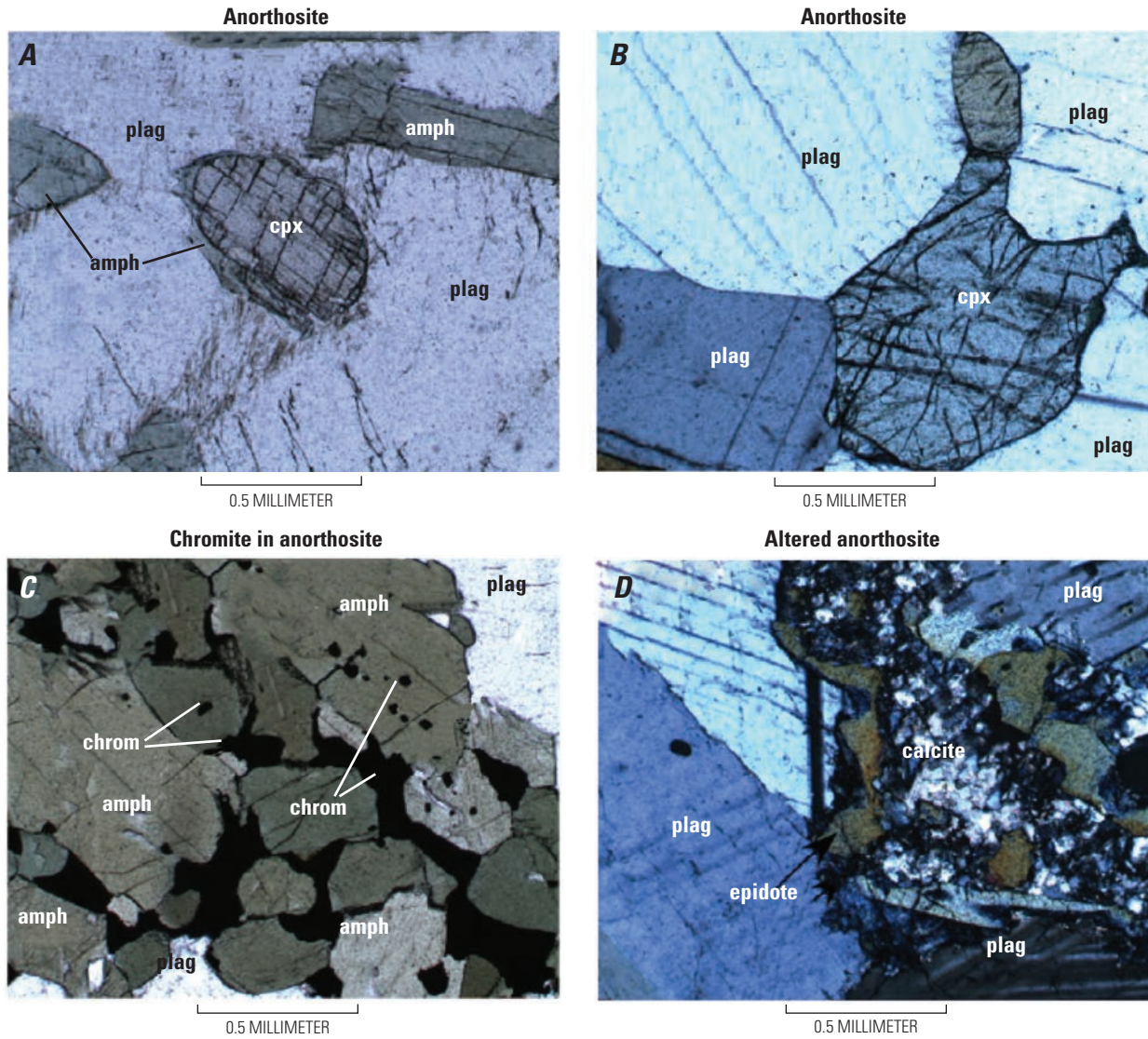
Figure 52.   Photomicrographs of anorthosites from the Fiskenæsset Complex. From Polat and others (2009, figs. 6*a,b,c,f*). *A,* Anorthosite illustrating plagioclase (plag) enclosing rounded, relict clinopyroxene (cpx). *B,* Anorthosite showing sharp, rounded boundaries between clinopyroxene (cpx) and plagioclase (plag). *C,* Chromite-bearing layer within an anorthosite. Rounded chromite (chrom) inclusions occur in amphiboles (amph), although amphibole inclusions can also be found in chromite. *D,* Anorthosite with calcite and epidote formation as the result of hydrothermal alteration.

Peridotite

Peridotitic rocks that host stratiform chromite deposits are coarse-grained and consist mainly of olivine and pyroxene minerals. Olivine grains are typically subhedral to anhedral with extensive serpentinization, such that only relict olivine remains. In the Burakovsky intrusion, for example, cumulus clinopyroxene and olivine account for the primary composition of the peridotites, which are located below the Main Chromitite Horizon. Minor secondary serpentine constitutes the remaining mineralogy (Higgins and others, 1997).

In the Stillwater Complex, peridotites predominantly make up the lower Peridotite Zone in the Ultramafic Series, which also hosts the main chromite-bearing seams. Olivine commonly forms the framework for the cumulus grains and occurs with a small amount of chromite. Orthopyroxene forms as oikocrysts that enclose partially reabsorbed olivines (McCallum, 1996). Roughly 2 to 15 percent of the peridotites in the Mountain View area of the complex contains intercumulus plagioclase. Other minor interstitial minerals include augite, phlogopite, and amphibole, which are listed in decreasing order of abundance. Apatite and sulfides account for only trace amounts of the peridotite mineralogy.

Peridotites in the Rum intrusion include massive equigranular, layered, and rare, chaotic intrusive breccias. The peridotites of the Eastern Layered Series of the Rum intrusion are feldspathic whereas the peridotites of the Western Layered Series frequently display harrisitic textures (fig. 53). In the Central Series the peridotites are mostly layered, highly slumped, and brecciated (fig. 54; Emeleus and others, 1986). Peridotites with internal layering are subparallel to the peridotite-allivalite contacts and defined by repeated variations in grain size, morphology and modal abundance of cumulus olivine, chromite, intergranular plagioclase, and pyroxene (Volker, 1983). Peridotite units may also have individual layers that are massive or modally graded. In rare cases, peridotite units are bounded by thin chromitite seams. In addition, some of the peridotite layers contain thin gabbroic veins that are generally parallel to the layering.

Peridotites in the Fiskenæsset Complex occur as lenses or sills in anorthosite (fig. 55); the lenses range from several centimeters to several meters in thickness (Polat and others, 2009). The peridotites may also be interlayered with anorthosite, chromitite, gabbro, and leucogabbro (figs. 55 and 56). The Fiskenæsset peridotites consist of olivine (30 to 70 percent), orthopyroxene (10 to 30 percent), clinopyroxene (5 to 10 percent), amphibole (10 to 30 percent), serpentine (5 to 10 percent), and accessory minerals, such as magnetite and chromite (<5 percent) (Polat and others, 2009). In some peridotite layers, chromite content can be 20 vol%. As with most ultramafic rocks in stratiform chromite deposits, olivine has been partially altered to serpentine and chlorite, and orthopyroxene and clinopyroxene have been altered to amphibole.
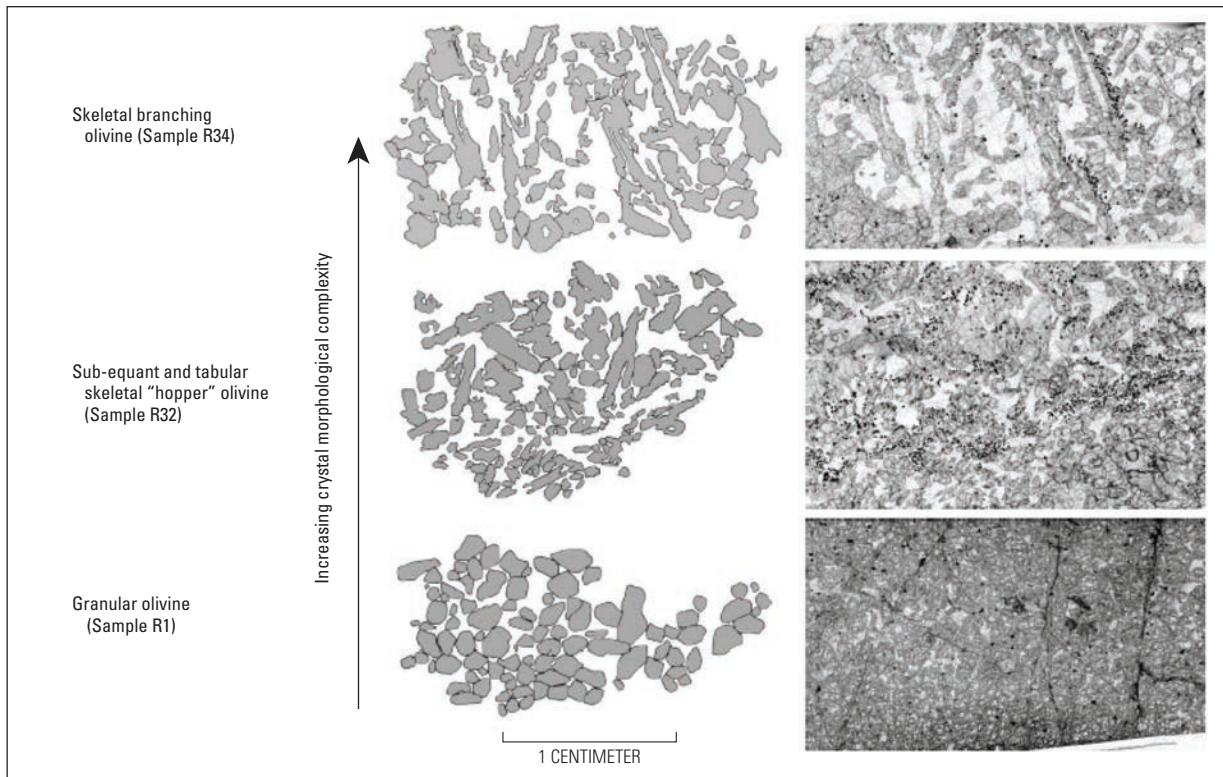
Figure 53.   Schematic cross section of peridotite layers in the Rum intrusion, progressing from peridotites with granular olivine into peridotites with harrisitic olivine and abundant feldspar. Photomicrographs and "edited" texture maps illustrate the increase in olivine grain size and changes in morphology. The 1-cm scale bar corresponds to both the photomicrographs and texture maps.
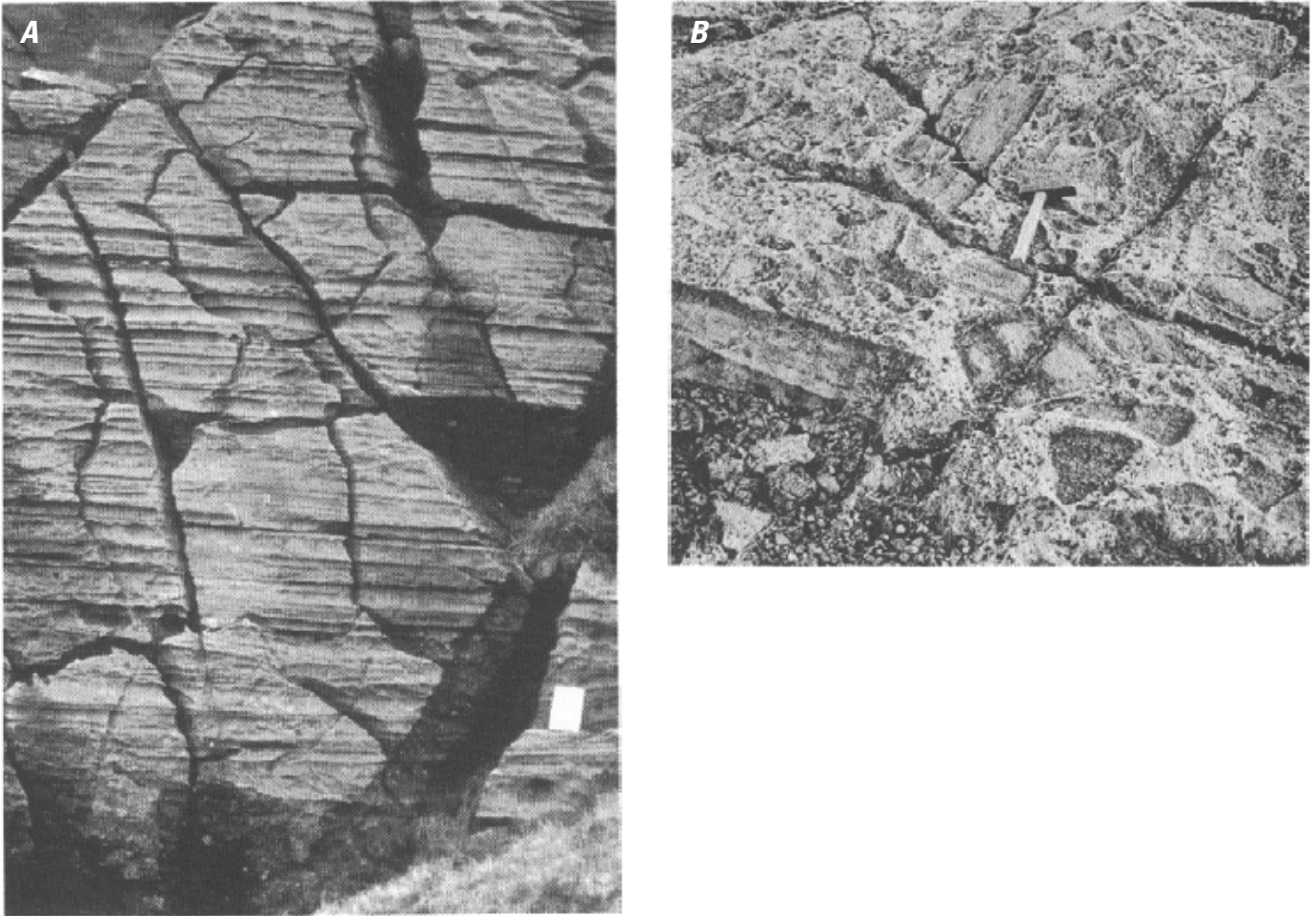
Figure 54.   Field photographs of peridotites from the Rum intrusion. *A,* Peridotite in Western Layered Series with fine-scale layering. White notebook is 20-cm high. From Emeleus and others (1996, fig. 7). *B,* Brecciated peridotite from the Central Layered Series. Hammer head is 15 cm. From Emeleus and others (1996, fig. 15).
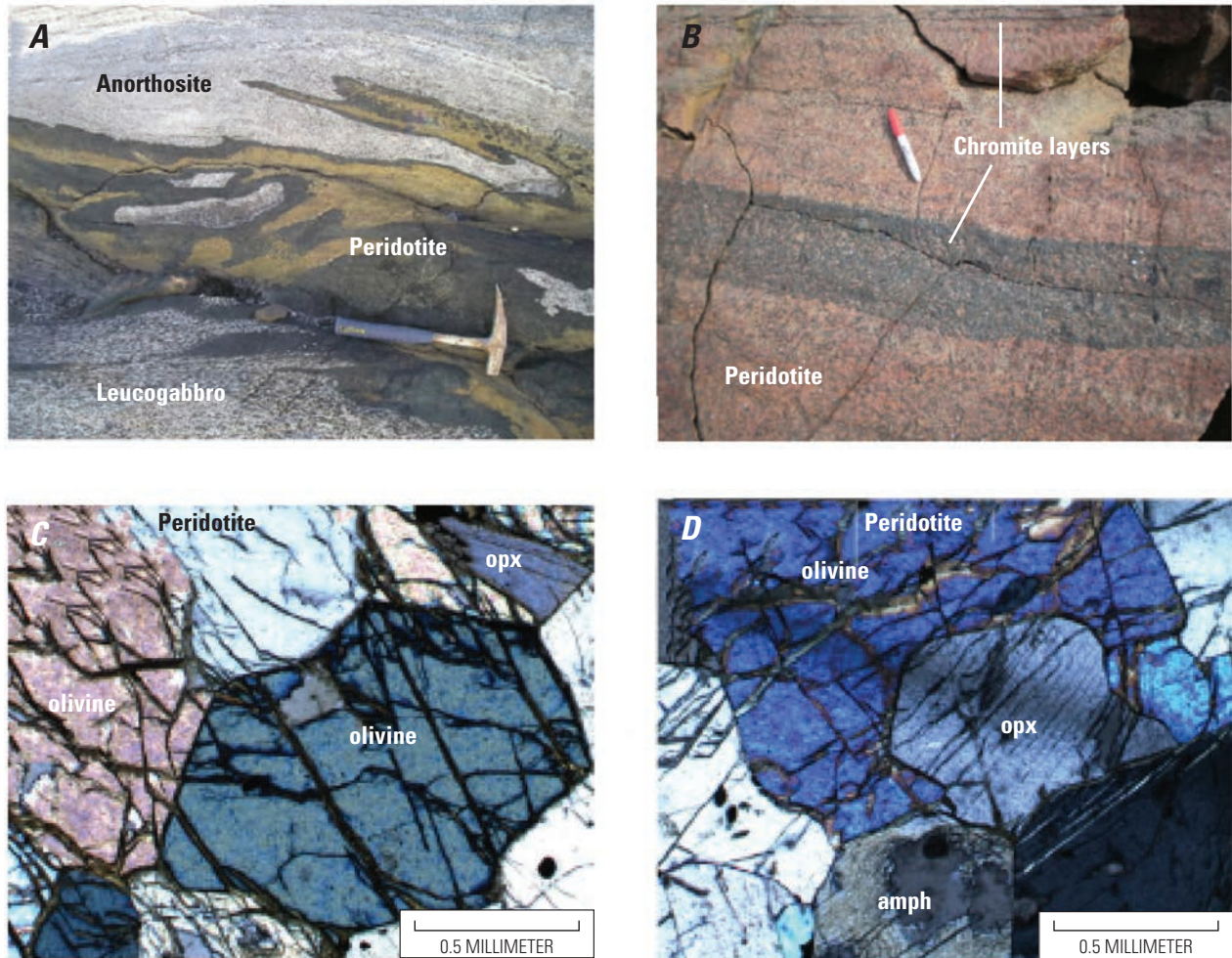
Figure 55.   Photographs showing field relationships of peridotites with surrounding lithology (*A* and *B*) in the Fiskenæsset Complex; photomicrographs of peridotite samples (*C* and *D*) illustrate typical mineralogy. *A,* Peridotite sill intruding anorthosite with anorthosite xenoliths. From Polat and others (2009, fig. 5*d*). *B,* Peridotite interlayered with chromite-bearing seams. From Polat and others (2009, fig. 5*f*). *C,* Photomicrograph of olivine-rich peridotite containing orthopyroxene (opx). From Polat and others (2009, fig. 7*c*). *D,* Photomicrograph of orthopyroxene-rich peridotite (bronzitite). From Polat and others (2009, fig. 7*d*).
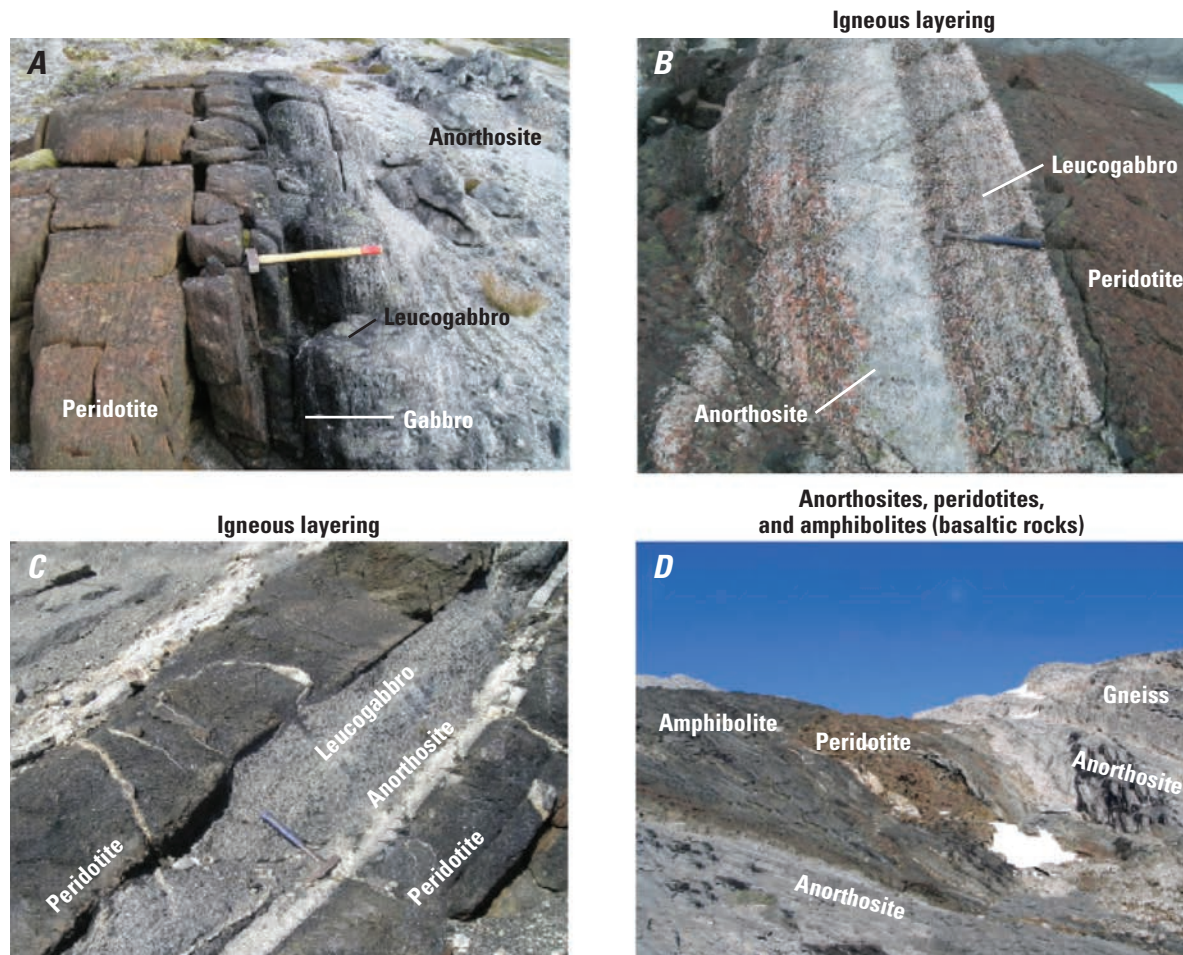
Figure 56. Field photographs showing lithological relationships between peridotite and surrounding layers in the Fiskenæsset Complex. *A*, Peridotite sill located within anorthosite layer. From Polat and others (2009, fig. 3*a*). *B*, Layering between peridotite, anorthosite, and leucogabbro. From Polat and others (2009, fig. 4*c*). *C*, Igneous layering of peridotite with leucogabbro and anorthosite layers. From Polat and others (2009, fig. 4*d*). *D*, Field relations between anorthosite, peridotite, and amphibolites. From Polat and others (2009, fig. 4*f*).

Dunite and Harzburgite

Dunite and harzburgite are also locally present in the ultramafic section of the stratiform complexes and host the chromitite seams in several example deposits such as the Great Dyke, Stillwater Complex, and Niquelândia Complex. They are generally abundant in olivine, with only minor amounts of pyroxene, chromite, and pyrope. Zeolite, calcite, and albite may occur as minor phases. Cumulus textures range from adcumulate to orthocumulate. Due to high-grade metamorphism in some of the deposits, olivine has frequently been altered to serpentine such that only relict olivine grains remain. Other secondary minerals include chlorite, lizardite, chrysotile, and talc.

At the base of the lower horizon in the Niquelândia Complex (Brazil), the dunite is partially serpentinized and consists of olivine and minor orthopyroxene relicts enclosed in a matrix of lizardite, chrysotile, and talc (Pimentel and others, 2004). Dunite in the Ipueira-Medrado Sill consists of highly serpentinized fine- and medium-grained olivine and chromite adcumulate, with minor postcumulus orthopyroxene, amphibole, and clinopyroxene (fig. 36; Marques and Ferreira-Filho, 2003). Partially (10 percent) to highly (80 percent) serpentinized harzburgite also occurs in the Ipueira-Medrado Sill, along with cumulus, fine- to medium-grained olivine (0.5 to 1.5 mm) and chromite (up to 0.5 mm); the main intercumulus mineral is orthopyroxene (fig. 57). Large orthopyroxene oikocrysts, a few centimeters in diameter, are a distinct feature in the harzburgites and enclose rounded cumulus olivine and chromite. Clinopyroxene and amphibole occur, in places, as additional postcumulus phases. Where amphibole is locally abundant, it forms large oikocrysts that enclose olivine, orthopyroxene, and embayed chromite, such that there is a close association between postcumulus amphibole and thin chromite-rich layers (Marques and Ferreira-Filho, 2003).
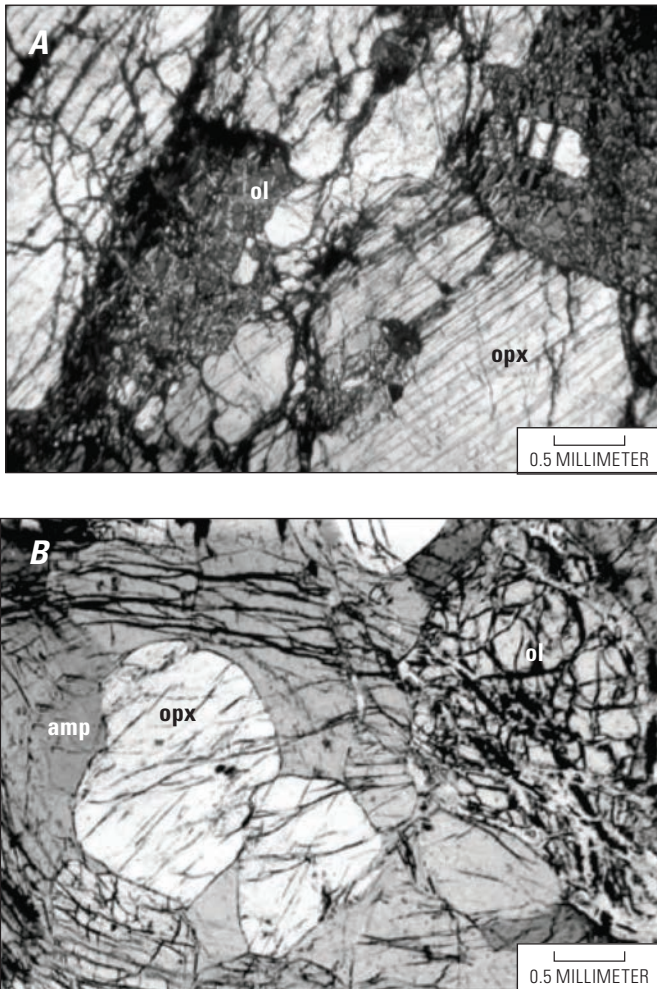
Figure 57.   Photomicrographs of harzburgite from the Ipueria-Medrado Sill. From Marques and Ferreira-Filho (2003, figs. 8*b,d*). *A,* Harzburgite illustrating olivine (ol) in reaction with orthopyroxene (opx). Cross-polarized light. *B,* Harzburgite with ~20-percent intercumulus amphibole (amp).

Figure 58.   Photomicrograph of dunite from the Ultramafic Sequence of the Great Dyke. From Wilson (1996, fig. 13*b*). Orthopyroxene (Op) is an interstitial mineral; fine-grained chromite (Ch) occurs near the margins of the cumulus olivine (Ol) and within the orthopyroxene.

Dunite, and harzburgites also define the Ultramafic Sequence of the Great Dyke. In the Darwendale Subchamber, these rocks are extreme adcumulates, but they become orthocumulates near the margins (Wilson and Tredoux, 1990). Similar changes are evident in the Wedza Subchamber, although to a lesser extent. Within the dunitic rocks, olivine grains are interlocking with standard planar boundaries and triple-point junctions (Wilson, 1996). Chromite is also a primary mineral and present throughout the dunite, comprising 1 to 4 vol% (fig. 58). However, chromite is generally concentrated at olivine grain margins or at triple-point junctions (fig. 31). Although some chromite is enclosed at the margins by olivine, no chromite occurs in the centers of olivine, which suggests chromite formation during the latter stages of olivine growth (Wilson, 1996). Minor amounts of pyroxene and zoned plagioclase also occur in dunite and locally enclose the chromite. Evidence of strain

or dislocation twinning related to the triple-point junctions is visible in olivine grains, and is most likely related to grain-coarsening or annealing processes.

Small-scale layering within cyclic units of dunite in the Great Dyke occurs frequently and can be observed on a continuous basis throughout the Darwendale Subchamber (Wilson, 1996). The layering arises due to grain-size variations and proportions of olivine to chromite. In many cyclic units, the continual occurrence of the centimeter-scale layering gives rise to hundreds or thousands of layers in a single outcrop. Laterally, the dunites vary petrographically as well, such that there is a reduction in grain size and an increase in the proportion of interstitial pyroxene toward the margins. As a result, the dunite layers present in the axis of the intrusion grade into harzburgite at the margins.

Poikilitic harzburgite becomes an important component in the Pyroxenite Succession of the Great Dyke and is more extensive than dunite in the smaller subchambers, such as Selukwe and Wedza, of the Ultramafic Sequence. The poikilitic harzburgite contains large (1 to 5 cm), optically continuous orthopyroxene crystals, which gives the rock a nodular appearance, because the orthopyroxene is more resistant to weathering than the surrounding olivine (Wilson, 1996). Olivine occurs within the orthopyroxene as a highly corroded and irregular mineral.

Poikilitic harzburgite is also the main host rock for the chromite-bearing seams of the Stillwater Complex. Cumulus chromite accounts for 1 to 2 percent of the mineralogy, but the predominant postcumulus mineral is poikilitic bronzite (Campbell and Murck, 1992). Depending on the reaction between cumulus olivine and the intercumulus liquid, the oikocrysts account for 10 to 30 percent of the rock (fig. 59). Intercumulus augite and plagioclase are present in minor amounts (<10 percent combined) (Campbell and Murck, 1992).

Figure 59. Photograph of poikilitic harzburgite located above the chromite-bearing seams of the Stillwater Complex. Orthopyroxene and plagioclase make up the poikilitic grains. Photo courtesy of Michael Zientek, U.S. Geological Survey.

Pyroxenite

Varieties of pyroxenite found in association with many of the stratiform chromite deposits include websterite, clinopyroxenite, and ferroan orthopyroxenite (bronzitite). Pyroxenites are typically cumulates with poikilitic textures that contain coarse-grained, subhedral to euhedral orthopyroxene or clinopyroxene oikocrysts, intercumulus plagioclase, and accessory mica minerals, such as phlogopite. Orthopyroxene and clinopyroxene crystals may also occur in the interstices, and plagioclase grains can be found as subhedral inclusions. In some deposits, olivine occurs as an intercumulus mineral, although frequently these grains have undergone extensive alteration and may only exhibit relict rims.

Feldspathic pyroxenite hosts many of the chromitite layers in the Critical Zone of the Bushveld Complex particulary the Lower Group chromitites (LG1 through LG7) and the Middle Group chromitites (MG1 through MG4) (Von Gruenewaldt and others, 1986; Scoon and Teigler, 1994; Kinnaird and others, 2002). A feldspathic bronzitite layer about 2.5 m above the LG6 chromitite seam contains 68 to 81 percent orthopyroxene and 5- to 16-percent plagioclase, with little or no euhedral chromite (Boorman and others, 2004). The chromitite seams of the Upper Group are hosted in pyroxenite, norite ,or anorthosite (fig. 60). Pyroxenite in the UG2 unit of the Upper Critical Zone, for example, consists of a plagioclase pyroxenite with granular (cumulus) orthopyroxene, interstitial plagioclase, and minor phlogopite (fig. 61; Mondal and Mathez, 2007).

Pyroxenite is the also dominant rock type in the Pyroxenite Succession of the Ultramafic Sequence within the Great Dyke. Mined chromitite layers occur in the lower part of the Pyroxenite Succession within Cyclic Unit 5 (fig. 9; Wilson, 1996; Wilson and Prendergast, 1987). The pyroxenite within the succession is extremely coarse-grained in the lower cyclic units, with pyroxene crystals as much as 10-mm-long (fig. 62). Orthopyroxene is the main pyroxene mineral at this level and crystals show well-defined glide twins (Wilson, 1996). Minor components include plagioclase and clinopyroxene, which usually occur at the triple-point junctions of the minerals. In the uppermost cyclic units of the Pyroxenite Succession, the pyroxenite is much finer grained than those of the lower cyclic units.

Most of the pyroxenites sampled in the gabbronorite zone of the Burakovsky intrusion are coarse-grained mesocumulates. Clinopyroxene and orthopyroxene crystals occur as cumulus phases within an intercumulus matrix, and are subhedral to euhedral, with apparent parallel exsolution lamellae (10 to 20 mm in width) (Higgins and others, 1997). Locally, olivine as an additional cumulus phase, which occurs as subhedral to euhedral crystals and exhibits numerous fractures. Many of the olivine grains are also either completely altered or exhibit only relict rims.

Figure 60. Feldspathic pyroxenite located above the Upper Group 3 (UG3) chromitite seam in the Bushveld Complex. Photo courtesy of Klaus Schulz, U.S. Geological Survey.
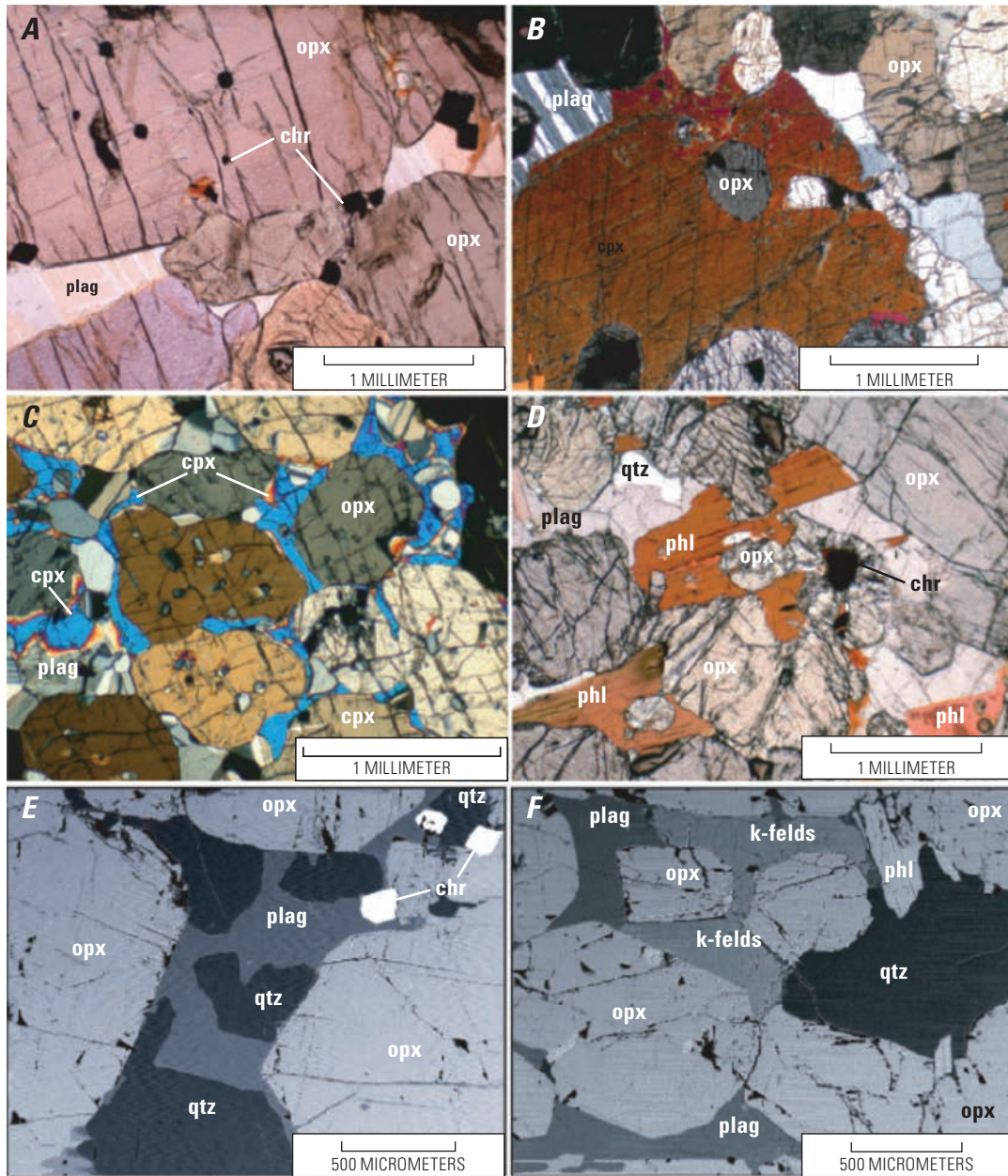
Figure 61. Photomicrographs from the Upper Group 2 (UG2) layer in the Bushveld Complex. From Mondal and Mathez (2007, fig. 4a-f). *A,* Pyroxenite with subrounded to euhedral chromite (chr) grains that are embedded in orthopyroxene (opx) and interstitial to plagioclase (plag) crystals. Plane-polarized light. *B,* Pyroxenite with clinopyroxene (cpx) oikocryst that contains rounded orthopyroxene chadacryst. Cross-polarized light. *C,* Pyroxenite with orthopyroxene oikocryst containing plagioclase chadacrysts. Clinopyroxene is an interstitial mineral. Cross-polarized light. *D,* Pyroxenite consisting of accessory quartz (qtz), chromite (chr), and phlogopite (phl). Plagioclase occurs interstitially between pyroxene grains. Plane-polarized light. *E* and *F,* Back-scattered electron images of pyroxenite with accessory chromite, plagioclase, K-feldspar, and phlogopite occurring in the interstices between pyroxene grains.
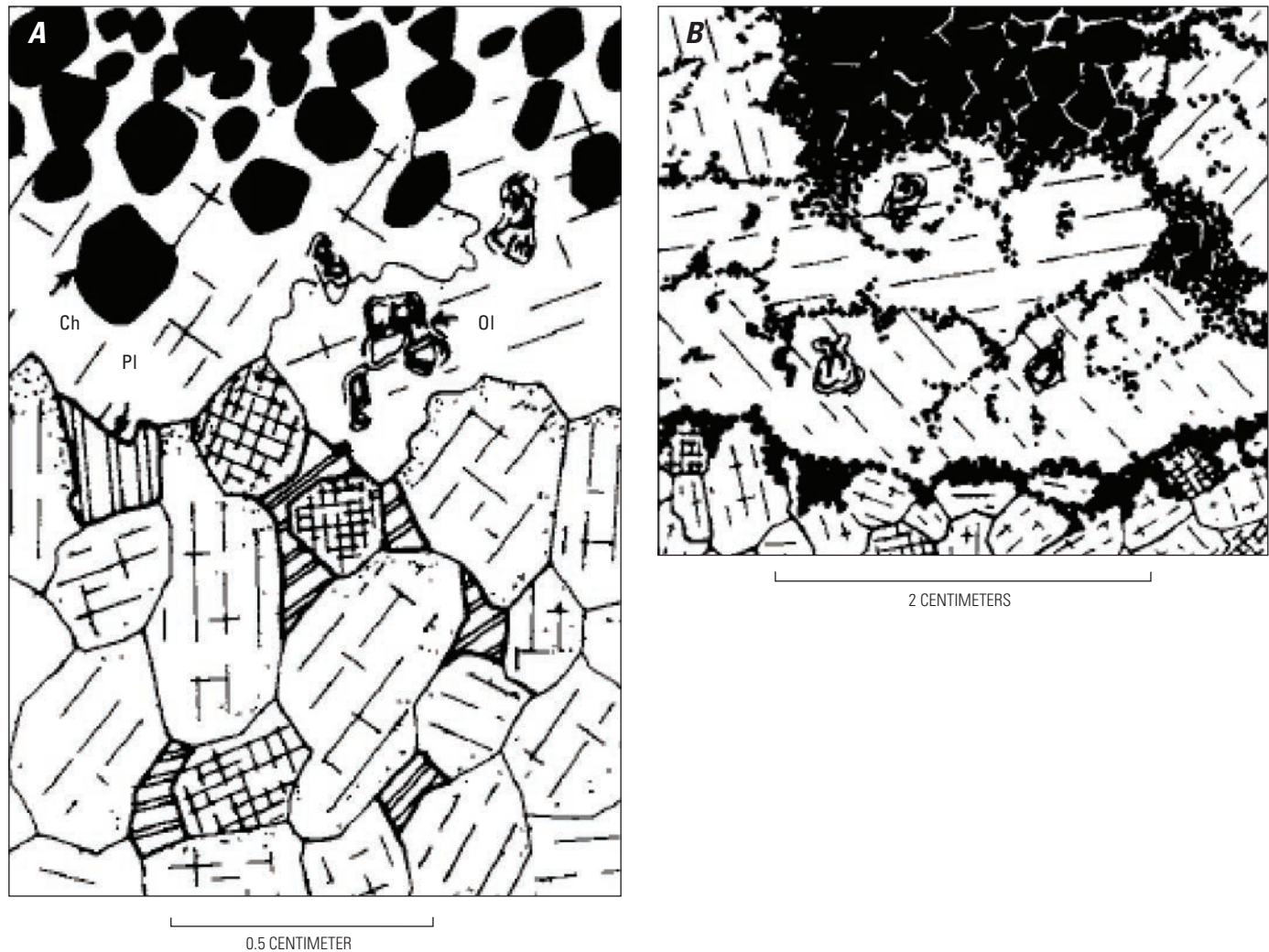
Figure 62.   Artistic rendering of photomicrographs illustrating the contact between the C5 chromitite seam and underlying orthopyroxenite of Cyclic Unit number 6 of the Great Dyke. From Wilson (1996, fig. 12). *A,* Optically continuous orthopyroxene crystals overlying cumulus orthopyroxene and enclosing relict olivine (Ol). Chromite (Ch) grains are large and occur in the disseminated chromitite footwall layer. Plagioclase (Pl) is a postcumulus mineral and located interstitial to the pyroxene. *B,* Cumulus orthopyroxene grains from the P6 pyroxenite layer overlain by fine-grained chromite. Relict olivine is replaced by optically continuous orthopyroxene and outlined by the fine-grained chromite.

Mineralogy

The mineralogy of igneous rocks that are host the chromitite seams in large, layered mafic-ultramafic intrusions includes chromite ± olivine ± clinopyroxene ± orthopyroxene ± plagioclase ± pyrrhotite ± pentlandite ± chalcopyrite ± PGE minerals (dominantly laurite, cooperite, and braggite) ± augite ± ilmenite ± rutile. Secondary minerals include serpentine, magnetite, kaemmererite, chlorite, biotite-phlogopite, amphibole, epidote, carbonate, talc, quartz, lizardite, and chrysotile. The sulfides (pyrrhotite, pentlandite, and chalcopyrite) and PGEs are described in the Hypogene Ore section of this model.

Olivine

Olivine is a typical cumulus mineral found in the peridotitic and pyroxenitic rocks that host stratiform chromite deposits. Olivine crystals can be anhedral, subhedral, or euhedral. Texturally, olivine can also appear rounded, elongated, or dendritic (for example, the Rum intrusion). Olivine grain sizes vary, with the bulk of diameters in the millimeter range. Generally, olivine has been partially fractured and altered to serpentine and chlorite.

In the layered succession of the Bushveld Complex, olivine appears both as a magnesian species in the LZ and CZ, and as an iron-rich species in the UZ. Several thousand meters

of olivine-free cumulates separate these two successions. The main chromitite layers occur in the Critical Zone, such that the bulk of olivine associated with the chromite ore is magnesian in composition rather than iron-rich. Furthermore, olivine is primarily associated with the LG1 to LG4 chromitite seams, which distinguishes them from the overlying chromitites that are devoid of olivine crystals (Kinnaird and others, 2002).

Cumulus olivine in the Eastern Layered Series (ELS) of the Rum intrusion is subhedral to anhedral or rounded, although olivine can also appear elongated, rod-like, or harrisitic locally (Bédard and others, 1988; Butcher and others, 1999). In addition, the individual olivine grains in the ELS show no zoning. The olivine minerals in the Western Layered Series (WLS) of the Rum intrusion, however, commonly display harrisitic or dendritic, skeletal textures (Butcher and others, 1999; O'Driscoll and others, 2006). The harrisitic olivine generally occurs in rocks that are interlayered with granular textured gabbro or feldspathic peridotite, and can be >30 cm in length and as much as 2 cm in thickness (Emeleus and others, 1996). Olivine crystals in gabbro and feldspathic peridotite, on the other hand, are typically subhedral in shape and considerably smaller (<2 mm) than harristic olivines in the harrisites (2 to 1,000 mm; O'Driscoll and others, 2006 and references therein). A cyclic stratigraphy occurs from gabbro or feldspathic peridotite up into harrisite, where small equant granular olivines are overlain by progressively larger and more deeply indented skeletal "hopper" olivines (fig. 53; Donaldson, 1977). Morphological changes also occur within the harrisite from hopper and tabular hopper olivines to dendritic, branching crystal morphologies. The main chromite-bearing seams occur interlayered with peridotite and allivalite in the ELS and interlayered with dunite and peridotite in the WLS.

In the Great Dyke, olivine grains in the Dunite Succession are interlocking with typical planar boundaries and triple-point intersections. Typically, the olivine shows strain or dislocation twinning, most likely related to the triple-point junctions and grain-coarsening or annealing processes (Wilson, 1996). Olivine located in the poikilitic harzburgite is rounded and contained within orthopyroxene, although some grains are irregular in form and highly corroded. Within the granular harzburgite, olivine occurs as discrete grains. As the proportion of olivine decreases, the olivine changes from discrete grains to highly irregular crystals that are interstitial to, and partly enclose, rounded orthopyroxene crystals.

Olivine in the Stillwater Complex occurs as a cumulus mineral in peridotites, harzburgites, troctolites, and olivine gabbros. The feldspathic harzburgites are the main host of the chromite-bearing seams in the Peridotite Zone of the Ultramafic Sequence. Alteration of olivine is varied, from a few veins of serpentine and magnetite to complete serpentinization with magnetite ± talc ± calcite.

Pyroxene

The most common varieties of pyroxene found in large, layered mafic-ultramafic intrusions associated with stratiform chromite deposits include ferroan enstatite (bronzite) and clinopyroxene. These varieties of pyroxene minerals generally occur as cumulus minerals or poikilitic intercumulus grains. Grain sizes range from several millimeters in the Great Dyke to as large as a few centimeters in the Bushveld Complex. Augite also occurs in some layered intrusions and is an intercumulus mineral in small modal proportions to the whole rock.

Orthopyroxene grains found in the Critical Zone of the Bushveld Complex are subhedral to euhedral and clearly separated or just touching in a subhedral plagioclase matrix (Boorman and others, 2004). The average grain size of orthopyroxenes in the Critical Zone is 0.99 mm, whereas the average maximum grain size is 3.0 mm, both smaller than those located in the underlying Lower Zone (where the average grain size is 1.13 mm and maximum grain size is 4.1 mm; Boorman and others, 2004). Foliation is also significantly less developed in orthopyroxene grains from the Critical Zone than in those from the Lower Zone. Therefore, the smaller average grain size, weak to absent lineations, and less developed foliation of orthopyroxene in the Critical Zone led Boorman and others (2004) to conclude that these mineralogical variances are most likely due to compaction-driven recrystallization during formation of the Lower Zone.

Primary igneous orthopyroxenes in the massive chromitites of the Ipueira-Medrado Sill are poikilitic oikocrysts (≤1.5 cm) that enclose dozens of small chromite crystals (0.1 to 0.2 mm) (fig. 57; Marques and Ferreira-Filho, 2003). These orthopyroxene oikocrysts are also surrounded by massive bands of larger annealed chromite crystals that range from 0.5 to 0.8 mm. In the Main Chromitite layer, orthopyroxene crystals are commonly altered to serpentine, chlorite, talc, and minor carbonate (Marques and Ferreira-Filho, 2003). In the Pyroxenite Succession of the Great Dyke, orthopyroxene is the main pyroxene mineral, and crystals show well-defined glide twins (Wilson, 1996). Crystals can reach lengths of as much as 10 mm in the lower cyclic units of the succession, although, the average size of the pyroxenes in the lower cyclic units is typically dependent on the size of the magma chamber. Clinopyroxene hosted in the Pyroxenite Succession is subspherical or ovoid in shape and responsible for the nodular texture of the pyroxenite, because it is more resistant to weathering.

Pyroxene in the Stillwater Complex occurs as a cumulus mineral in the form of orthopyroxene, clinopyroxene (augite), and pigeonite (now inverted orthopyroxene) (McCallum, 1996). Orthopyroxene can be found in bronzitite, harzburgite, norite, and gabbronorite as a cumulus mineral, although the main chromite-bearing seams are located within the harzburgite layers. In all the other rock types, orthopyroxene

is a post-cumulus mineral. Clinopyroxene is less abundant than orthopyroxene, and occurs as a cumulus mineral in gabbronorites and olivine gabbros. Elsewhere in the complex, clinopyroxene is an intercumulus mineral. Within the Peridotite Zone, clinopyroxene oikocrysts are unzoned and increase in abundance near the top of the Bronzitite Zone. In the anorthosites of the Fiskenæsset Complex, clinopyroxene occurs as rounded inclusions that are enclosed by plagioclase (Polat and others, 2009). Clinopyroxene may also occur as inclusions within amphibole or be an intercumulus mineral between plagioclase grains. Typically, intercumulus clinopyroxene has been altered to amphibole along cleavage planes, although in some samples, the contacts between the amphibole host and clinopyroxene inclusions are sharp and rounded.

Plagioclase

Plagioclase occurs in several different rock types associated with chromitite seams in large, layered igneous intrusions, from mafic gabbros to ultramafic peridotites. Typically, plagioclase crystals are subhedral to euhedral and small (1 to 2 mm), and occur as cumulus or intercumulus grains. However, large grains (≤1 cm) have been observed in the Bushveld and other complexes. Throughout the Ultramafic Series of the Stillwater Complex, for example, grain sizes of the cumulus plagioclase, even within just one thin section, can range from <0.1 to ~1 cm (McCallum, 1996).

In addition, the base of the Critical Zone in the eastern limb of Bushveld Complex has been defined as the point at which intercumulus plagioclase within the pyroxenite increases from 2 to 6 percent (Cameron, 1978, 1980). Boorman and others (2004), however, report that above the Lower Zone-Critical Zone boundary, subhedral plagioclase accounts for 5 to 16 percent of the feldspathic pyroxenite mineralogy; orthopyroxene and chromite make up the remainder. Just below the MG chromitite layers, Boorman and others (2004) also observed thin, lenticular segregations of subhedral to anhedral plagioclase (fig. 63). Abundant, euhedral cumulus plagioclase between the MG2 and MG3 chromitite layers marks the base of the Upper Critical Zone in the Bushveld Complex (Eales and others, 1990; Maier and others, 1996; Boorman and others, 2004). Plagioclase also shows widespread crystal overgrowths in the Upper

64Rpl N = 1,914
AF = 67.2

2.0 MILLIMETERS
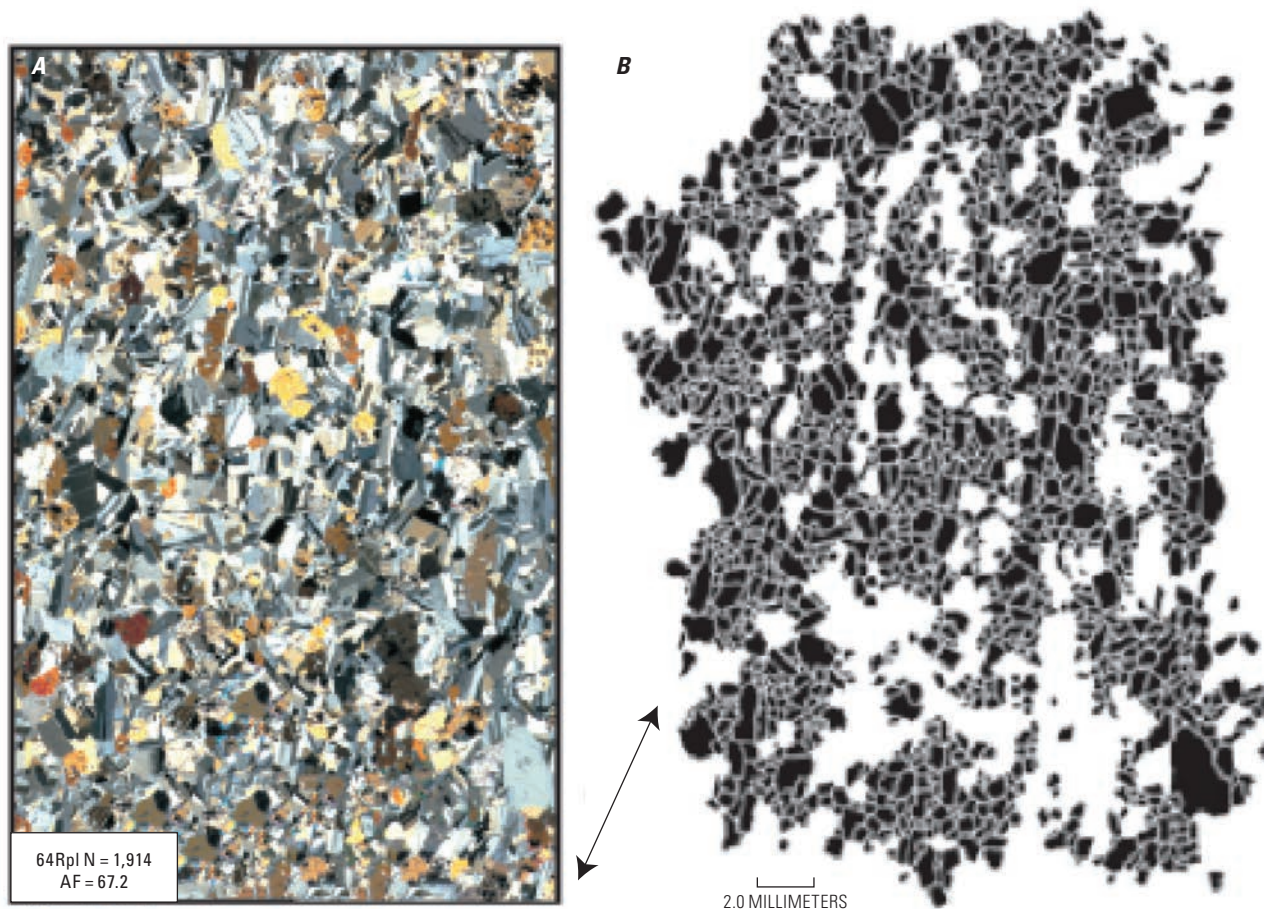
Figure 63. *A*, Photomicrograph and *B*, corresponding binary image of plagioclase texture below the magnesium (MG) chromitite seams in the Bushveld Complex. From Boorman and others (2004, fig. 3). Alignment factor (AF) and number of grains analyzed (N). Arrows show the orientation of the mineral foliation.

Critical Zone, Merensky Reef, and Bastard Unit, with normal, reversed, and oscillatory zoning (Naldrett and others, 1987, 1988).

The Fiskenæsset anorthosite complex contains plagioclase that is equidimensional and generally uniform in size (2 mm to 2 cm) (Ghisler, 1970). The size of plagioclase found in cumulate leucogabbros varies from a few mm to as large as 30 cm (fig. 64A; Polat and others, 2009). Recrystallization of plagioclase is common in the anorthosites and frequently characterized by deformation lamellae (fig. 64B). Plagioclase occurs as a dominant mineral (30 to 60 percent) in the amphibolites of the Fiskenæsset Complex as well (fig. 64C and D). Myers and Platt (1977) report that primary plagioclase can be zoned. In some cases, small secondary plagioclase has developed by metamorphic recrystallization at the margins of the primary plagioclase grains. However, compositions of the primary and secondary plagioclase are similar.

Ilmenite and Rutile

Ilmenite occurs in very few deposits. Where it does occur, as in the Fiskenæsset, it accounts for no more than 0.7 percent of the rock (Ghisler, 1970). Overall, ilmenite is anhedral, 0.2 to 0.5 mm in size, and occurs either as an intercumulus mineral or within chromite grains (fig. 35A and B). Ilmenite in the Fiskenæsset Complex, for example, is consistently associated with more abundant rutile. Rutile may occur as large anhedral, intercumulus grains (≤1.5 mm) or as small grains in and surrounding silicates. Rutile is also found as inclusions in and along grain boundaries of chromite grains in the Fiskenæsset anorthosite complex and takes the form of irregular scattered grains or needles that are 0.015 to 0.03 mm in length (Ghisler, 1970). Typically, the rutile inclusions form a network controlled by (100) and (111) directions of the host mineral.
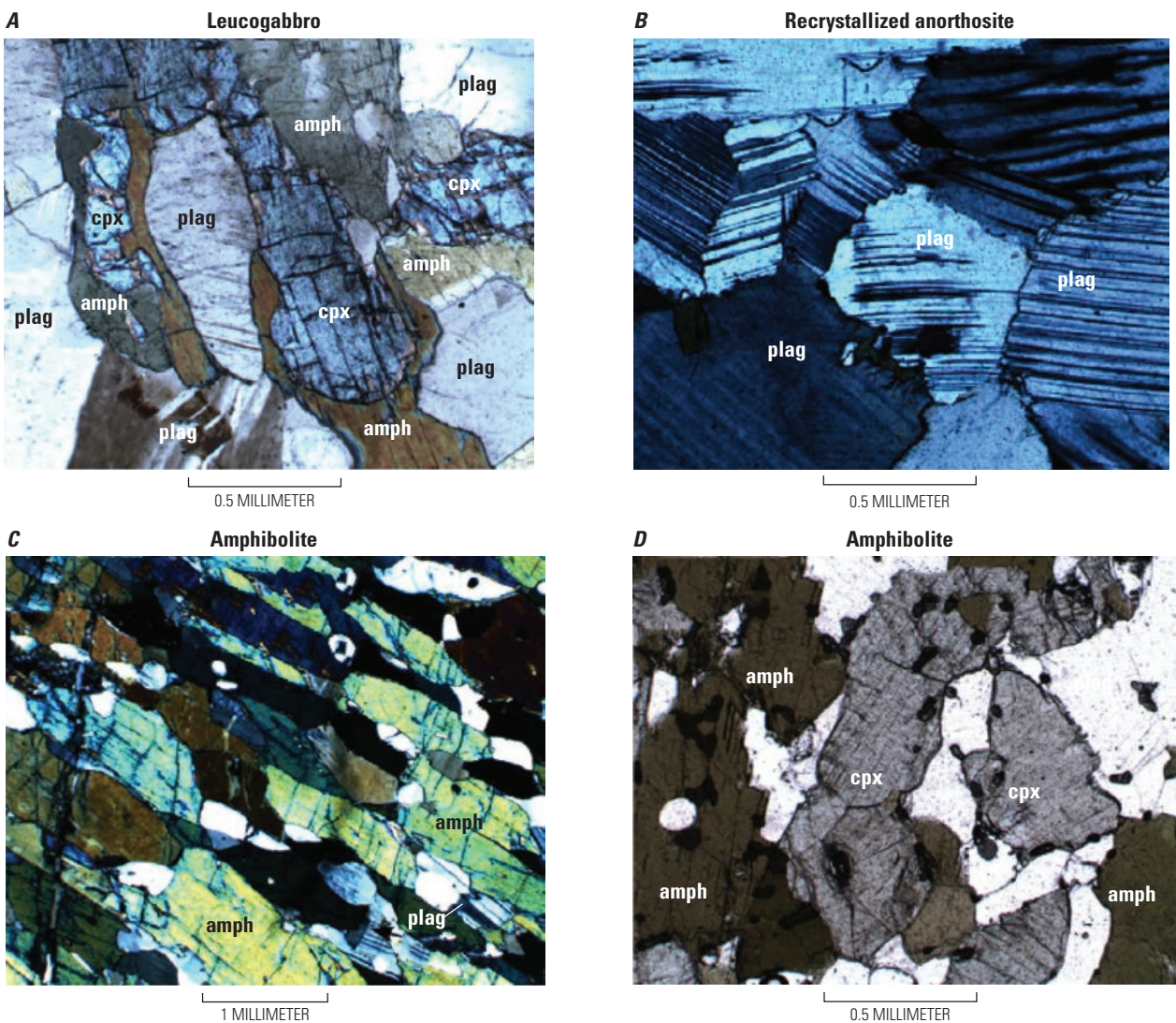
Figure 64.   Photomicrographs illustrating mineralogy of plagioclase from the Fiskenæsset Complex. *A,* Plagioclase (plag) in leucogabbro. From Polat and others (2009, fig. 7*a*). *B,* Recrystallized plagioclase (plag) with deformation lamellae. From Polat and others (2009, fig. 6*e*). *C,* Amphibolite containing oriented amphibole (amph) and plagioclase (plag). From Polat and others (2009, fig. 7*e*). *D,* Amphibolite with amphibole (amph), clinopyroxene (cpx), and plagioclase (plag). From Polat and others (2009, fig. 7*f*).

Most chromitites in the Bushveld Complex contain rutile, which may occur as inclusions in the chromite or as marginal adhering grains (Cameron, 1977). Adhering rutile can be a problem, however, during the purification process of chromite ore, because microscopic investigation reveals that rutile is not totally removed.

Major and Trace-Element Geochemistry

Despite a wealth of data, gaps in the coverage between the different intrusions, as well as within a particular intrusion, hinder the ability to synthesize a coherent geochemical model of the complexes as a whole. In addition, due to the overwhelming number of publications regarding the trace element geochemistry of large, layered mafic-ultramafic intrusions and wide variety of rock types contained within the various example deposits, discussion of the major and trace element geochemistry of the associated igneous rocks will be limited to the layers that either contain the chromitite seams or help resolve issues related to the theory of stratiform chromite deposit formation. Details on the geochemistry of the anorthosites, particularly with respect to their tin and rare earth element ores (Crocker and others, 2001), will not be covered further in this model.

Parental Magma

The presence of orthopyroxenite in many of the stratiform chromite deposits suggests a high-Si, high-Mg parental magma. High K, light rare earth elements (LREE), including and Zr contents in the source magmas suggest upper crustal contamination, either through assimilation during magma ascent or through incorporation into the mantle by previous subduction of sediments (Hatton and Von Gruenewaldt, 1990).

Bushveld Complex

Several different magma types have been identified in the formation of the Bushveld Complex. Mapping of the Marginal Zone rocks and sills in the immediate floor of the Western and Eastern limbs resulted in the recognition that the rocks of the Marginal Zone are not representative of parent magmas due to variable cumulus enrichment and the complexity of rock types present (Eales and Cawthorn, 1996). As a result, the Marginal Zone has been regarded as a precursor, rather than a parental source of the main intrusion. Major and trace-element geochemistry (table 14) has suggested that the parental magmas could be pyroxenitic komatiites (Cawthorn and Davies, 1983), siliceous high-magnesia basalts (Barnes, 1989), or boninites (Hatton and Sharpe, 1989).

Seabrook and others (2005) identified two separate trends in Cr and MgO concentrations for Critical Zone and Main Zone whole rock samples. In particular, norites, pyroxenites, and mottle anorthosites from the Critical Zone contain higher Cr contents compared to Main Zone norite and gabbronorites at a given weight percent MgO (fig. 65). As a result, Cr/MgO ratios are useful when distinguishing mafic

Table 14. Proposed compositions of the parental magmas to various lithological sequences in the Bushveld Complex.

[From Eales and Cawthorn (1996, table 21). T, total; Mg#, $Mg/(Mg+Fe^{2+})$. Major element compositions are reported in weight percent; trace element compositions are in parts per million (ppm)]

	Lower Zone[a]	Marginal Zone[b,c]	Critical Zone[b]	Main Zone[b]	Upper Zone[d]
	Oxides (weight percent)				
SiO_2	55.70	53.17	48.50	50.7	49.32
TiO_2	0.36	0.36	0.75	0.41	0.81
Al_2O_3	12.74	11.36	16.49	16.03	15.67
FeO (T)	8.80	10.72	12.41	9.14	12.77
MnO	0.09	0.20	0.19	0.17	0.19
MgO	12.44	14.93	7.57	9.21	6.08
CaO	6.96	7.47	11.15	11.14	10.83
Na_2O	2.02	1.57	2.17	2.52	2.94
K_2O	1.03	0.17	0.14	0.23	0.25
P_2O_5	0.10	0.07	0.18	0.08	0.07
	Ratios				
Mg#	71.5	71.4	52.1	64.2	45.9
	Trace elements (ppm)				
Ni	292	337	93	162	77
Cr	970	1,240	226	205	111
Rb	37	4	3	7	4
Sr	195	183	359	324	350
Ba	439				
Zr	70	47	34	20	31
Y		15	21	12	25

[a]Davies and others (1980).
[b]Sharpe (1981).
[c]Sharpe and Hulbert (1985).
[d]Davies and Cawthorn (1984).

Notes:
Marginal Zone composition related to average B1 magma by Sharpe (1981), though Sharpe and Hulbert (1985) considered the B1 magma as parental magma to the Lower Zone. Critical Zone parental magma coincides with the average B2 magma of Sharpe (1981), and the average B3 magma with the Main Zone.
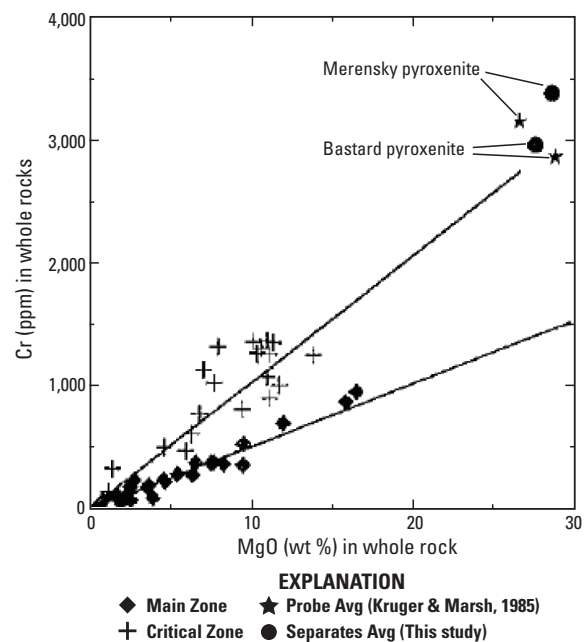
Figure 65. Plot of chromium (Cr, in parts per million) compared to MgO (weight percent) for whole rock samples from the Critical and Main Zones of the Bushveld Complex. From Seabrook and others (1995, fig. 7).

minerals in rocks that originated in Critical Zone magma versus Main Zone magma. Cawthorn (1999) also reported a positive correlation between whole rock Cr and MgO of pyroxenites, norites, and anorthosites in the Merensky Reef and footwall units of the Upper Critical Zone. However, the Mg # of cumulates from the Lower and Lower Critical Zone alternate between decreasing and increasing trends with stratigraphic height (Eales, 2000). Therefore, the differences in the Mg # of cumulates above and below the chromitite seams suggest that the mixing of primitive and evolved magmas cannot alone explain chromitite formation (Eales, 2000). On top of that, the high average Cr contents for the Lower and Critical Zones in spite of the absence of a Cr-depleted residua in the overlying Main Zone argue the need for a deposit model that allows for injection of a second magma during formation. Whole rock analyses and orthopyroxene separates determined by x-ray fluorescence (XRF) analysis for samples from the Critical Zone are given in table 15.

Few studies have examined the REE contents of the Bushveld Complex, particularly those layers that host the chromitite seams (Harmer and Sharpe, 1985; Cawthorn and others, 1991; Maier and Barnes, 1998). This is due in part to the hybridization of the different parent magmas as well as the difficulty in estimating the amount of postcumulus material where the REE are concentrated. However, Maier and Barnes (1998) determined that the concentrations of REE in the Lower and Critical Zones of the Bushveld Complex are LREE- and Th-enriched (table 16) relative to the Main Zone cumulates. The LREE elements include La, Ce, Sm, and Nd. These results suggest that the Bushveld Complex may have crystallized from two distinct parental magma sources, with mixing between the two magmas occurring in the Lower Zone.

The average major and trace element compositions of the main host rocks of the Upper Critical Zone in the Bushveld Complex, which host some of the PGE-bearing chromitite seams, such as the UG1, UG2, and UG3, are listed in table 17.

Table 15.   Major and trace element concentrations for whole rock and mineral separates from select zones of the Bushveld Complex.

[From Seabrook and others (1955). Major element concentrations reported in weight percent; trace element contents are in parts per million (ppm); minimum value given above maximum value; b.d., below detection]

	Critical Zone				Main Zone			
	Orthopyroxene		Whole Rock		Orthopyroxene		Whole Rock	
	Minimum	Maximum	Minimum	Maximum	Minimum	Maximum	Minimum	Maximum
	Oxides (weight percent)							
SiO_2	53.00	53.98	48.92	51.49	51.91	52.88	50.07	53.19
TiO_2	0.19	0.28	0.12	0.17	0.35	0.48	0.18	0.31
Al_2O_3	1.61	2.18	19.69	30.14	0.91	2.36	16.47	28.28
Fe_2O_3	12.49	14.78	2.01	5.68	14.33	20.29	2.33	7.66
MnO	0.19	0.27	0.02	0.11	0.23	0.40	0.05	0.14
MgO	26.84	28.99	1.30	11.20	19.98	24.90	1.71	9.60
CaO	1.49	2.11	10.09	14.52	1.98	9.81	9.78	13.69
Na_2O	b.d.	b.d.	1.69	2.33	b.d.	0.32	2.06	3.19
K_2O	b.d.	b.d.	0.04	0.09	b.d.	0.08	0.15	0.35
P_2O_5	b.d.	0.06	b.d.	0.02	b.d.	0.02	b.d.	0.04
Total	98.58	99.79	99.47	100.36	98.33	100.35	99.25	100.46
	Trace elements (parts per million) and Ratios							
Cr	2,459	3,023	154	1,334	779	1,095	99	541
Cr/MgO	92	107	88	184	35	63	24	154

Table 16.   Range in rare earth element concentrations from selected zones in the Bushveld Complex.

[From Maier and Barnes (1998). Mg# concentrations from Eales and Cawthorn (1996). Concentrations are in parts per million; <, less than]

	Main Zone	Upper Critical Zone[a]		Lower Critical Zone	
	Gabbronorite	Pyroxenite	Norite	Pyroxenite	Harzburgite
	Trace elements (parts per million)				
La	1.75–2.38	0.27–3.10	0.64–1.40	<0.1–7.52	0.68–1.16
Ce	3.73–5.05	<2.0–8.88	1.32–3.56	2.11–15.64	<2.0–2.87
Nd	1.22–2.76	<1.0–2.62	<1.0–1.05	<1.0–6.26	<1.0
Sm	0.31–0.78	0.14–0.72	0.11–0.25	<0.1–0.86	0.14–0.23
Eu	0.24–0.52	0.04–0.26	0.16–0.30	0.03–0.21	0.03–0.07
Tb	<0.05–0.13	<0.05–0.17	<0.05	0.03–0.13	<0.05–0.11
Yb	0.24–0.55	0.35–0.60	0.09–0.27	0.16–0.55	0.17–0.25
Lu	0.05–0.09	0.06–0.12	0.02–0.06	0.02–0.08	0.02–0.04
Th	0.09–0.19	<0.1–0.70	0.05–0.20	<0.1–1.65	<0.1–0.16
	Ratios				
Eu/Eu*	1.45–2.15	0.61–1.38	2.23–5.8	0.48–1.14	0.46–1.68
Ce/Sm	4.9–12.0	11.3–22.8	12.0–20.2	11.1–23.1	0.0–20.1
Mg#		79–83		81–85	

[a]Range reported for only those layers below the Upper Group 2 (UG2) chromitite seam.

Table 17. Average compositional data for dominant lithology of the Upper Critical Zone.

[From Eales and Cawthorn (1996, table 1). Trace element concentrations reported as parts per million; b.d., below detection limit]

	Harzburgite	Pyroxenite	Norite	Anorthosite
	Oxides (weight percent)			
SiO_2	43.75	52.93	50.67	49.20
TiO_2	0.15	0.25	0.09	0.06
Al_2O_3	4.08	4.78	22.24	30.63
Fe_2O_3	15.76	13.04	4.75	1.53
MnO	0.22	0.25	0.07	0.02
MgO	33.45	24.33	9.13	1.31
CaO	3.27	3.86	11.22	14.77
Na_2O	0.38	0.61	1.85	2.43
K_2O	0.13	0.13	0.13	0.14
P_2O_5	0.03	0.01	0.01	0.01
Total	99.89	99.01	99.77	99.98
	Trace elements (parts per million)			
Rb	b.d.–8	b.d.–20	b.d.–10	b.d.–10
Sr	70	30–70	100–400	400–500
Y	b.d.–7	b.d.–15	b.d.–8	b.d.–10
Zr	b.d.–10	b.d.–50	b.d.–15	b.d.–15
Zn	80	60–160	b.d.–60	b.d.–20
Cu	20–50	20–80	b.d.–50	b.d.–40
Ni	1,500	400–1,200	50–500	d.b.–100
Co	160	80–200	10–100	d.b.–20
Cr	1,000	2,000–4,000	100–2,000	d.b.–100
V	50	90–150	3–30	d.b.–30
Sc	10	20–50	3–30	d.b.–7

Of particular note, the compositions of orthopyroxene in norite from the Lower and Critical Zones show an increase in Mg # with stratigraphic height (fig. 66). On the other hand, with one exception, orthopyroxene from norites within the Middle Group chromitite layers in the Upper Critical Zone of the Bushveld show a regular decrease with stratigraphic height in Mg # from 83 to 79 (fig. 67; Teigler and Eales, 1996). Experimental studies on rocks from the Upper Critical Zone have revealed that plagioclase joins orthopyroxene in the crystallization sequence when the Mg # of orthopyroxene (Mg #$_{opx}$) <83 (Cawthorn, 2002). Additional investigations (Cameron, 1982; Cawthorn and Barry, 1992) have shown that norites from the Upper Critical Zone contain orthopyroxene with Mg #s that are equal to 83, supporting the results of the experimental studies. However, the Mg #$_{opx}$ does not go higher than 83 in the entire Upper Critical Zone for both the western and eastern limbs of the Bushveld (Cawthorn, 2002). As a result, rocks of the Upper Critical Zone likely formed from plagioclase-saturated magmas.

Stillwater Complex

Trace-element geochemistry has been used to test the validity of the two-magma hypotheses for the formation of the Stillwater Complex. Due to the different crystallization sequences of the Ultramafic Series and Lower Banded Series versus the Middle Banded Series, Irvine and others (1983) proposed that the source of the former magma was a U-type and the latter an A-type (table 18). In particular, the U-type magma of Ultramafic Series and Lower Banded Series would have contained high MgO contents, relatively high SiO_2 contents,
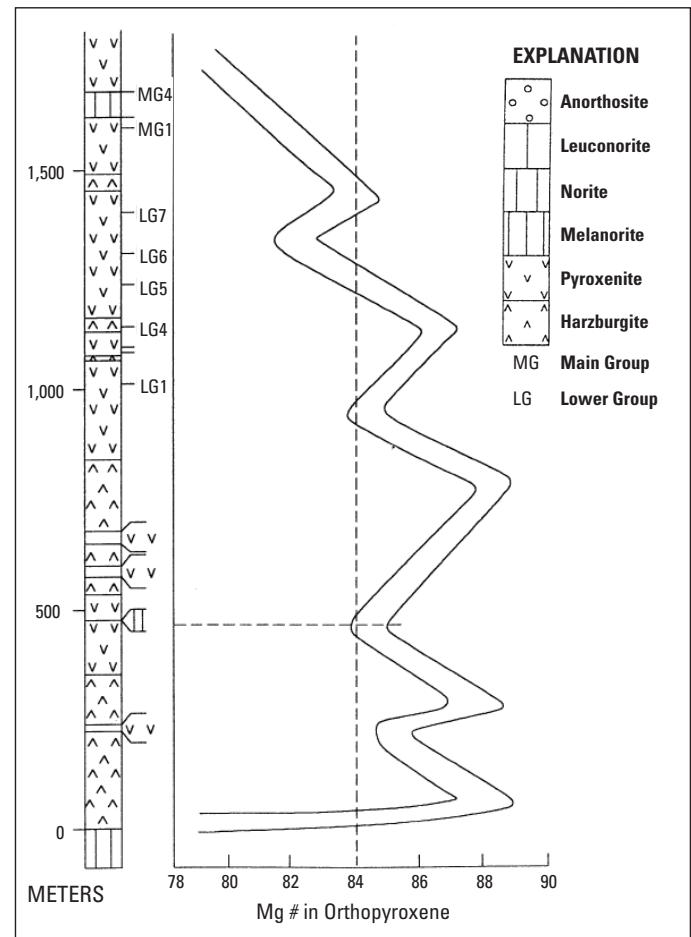
Figure 66. Plot of Mg # for orthopyroxene in the Lower and Critical Zones of the western Bushveld Complex versus stratigraphic position (Teigler and Eales, 1996). Host rocks include harzburgite, pyroxenite, and norite. Positions of Lower Group chromitite seams LG1–LG7 and Middle Group chromitites MG1 and MG4 shown. Abbreviation: Mg#, $Mg/(Mg+Fe^{2+})$.

and low alkalis, CaO, Al_2O_3, and TiO_2 compositions, making them comparable to modern boninites (McCallum, 1996). For the Middle Banded Series (A-type magma), the parent magma would have been more tholeiitic and hyper-aluminous.

Orthopyroxene mineral composition (table 19) throughout the Peridotite Zone of the Stillwater Complex changes with stratigraphic height (fig. 68), showing an upward increase in Mg # and decreasing LREE abundance that levels out above the lowermost 400 m of the complex (Lambert and Simmons, 1987; McCallum, 1996). Similar trends in minor elements are observed in olivines and other pyroxene minerals (Raedeke and McCallum, 1984). In addition, the Cr_2O_3 content of the orthopyroxene is generally high at ~0.6 percent and the REE abundances confirm a standard heavy rare earth element (HREE) enriched pattern in which (Ce/Yb)$_n$ <0.15, where the subscript n refers to the normalization of elemental abundances to chondritic values (Lambert and Simmons, 1987; Papike and others, 1995). However, the REE abundances occur within a small range such that their patterns are actually
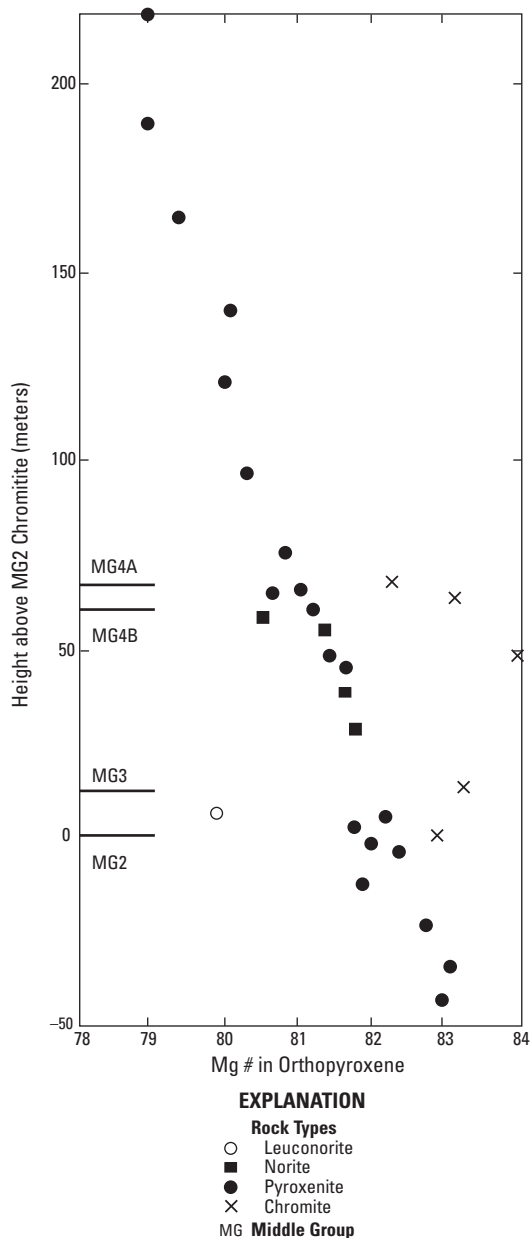
Figure 67.   Plot of Mg # for orthopyroxene through the Middle Group chromitite layers versus stratigraphic position (Teigler and Eales, 1996). Excluding the anomalously low leuconorite sample (open circle), there is a upward decreasing trend in Mg #. Note that the Mg # for norites between the MG3 and MG4 chromitite layers are higher than the overlying pyroxenites, which is reflected in the absence of cumulus plagioclase in these layers (Cawthorn, 2002). Abbreviation: Mg #, $Mg/(Mg+Fe^{2+})$.

subparallel (fig. 69). A significant Eu anomaly is also observed (Lambert and Simmons, 1987). These findings are consistent with formation of the Peridotite Zone and Ultramafic Series through multiple injections and fractional crystallization of magma from the upper mantle. Furthermore, the $(Ce/Sm)_n$ ratios are non-chondritic, suggesting the parent magma was LREE enriched or that partial melts were contaminated by LREE enriched crustal rocks during ascension to the magma chamber.

Table 18.   Proposed compositions of parent magmas for the Ultramafic and Lower Banded Series (U-type) and Middle Banded Series (A-type).

[From Irvine and others (1983). Concentrations reported in weight percent]

Oxides	U-type	A-type
SiO_2	47.44	51.49
TiO_2	0.15	0.49
Al_2O_3	5.31	17.87
Fe_2O_3	1.05	0.98
FeO	8.49	7.95
MnO	0.16	
MgO	32.31	6.37
CaO	3.21	11.77
Na_2O	0.51	2.59
K_2O	0.21	0.16
P_2O_5	0.02	
Cr_2O_3	0.91	
NiO	0.23	
Total	100.00	99.67

Table 19.   Range in major and trace element compositions of cumulus orthopyroxene from Iron and Lost Mountain, Stillwater Complex.

[From Lambert and Simmons (1987). Major element compositions determined by microprobe analyses and reported in weight percent; trace element compositions obtained by isotope dilution analyses and reported in parts per million; Mg# calculated from $Mg/(Mg + Fe^{2+})$ assuming oxidation ratio R = 90 for $Fe^{2+}/(Fe^{2+} + Fe^{3+})$; b.d., below detection limit]

	Iron Mountain	Lost Mountain
	Oxides (weight percent)	
SiO_2	55.09–56.30	54.20–56.32
Al_2O_3	1.16–1.63	1.13–1.59
TiO_2	0.08–0.121	0.07–0.34
Cr_2O_3	0.39–0.55	0.35–0.60
FeO	9.80–12.43	8.73–13.39
MnO	0.19–0.28	0.20–0.28
MgO	29.34–30.67	28.34–32.13
CaO	0.70–2.61	1.19–2.12
Na_2O	b.d.–0.02	b.d.–0.02
K_2O	b.d.	b.d.
NiO	0.04–0.13	0.04–0.11
Total	100.18–101.22	99.39–101.38
	Rare earth elements (parts per million)	
La	0.045–0.120	0.024–0.190
Ce	0.116–0.295	0.099–0.471
Nd	0.098–0.220	0.056–0.354
Sm	0.044–0.079	0.028–0.152
Eu	0.014–0.028	0.007–0.030
Gd	0.070–0.122	0.056–0.238
Dy	0.141–0.236	0.110–0.405
Er	0.120–0.192	0.091–0.312
Yb	0.147–0.240	0.115–0.392
	Ratios	
Mg#	0.81–0.85	0.79–0.87
$(Ce/Nd)_n$	0.79–1.05	0.60–1.13
$(Ce/Yb)_n$	0.20–0.47	0.41–0.91
$(Ce/Sm)_n$	0.59–0.92	0.10–0.56

Stillwater Orthopyroxenes
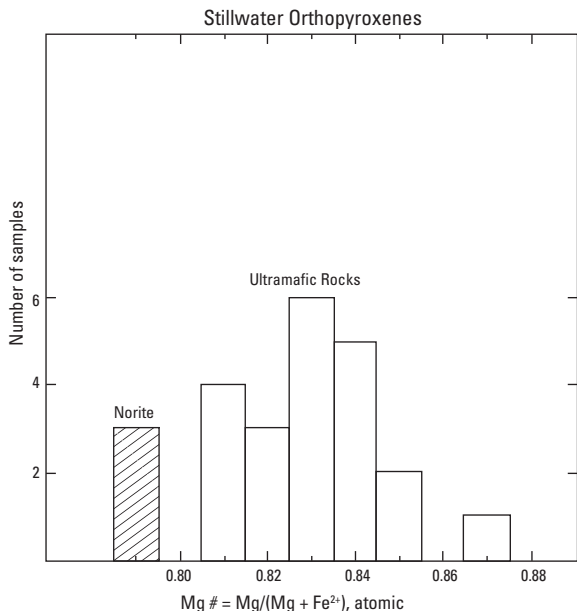
Figure 68.   Histogram of Mg #s, where Mg # = Mg/(Mg + Fe^{2+}), for orthopyroxene minerals within the Stillwater Complex. From Lambert and Simmons (1987, fig. 5).

Ultramafic Series Orthopyroxenes
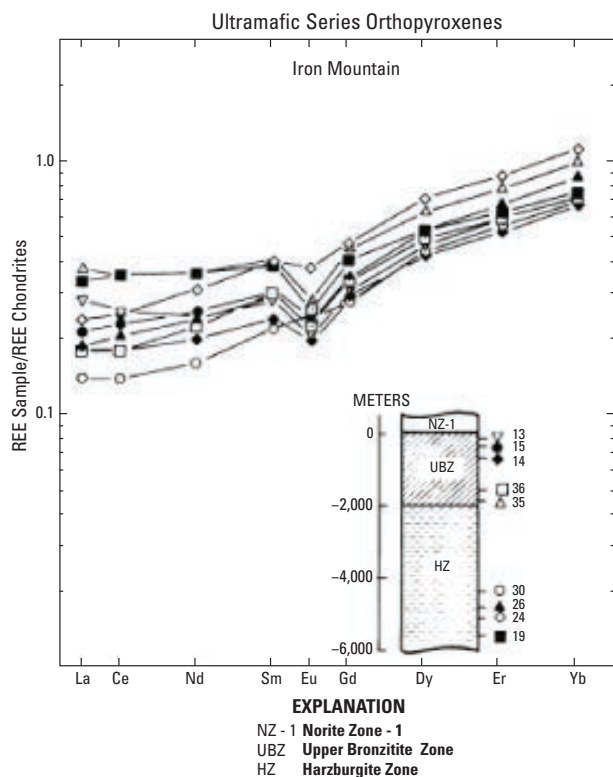
Figure 69.   Chondrite normalized rare earth element (REE) pattern for orthopyroxene grains in the Ultramafic Series of the Stillwater Complex. Stratigraphic relationships located on inset stratigraphic column. From Lambert and Simmons (1987, fig. 6).

Kemi Intrusion

The chemical compositions of least altered cumulates near or interbedded with the stratiform chromitite are presented in table 20 (Alapieti and others, 1989). The MgO contents remain relatively constant in the lower part of the intrusion up until the upper part of the peridotites, and then decline progressively toward the roof of the intrusion. The CaO concentrations are elevated in those samples where augite is a cumulus mineral. The Ni content is fairly constant, at about 0.1 wt%, in the lower layers of the intrusion and then begins to decline in the upper peridotites (Alapieti and others, 1989). Both Na$_2$O and Sr concentrations increase gradually from the lower layers of the intrusion upward. These results are consistent with formation of the Kemi intrusion by new pulses of magma entering a contaminated magma chamber.

Rum Intrusion

Several studies (Brown, 1956; Dunham and Wadsworth, 1979; Tait, 1985; Faithfull, 1985) have revealed geochemical complexities in the peridotite and allivalite layers of the Rum intrusion. The analyses of Brown (1956) and Dunham and Wadsworth (1979) indicate that the olivine and plagioclase within the peridotite layers and in some of the allivalite layers shifted to more evolved compositions toward the top (table 21). Subsequent work (Faithfull, 1985; Tait, 1985) has identified similar trends but also demonstrated that more evolved compositions can occur at the base of the peridotite layers (table 22). Specifically, XRF analyses of peridotites from cyclic unit 10 show that there is a steep gradient in the Ni content of olivine across the peridotite-allavite boundary (table 23). The changes

Table 20.   Chromite compositions from select lithologies in the Kemi intrusion.

[From Alapieti and others (1989). Concentrations reported in weight percent (wt%). 1, Chromite-olivine orthocumulate in lower part of main chromitite layer, with poikilitic postcumulus augite; 2, Chromite mesocumulate in lower part of main chromitite layer containing poikilitic postcumulus aguite; 3, Chromite harzburgite, middle part of main chromitite layer; 4, Chromite mesocumulate in upper part of main chromitite layer with poikilitic postcumulus bronzite; 5, Chromite-bearing wehrlite with intercumulus augite located about 30 m above main chromitite layer; 6, Harzburgite with intercumulus augite located about 100 meters above the uppermost chromitite layer]

Oxides	1	2	3	4	5	6
SiO$_2$	14.17	10.3	39.49	6.56	44.01	43.24
TiO$_2$	0.38	0.36	0.1	0.43	0.10	0.11
Al$_2$O$_3$	11.24	12.09	2.17	12.98	2.99	3.82
Fe$_2$O$_3$	3.54	3.72	2.86	4.59	2.63	4.26
Cr$_2$O$_3$	34.35	41.91	6.02	41.62	1.73	0.36
FeO	12.75	13.42	10.29	16.52	9.48	8.64
MnO	0.21	0.27	0.19	0.25	0.21	0.20
MgO	20.32	17.25	38.65	16.67	33.49	35.86
CaO	2.96	0.62	0.10	0.37	5.33	3.26
Na$_2$O	0.06	0.06	0.09	0.00	0.00	0.17
K$_2$O	0.00	0.00	0.00	0.00	0.01	0.07
P$_2$O$_5$	0.01	0.00	0.01	0.00	0.01	0.01

Table 21.   Olivine compositions from the Rum intrusion.

[Concentrations reported in weight percent. ELS, Eastern Layered Series; WLS, Western Layered Series; b.d., below detection limit; tr., trace amounts; n.f., not found]

Oxides	Olivine in allivalite (Unit 10)[a]	Olivine in peridotites (Unit 10)[a]	Olivines in ELS (Unit 10)[b]	Olivines in WLS (Unit B)[b]
SiO_2	39.87	40.04	38.88–40.66	38.40–40.79
Al_2O_3	0.00	0.81		
Fe_2O_3	0.86	0.47		
FeO	13.20	11.33	11.56–19.36	10.96–20.25
MgO	45.38	45.64	41.40–47.83	40.42–47.39
CaO	0.25	0.19	n.f.–0.14	n.f.–0.18
Na_2O	0.04	0.06		
K_2O	0.01	0.06		
H_2O^{+110}	0.33	0.42		
H_2O^{-100}	0.10	b.d.		
TiO_2	0.03	0.38		
P_2O_5	0.01	b.d.		
MnO	0.22	0.23	n.f.–0.33	n.f.–0.38
Cr_2O_3	tr.	0.08		
NiO	n.d.	0.02	n.f.–0.33	n.f.–0.40
CoO	n.d.	b.d.		
Total	100.3	99.79	99.67–100.66	

[a]Brown (1956).

[b]Dunham and Wadsworth (1978).

in the Fe/Mg ratios of the olivines also suggests that the olivine has undergone reequilibration. Furthermore, an increase in Al_2O_3, CaO and SiO_2 in the upper peridotite relative to lower periditote is most likely due to the decrease in olivine content relative to plagioclase and pyroxene (table 22; Tait, 1985). These results indicate that crystal fractionation cannot alone explain the formation of the layers; rather, assimilation of feldspathic wallrock and late-stage exchanges of interstitial melt may have been important factors (Bédard and others, 1988).

Burakovsky Intrusion

Major element data for whole rocks and individual olivine grains in the Burakovsky intrusion vary with stratigraphic height (tables 24 and 25), suggesting formation via crystal differentiation of a mafic parent magma followed by repeated pulses of new magma into the chamber (Sharkov and others, 1995). In addition, the Mg # for olivine crystals from the Ultramafic Zone range from 81.9 to 86.9, whereas the Mg # for the Main Chromite Horizon is 86.0 and olivine in the overlying Pyroxenite Zone averages 83.3 (table 25) (Sharkov and others, 1995; Higgins and others, 1997). Koptev-Dvornikov (1995) reported the average Mg # for the Burakovsky intrusion is 84, which is consistent with Mg #s from other large layered stratiform complexes.

Table 22.   Major chemical compositions for peridotites and allivalites from the Rum intrusion.

[Major element chemistry reported in weight percent; analyses recalculated as anhydrous; loss on ignition values range 0.3 to 0.4 (Tait, 1985); tr., trace amounts]

Oxides	Lower Peridotite (Unit 10)[a]	Upper Peridotite (Unit 10)[a]	Allivalite (Unit 10)[a]	Peridotite Unit 10[b]	Allivalite Unit 10[b]	Allivalite Unit 32
SiO_2	40.42	43.52	47.88	41.06	47.33	45.56
Al_2O_3	4.53	8.44	16.81	4.82	20.08	21.17
Fe_2O_3				2.07	0.55	1.10
FeO[c]	12.85	10.97	5.98	9.46	3.24	5.59
MgO	37.80	28.82	13.13	36.15	12.53	11.48
CaO	3.71	7.06	14.04	4.27	14.47	11.42
Na_2O	0.23	0.64	1.74	0.65	1.34	1.99
K_2O	0.02	0.03	0.05	0.02	0.07	0.16
H_2O^{+110}				0.97	0.21	1.21
H_2O^{-100}				0.06	0.14	0.07
TiO_2	0.20	0.16	0.24	0.15	0.15	0.40
MnO	0.20	0.19	0.09	b.d.	tr.	0.02
P_2O_5	0.01	0.02	0.01	0.17	0.08	0.10
Cr_2O_3				0.51	0.18	0.02
Total	100.00	100.00	100	100.36	100.37	100.29

[a]Tait (1985).
[b]Dunham and Wadsworth (1978).
[c]All iron is assumed to be FeO in Tait (1985) dataset.

Table 23.   Trace element concentrations of peridotites and allivalites from the Rum intrusion.

[From Tait (1985). Trace element chemistry reported in parts per million; analyses recalculated as anhydrous; loss on ignition values range 0.3 to 0.4]

Trace elements	Lower peridotite (Unit 10)	Upper peridotite (Unit 10)	Allivalite (Unit 10)
Ba	10	11	16
Ce	0	0	8
Co	140	135	56
Cr	6,410	2,504	752
Cu	63	374	45
La	0	0	7
Ni	1,913	1,617	253
Nb	0	0	0
Pb	4	4	8
Rb	3	3	1
Sc	14	19	32
Sr	66	115	228
Th	0	3	0
U	0	0	0
V	76	62	84
Zn	76	59	24
Zr	22	23	26

Table 24.   Major element analyses (in weight percent) of igneous whole rocks from the main chromite-bearing zones of the Burakovsky intrusion.

[From Sharkov and others, 1995]

Oxides	Ultramafic Zone		Main Chromite Horizon	Pyroxenite Zone	
	20/167	174/83	68/673	68/449	27/67
SiO_2	40.08	43.70	36.07	52.11	51.45
TiO_2	0.23	0.18	0.1	0.28	0.47
Al_2O_3	3.10	4.74	0.89	5.76	2.24
FeO^a		10.18			
$Fe_2O_3{}^b$	12.08		17.12	8.5	8.13
MnO	0.11	0.15	0.19	0.16	0.18
MgO	33.41	26.13	37.25	18.37	19.37
CaO	3.06	4.22	1.82	12.99	14.97
Na_2O	0.31	1.06	0.07	0.99	0.56
K_2O	0.16	0.14	0.01	0.07	0.08
P_2O_5		0.04	0.01	0.02	0.01
LOI	6.57	8.08	6.39	1.5	1.59
Total	99.11	98.62	99.92	100.75	99.05

[a]Total Fe as FeO.

[b]Total Fe as Fe_2O_3.

Table 25.   Major element compositions of olivine grains from relevant zones within the Burakovsky intrusion.

[Concentrations reported in weight percent. Mg #, $Mg/(Mg + Fe^{2+})$; b.d., below detection limit]

	Ultramafic Zone				Main Chromite Horizon	Pyroxenite Zone	
	200/444.7[a]	333/496.5[a]	248/190[a]	20/1627[b]	27/67[b]	262/10[b]	68/449[b]
	Oxides						
SiO_2	40.3	39.4	39.5	39.85	40.62	39.81	40.13
FeO	12.6	17.1	16.7	14.21	13.29	15.25	16.20
MnO	0.17	0.22	0.21	0.23	0.21	0.22	0.23
MgO	47.1	43.3	43.7	45.61	45.78	43.64	44.09
CaO	0.04	0.05	0.03	0.07	b.d.	b.d.	b.d.
NiO	0.54	0.37	0.40	b.d.	0.41	0.43	0.42
Total	100.8	100.4	100.5	99.97	100.31	99.35	101.07
	Ratios						
Mg #	86.9	81.9	82.3	85.1	86.0	83.6	82.9

[a]Electron microprobe analyses of olivine crystals from the upper subzone of the Ultramafic Zone (Higgins and others, 1997).

[b]Microprobe analyses of olivine crystals (Sharkov and others, 1995).

Trace element data for ultramafic rocks from the Ultramafic Zone are listed in table 26. In general, the chrondrite-normalized REE plots for these rocks have negative slopes (fig. 70) (Snyder and others, 1995). In addition, the samples show enrichment in LREE, suggesting that the parental magma for these rocks was also LREE enriched. Furthermore, the calculated parental magma would have $(Ce/Yb)_n$ ratio of 2.6, a $(Nd/Sm)_n$ ratio of 1.1, and a $(Dy/Yb)_n$ ratio of 1.6 (Snyder and others, 1995). This would also indicate that the source region for the parental magma was LREE enriched or that the melt underwent crustal contamination upon ascension to the magma chamber.

Table 26.   Trace element abundances of whole rock samples from the Ultramafic Zone of the Burakovsky intrusion.

[From Snyder and others (1996, table 1). Concentrations reported in parts per million (ppm)]

Element	248/190	200/444	28/223[a]	Parent
Sc	22.2	12.7	11.2	13.9
V	72.7	49.9	76.8	103.7
Cr	3,379.1	6,915.5	3,744.4	2,431.4
Co	104.8	102.1	124.9	60.0
Ni	1,461.7	2,359.4	1,947.7	220.6
Cu	23.1	221.7	84.3	107
Rb	0.34	0.07	8.3	11.4
Sr	26.8	13.7	81.2	7.63
Y	3.04	1.79	5.61	7.63
Zr	6.96	2.8	40.4	55
Nb	0.27	0.1	1.88	2.58
Ba	3.03	8.12	115.7	36.8
La	0.92	0.49	5.8	2.22
Ce	2.4	1.39	13.2	6.31
Nd	1.76	1.02	6.64	4.63
Sm	0.54	0.3	1.47	1.36
Eu	0.17	0.1	0.39	0.45
Gd	0.53	0.31	1.27	1.74
Tb	0.09	0.05	0.2	0.27
Dy	0.6	0.33	1.13	1.55
Ho	0.11	0.07	0.2	0.27
Er	0.31	0.17	0.54	0.74
Tm	0.04	0.02	0.06	0.08
Yb	0.25	0.16	0.47	0.64
Lu	0.03	0.02	0.06	0.08
Hf	0.19	0.11	1.05	1.43

[a]Border group sample.

EXPLANATION

- parent
- 200/444.7
- 249/190
- +10% parent
- +22% parent
- +33% parent
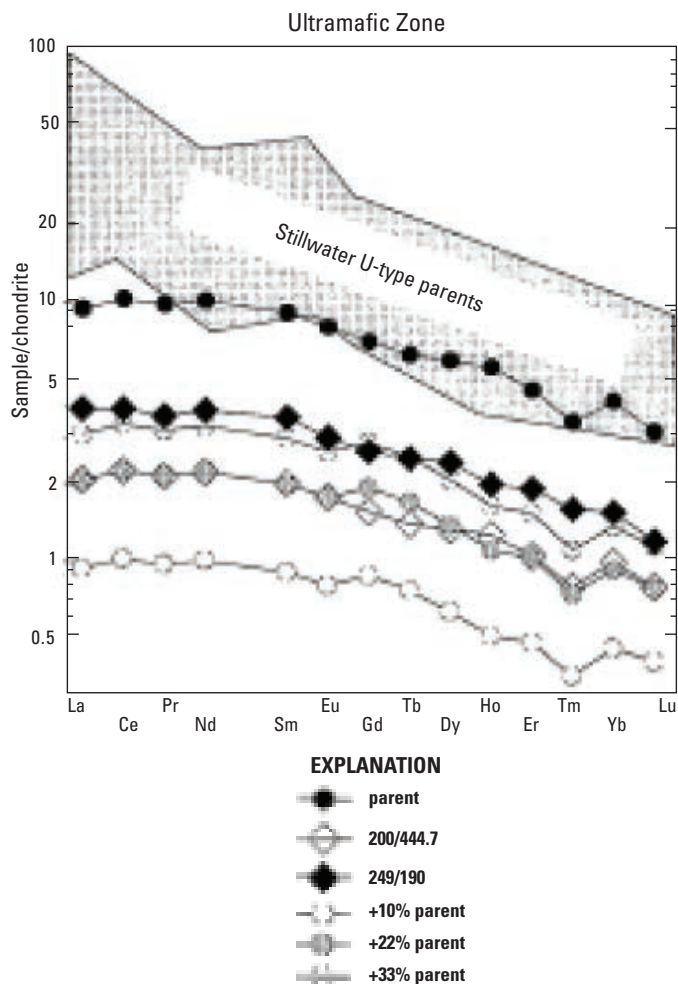
Figure 70.   Chondrite-normalized rare earth element (REE) plot of whole rocks samples from the Ultramafic Zone of the Burakovsky Intrusion. From Snyder and others (1996, fig. 3). Calculated parent magma shown as well as various mixtures of a model dunite cumulate containing trapped parental magma (10, 22, and 33 percent). Shaded area represents composition of U-type parent magmas from the Stillwater Complex (after Papike and others, 1995).

Ipueria-Medrado Sill

Variations in olivine and orthopyroxene compositions from harzburgite samples in the Ultramafic zone of the Ipueira-Medrado Sill suggest a magmatic evolution with two intervals divided by the Main Chromitite layer (Marques and Ferreira-Filho, 2003). Specifically, the Lower Ultramfic unit, which occurs below the Main Chromitite layer, contains minerals with Mg #s, where the Mg #s are reported as $100 \times Mg/(Mg + Fe^{2+})$, that are fairly constant and evolve gradually upward toward more Mg-rich compositions (table 27; fig. 71). This suggests that the Lower Ultramafic Unit formed in an open-system magma chamber that experienced frequent replenishment from a primitive magma source. Above the Main Chromitite layer, in the Upper Ultramafic Unit, there is a rapid evolution toward more Fe-rich compositions with increasing stratigraphic height,

such that Mg # (Fo for olivine, En for orthopyroxene) decreases upward (figs. 71 and 72). As a result, the unit most likely formed in a closed, fractionating magma chamber with minimal influxes of new, undepleted magma.

Similar trends are observed in the Ni contents of the olivine grains. In ultramafic rocks located below the Main Chromitite seam, the Ni content increases from about 2,000 ppm to 4,700 ppm, whereas above the Main Chromitite seam, the Ni concentration decreases from ~4,100 ppm to 1,800 ppm (Marques and Ferreira-Filho, 2003). The Ni contents in olivine also show a positive correlation with Mg and a negative correlation with Mn (fig. 71). In addition, both the Cr and TiO_2 contents of orthopyroxene show general positive correlations with MgO and negative correlations with Al_2O_3 (fig. 72; Marques and Ferreira-Filho, 2003).

Table 27. Range in compositions of olivine and orthopyroxene grains in harzburgites from the Ultramafic zone of the Ipueira-Medrado Sill.

[From Marques and Ferreira-Filho (2003). Abbreviations: LUU, Lower Ultramafic Unit; UUU, Upper Ultramafic Unit; b.d., below detection limit]

		Olivine		Orthopyroxene	
		LUU	UUU	LUU	UUU
Oxides (weight percent)					
SiO_2	min	40.04	39.39	54.68	53.58
	max	41.58	41.08	56.45	56.57
TiO_2	min			0.07	0.01
	max			0.18	0.21
Al_2O_3	min			1.52	1.96
	max			3.61	4.24
Cr_2O_3	min	<0.01	<0.01	0.12	0.09
	max	0.20	0.03	0.27	0.25
Fe_2O_3	min			0.27	0.67
	max			2.35	1.22
FeO	min	6.53	9.78	3.66	7.45
	max	12.98	15.95	8.88	10.99
MnO	min	0.10	0.07	0.10	0.12
	max	0.19	0.20	0.21	0.29
NiO	min	0.30	0.25	0.06	b.d.
	max	0.48	0.48	0.15	0.09
MgO	min	45.97	43.55	31.42	29.92
	max	51.32	48.30	32.96	32.96
CaO	min			0.21	0.19
	max			0.50	0.47
Na_2O	min			<0.01	<0.01
	max			0.01	0.01
K_2O	min			<0.01	<0.01
	max			0.04	0.04
Total	min	99.49	99.37	99.28	99.25
	max	100.29	99.98	100.38	100.38
Ratios					
Mg#	min	86.04	82.95	86.31	82.91
	max	93.34	89.73	94.49	88.74

EXPLANATION

- Norite
- Gabbro
- Chain-textured chromitite
- Chromitite (Lumpy ore)
- Pyroxene-rich harzburgite
- Harzburgite
- Dunite
- ppm   parts per million

Figure 71. Variations with stratigraphic height in olivine compositions from harzburgites and chromitite samples from the Ipueria-Medrado Sill. From Marques and Ferreira-Filho (2003, fig. 12).
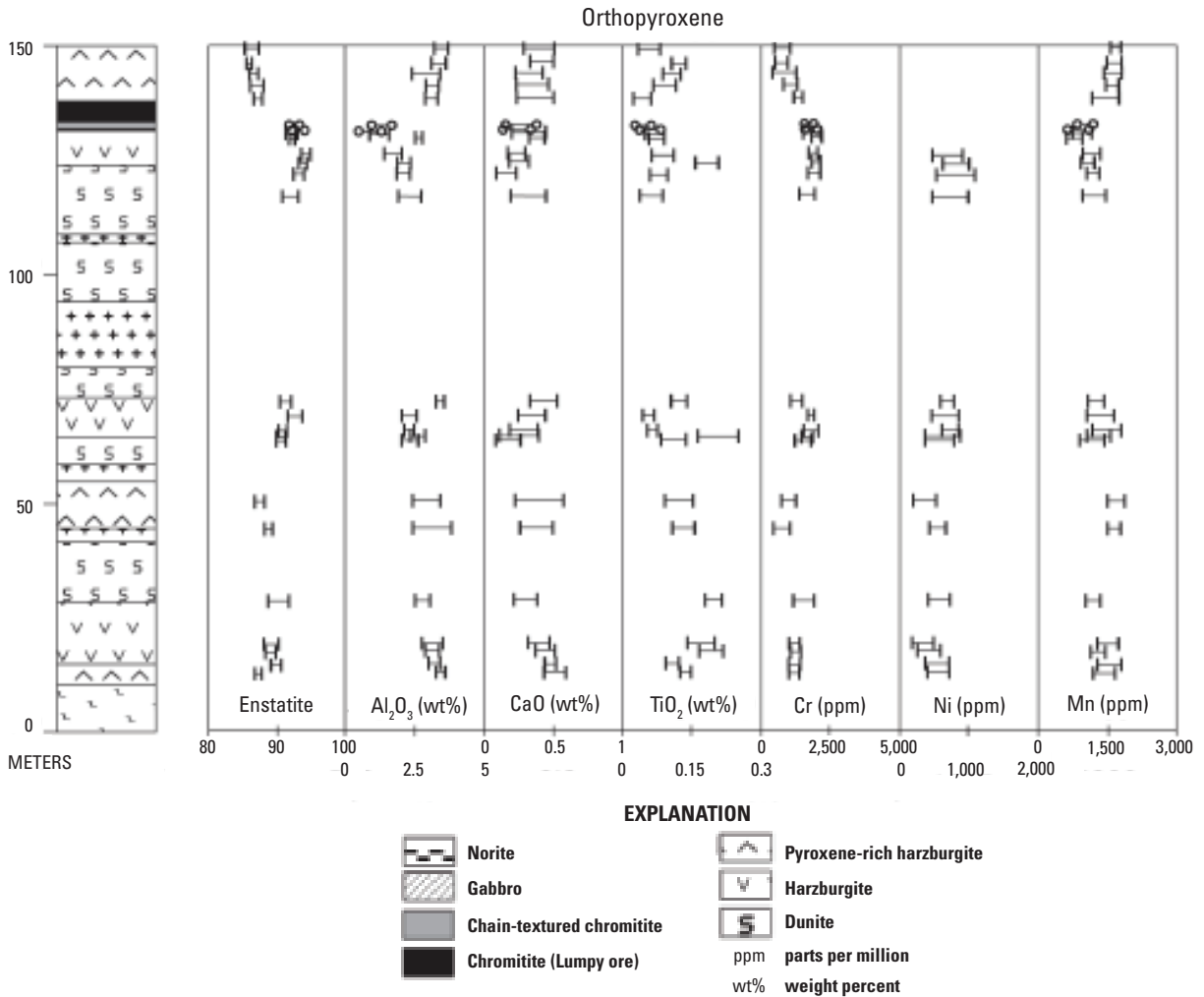
Figure 72. Variations with stratigraphic height in orthopyroxene compositions from harzburgites and chromitite samples from the Ipueria-Medrado Sill. From Marques and Ferreira-Filho (2003, fig. 12).

Fiskenæsset Anorthosite Complex

Chromitite layers in the Fiskenaesset anorthosite complex, from tens of centimeters up to 20-m thick, are predominantly located in the Anorthosite unit and at the top of the Upper Leucogabbro unit (Ghisler, 1976; Myers, 1985). Chromite-bearing seams may also occur embedded in the peridotite layers of the Ultramafic Unit (Polat and others, 2009).

Major and trace element geochemistry of the anorthosites reveal moderate variations in SiO_2, Al_2O_3, CaO, and Na_2O (table 28; Polat and others, 2009). However, there are large variations in the TiO_2, MgO, Fe_2O_3, and K_2O contents (table 28). The Zr, Ni, and Cr concentrations also have wide compositional ranges. Furthermore, although the Al_2O_3/TiO_2 ratios are super-chondritic, the Ti/Zr and Zr/Y ratios vary from subchondritic to super-chondritic (table 28).

The anorthosites can be subdivided into four different groups based on their REE patterns (table 28; fig. 73). Moderately depleted to moderately enriched REE patterns make up Group 1, with $La/Sm_{cn} = 0.65 - 1.60$, $Gd/Yb_{cn} = 0.80 - 1.14$, $La/Yb_{cn} = 0.51 - 1.18$ (table 28). Group 2 anorthosites have moderately to strongly enriched LREE and moderately depleted HREE profiles, with $La/Sm_{cn} = 1.94 - 6.17$, $Gd/Yb_{cn} = 1.46 - 1.75$, and $La/Yb_{cn} = 3.07 - 11.07$ (Polat and others, 2009). Group 3 anorthosites possess strongly fractionated LREE and HREE patterns, with $La/Sm_{cn} = 4.71 - 10.99$, $Gd/Yb_{cn} = 3.03 - 3.55$, $La/Yb_{cn} = 23.06 - 50.73$, whereas Group 4 anorthosites display concave-upward REE patterns, with $La/Sm_{cn} = 10.61 - 13.44$, $Gd/Yb_{cn} = 0.39 - 0.59$, and $La/Yb_{cn} = 2.41 - 7.58$ (Polat and others, 2009). Large positive Eu anomalies are present in all groups (Eu/Eu* = 1.56 - 14.27).

Table 28. Major weight percent and trace element data for anorthosites from the Fiskenæsset anorthosite complex.

[From Polat and others (2009). Abbreviations: subscript cn, chondrite normalized values; Mg #, Mg/(Mg + Fe^{2+}); LOI, loss on ignition; n.d., not determined]

	Group 1		Group 2		Group 3		Group 4	
	Minimum	**Maximum**	**Minimum**	**Maximum**	**Minimum**	**Maximum**	**Minimum**	**Maximum**
Oxides (weight percent)								
SiO$_2$	45.60	47.30	46.1	46.8	49.30	52.60	46.90	47.40
TiO$_2$	0.06	0.28	0.03	0.06	0.03	0.07	0.05	0.05
Al$_2$O$_3$	26.5	31.9	31.6	33.1	29.5	31.5	28.1	28.1
Fe$_2$O$_3$	1.80	4.10	0.7	3.9	0.9	1.8	8.5	9.3
MnO	0.03	0.06	0.01	0.14	0.01	0.03	0.21	0.27
MgO	1.1	4.3	0.3	1.2	0.2	0.7	2.3	2.3
CaO	15.9	17.5	14.9	17.1	12.0	13.1	9.8	10.1
K$_2$O	0.1	0.2	0.1	0.2	0.3	0.5	0.6	0.6
Na$_2$O	1.2	1.8	1.7	1.9	3.5	3.9	2.6	2.7
P$_2$O$_5$	0.01	0.03	0.01	0.02	0.01	0.01	0.02	0.03
LOI	0.51	1.08	0.35	0.65	0.41	0.58	0.50	0.55
Trace elements (parts per million)								
Cr	11	217	9	15	200	237	10	12
Co	9	28	4	8	3	6	19	23
Ni	25	85	7	11	7	22	13	14
Rb	0.3	3.1	0.5	5.9	2.3	14.5	20.6	21.4
Sr	73	95	83	111	115	149	131	145
Ba	7	29	31	89	33	107	95	158
Sc	6	21	2	4	n.d.	n.d.	5	14
V	21	78	12	17	16	27	14	14
Ta	0.005	0.048	0.006	0.013	0.001	0.003	0.009	0.013
Nb	0.060	0.309	0.037	0.186	0.019	0.045	0.098	0.131
Zr	2.10	19.1	6.0	14.1	1.44	5.0	3.49	36.2
Th	0.025	0.112	0.035	1.722	0.021	0.025	0.591	0.601
U	0.006	0.131	0.028	0.186	0.015	0.024	0.029	0.036
Y	1.5	6.9	0.6	3.1	0.2	0.5	4.9	12.2
La	0.269	1.301	0.225	3.794	0.984	1.530	7.027	7.566
Ce	0.637	2.803	0.488	6.514	1.394	2.202	9.797	11.492
Pr	0.092	0.367	0.063	0.635	0.127	0.192	0.726	0.904
Nd	0.453	1.683	0.282	2.159	0.429	0.732	1.930	2.467
Sm	0.157	0.525	0.075	0.397	0.067	0.150	0.363	0.428
Eu	0.157	0.348	0.203	0.307	0.313	0.359	0.363	0.393
Gd	0.247	0.870	0.100	0.532	0.074	0.146	0.507	0.997
Tb	0.058	0.166	0.016	0.091	0.008	0.018	0.097	0.215
Dy	0.293	1.166	0.101	0.562	0.042	0.100	0.739	1.669
Ho	0.063	0.258	0.020	0.108	0.009	0.018	0.181	0.414
Er	0.184	0.780	0.060	0.296	0.025	0.049	0.616	1.470
Tm	0.026	0.113	0.008	0.040	0.003	0.006	0.098	0.258
Yb	0.171	0.740	0.053	0.252	0.020	0.034	0.716	2.092
Lu	0.025	0.110	0.008	0.036	0.003	0.005	0.115	0.377
Cu	4	33	n.d.	n.d.	n.d.	n.d.	n.d.	n.d.
Zn	14	45	2	27	2	7	21	52
Ga	32	49	50	53	38	52	45	59
Pb	0.55	1.57	1.61	2.53	0.62	1.86	1.27	1.71
Ratios								
La/Sm$_{cn}$	0.65	1.60	1.94	6.17	4.71	10.99	10.61	13.44
Gd/Yb$_{cn}$	0.80	1.14	1.46	1.75	3.03	3.55	0.39	0.59
La/Yb$_{cn}$	0.51	1.18	3.07	11.07	23.06	50.73	2.41	7.58
Eu/Eu*	1.56	3.00	2.08	7.15	6.46	14.27	1.84	2.58
Al$_2$O$_3$/TiO$_2$	109	512	523	1150	448	860	576	600
Ti/Zr	50	243	13	53	41	284	8	80
Zr/Y	1.3	4.5	2.9	10.9	3.1	16.2	0.7	3.0
Y/Ho	22.3	27.5	26.1	28.4	26.2	28.0	27.4	29.4
Mg#	49.00	69.00	38	47	27	42	33	35
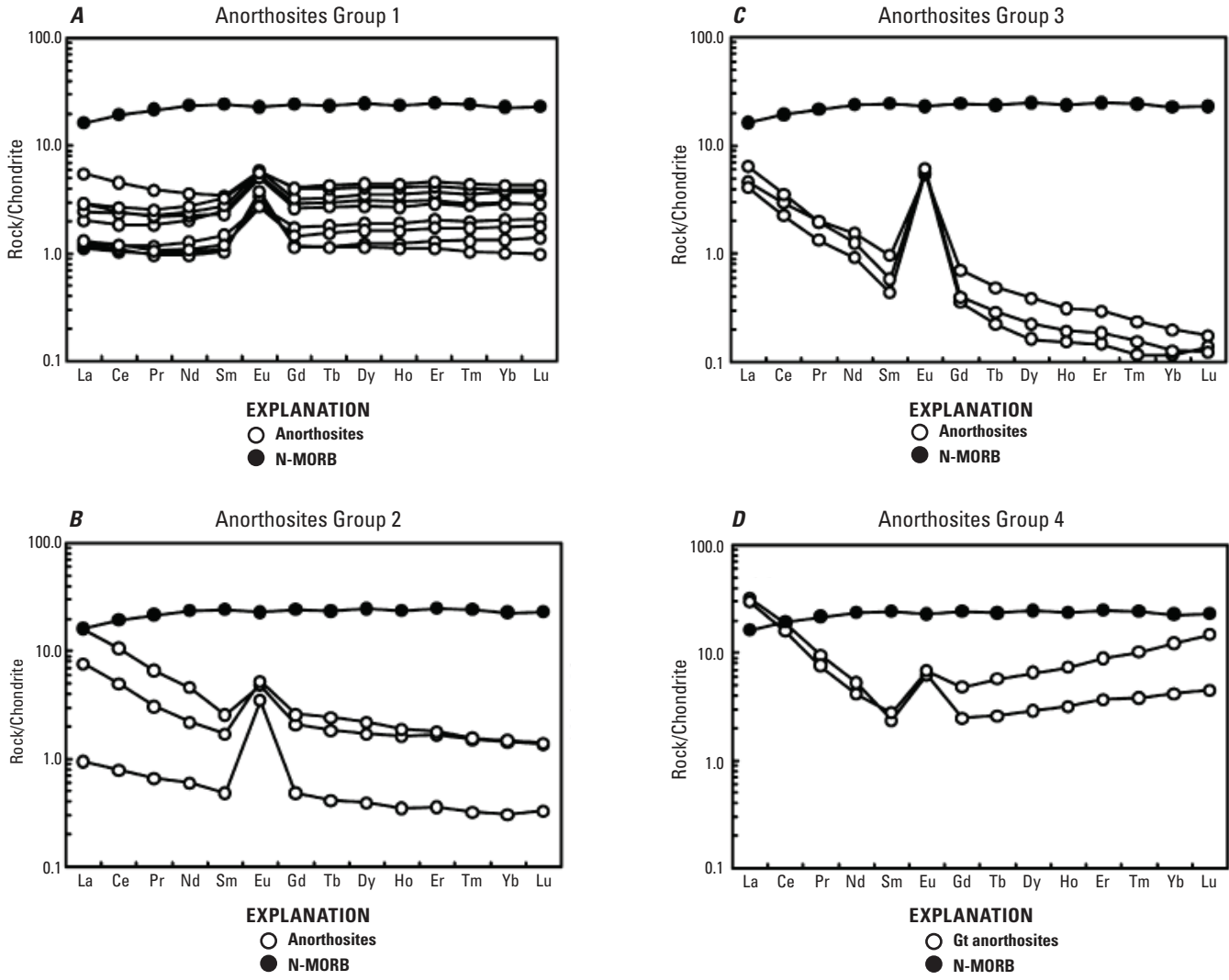
Figure 73. Chondrite-normalized rare earth element (REE) patterns for anorthosites from the Fiskenaesset anorthosite complex. Normalization values from Sun and McDonough (1989) and N-MORB from Hofmann (1988). Abbreviations: gt; garnet; N-MORB, Normal Mid-Ocean Ridge Basalt.

Isotope Geochemistry

Much of the isotope geochemistry of the associated igneous rocks has already been covered in the Geochemical Characteristics section of this report (see tables 11–13). This overlap has arisen due to the complex nature of chromitite seams within large, layered igneous intrusions, particularly with respect to their geochemical signatures and relationships. A review is provided here for those deposits where extensive isotope geochemistry research has been completed. However, the Nd isotope system stands out as the most widely used parameter when analyzing the formation of large mafic-ultramafic layered intrusions. In particular, the ε_{Nd} values for the intrusions are mostly negative, indicating that some degree of crustal contamination has occurred during formation (table 29).

Bushveld Complex

Sulfur concentrations and isotope ratios in the Bushveld have been used to suggest that a predominantly magmatic sulfur source influenced sulfide mineralization. Liebenberg (1970), for example, reported the sulfur contents of the Bushveld magma as 238 ppm. In addition, the sulfur content of the ultramafic rocks of the Upper Zone varies sympathetically with Ni, Cu, Co, and Zn. As a result, the variation in the amount of magmatic sulfur was most likely responsible for the variable sulfide concentrations in the layered sequence of the Bushveld. More specifically, during crystallization of rocks in the Critical Zone, the sulfur content of the magma decreased to the point where a Cu-sulfide-bearing immiscible liquid formed, creating the norite and anorthosite in that sequence. An increase in sulfur content following formation of the Critical Zone resulted in the formation of the copper-nickeliferous sulfides in the Merensky Reef (Liebenberg, 1970). With respect to sulfur isotope ratios, values for $\Delta^{33}S$ of the parental Platreef magma proxy vary from 0.11 to 0.21 ‰, with a narrow range of $\delta^{34}S$ from 1.3 to 3.2 ‰, suggesting that the Bushveld magma was saturated in sulfur (table 12; Penniston-Dorland and others, 2008). Platreef ore horizon rocks record $\Delta^{33}S$ values that range from 0.03 to 0.55 ‰ and $\delta^{34}S$ values from 2.7 to 11.4 ‰, indicating the Bushveld magma lost sulfur during mineralization of the Platreef ore horizon.

Table 29. Summary of $^{143}Nd/^{144}Nd$ and εNd values for key stratiform complexes.

[Value in parentheses is an average]

Deposits	Stratigraphic location unit	Unit	Lithology	$^{143}Nd/^{144}Nd$	ε_{Nd}	References
Bushveld Complex (South Africa)	Lower Zone		Pyroxenite and harzburgite	0.511393–0.511549	–6.0 to –5.4	1, 2, 3
	Lower Critical Zone	LG chromitite	Pyroxenite	0511462–0.511513		
	Upper Critical Zone		Chromitite, norite and anorthosite	0.5111000–0.511428	–7.6 to –6.3	
	Lower Main Zone		Norite and gabbronorite	0.511604–0.511792	–7.9 to –6.4	
Muskox intrusion (Canada	Cyclic units		Clinopyroxenite, websterite, dunite	0.511330–0.512945	–11.4 to –0.1	4
	Keel Dyke		Gabbronorite	0.512290		
Stillwater Complex (Montana, USA)	Ultramafic Series	Peridotite zone	Peridotite and chromitite	0.511714–0.513422	–5.6 ±1.7	5, 6
Rum intrusion (Scotland)		Units 8–15	Peridotite, troctolite, gabbro	0.51281–0.5123	–2.2 ± 3.9	7, 8
		Undefined cyclic units	Feldspathic peridotites Allavite	0.51271–0.51253 0.51249–0.5123		
Great Dyke (Zimbabwe)	Entire intrusion			0.511068–0.514724	+0.4 ± 5.0	9
Ipueria-Medrado Sill (Brazil)	Ultramafic Zone	Lower Ultramafic Unit	Harzburgite	0.510930–0.511553	–3.9 to –6.7	10
	Upper Ultramafic Unit		Amphibole-rich harzburgite Amphibole-free harzburgite	0.511314–0.511772	–6.3 to –6.8 –4.7	
Niquelândia Complex (Brazil)	Lower sequence		Peridotite, pyroxenite, gabbronorite, chromitite	0.551874–0.513730	–10.83 to 6.48 (–5.8)	11, 12, 13
	Upper sentence		Gabbro, anorthosite, amphibolite	0.512439–0.513618	–0.27 to 7.67	
	Lower sentence		Crustal xenoliths	0.511396–0.511469	–12.5	

References cited: 1. Schoenberg and others, 1999; 2. McCandless and others (1999); 3. Maier and others (2000); 4. Day and others, 2008; 5. Lambert and others, 1994. 6. DePaolo and Wasserburg, 1979; 7. Palacz, 1985; 8. O'Driscoll and others (2009b); 9. Mukasa and others (1998); 10. Marques and others, 2003; 11. Rivalenti and others, 2008; 12. Girardi and others, 2006; 13. Pimentel and others, 2004.

As mentioned in the "Geochemical Characteristics" section above, contrasting initial Sr isotopic compositions recorded in the Lower, Critical, and Lower Main Zones of the Bushveld Complex suggest numerous magma influxes (fig. 4 for stratigraphic relations). This, along with concomitant mixing, crystallization, and deposition of cumulates, suggest formation in an open system, and has been referred to as the "Integration stage" (Kruger, 1994, 2005; Kinnaird and others, 2002). In the Lower Zone, the initial $^{87}Sr/^{86}Sr$ ratio of the harzburgite averages ~0.705, whereas in orthopyroxenite from the Lower Critical Zone and norite and anorthosite in the Upper Critical Zone, the average initial $^{87}Sr/^{86}Sr$ reaches ~0.7064 (table 13; Molyneux, 1974; Cameron, 1978, 1982; Kruger, 1994; Kinnaird and others, 2002). Interstitial plagioclase in the LG chromitites of the Critical Zone record initial Sr ratios that vary from 0.7066 to 0.7070, with the highest initial Sr ratio ($^{87}Sr/^{86}Sr$ = 0.7080) occurring in the MG3 chromitite package of the Upper Critical Zone (Kinnaird and others, 2002). These abrupt increases in Sr isotopic compositions suggest that the intruding parent melt experienced massive contamination upon contact with the roof of the chamber, causing incorporation of the floating granophyric liquid and forcing the precipitation of chromite (Kruger 1999; Kinnaird and others, 2002).

The initial Sr isotopic ratio across the boundary between the Upper Critical Zone and Main Zone of the Merensky Reef changes from 0.705 to 0.706 (table 13; Hatton and others, 1986), and then jumps to 0.7085 moving upward stratigraphically from the Upper Critical Zone to the Main Zone (Kruger and Marsh, 1982); this indicates the addition of magma of a distinct and different composition at this level. During the closed-system "Differentiation stage" in the Upper Main Zone (initial $^{87}Sr/^{86}Sr$ = 0.7084) and Upper Zone (initial $^{87}Sr/^{86}Sr$ = 0.7072), no major magma influxes occurred (Kinnaird and others, 2002; Kruger, 2005). As such, the thick magma layers at this level of the Bushveld Complex formed by fractional crystallization. Near the Pyroxenite Marker, however, a single, very large, and final magma addition occurred, which is recorded by a sharp decline in Sr_i ($^{87}Sr/^{86}Sr$ = 0.7073) (Kruger and others, 1987; Cawthorn and others, 1991).

With respect to Re-Os isotope systematics, the initial $^{187}Os/^{188}Os$ ratios of pyroxenites of the Bastard Unit yield a value of 0.151 (table 13; Schoenberg and others, 1999). The Re-Os isochron defined by this dataset suggests an age of 2,043 ± 11 Ma, which is consistent with other cited crystallization ages of the Bushveld Complex (for instance, Hamilton, 1977; Sharpe, 1985; Kruger and others, 1987). Remarkably, the isochron fit indicates significant Os isotopic homogeneity in the Bastard Unit at the time of crystallization insofar as the initial $^{187}Os/^{188}Os$ ratio (0.1506) is much more radiogenic than the chondritic mantle (0.128) at 2.04 Ga. As a result, Os isotopic homogeneity most likely occurred after considerable crustal contamination. The Rb-Sr data for the pyroxenites yield an errorchron age of 2,027 ± 160 Ma and an initial $^{87}Sr/^{86}Sr$ ratio of 0.70772, also suggesting crustal contamination occurred. Unlike Os, however, the Sr isotopes exhibit more heterogeneity (Kruger, 1992; Schoenberg and others, 1999).

The initial $^{187}Os/^{188}Os$ ratios of PGE enriched sulfides and whole rocks below the Merensky Reef are, on the other hand, highly variable and radiogenic, with values ranging from 0.168 to 0.181 (table 13; Schoenberg and others, 1999). Interstitial phases in the Critical Zone chromitite layers and chromite separates reveal initial $^{187}Os/^{188}Os$ values that are near chondritic (~0.120) in the Lower Group chromitites, 0.137 for Middle Group chromitites, and 0.150 for the UG2 chromitite layer. The γ_{Os} values (where γ_{Os} is the percentage difference between the Os isotopic composition of a sample and the average chondritic composition at that time; Shirey and Walker, 1998) vary from +10 to +55 and argue for assimilation and mixing of crustally contaminated melts with mantle-derived magmas (Schoenberg and others, 1999).

Stillwater Complex

The Nd isotopic ratios of samples taken from different stratigraphic levels in the Stillwater Complex result in an $\varepsilon_{Nd(2701)}$ of −1.6 ± 0.6 (table 13; DePaolo and Wasserburg, 1979). A wider range in initial ratios (ε_{Nd} = +1.9 to −5.2) observed by Lambert and others (1989, 1994) led them to conclude that two isotopically distinct magmas were involved in the formation of the complex. However, the samples that showed the most negative values (ε_{Nd} = −2.7 to −5.2) came from the sulfide-rich zone at the base of the complex and the lowermost chromitite seam, suggesting perhaps contamination from a local source rather than introduction of a second magma type (McCallum, 1996). With respect to initial $^{187}Os/^{188}Os$ ratios, the A, C, H and J chromitites in the Ultramafic Series average 0.92 ± 0.02 at 2.7 Ga, which is within the range of chondritic values at that time (Marcantonio and others, 1993). The G, H, I and K chromitites studied by Lambert and others (1994) are also near-chondritic. However, higher initial values ($^{187}Os/^{188}Os_{avg}$ = 1.15 ± 0.04) are reported for samples from the J-M Reef, chromitites from the B chromitite, and chromitites within the Bronzitite Zone. In addition, the Re/Os ratios of the J-M Reef are much higher than the chromitites (Lambert and others, 1994).

Another factor to consider is the presence of molybdenite in the G-chromitite seam of the Stillwater Complex, which would suggest that hydrothermal fluids mobilized Re, and perhaps Os, shortly after crystallization (Marcantonio and others, 1993). As a result, the recorded Os isotopic variability could be explained by hydrothermal processes rather than assimilation of continental crust. The initial osmium isotopic ratios would then indicate derivation from a mantle-derived magma with little to no interaction with the continental crust prior to crystallization.

The Pb isotopic compositions of leached plagioclase crystals suggest the addition of a crustal component (Wooden and others, 1991; McCallum and others, 1992). A broad trend in $^{207}Pb/^{204}Pb$ versus $^{206}Pb/^{204}Pb$ occurs for samples throughout the Stillwater and is parallel to the 2.7 Ga isochron. In the Basal Series and lowermost Ultramafic Series, however, data plot slightly above the main trend defined by the Banded Series, suggesting local contamination occurred in the lower part of the complex during emplacement.

With respect to stable isotope systems, the $\delta^{18}O$ composition of Stillwater magma(s), based on plagioclase-basalt fractionation factors, varies from 4.7 to 6.7 ‰, with an average value of 5.9 ‰ (table 11; Dunn, 1986). Most values, however, lie close to the average value, making the Stillwater magma(s) coincident with the range of values obtained for mantle-derived melts. In addition, uniform $\delta^{34}S$ values occur throughout the complex with the exception of the sulfides in the Basal Series (table 12; Zientek and Ripley, 1990). This suggests crystallization from a homogeneous sulfur reservoir, and one most likely derived from the mantle. As such, the stable isotopes do not indicate the presence of large amounts of crustal contamination.

Great Dyke

Investigations into the Rb-Sr, Sm-Nd, and Pb-Pb isotope systematics have revealed that the Great Dyke experienced slight crustal contamination or originated from an uncontaminated but enriched mantle source. Uniform initial Sr, Nd, and Pb isotope ratios between subchambers led Mukasa and others (1998) to conclude that the Great Dyke formed in a subduction and continental collision environment. Using a larger Sm-Nd dataset, Oberthür (2002) discovered evidence for variable amounts of crustal contamination and concluded that the contamination occurred during emplacement. To resolve the debate, Schoenberg and others (2003) examined the Re-Os isotopic systematics of the Great Dyke. Initial $^{187}Os/^{188}Os$ ratios for chromite separates in ten of the massive chromitite seams resulted in a relatively narrow range of values, from 0.1106 to 0.1126 (table 13). This range is only slightly higher than expected for the value of coeval primitive upper mantle

(0.1107), making the ratios chondritic to very modestly suprachondritic, and far above estimates for the subcontinental lithospheric mantle (SCLM) at that time. As a result, crustal contamination of the Great Dyke magma would be minimal, at 0 to 33 percent. To explain this, Schoenberg and others (2003) suggested that a reservoir with a somewhat higher than average Re/Os ratio (relative to the primitive upper mantle) and within a heterogeneous mantle, acted as the parent magma of the Great Dyke. To account for the lack of contamination by continental crust or SCLM, the mantle upwelling, or "plume," would have formed in a failed rift setting and escaped by vertical volume or dissemination in conduits already primed by previous intrusions.

Rum Intrusion

The $^{87}Sr/^{86}Sr$ values of the Rum intrusion for Units 8 through 15 in the Eastern Layered Series (ELS) vary from 0.7036 to 0.7043 (table 13; Palacz, 1984; Palacz, 1985; Palacz and Tait, 1985; Renner and Palacz, 1987). In the overlying feldspathic peridotites, the $^{87}Sr/^{86}Sr$ ranges from 0.7049 to 0.7053, and in the allivalite, the $^{87}Sr/^{86}Sr$ is ~0.706 (table 13). Together with Sm-Nd isotopic data, these set of values and their respective positions within the intrusion suggest that the ELS formed from uncontaminated batches of picritic magma that were injected into a magma chamber containing crustally contaminated and relatively evolved basaltic magma. The $^{206}Pb/^{204}Pb$ values for the ELS peridotites, troctolites, and gabbros vary from 18 to 17.1, from 15.41 to 15.22 for $^{207}Pb/^{204}Pb$, and from 38.25 to 37.4 for $^{208}Pb/^{204}Pb$ (Palacz, 1985). Furthermore, when $^{208}Pb/^{204}Pb$ is plotted against $^{206}Pb/^{204}Pb$, the data cluster in the upper right of the diagram (fig. 74), suggesting
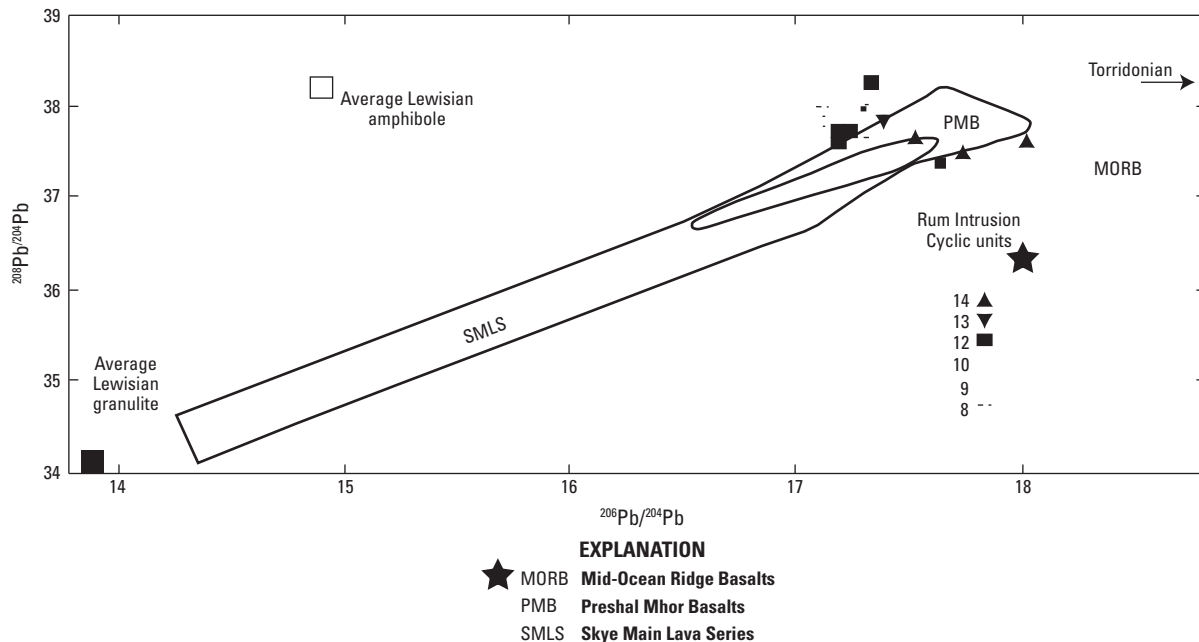
Figure 74. Plot of $^{208}Pb/^{204}Pb$ versus $^{206}Pb/^{204}Pb$ for peridotites, troctolite, and gabbros from cyclic units 8, 9, 10, 12, 13, and 14 of the Rum intrusion. From Palacz (1985, fig. 5*b*).

contamination by upper crustal amphibolite-facies Lewisian gneiss. The $\delta^{18}O$ values of whole rocks from the ELS vary from −5.1 ‰ to +10.7 ‰ (table 11; Forester and Harmon, 1983; Greenwood and others, 1992). The extent of this range suggests that heated meteoric waters must have reacted, to varying degrees, in some parts of the intrusion.

Initial $^{187}Os/^{188}Os$ for rocks from the Rum intrusion range from 0.1305 to 0.1349, which is atypical of values for the convecting upper mantle (O'Driscoll and others, 2009b). However, this range falls within the scope reported for recently erupted picrites and basalts from Iceland ($^{187}Os/^{188}Os$ = 0.1269–0.1369; Skovgaard and others, 2001) and Paleogene picrites and basalts from Baffin Island and West Greenland ($^{187}Os/^{188}Os$ = 0.1267–0.1322; Dale and others, 2009). Individual units within three stratigraphic levels preserve a range of initial $^{187}Os/^{188}Os$ values, with γ_{Os} values extending from +3.4 to as high as +35.7 (O'Driscoll and others, 2009b). With respect to the chromitite seams alone, the γ_{Os} values are also suprachondritic (γ_{Os} = +5.5 to +7.5). Unlike the Stillwater Complex, however, where γ_{Os} and Os isotopic heterogeneity decrease within increasing stratigraphic height, the highest γ_{Os} values in the Rum intrusion (O'Driscoll and others, 2009b) occur at an intermediate level. Due to the observed isotopic heterogeneity, the Re-Os data do not define an isochron in the suite of rocks examined, nor within the various units. Instead, the heterogeneity suggests that the composition of the magmas replenishing the original magma chamber may have been heterogeneous in nature and (or) that, similar to the Sr, Nd, and Pb isotopic data, crustal assimilation may have been involved.

Depth of Emplacement

Large, layered mafic-ultramafic intrusions have been emplaced at a variety at depths, and as such there is no consensus on the typical depths at which one would expect a stratiform complex to occur. Furthermore, estimates for the depth of emplacement are unavailable for most of the example deposits covered in this model. This arises, in part, due to the difficulty of assessing the size of the layered mafic-ultramafic intrusions where the stratiform chromite deposits are located. At present, estimates are only available for the Bushveld Complex and the Stillwater Complex. The estimated depth of emplacement for the Rustenburg Layered Suite of the Bushveld Complex is 9 km (Harmer, 2000). In the Stillwater Complex, the depth of emplacement has been reported as 10 to 15 km (McCallum, 1996).

Petrology of Associated Sedimentary Rocks

Stratiform chromite deposits are not associated with sedimentary rocks.

Petrology of Associated Metamorphic Rocks

Importance of Metamorphic Rocks to Deposit Genesis

Postcrystallization metamorphism has affected many of the igneous complexes and their stratiform chromite deposits. However, the chromite has been well preserved regardless of the degree of metamorphism of the igneous rocks. Serpentinization is common to pervasive in olivine-bearing lithologies such as peridotite, dunite, harzburgite, and troctolite. The most important metamorphic mineral in stratiform chromite deposits from a diagnostic and economic assessment standpoint, however, is magnetite.

Magnetite associated with stratiform chromite deposits often occurs as a late-stage or alteration mineral formed during serpentinization of minerals interstitial to chromite. In these cases, the magnetite forms rims on the outer edges of the chromite grains. If the chromite has been deformed or stressed, then magnetite may also be found within the cracks of chromite grains. Depending on degree of subsequent metamorphism, the composition of the rims or cracks may approach ferrichromite, which can lower the Cr/Fe ratio and produce non-economically viable ore.

Magnetite may also be found as inclusions within the chromite of the stratiform chromitite seams. In the Fiskenæsset anorthosite complex, for example, inclusions of magnetite are densely distributed throughout the chromite grains, varying in size from a few microns to 0.015 mm, and are mostly regular and rounded in shape (fig. 75; Ghisler, 1970). The smallest magnetite grains appear to be arranged according to crystallographic direction. The size of the magnetite inclusions also decreases from the center to the edges of the chromite grains. In addition, large areas of magnetite occur with lamellae of chromite along chromite grain boundaries (fig. 75).
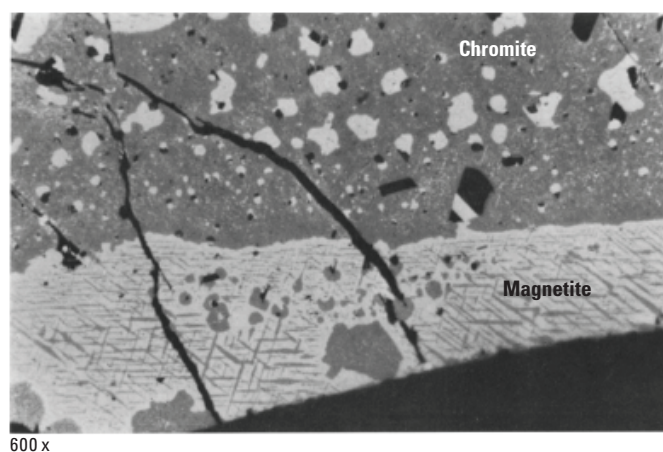
600 x

Figure 75. Reflected light photomicrograph of chromitite from the Fiskenæsset Complex illustrating two types of magnetite (white) within a chromite grain (grey). Image taken at 600x. From Ghisler (1970, fig. 14).

Other metamorphic minerals that may be present in the stratiform chromite deposits and closely associated layers include micaceous minerals like chlorite and clinochlore; serpentine group minerals such as lizardite, chrysotile, antigorite, and bastite; carbonate minerals like calcite, magnesite, and dolomite; and silicate minerals, such as quartz and talc. For example, the ultramafic sequence of the Campo Formoso layered intrusion originally contained 400 to 500 m of peridotites. During regional metamorphism, however, the peridotites were altered to lizardite-chrysotile-chromite-magnetite-bastite (Garuti and others, 2007). After a second episode of metamorphism, the lizardite-chrysotile-chromite assemblage was replaced by later generations of chlorite and antigorite, whereas abundant chromian clinochlore developed in the chromite rich zones of the complex. A third stage of metamorphism occurred that involved carbonatization, steatitization, and silicification, where the chlorite-rich assemblages were replaced by magnesite, talc, dolomite, calcite, and quartz (Garuti and others, 2007). Two rare Cr-bearing hydroxycarbonates, stictite and barbertonite, have also been identified (Boukili and others, 1984; Calas and others, 1984).

Hypothesis of Deposit Formation

The most commonly cited hypotheses regarding the formation of large, layered mafic-ultramafic intrusions where stratiform chromite deposits are located include: (1) the mixing of a parent magma with a more primitive magma during magma chamber recharge (Todd and others, 1982; Irvine and others, 1983; Eales, 1987; Naldrett and others, 1987, 1990; Eales and others, 1990) and (2) contamination of the parent magma by localized assimilation of country rock at the roof of the magma chamber (Irvine, 1975). The mixing of magmas would produce a partially differentiated magma, which could then be forced into the chromite stability field and result in the massive chromitite layers found in stratiform complexes (Irvine, 1977). On the other hand, contamination of magma with felsic crustal rocks could force the magma off the cotectic and into the chromite stability field, which would then enable the formation of massive chromitite layers such as those found in stratiform chromite deposits (Irvine, 1975). Even small amounts of silica and alkalies, when mixed with a basaltic or picritic melt, can suppress olivine crystallization and leave chromite as the only crystallizing phase until the composition of the magma returns to the cotectic.

Opponents to the magma mixing theory argue that the presence of numerous, sharply bound layers that alternate between >99-percent chromite and <1-percent chromite would require frequent, abrupt, mixing episodes and almost complete expulsion of interstitial melt (Boudreau, 1994). Melt

inclusions have also been used as evidence against mixing of primitive magma with fluid or residual fractionated magma (Spandler and others, 2005). In addition, replacement features associated with some of the chromitite layers suggest chromite was redistributed and concentrated during late-stage metasomatic processes (Boudreau, 1994).

With respect to assimilation of country rock by the parent magma, melt inclusions have proved meaningful. For example, inclusions (5 to 100 mm in diameter) within chromite grains from the Kemi intrusion include albite, phlogopite, amphibole, hornblende, millerite, galena, chlorite and zircon (Alapieti and others, 1989). Their presence has been interpreted to represent trapped droplets of contaminant salic melt that may be related to the composition of the border rock. Similarly, ores from the G chromitite seam of the Stillwater Complex, above the Benbow mine headframe, reveal isolated multiphase inclusions or inclusion clusters occur within the core zones of at least 20 percent of the chromite grains (Spandler and others, 2005). As a result, periodic injections of a high-Mg basaltic parent magma into the magma chamber during accumulation of the Peridotite Zone could explain chromite formation in the Stillwater Complex, such that the parent magma, if at high enough temperatures (>1,400 °C), would rise to the roof of the magma chamber. Partial fusion of metasedimentary country rocks or previously crystallized mafic rocks at the roof of the chamber would then form high-Na trondjemitic liquids (Spandler and others, 2005). Mixing between the trondjemite and parent magma at the roof of the chamber would subsequently lead to localized hybridization and rapid cooling of the melt, and thus facilitate chromite precipitation. However, efficiently mixing a viscous liquid of low density with a large body of underlying denser magma to produce uniform, laterally extensive chromite layers has been difficult to explain.

Recently, it was discovered that thin, subsidiary chromitite seams in the Rum intrusion have different compositions than those of the disseminated chromite in the surrounding peridotite and troctolite. This led O'Driscoll and others (2009a) to propose that the layered intrusion formed by downward infiltration of a picritic melt. According to their model, the infiltrating melt would dissolve and assimilate cumulus olivine and plagioclase residing in the troctolite crystal mush.

Despite the lack of a definitive model, ongoing investigations continue to provide insights into possible mechanisms that may account for the formation of massive stratiform chromite deposits and their large, layered host intrusions. Similarities and differences between the physical, structural, geochemical, and geophysical attributes of stratiform chromite deposits can further elucidate those aspects that are critical for refinement of the deposit model. In addition, these similarities and differences may provide guidance for continued assessment and exploration.

Exploration/Resource Assessment Guides

Geological

Chromitite seams that are economically significant are most commonly associated with peridotite and pyroxenite in the lower ultramafic parts of the layered intrusions. The mafic-ultramafic intrusions where the stratiform chromite deposits are located typically display an overall shape that is layered, differentiated, and sill- or funnel-like. The occurrence of disseminated chromite is also evident in the host rocks of the chromitite or chromite-rich seams.

Geochemical

Parent magmas of large, layered mafic-ultramafic intrusions typically have high SiO_2 and MgO content, which is evident from the early crystallization of high magnesian orthopyroxene after extensive olivine crystallization (Wilson, 1996). In addition, chromitites from layered mafic-ultramafic igneous intrusions contain high levels of Cr and demonstrate strong associations with PGE. The rocks are also characterized by high Mg contents and low Na, K, and P compositions.

Geophysical

A marked velocity contrast exists between the chromitite seams and associated igneous rocks of the Bushveld Complex. This marked velocity contrast enables the use of radar reflectivity and BHR surveys in assessing the economic viability of potential drilling sites. These geophysical properties may also occur in other large, layered mafic-ultramafic intrusions, but additional research in this area is warranted before a clear consensus can be reached.

Attributes Required for Inclusion in Permissive Tract at Various Scales

Stratiform chromite deposits are laterally extensive igneous layers of massive chromitite within a larger mafic-ultramafic intrusive body that was typically emplaced in a stable cratonic setting or along a rift zone during the Archean or Early Proterozoic. The layered intrusions are typically funnel or saucer shaped and extend from 2 to 180 km, with depths that can reach as much as 15 km. The thicknesses of the chromitite seams within the mafic-ultramafic intrusions range from <1 cm to as much as 8 m.

The rocks of the layered series where the chromitite seams are located are predominantly cumulates. The layered series ideally ranges from an ultramafic package at the base through various pyroxenite and peridotite layers to mafic cumulates at the top. This requires that the chromitite seams associated with stratiform chromite deposits occur toward the bottom of the layered intrusions. In addition, the cyclic recurrence of the chromitite seams within the layered intrusions indicates that necessary igneous processes occurred within the intrusion, although the exact mechanisms involved are still widely debated.

Geoenvironmental Features and Anthropogenic Mining Effects

Weathering Processes

Weathering processes associated with mine wastes from processing ore are dominated by interactions with chromite; trace amounts of sulfide minerals such as pyrrhotite, chalcopyrite, and pentlandite; and associated gangue minerals including olivine, orthopyroxene, clinopyroxene, and plagioclase. Chromite occurs in mine waste in minor amounts due to imperfect grinding of ore prior to producing a chromite concentrate. Sulfide minerals are typically found in economically insignificant amounts, although PGM, some of which are sulfides, may be extracted as a byproduct. The processing of chromite concentrates produces a variety of chromium-bearing solid phases in the chromite ore-processing residue (COPR), which include brownmillerite, hydrocalumite, hydrogarnet, and ettringite, in addition to periclase, larnite, brucite, calcite, and aragonite (Hillier and others, 2003), all of which affect the geochemical behavior of chromium in the environment.

The environmental geochemistry of chromite deposits and their associated mine wastes has been the subject of few studies (Tiwary and others, 2005; Meck and others, 2006). However, an extensive literature exists on the general environmental geochemistry of chromium (Rai and others, 1989; Saleh and others, 1989; Ball and Nordstrom, 1998; Oze and others, 2007). Likewise, numerous studies have investigated chromium geochemistry in soils formed from ultramafic rocks (Fendorf, 1995; Cooper, 2002; Oze and others, 2004a,b; Garnier and others, 2006, 2008, 2009) and groundwaters unrelated to mining (Robles-Camacho and Armienta, 2000; Fantoni and others, 2002; Ball and Izbicki, 2004). In addition, numerous investigations have been conducted on the environmental geochemistry of chromite ore-processing residue, which can be located near mine sites or far away at chemical manufacturing facilities (Burke and others, 1991; Hillier and others, 2003; Becker and others, 2006; Moon and others, 2008).

Most of the environmental concerns associated with stratiform chromite deposits focus on the solubility of chromium and its oxidation state. Chromium can occur as Cr(III) or Cr(VI). Trivalent chromium is an essential micronutrient for

humans, but hexavalent chromium is highly toxic (Katz and Salem, 1993). In mine wastes, and in ultramafic rocks in general, chromite is the primary source of chromium. Chromite dissolution can be described by the reaction:

$$FeCr_2O_4 + 8\ H^+ \rightarrow Fe^{2+} + 2Cr^{3+} + 4\ H_2O. \qquad (1)$$
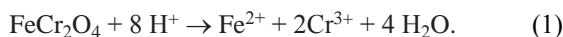
Under reducing conditions, the solubility of chromite is exceedingly low, except at low pH (<5) (fig. 76). In more oxygenated environments, dissolved iron will oxidize and hydrolyze as described by the reaction:

$$Fe^{2+} + \tfrac{1}{4}\ O_2 + 5/2\ H_2O \rightarrow Fe(OH)_3 + 2\ H^+, \qquad (2)$$
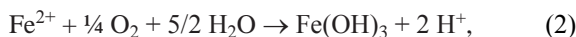
which effectively removes iron from solution. Under these conditions, the solubility of trivalent chromium is probably limited by the solubility of $Cr(OH)_3$ or $(Cr, Fe)(OH)_3$ (Rai and others, 1989), as described by the reaction:

$$Cr(OH)_3 + 3\ H^+ \rightarrow Cr^{3+} + 3\ H_2O, \qquad (3)$$
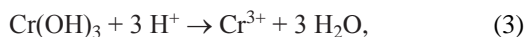
which can confine the concentrations to near the drinking water limit for pH values between 5 and 13 (fig. 77). In contrast, Cr(VI) is extremely soluble at all pH values (Ball and Nordstrom, 1998; Oze and others, 2007).

The toxicity of chromium depends on its oxidation state. Hexavalent chromium is far more toxic to humans and other organisms than trivalent chromium (Katz and Salem, 1993). The Eh corresponding to the $CrO_4^{2-}/Cr(OH)_3$ oxidation-reduction couple (~0.4 V at pH 7 and 25 °C) is fairly high (fig. 78), which means that under geochemically reasonable conditions, the only oxidants likely to oxidize Cr(III) to Cr(VI) are manganese [Mn(IV)] oxides and dissolved oxygen (Rai and others, 1989; Oze and others, 2007). Laboratory and field studies have demonstrated that Mn(IV) oxide is an effective and rapid oxidizer of Cr(III) (Rai and others, 1989; Saleh and others, 1989; Oze and others, 2007). Oxidation of Cr(III) by dissolved oxygen is extremely sluggish, and may only be an important mechanism in groundwaters with long residence times not representative of most mine-site hydrologic settings (Rai and others, 1989; Ball and Izbicki, 2004; Oze and others, 2007).

Solid phases found in chromite ore-processing residues represent potential sources of chromium to surface and groundwaters. Chromite and brownmillerite [Ca_2 (Fe, Al, Cr)$_2O_5$] are potential sources of Cr(III); hydrocalumite [Ca_2 (Al, Fe)(OH)$_6$ (CrO$_4$)$_{0.5}$ • 3H$_2$O], hydrogarnet [Ca_3 (Al, Fe)$_2$ (H$_4$O$_4$, CrO4)$_3$], and ettringite [Ca_6 Al$_2$ (SO$_4$, CrO$_4$)(OH)$_{12}$ • 26H$_2$O] are potential sources of Cr(VI) (Hillier and others, 2003). Leachates from ore-processing residue can also lead to the formation of several poorly characterized, efflorescent hexavalent chromium salts, such as $Ca_3Al_2O_6 \cdot CaCrO_4$, $Ca_3(CrO_4)_2$, and $FeCrO_4(OH)$ (Burke and others, 1991).

Trace sulfide minerals, chiefly pyrrhotite, chalcopyrite, and pentlandite, associated with these deposits may represent potential sources of acid drainage and dissolved trace
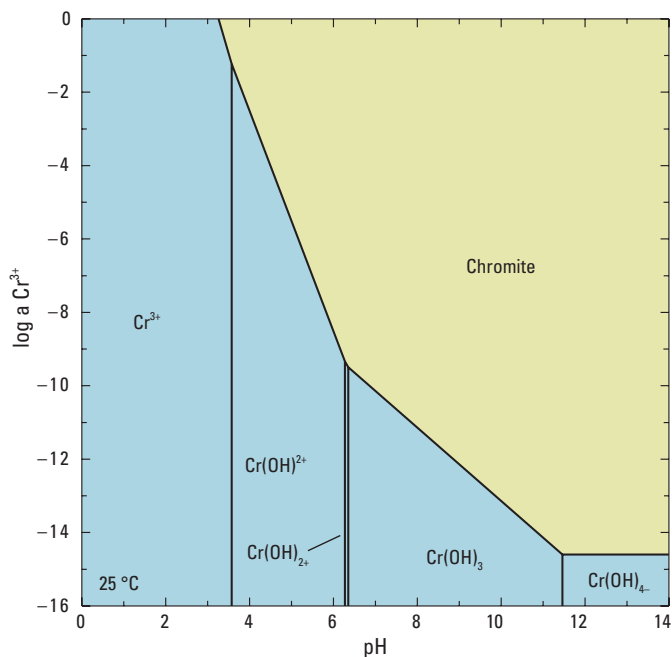
Figure 76. Diagram showing the solubility of chromite and the dominant speciation of dissolved chromium as a function of log aCr^{3+} and pH at 25 °C. Diagram was calculated using the Geochemist's Workbench, using the data from Ball and Nordstrom (1998) and the WATEQ4F database from Ball and Nordstrom (1991).
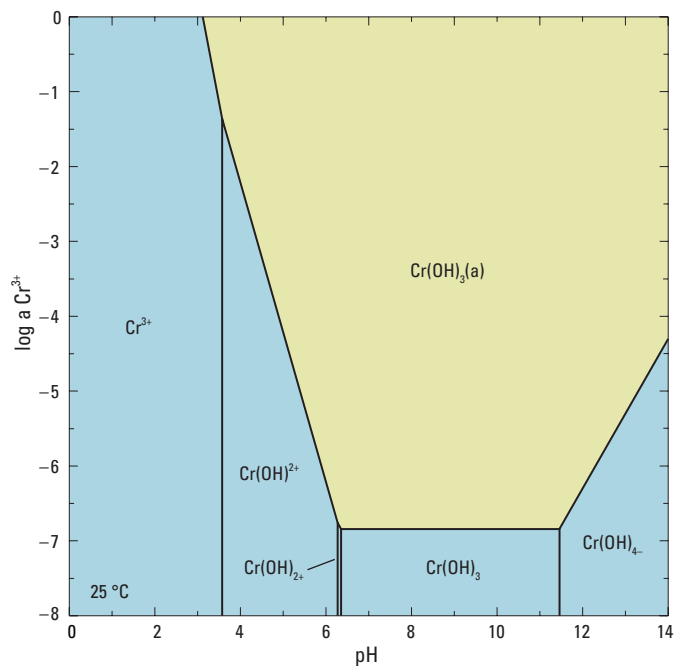
Figure 77. Diagram showing the solubility of amorphous chromium hydroxide and the dominant speciation of dissolved chromium as a function of log aCr^{3+} and pH at 25 °C. Diagram was calculated using the Geochemist's Workbench, using the data from Ball and Nordstrom (1998) and the WATEQ4F database from Ball and Nordstrom (1991).
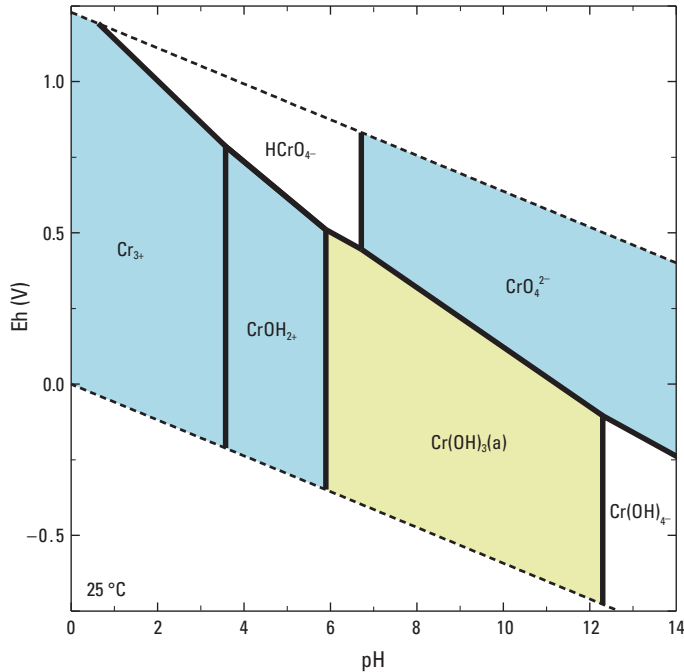
Figure 78. Diagram showing the stability of amorphous chromium hydroxide and the dominant speciation of dissolved chromium as a function of Eh and pH at 25 °C. Diagram was calculated using the Geochemist's Workbench, using the data from Ball and Nordstrom (1998) and the WATEQ4F database from Ball and Nordstrom (1991).

metals. The oxidation of pyrrhotite, and other sulfide minerals proceeds with either dissolved oxygen (O_2) or dissolved ferric iron (Fe^{3+}) as the oxidizing agent. Dissolved oxygen is the most important oxidant at pH values above ~4, whereas ferric iron dominates below ~4 (Williamson and others, 2006). The aqueous oxidation of pyrrhotite by dissolved oxygen can be described by the reaction:

$$Fe_{1-x}S + (2-x/2) O_2 + x H_2O ® (1-x) Fe^{2+} + SO_4^{2-} + 2x H^+, \quad (4)$$
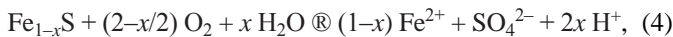
where x ranges from 0.000 to 0.125, although reaction 4 technically represents the mass action of numerous intermediate reactions. In the oxidative weathering of pyrrhotite, a common initial reaction is the oxidation of pyrrhotite to either pyrite or marcasite as described by the reaction:

$$2 Fe_{1-x}S + (1/2-x) O_2 + (2-4x) H^+ \rightarrow FeS_2$$
$$+ (1-2x) Fe^{2+} + (1-2x) H_2O. \quad (5)$$
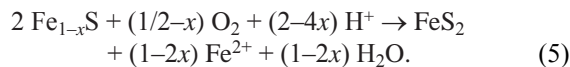
Textural evidence of marcasite replacement of pyrrhotite is common in pyrrhotitic mine wastes (Jambor, 1994, 2003; Hammarstrom and others, 2001). This reaction can lead to pyrite or marcasite oxidation as described by the reaction:

$$FeS_2 + 7/2 O_2 + H_2O \rightarrow Fe^{2+} + 2 SO_4^{2-} + 2 H^+. \quad (6)$$
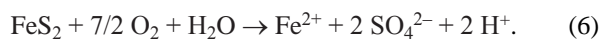
The aqueous oxidation of pyrrhotite by ferric iron can be described by the reaction:

$$Fe_{1-x}S + (8-2x) Fe^{3+} + 4 H_2O \rightarrow (9-3x) Fe^{2+} + SO_4^{2-} + 8 H^+. (7)$$
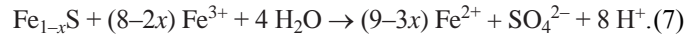
The aqueous oxidation of pyrite by ferric iron can be described by the reaction:

$$FeS_2 + 14 Fe^{3+} + 8 H_2O \rightarrow 15 Fe^{2+} + 2 SO_4^{2-} + 16 H^+. \quad (8)$$

For reactions 7 and 8, where ferric iron is the oxidant, ferrous iron must be oxidized to ferric iron to perpetuate the reaction as described by the reaction:

$$Fe^{2+} + ¼ O_2 + H^+ \rightarrow Fe^{3+} + ½ H_2O. \quad (9)$$
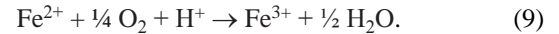
The rate of the oxidation of ferrous iron to ferric iron is greatly enhanced by the iron oxidizing bacterium *Acidithiobacillus ferrooxidans.* Singer and Stumm (1970) observed that *A. ferrooxidans* increased the rate of oxidation of ferrous iron to ferric iron by a factor of 100,000 compared to the abiotic rate. In the case of both sets of reactions for pyrite and pyrrhotite, additional acid is generated by the oxidation and hydrolysis of the aqueous ferrous iron as described by the reaction:

$$Fe^{2+} + ¼ O_2 + 5/2 H_2O \rightarrow Fe(OH)_3 + 2 H^+, \quad (10)$$
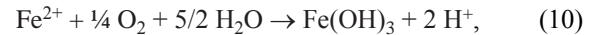
which also produces the orange and brown precipitates that typify acid-mine drainage.

The oxidative weathering of chalcopyrite by dissolved oxygen can be described by the reaction:

$$CuFeS_2 + 4 O_2 \rightarrow Cu^{2+} + Fe^{2+} + 2 SO_4^{2-}, \quad (11)$$

which does not generate acid. However, the continued oxidation and hydrolysis of iron, as described by reaction 10, will form acid. The oxidative weathering of chalcopyrite by ferric iron can, therefore, be described by the reaction:

$$CuFeS_2 + 16 Fe^{3+} + 8 H_2O ® Cu^{2+}$$
$$+ 17 Fe^{2+} + 2 SO_4^{2-} + 16 H^+. \quad (12)$$
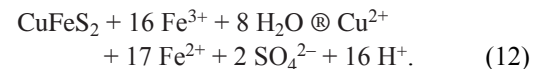
Similarly, continued oxidation of ferrous iron will generate additional acid.

Likewise, the oxidative weathering of pentlandite $[(Fe_{0.5}Ni_{0.5})_9S_8]$ by dissolved oxygen can be described by the reaction:

$$(Fe_{0.5}Ni_{0.5})_9S_8 + 15.5 O_2 + H_2O ® 4.5 Fe^{2+}$$
$$+ 4.5 Ni^{2+} + 8 SO_4^{2-} + 2 H^+. \quad (13)$$
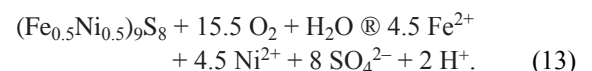
The oxidative weathering of pentlandite by ferric iron can be described by the reaction:

$$(Fe_{0.5}Ni_{0.5})_9S_8 + 66 Fe^{3+} + 32 H_2O ® 70.5 Fe^{2+}$$
$$+ 4.5 Ni^{2+} + 8 SO_4^{2-} + 64 H^+. \quad (14)$$
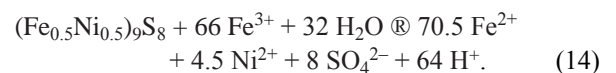
The continued oxidation and hydrolysis of ferrous iron will generate additional acid.

Pyrrhotite and other monosulfides, such as chalcopyrite, can also undergo non-oxidative dissolution under anoxic conditions when exposed to acid, as described by the respective reactions:

$$Fe_{1-x}S + (2-2x)\ H^+ + x\ H_2 \circledR (1-x)\ Fe^{2+} + H_2S, \quad (15)$$

and

$$CuFeS_2 + 4\ H^+ \circledR Cu^{2+} + Fe^{2+} + 2\ H_2S, \quad (16)$$
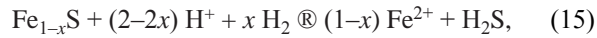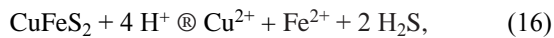
which effectively decouples iron and sulfur oxidation. Both of these reactions consume acid.

Gangue minerals in the host rocks should tend to react and consume the minor amounts of acid generated by the oxidation of trace sulfide minerals. Silicate minerals commonly found with stratiform chromite deposits, such as olivine, orthopyroxene, and plagioclase, can neutralize minor amounts of acid generated by the oxidation of trace sulfide minerals as described by the respective idealized reactions:

$$Mg_2SiO_4 + 4\ H^+ \circledR 2\ Mg^{2+} + H_4SiO_{4(aq)}, \quad (17)$$

$$MgSiO_3 + 2\ H^+ + H_2O \circledR Mg^{2+} + H_4SiO_{4(aq)}, \quad (18)$$

and

$$CaAl_2Si_2O_8 + 2\ H^+ + H_2O \circledR Ca^{2+} + Al_2Si_2O_5(OH)_{4(s)}. \quad (19)$$
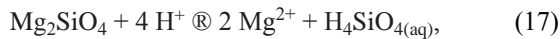
Solid solution of ferrous iron for magnesium in the olivine and orthopyroxene can partially counteract the acid neutralization due to oxidation and hydrolysis of the ferrous iron (reaction 10). Olivine is one of the most reactive silicate minerals with respect to acid neutralization (Jambor and others, 2002; 2007).

Pre-Mining Baseline Signatures in Soil, Sediment, and Water

Several accounts of baseline signatures in unmined areas of stratiform chromite deposits have been documented. Media sampled include soil, stream sediment, and water. Soil samples collected from a traverse across the central section of the Great Dyke deposit, where no significant mining had taken place, contain a maximum of 0.75 wt% Ni, 8 wt% Cr, and As that commonly exceeds 150 mg/kg. Chromium values are rarely below 1 wt% adjacent to the chromitite seams (Roberts, 1996). The Cr concentrations reported by Roberts (1996) are consistent with the findings reported by James (1957). This study on the soils of and surrounding the Great Dyke deposit produced a local background concentration of ~1 to 3 wt% Cr that varies little with depth. In general, concentrations above 4 wt% were considered anomalous and most transects analyzed contain maximums of 8 to 12 wt% Cr directly above the chromitite seams (James, 1957).

A geochemical survey of soils and stream sediments from the western Bushveld Complex indicates anomalous Cr concentrations above Cr-rich layers compared to surrounding lithologies. Concentrations are as much as 16 wt% Cr and are generally >0.2 wt% near chromitites (Wilhelm and others, 1997). Some areas of high Cr coincide with anomalous concentrations of gold (Au), Pd, and Pt. Wilhelm and others (1997) collected samples on a preselected grid at 1/km² sampling density, and although some locations coincide with mining activity, the anomalous signatures also exist in unmined areas. In comparison, soils above ultramafic rocks unrelated to stratiform chromite deposits have been reported with significant concentrations of Cr (0.2 to 1.8 wt%), Mn (0.1 to 0.2 wt%), and Ni (0.2 to 7.3 wt%) (Oze and others, 2004 a,b; Garnier and others, 2006, 2009).

The chemistry of water samples collected near the Stillwater Complex in the 1980s was described by Nigbor and others (1985). The samples were collected before active modern mining of PGEs by the Stillwater Mining Company, but after earlier mining of Cr (3 mines), Ni-Cu (1 mine), and PGMs (1 mine) had ceased. The concentrations of Cr were below 50 µg/L in surface waters not impacted by early mining, which conforms with the World Health Organization (WHO) drinking water guideline (table 30). Results did indicate, however, high Cd concentrations (≤30 µg/L) in samples both upstream of mines and in areas not affected by mining, suggesting a naturally high background (Nigbor and others, 1985).

Past and Future Mining Methods and Ore Treatment

Stratiform chromite deposits are mined using predominantly underground mining methods, although some surface mining has occurred. Various underground mining methods are used; some examples follow. The shallow dipping chromite seams of the Great Dyke deposit were mined by a long wall underground method; some small open-pit methods were also used locally (James, 1957). In a 1994 report on mining at the Great Dyke mine, a new mining technique, using a wire cutting technique developed by the stone cutting industry and applied to mining narrow orebodies of gold, was employed to excavate the narrow chromitite seams (Roberts, 1994). Underground mining at the Bushveld Complex, on the other hand, is commonly done by the room and pillar mining method (Pickering, 2004). The Mouat mine of the Stillwater Complex, operated during World War II and the Korean War, used the shrinkage stope method to remove ore underground (Price, 1963).

Table 30. Environmental guidelines for chromium in various media.

[mg/L, milligrams per liter; mg/kg, milligrams per kilogram; USEPA, U.S. Environmental Protection Agency; WHO, World Health Organization; CCME, Canadian Council of Ministers of the Environment; CMC, criterion maximum concentration; CCC, criterion continuous concentration; TEC, threshold effects concentration; ISQG, interim sediment quality guideline; PEL, probable effects level; PEC, probable effects concentration]

Medium/criterion	Units	Cr total	Cr(III)	Cr(VI)	Source
Human health					
Drinking water	mg/L	100			USEPA (2009a)
	mg/L	50			WHO (2008)
	mg/L	50			CCME (2008)
Residential soil	mg/kg		120,000	0.29	USEPA (2009a)
	mg/kg	64		0.4	CCME (1999a)
Industrial soil	mg/kg		1,500,000[a]	5.6	USEPA (2009a)
	mg/kg	87		1.4	CCME (1999a)
Aquatic ecosystem health					
Surface water (acute: CMC)	mg/L		570[b]	16	USEPA (2009b)
Surface water	mg/L		8.9	1	CCME (1999b)
Surface water (chronic: CCC)	mg/L		74[b]	11	USEPA (2009b)
Sediment TEC	mg/kg	43.4			MacDonald and others (2000)
Sediment ISQG	mg/kg	37.3			CCME (1999c)
Sediment PEC	mg/kg	111			MacDonald and others (2000)
Sediment PEL	mg/kg	90			CCME (1999c)
Saltwater (acute)	mg/L			1,100	USEPA (2009b)
Saltwater	mg/L		56	1.5	CCME (1999b)
Saltwater (chronic)	mg/L			50	USEPA (2009b)

[a]Values in excess of 1,000,000 mg/kg for same contaminants are used by the USEPA for risk screening purposes.

[b]Hardness-dependent water-quality standards; value is based on a hardness of 100 mg/L $CaCO_3$; CMC (dissolved) = $\exp\{0.8190[\ln(\text{hardness})]+3.7256\}$ (0.316); CCC (dissolved) = $\exp\{0.8190[\ln(\text{hardness})]+0.6848\}$ (0.860).

Once mined, the chromite ore goes through various stages of processing, with the beginning step typically hand-sorting and screening. Fine material and coarse material, which have been crushed and ground, are separated either by gravity or electromagnetic methods. The concentrate is then sent to one of three types of beneficiation plants for processing.

Most of the world's chromite (~95 percent) is concentrated and then smelted by electric furnaces to make ferrochromium for use in stainless steel, other alloys, and Cr metal (International Chromium Development Association (ICDA), 2010). High temperature reduction of chromite is accomplished by smelting and produces alloys of Fe, Cr, Si, and C in various ratios, along with minor impurities, such as, sulfur, phosphorus, and titanium. Chromite smelting products include high-C ferrochromium, low-C ferrochromium, and ferrochromium-silicon ferroalloys (Boyle and others, 1993).

High-C ferrochromium is conventionally produced in electric arc furnaces. Chromite ore is combined with a reductant, such as coke, and fluxes, such as silica (quartzite or gravel), dolomite for addition of MgO, limestone for addition of CaO, and corundum, bauxite, or other aluminosilicates for Al_2O_3 additions. Typically, there is an optimal particle size for the chromite feed; particles need to be small enough to facilitate the upward escape of furnace gases during smelting, but not so small that they are blown about within the furnace and lost to the environment or slag. Commonly, chromite fines are made into briquettes by adding binding agents or pelletized with a flux and coke or coal reductant. The use of plasma arc furnaces eliminates the need to limit the minimum particle size used in the feed, and chromite fines can then be efficiently processed (Boyle and others, 1993).

In addition to high-C ferrochromium, chromite smelting products include low-C and medium-C ferrochromium and ferrochromium-silicon products. First, high-C ferrochromium can be refined with oxygen in top- or bottom-blown converters to lower the amount of C in the product. A less expensive method is to produce ferrochromium-silicon, which can be used as an end-product or refined to low-C ferrochromium. Ferrochromium-silicon is manufactured by combining chromite ore, silica, and a reductant (coke), and then smelting it in an electric arc furnace. Also, high-C ferrochromium can be resmelted with silica and coke, or molten high-C ferrochromium can be combined with silicon metal or ferrosilicon to produce ferrochromium-silicon. The most common method to create low-C or medium-C ferrochromium is through a process called basic Perrin. Some modifications to this method have been employed, but the method generally includes Cr-rich slag, that is produced in an open-arc furnace from the addition of chromite and lime, and then mixed with an intermediate alloy from refining ferrochromium-silicon in a ladle. One other method also exists that does not rely on silicon as the driver of the reactions. In this method, high-C ferrochromium is mixed with high

purity silica sand and solid metal oxide, such as FeCr powder; the mixture is then briquetted, dried, and heated in a vacuum to 1,370 °C (Boyle and others, 1993).

Concentrate which is not smelted for ferrochromium production may be processed by kiln roasting and dissolution to make Cr chemicals. This makes up ~2 percent of the world's chromite production (ICDA, 2010). The beneficiation process to make Cr chemicals involves an end product of sodium chromate or sodium dichromate. The waste generated by this process is termed COPR, and large quantities of this have been, and are still being, generated at numerous urban sites. Details of the beneficiation process in two former producing areas are presented below, because wastes in these areas have environmental impacts discussed in detail in subsequent sections.

Some of the earliest processing occurred at numerous plants in Hudson County, New Jersey between 1905 and 1976 (Burke and others, 1991). The ore, which was imported from around the world, contained between 45 to 50-percent Cr and was pulverized, mixed with lime and soda ash, and heated at 1,100 to 1,150 °C to convert Cr(III) to the more soluble Cr(VI). The hexavalent Cr, as sodium chromate, was leached and crystallized after acidification to sodium dichromate. The remaining material was reprocessed a second time before being discarded as waste. Another early production area was in the United Kingdom, where the ore was processed in a similar manner to methods used in New Jersey. From 1830 to 1968, the processing of chromite ore in Glasgow, Scotland, involved grinding and mixing ore with alkali carbonate (K_2CO_3 and (or) Na_2CO_3) and lime or dolomite and roasting to 1,150 °C to oxidize Cr(III) to Cr(VI). The soluble Cr(VI) was leached out with water and precipitated as dichromate (Farmer and others, 1999). This beneficiation process, which involves lime or dolomite, is no longer used in the USA or in Scotland but is still actively used in other parts of the world such as China, Russia, Kazakhstan, India, and Pakistan, accounting for ~60 percent of global sodium dichromate production. The remaining processing plants employ similar methods without the addition of lime or dolomite (Darrie, 2001).

In addition to metallurgical and chemical beneficiation, chromite ore is processed by milling and sizing to make Cr-containing refractory products and foundry sands (Papp, 2007). About 3 percent of the world's production of chromite is accounted for by this process (ICDA, 2010).

Chromite ore-processing facilities are commonly near or at the mine sites, although some plants are fed by several mines. Chromite ore producers are among the leading ferrochromium producers. Some chromite ore is transported to, and processed in, other locations. For example, the United States does not produce significant amounts of chromite ore, but U.S. industries import vast quantities of chromite ore to produce ferrochromium, Cr chemicals, and chromite refractories (Papp and Lipen, 2001). In addition, stainless steel production commonly occurs in geographically different regions than ferrochromium production, resulting in shipment of material over long distances (Papp, 2007).

Volume of Mine Waste and Tailings

The amount of mine waste ultimately depends upon the grade and size of the deposit, and the amount of waste rocks that must be removed to access the ore. Typical grades for stratiform chromite deposits range between 25- and 55-percent Cr_2O_3 (Cawthorn and others, 2005), which translates to roughly 40- to 80-percent chromite. Thus, 20 to 60 percent of the material mined is waste. It is estimated that 7.6 million tons of solid waste including overburden material, waste rock, and subgrade ore has been generated by opencast mining in the Sukina ultramafic belt, India, although there is ongoing debate as to whether this belt is podiform or stratiform in type (Tiwary and others, 2005).

Throughout the world, millions of tonnes of COPR have been deposited in populated areas. It estimated that 2 to 3 million tons of COPR was generated between 1905 and 1976 from three chromite ore-processing plants in Hudson Country, New Jersey (Burke and others, 1991). The amount of COPR produced was 1.5 times that of the chromite product. COPR was also deposited in Maryland, Ohio, and New York; about 1 million tonnes of COPR was disposed of at a marine terminal in Baltimore, Maryland alone (Moon and others, 2006). Approximately 2.5 million tonnes of COPR was generated from 1830 to 1968 in Glasgow, Scotland (Farmer and others, 1999). Also in the United Kingdom, several hundred thousand tonnes of waste were generated between 1880 and 1968 at a chromite ore-processing facility in Little Lever, England (Breeze, 1973). However, chromite ore processing has ceased in the United States and United Kingdom. This is in contrast to China, which currently produces about 1 million tonnes of COPR each year, totaling over 6 million tonnes to date (Wang and others, 2007).

Mine Waste Characteristics

Chemistry

Total chromium and hexavalent Cr are the most common constituents reported in mine waste from stratiform chromite deposits (table 31). The concentrations of Cr(VI) for all mine waste in table 31 exceed the environmental guidelines for residential and (or) industrial soils shown in table 30. Most research has focused on characterizing COPR, although two studies reported between 0.4 and 11 wt% total Cr for overburden waste material from the Sukinda mine area, excluding one anomalous oxidized ore sample with 22 wt% Cr (Godgul and Sahu, 1995; Tiwary and others, 2005; table 31). In the Sukinda mine overburden, Ni and Zn reached 16,800 mg/kg and 843 mg/kg, respectively (Tiwary and others, 2005). No published data on tailing or slag chemistry from stratiform Cr ore processing have been identified.

Table 31. Concentrations of total chromium and Cr(VI) in mine waste from stratiform chromite deposits.

[All Cr(VI) concentrations reported exceed a soil environmental guideline (table 30). wt%, weight percent; mg/kg, milligrams per kilogram; <, less than; –, not reported or not analyzed; COPR, chromite ore-processing residue]

Sample type	Location	Statistic	Chromium (wt%)	Cr(VI) (mg/kg)	Reference
Overburden waste	Sukinda, India	n=3	3.7–6.5	–	Tiwary and others (2005)
Overburden waste	Sukinda, India	n=17	0.37–22	–	Godgul and Sahu (1995)
COPR	Glasgow, Scotland	n=15 averages	0.02–1.4	<5–2,900	Bewley and others (2001)
COPR	Glasgow, Scotland	n=5	0.06–1.6	–	Deakin and others (2001)
COPR soil	Glasgow, Scotland	n=3 sites	0.9–2.5	290–4,700	Farmer and others (1999)
COPR	New Jersey, U.S.	n=1	2.1	0.56	Moon and others (2008)
COPR	New Jersey, U.S.	n=3	1.6–2.8	590–2,100	Dermatas and others (2006a)
COPR	New Jersey, U.S.	n=6	1.7–2.3	590–2,100	Dermatas and others (2006b)
COPR soil	New Jersey, U.S.	n=2	0.18–1.0	105–460	James (1994)
COPR soil	New Jersey, U.S.	n=1	2.6	–	Weng and others (2002)
COPR	Mid-Atlantic coast of U.S.	n=1	2.8	4,900–7,700[a]	Tinjum and others (2008)
COPR	China	n=1	3.9	10,700	Wang and others (2007)

[a]Range for various particle size fractions.

The chromium concentrations and geochemistry of COPR bear significantly on the environmental behavior of this significant waste type. The COPR in Hudson County, New Jersey, contains between 2- and 7-percent Cr according to Burke and others (1991). Moon and others (2007b) reported as much as 5 wt% Cr, with Cr(VI) concentrations of <2 wt% for COPR from New Jersey; the chemistry of one of their samples is given in table 31 (Moon and others, 2008). For material from this same area, Dermatas and others (2006b) reported total Cr of 1.7 to 2.3 wt% and Cr(VI) from 590 to 2,100 mg/kg (table 31); hexavalent Cr makes up between 3 and 13 percent of the total Cr. Dermatas and others (2006a) reported 1.6 to 2.8 wt% total Cr. Tinjum and others (2008) reported a total Cr concentration of 2.8 wt% and an average of 6,100 mg/kg Cr(VI) for various particle sizes of COPR from the mid-Atlantic coast of the U.S. (table 31). The COPR material is highly alkaline (pH 8 to 13). Soils at COPR sites in New Jersey are also reported to contain variable concentrations of chromium. James (1994) reported 0.18 to 1.0 wt% total Cr and 105 to 460 mg/kg Cr(VI) for two surface soils (table 31). Wang and others (2002) reported total Cr of 2.6 wt% for a surface soil sample. At least 15 percent of soil samples collected from numerous COPR-contaminated areas in Hudson County are reported to contain >1 wt% Cr, with hexavalent Cr making up 1 to 50 percent of the total Cr (Burke and others, 1991).

Chromite ore-processing residues from a factory in Glasgow, Scotland, were used extensively as land infill material, and contain 4 to 6 wt% Cr (Geelhoed and others, 2002). At the same site, Deakin and others (2001) reported lower total Cr concentrations of 0.06 to 1.6 wt%. Soils in COPR disposal areas contain as much as 2.5 wt% total Cr; individual colored nodules within the soils contain up to 3.6 wt% Cr (Farmer and others, 1999). Farmer and others (1999) also reported that 49 to 98 percent of the total Cr is present as Cr(VI) (table 31). For similar types of soils in the Glasgow area, Bewley and others (2001) reported average

Cr concentrations ranging from 0.02 to 1.4 wt% and average Cr(VI) concentrations ranging from <5 to 2,900 mg/kg. The pH of leachate associated with this material is alkaline— nearly 12 (Geelhoed and others, 2002). For comparison, a sample of COPR produced by a chemical plant in Henan, China, contains ~4 wt% Cr and 1 wt% Cr(VI) (Wang and others, 2007; table 31).

As stated in the preceding discussion, the production of sodium dichromate is dominated by processes using lime or dolomite, and the sites previously mentioned reflect the chemistry of the waste product (COPR) from this process. The remaining facilities producing sodium dichromate do not use lime or dolomite in the processing of ores. The wastes generated at these facilities generally contain less Cr than the lime-added process. In modern, lime-free chromite ore-processing plants, the waste generated is processed to reduce the Cr(VI) concentration to between 0.1 to 0.2 percent. This waste is then commonly treated with ferrous iron or sulfur-containing reducing agents to reduce the Cr(VI) to concentrations of <1 mg/kg (Darrie, 2001).

Platinum-group minerals are associated with the chromitite layers in the Bushveld Complex. Because these minerals occur between chromite grains, are very fine grained, and are associated with base-metal sulfides, they concentrate together with silicate impurities in tailings (Von Gruenewaldt and Hatton, 1987). The sum of PGE concentrations in tailings from the Bushveld Complex ranges from 1.02 to 10.4 mg/kg. In general, the order of abundance is Pt, Ru >Pd >Rh; many of the platinum group elements are recovered from the tailings for a profit. In the late 1980s, Von Gruenewaldt and Hatton (1987) estimated that the tailings dumps in the Bushveld Complex contain ~11,300 kg of PGE with about 1,100 kg added annually. Copper (Cu) (as much as 130 mg/kg) and Ni (as much as 440 mg/kg) are also found in the tailings.

Mineralogy

A significant amount of research has been done characterizing the mineralogy of COPR, and findings are detailed below. In contrast, little to nothing has been published on the mineralogy of slags or tailings produced by the processing of stratiform chromite ores.

The mineralogy of COPR from Glasgow, Scotland, is generally >10 wt% Cr(VI)-bearing hydrogarnet, brownmillerite, and glass, with lesser amounts (~5 to 10 wt%) of brucite, periclase, Cr(VI)-bearing hydrocalumite, calcite, and chromite (Geelhoed and others, 2001; Thomas and others, 2001). In addition to these phases, minor amounts of aragonite, larnite, and ettringite may also be present (Hillier and others, 2003). The significant amount of amorphous material contained in the COPR (for example, glass) is likely Cr-poor. The minerals present can be characterized as primary ore minerals (chromite), high temperature minerals which likely formed during roasting (brownmillerite, larnite, and periclase), and minerals formed from leaching and weathering (brucite, calcite, aragonite, ettringite, hydrocalumite, hydrogarnet). Of the total Cr present, most is present as Cr(III), with ~60 to 70 percent of total Cr in refractory chromite, and ~15-percent total Cr in brownmillerite. The remaining 20 to 25 percent of Cr is present as Cr(VI) in hydrogarnet and hydrocalumite. Minor amounts of Cr(VI) can also be present in ettringite (Hillier and others, 2003).

Similar mineral assemblages were reported for COPR from New Jersey and Maryland (Moon and others, 2007a). The authors of this study reported the major minerals as brownmillerite, periclase, and lime (CaO), and the weathering products as hydrogarnet, hydrotalcite, brucite, and hydrated lime. Ettringite may also form, which can cause heaving of waste piles. Quantitative mineralogy for one sample of COPR from New Jersey was reported in Moon and others (2008): they reported that 42 wt% of the sample is amorphous, 27 wt% is brownmillerite, 9 wt% is calcite, and the following list of minerals are 5 wt% or less: brucite, hydroandradite, katoite, periclase, quartz, quinitinite-2H, sjoegrenite, albite, and calcium-aluminum oxide chromium hydrate. The amorphous material is likely to be predominantly calcium silicate hydrates (Dermatas and others, 2006a). Mineralogy presented by Dermatas and others (2006b) is consistent with the findings of Moon and others (2007a, 2008); a few differences include more brownmillerite (38 to 46 wt%) and hydrogarnet (9 to 10 wt%), less calcite (2 wt%), and the presence of hydrotalcite (4 wt%), and locally ettringite (2 wt%), and afwillite (2 wt%). Chromium salts in COPR from New Jersey have been identified as calcium chromate ($CaCrO_4$), tribasic calcium chromate $[Ca_3(CrO_4)_2]$, calcium aluminochromate ($Ca_3Al_2O_6 \cdot CaCrO_4$), and basic ferric chromate $[FeCrO_4(OH)]$ (Burke and others, 1991).

Acid-Base Accounting

Acid-base accounting is rarely reported for stratiform chromite mine waste. A few examples are reported below. In general, COPR is a highly alkaline material due to the addition of lime or dolomite during the processing of the ore. As a result, the pH of COPR material is generally between 8 and 13. The acid neutralization capacity for a sample of COPR from New Jersey is ~5 eq kg^{-1} of acidity to attain a pH of 9 from an initial pH of 12.5 (Moon and others, 2008). Experiments by Tinjum and others (2008) illustrated that a very large amount of acid (8 mol HNO_3) was required to lower the pH of 11.7 of mid-Atlantic COPR to near neutral (pH 7.5). This is less than the 13 mol H$^+$/kg that was reported by Geelhoed and others (2002) for COPR from Glasgow. Despite differences in analytical procedures used in the determination described above, these studies indicate that COPR has a high acid neutralizing capacity. This fact is relevant when remediation strategies are evaluated due to the pH-based speciation and related toxicity of Cr.

Element Mobility Related to Mining in Groundwater and Surface Water

Chromite, the dominant chromium host in stratiform chromite deposits, is a mineral that is refractory and extremely resistant to alteration, which greatly inhibits its mobility to ground and surface waters. Trivalent Cr in chromite is more stable under reducing and acidic conditions, whereas the more toxic hexavalent form is stable under oxidizing and alkaline environments (fig. 78). Pore waters are commonly alkaline in the ultramafic rock that hosts the stratiform chromite deposits. Alkalinity decreases with increased Fe(III) content from the oxidation of Fe(II); this oxidation thereby increases the leaching and removal of basic hydroxides. The oxidation of Fe(II) and alkaline conditions of the ultramafic rocks indicate a potential conversion of Cr(III) to Cr(IV) at the chromite-water interface. Mining practices that enhance oxidation may exacerbate this conversion and enhance the release of toxic Cr(VI) into adjacent ground and surface water (Godgul and Sahu, 1995).

The mining of altered and lateritized (oxidized) chromite deposits in Sukinda, India, for example, has mobilized Cr into surface and groundwaters (Godgul and Sahu, 1995; Tiwary and others, 2005). Although there is debate over the genetic classification of the Sukinda deposits (either stratiform or podiform chromite), the environmental behavior of the deposit is relevant to any ultramafic hosted chromite deposit; thus, it is included in this discussion. The chromite contains microfractures from the weathering of interstitial materials surrounding the chromite grains. Because the chromite-bearing ultramafic rocks have been altered, Al, Mg, and Si

have been leached and Fe(II) oxidized. The friable texture of the chromite grains and release of surrounding cations in its structure indicate that Cr(III) could leach into the surrounding waters. Mine effluent, including drainage from quarry floors and seeps, generally contains between 17 and 480 µg/L Cr, the majority of which is commonly Cr(VI) (Godgul and Sahu, 1995; Tiwary and others, 2005; table 32). One anomalous sample with 1,791 µg/L Cr was reported by Godgul and Sahu (1995), where all of the Cr in the sample is Cr(VI) (table 32). Groundwater, including that from village wells, generally contains <50 µg/L total Cr, which conforms with the WHO drinking water guideline (table 33); but one sample did contain 450 µg/L Cr(VI) from a bore hole (Godgul and Sahu, 1995; Tiwary and others, 2005). The groundwater samples contain mixed proportions of Cr(III) to Cr(VI) (table 32) because Cr is likely scavenged when groundwater percolates through the laterite (Godgul and Sahu, 1995). In general, surface water downstream of mine effluent contains higher Cr than the groundwater samples, with as much as 146 µg/L Cr, most of which is Cr(VI) (table 32). Many of the concentrations of total Cr and Cr(VI) in the Sukinda chromite deposits exceed aquatic toxicity guidelines (table 32). In addition, the near neutral to slightly acidic pH and reducing potential from dense vegetation surrounding the rivers may discourage the stability of mobile Cr(VI) (Godgul and Sahu, 1995). Leachate tests on overburden waste material suggest that it is the likely source of the Cr in the ground and surface waters (Tiwary and others, 2005).

Soil samples from a COPR disposal site in Hudson Country, New Jersey, contain ~2.5 wt% Cr. The soils were leached using simulated rainwater with a wide range of pH values (Weng and others, 1994), and at various temperatures for the pH 4.3 water (Weng and others, 2002). These experiments showed that significant amounts (about 1 percent of the total Cr content) of Cr(VI) leached out at pH values of 4.5 and 12 and at the warmer temperatures (23 and 38 °C). The results of the experiments also indicate that most of the Cr in the soil is the less-leachable trivalent chromium, and trivalent chromium only leaches out in solutions with a pH <5 (Weng and others, 1994). Under acidic soil conditions, Cr(VI) is reduced to Cr(III) by Fe(II) or organic matter and adsorbed. Organic matter is also capable of reducing Cr(VI) to Cr(III) at neutral and high pH values (Weng and others, 1994). Alkaline and warm conditions, however, increase the potential for Cr(VI) to be leached (Weng and others, 1994, 2002). The leaching of Cr(VI) from these soils after decades suggests that there is a slow and continuous oxidation of Cr(III) to Cr(VI) and leaching by rainfall (Weng and others, 2002). Another indicator of the mobility of Cr(VI) from the New Jersey soils is the presence of chromate salt phases, such as $CaCrO_4$, on the soil surface during dry periods of evaporation (James, 1994). These salts then disappear after rain events. Burke and others (1991) also noted that surface enrichment in Cr due to the upward

mobility of these salts via capillary action is dependent on meteorological conditions, because the soluble salts leach Cr(VI) into surface water and groundwater. Groundwater associated with COPR has been reported to contain 30 mg/L Cr.

The COPR has also been studied as a possible source of Cr(VI) in surface water and groundwater in Glasgow, Scotland (Geelhoed and others, 2001). Leaching of a COPR sample with an amount of solution equivalent to four years of rainfall yielded a leachate containing Cr(VI) concentrations almost 100 times greater than the WHO drinking water guideline of 50 µg/L (Geelhoed and others, 2001; World Health Organization, 2008). As was reported for leaching tests on COPR from New Jersey, COPR from Glasgow leached the highest amounts of Cr(VI) at high pH values, where mineral solubility is thought to control concentrations (Geelhoed and others, 2002). At neutral and low pH values, Cr(VI) concentrations were likely controlled by sorption, and only Cr(III) was present at low pH (pH < 4) (Geelhoed and others, 2002). At sites where COPR was used as landfill in Glasgow, groundwaters contain as much as 91 mg/L Cr, far exceeding the drinking water guideline, and surface waters contain as much as 6.5 mg/L Cr (Farmer and others, 2002; table 32). Whalley and others (1999) reported groundwater concentrations of 169 mg/L total Cr and 153 mg/L Cr(VI), and surface water concentrations of as much as 6.2 mg/L Cr(VI). Water pH ranged from 7.5 to 13 and Cr was predominantly in the hexavalent form as CrO_4^{2-} (Whalley and others, 1999; Farmer and others, 2002). Pore waters extracted from the COPR contained as much as 125 mg/L Cr ,with the majority in the hexavalent form (Farmer and others, 2002; table 32).

In addition to the leaching of Cr from COPR in Glasgow, Scotland, waste from a chromite ore-processing plant that operated from 1880 to 1968 in Little Lever, England, is a source of Cr in surface waters (Breeze, 1973). The waste material, reaching 100,000 tonnes, leaches an estimated 3 to 5 tonnes of soluble Cr every year into the nearby Croal River. The concentration of Cr is between 0.2 and 0.5 mg/L in the river, 1.5-km downstream of the waste piles; these concentrations exceed drinking water and some aquatic ecosystem guidelines. Based on leaching tests, the waste material contains as much as 6,000 mg/kg soluble Cr (Breeze, 1973).

Surface water chemistry collected downstream of chromite and asbestos mine dumps in Zimbabwe was reported by Meck and others (2006) (table 32). The concentrations of Cr (average of 2,200 µg/L), as well as of Ni (average 160 µg/L), Pb (average of 80 µg/L), and Cd (average 40 µg/L), exceed both WHO drinking water and USEPA aquatic toxicity guidelines. The concentrations of Cu (average of 130 µg/L) exceed aquatic toxicity guidelines; the concentrations of Sb (average of 960 µg/L) exceed drinking water guidelines. Currently, rural communities in Zimbabwe use stream water as a drinking water source (Meck and others, 2006).

Table 32. Dissolved metal concentrations in waters from or downstream of stratiform chromium deposits.

[Concentrations in micrograms per liter. Values that exceed drinking water or aquatic ecosystem guidelines are in bold (tables 30 and 33); avg, average; std dev, standard deviation; ~, approximate; n.r., not reported or not analyzed; n.d., not detected; COPR, chromite ore-processing residue; < less than]

Mining/processing area	Water type	Water source	Statistic	pH	Cr[a]	Cr(VI)	Reference
Zimbabwe	Surface water	Downstream of waste dumps	avg ± std dev	neutral (~10)	**2,200±1,553**	n.r.	Meck and others (2006)
Sukinda (India)	Surface water	River downstream of mine effluent	range (n=4)	7.5–8.2	**17–68**	n.d.–**64**	Godgul and Sahu (1995)
Sukinda (India)	Surface water	Floor of mine quarry	range (n= 8)	7.0–8.9	**17–1,791**	n.d.–**1,791**	Godgul and Sahu (1995)
Sukinda (India)	Groundwater	Village wells	range (n=3)	7.0–7.3	17	n.d.–**17**	Godgul and Sahu (1995)
Sukinda (India)	Surface water	River downstream of mine effluent	range (n=4)[b]	6.5–7.6	**49–146**	**23–104**	Tiwary and others (2005)
Sukinda (India)	Surface water	Mine effluent	range (n=9)[b]	6.1–7.6	**55–480**	**20–125**	Tiwary and others (2005)
Sukinda (India)	Groundwater	Shallow and deep wells	range (n=11)[b]	5.6–7.4	9–43	n.d.–**450**	Tiwary and others (2005)
Stillwater (Montana, USA)	Surface water	Baseline streams	maximum	n.r.	<50	n.r.	Nigbor and others (1985)
Stillwater (Montana, USA)	Surface water	Downstream of mine waste	maximum	n.r.	**140**	n.r.	Nigbor and others (1985)
Stillwater, Montana, USA)	Surface water	Adits	maximum	n.r.	82	n.r.	Nigbor and others (1985)
Glasgow (Scotland)	Surface water	Sites where CORP used at landfill	range	7.8–8.2	**110–6,300**	**160–6,500**	Farmer and others (2002)
Glasgow (Scotland)	Groundwater	Sites where CORP used at landfill	range	7.1–12.5	**<10–91,000**	**<10–82,000**	Farmer and others (2002)
Glasgow (Scotland)	Pore water	Pore water extracted from COPR	range	11.1–12.3	**7,400–125,000**	**7,000–79,500**	Farmer and others (2002)
Glasgow (Scotland)	Groundwater	Under COPR landfill	n=1	13	**169,000**	**153,000**	Whalley and others (1999)
Glasgow (Scotland)	Surface water	Directly downstream from CORP landfill	range (2 sites)[c]			**3,100–6,200**	Whalley and others (1999)
Glasgow (Scotland)	Surface water	Downstream from CORP drainage	n=13	n.r.	**<7–1,100**	n.r.	Whalley and others (1999)

[a]Freshwater criterion for Cr are hardness dependent and calculated based on a hardness of 100 mg/L CaCO₃.

[b]Results include some sites sampled both pre and postmonsoon season. Fe, Cu, and total Cr are for postmonsoon season sampling only.

[c]Each site was sampled on numerous occasions.

Table 33. Environmental guidelines relevant to mineral deposits exclusive of chromium.

[mg/kg, milligrams per kilogram; µg/L, micrograms per liter; mg/L, milligrams per liter; USEPA, U.S. Environmental Protection Agency; WHO, World Health Organization]

Element	Human Health			Drinking water µg/L	Aquatic Acute toxicity µg/L	Ecosystem Chronic toxicity µg/L
Media Units	Residential soil mg/kg	Industrial soil mg/kg	Drinking water µg/L			
Source	USEPA (2009a)			USEPA (2009b)	WHO (2008)	USEPA (2009b)
Al	77,000	990,000	200		750	87
As	23	160	10	10	340	150
Cd	70	810	5	3	2[a]	0.25[a]
Cu	3,100	41,000	1,300	2,000	13[a]	11[a]
Fe	55,000	720,000	300			1,000
Hg	6.7	28	2	6	1.4	0.77
Mn	1,800	23,000	50	400		
Mo	390	5,100		70		
Ni	1,600	20,000		70	470[a]	52[a]
Pb	400	800	15	10	65[a]	2.5[a]
Se	390	5,100	50	10		5
U	230	3,100		15		
Zn	23,000	310,000	5,000		120[a]	120[a]

[a]Hardness-dependent water-quality standards; value is based on a hardness of 100 mg/L $CaCO_3$.

Water samples collected near the Stillwater Complex in the 1980s, before active modern PGE mining, but after early mining had ceased, contain concentrations of Cr reaching 140 µg/L downstream of mine waste (Nigbor and others, 1985; table 32). Waters collected from one inactive adit contain 82 µg/L Cr. Furthermore, the concentrations of Fe, Mn, and Se in water from at least one adit exceed USEPA water quality criteria (Nigbor and others, 1985).

Overall, the concentrations of total Cr and hexavalent Cr commonly exceed either drinking water or aquatic ecosystem guidelines, indicating significant mobility of Cr from stratiform chromite deposit mine waste (table 32).

Smelter Signatures

Smelters in northern Sweden process ore from the Kemi deposit, located in Finland, and contribute to airborne Os based on chemical and isotopic studies of lichen, a bioindicator (Rodushkin and others, 2007). This suggests that the Os is released in the form of OsO_4, a toxic air contaminant. Although gaseous Os located 1 km from smelting operations is below regulatory limits, there may be health effects from chronic long-term exposure (Rodushkin and others, 2007). Another study found elevated Cr concentrations in mosses, another bioindicator, surrounding the Kemi deposit ore-processing facilities, including a refined steel plant in Finland (Poikolainen and others, 2004).

Pit Lakes

Data were not available on pit lakes from the mining of stratiform chromite deposits.

Ecosystem Issues

Dissolved chromium and other toxic metals in surface waters is a major threat to aquatic ecosystems which surround waste rock and tailings from stratiform chromite mining. The toxicity of Cr, and other metals such as Cd, Cu, Pb, Ni, Ag, and Zn, to aquatic ecosystems is dependent on water hardness; higher concentrations of metals are needed to exceed toxicity limits at higher hardness values (U.S. Environmental Protection Agency, 2009b). Hardness is a measure of the concentrations of calcium (Ca) and Mg. The hardness is expressed in terms of an equivalent concentration of $CaCO_3$, typically in milligrams per liter. The USEPA has presented hardness-dependent expressions for both acute (1-hour exposure) and chronic (4-day exposure) toxicity (U.S. Environmental Protection Agency, 2009b; tables 30 and 33).

For stratiform chromite deposits, the ecosystem threats are greatest from dissolved hexavalent chromium. Chromium from chromite has limited solubility except under acidic conditions (fig. 76), and chromium occurs in the trivalent state, which has much lower toxicity to aquatic organisms (table 30). Furthermore, because of the high Eh of the $Cr(VI)/Cr(OH)_3$ oxidation-reduction couple, few naturally occurring oxidants are available to oxidize Cr(III) to Cr(VI) (fig. 78). Chief among these naturally occurring oxidants are manganese oxides and dissolved oxygen (Rai and others, 1989; Oze and others, 2007). Manganese oxides can oxidize Cr(III) rapidly, whereas the rate of oxidation by dissolved oxygen is slow (Rai and others, 1989; Saleh and others, 1989; Ball and Izbicki, 2004; Oze and others, 2007). Thus, dissolved oxygen may not be an effective oxidant of Cr(III) in mine settings unless mine-waste leachate enters groundwater aquifers with long residence times, and then later reenters the surface-water environment. In contrast, chromium in leachate from chromite ore-processing residues, which may or may not be near the

site of initial mining, is likely to be in the hexavalent form and may pose significant environmental challenges. In terms of sediment toxicity to aquatic organisms, threshold and preliminary effects concentrations (TECs and PECs, respectively) are based on total chromium concentrations. However, laboratory bioassay studies have demonstrated that sediment toxicity is primarily due to hexavalent chromium and that acid-volatile sulfide (AVS) and organic matter can effectively reduce hexavalent chromium to the less toxic trivalent form (Berry and others, 2004; Besser and others, 2004). In fact, no-effects chromium concentrations have been estimated as high as 1,310 mg/kg Cr on the basis of laboratory bioassays results from sediments downstream of a COPR site; the limited toxicity of chromium was attributed to the mitigating effects of AVS (Becker and others, 2006).

Acidic mine drainage and associated dissolved metals may be only a minor concern at stratiform chromite mines due to the low concentrations of sulfide minerals in the ores coupled with the acid-neutralizing potential of silicate minerals, such as olivine, orthopyroxene, and plagioclase feldspar. However, in layered mafic-ultramafic complexes with higher accumulations of sulfide minerals due to Ni-Cu and PGM mineralization, dissolved Fe, Cu, and Ni may be additional concerns (Campbell and Murck, 1993).

Human Health Issues

Human health concerns associated with stratiform chromite deposits and their associated mine wastes also center around chromium and its oxidation state. Hexavalent chromium is 10 to 1,000 times more toxic to humans than trivalent chromium, depending upon pathway (Katz and Salem, 1993). The USEPA has set primary maximum contaminant limits (MCL) for total Cr and a number of other potentially relevant contaminants (U.S. Environmental Protection Agency, 2009a,b; tables 30 and 33). Trivalent chromium associated with chromite has limited solubility, generally below the MCL, except at low pH (fig. 76). Hexavalent chromium has significantly higher solubility but is unlikely to form in the vicinity of mine waste piles except where manganese oxides are present and can promote the oxidation of trivalent to hexavalent chromium. Dissolved oxygen may only be effective in oxidizing trivalent to hexavalent chromium when leachates from mine waste or tailings piles enter a groundwater system with long residence times, and this water may be used for drinking water away from the site (Ball and Izbicki, 2004). For example, in the vicinity of the Sukinda chromite mine, India, the chromium concentrations of 8 out of 14 postmonsoonal surface water and groundwater samples were above the WHO drinking standard (50 mg/L) (Tiwary and others, 2005). Likewise, surface water and groundwater in the vicinity of chromite ore-processing residue piles can have high concentrations of chromium, dominated by hexavalent chromium. Whalley and others (1999) and Farmer and others (2002) reported groundwater samples in the vicinity of COPR

piles near Glasgow, Scotland, reaching 169 mg/L total Cr (153 mg/L Cr(VI)). Soils and chromate dusts from chromite ore-processing residues also may represent significant threats to human health. Lioy and others (1992) found dusts in the vicinity of COPR piles to be an important potential pathway for affecting humans.

Climate Effects on Geoenvironmental Signatures

The understanding of the effects of various climate regimes on the geoenvironmental signature specific to stratiform chromite deposits is limited. Metal concentrations in mine drainage in arid environments may be greater than that in more temperate climates, because of the concentrating effects of mine-effluent evaporation and the resulting "storage" of metals in highly soluble chromate salts.

Knowledge Gaps and Future Research Directions

The value of hosted commodities in stratiform chromite deposits (such as PGEs, nickel, chromium, and vanadium) increases the likelihood of continued scientific investigation of their host intrusions well into the foreseeable future. In fact, much of the current research on layered mafic-ultramafic intrusions focuses on PGE mineralization. Modern technological advances, both in terms of mining and as commodity usage, will continue to drive the need for stratiform chromite ore as well as additional exploration.

The challenge for any model is to account appropriately for geochemical, field-based, and petrological constraints. In order to more fully evaluate the petrogenesis of stratiform chromite deposits, the need exists for research to further integrate detailed geological mapping, core logging and petrographic analysis with high-resolution geochemical data. For example, most of the chromitite seams of the Bushveld Complex in the Dwars River area lack primary olivine, which contradicts the classic model of Irvine (1977) where mixing of olivine- and pyroxene-saturated magmas generates the cumulus chromite (Voordouw and others, 2009). Without field evidence and relationships, geochemical data prove inadequate when attempting to understand how stratiform chromite deposits formed.

In addition, there is evidence that more than one generation of chromite exists within stratiform chromite deposits. The subsidiary chromitite seams in the Rum intrusion, for example, are thinner (~1 mm) and discontinuous compared to the main chromitite seams, which are 2- to 4-mm thick, laterally extensive, and host significant sulfide and PGE concentrations (O'Driscoll and others, 2009a). Moreover, chromite in subsidiary chromitite seams in the Rum intrusion is enriched in Mg and Al, whereas the disseminated chromite in the surrounding peridotite and troctolite is Fe- and Cr-rich. As a result, O'Driscoll and others (2009a) proposed that an

infiltrating melt dissolved and assimilated cumulus olivine and plagioclase in the preexisting, residual troctolite crystal mush. By extension, further investigation into the occurrence of secondary chromitite seams within other large-layered mafic-ultramafic intrusions would greatly enhance understanding of deposit formation and the causes of massive chromitite crystallization within these systems.

Another issue to address is the failure of petrogenetic field diagrams (Irvine, 1967; Dick and Bullen, 1984) to assess provenance in younger stratiform chromite deposits. In particular, the compositions of within-seam chromite of the Tertiary Rum intrusion are very different than the detrital chromites, which most likely originate from the disseminated chromite (Power and others, 2000). In fact, the detrital chromites plotted in the stratiform chromite field whereas the within-seam chromites plotted within the ophiolite field. Furthermore, because formation of large stratiform chromite deposits may have involved an influx of fresh magma into a mainly crystallized and highly fractionated magma chamber, the mechanisms of formation and chemistry of the parental magma of the within-seam chromite may be different from those of the disseminated chromite. In addition, disseminated chromite is more susceptible to subsolidus reequilibration than within-seam chromite, which could result in substantially different chemical compositions. One solution would be to update the petrogenetic field diagrams with current data so that the fields can be reassessed. Otherwise, petrogenetic discrimination diagrams may not be appropriate to use in provenance studies for young intrusive bodies.

References

Alapieti, T.T., Filén, B.A., Lahtinen, J.J., Lavrov, M.M., Smolkin, V.F., and Voitsekhovsky, S.N., 1990, Early Proterozoic layered intrusions in the northeastern part of the Fennoscandian Shield: Mineralogy and Petrology, v. 42, p. 1–22.

Alapieti, T.T., Kujanpää, J., Lahtinen, J.J., and Papunen, H., 1989, The Kemi stratiform chromitite deposit, Northern Finland: Economic Geology, v. 84, p. 1057–1077.

Alexander, E.C., Evensen, N.M., and Murthy, V.R., 1973, ^{40}Ar-^{39}Ar and Rb-Sr studies of the Fiskenæsset Complex, west Greenland: Eos, Transactions of the American Geophysical Union, v. 54, no. 11, p. 1227.

Allègre, C.J., and Luck, J.-M., 1980, Osmium isotopes as petrogenetic and geologic tracers: Earth and Planetary Science Letters, v. 48, no. 1, p. 148–154.

Amelin, Y.V., Heaman, L.M., and Semenov, V.S., 1995, U-Pb geochronology of layered mafic intrusions in the eastern Baltic Shield—Implications for the timing and duration of Paleoproterozoic continental rifting: Precambrian Research, v. 75, p. 31–46.

Appel, C.C., Appel, P.W.U., and Rollinson, H.R., 2002, Complex chromite textures reveal the history of an early Archaean layered ultramafic body in West Greenland: Mineralogical Magazine, v. 66, no. 6, p. 1029–1041.

Bailly, L., Auge, T., Cocherie, A., Trofimov, N.N., Golubev, A.I., Tkachev, A.V., and Cherkasov, S.V., 2009, New data on the age of the Burakovsky Layered intrusion, Karelia: Doklady Earth Sciences, v. 426, no. 4, p. 534–538.

Ball, J.W., and Izbicki, J.A., 2004, Occurrence of hexavalent chromium in ground water in the western Mojave Desert, California: Applied Geochemistry, v. 19, p. 1123–1135.

Ball, J.W., and Nordstrom, D.K., 1991, User's manual for WATEQ4F, with revised thermodynamic data base and test cases for calculation speciation of major, trace, and redox elements in natural waters: U.S. Geological Survey Open-File Report 91–183, 188 p.

Ball, J.W., and Nordstrom, D.K., 1998, Critical evaluation and selection of standard state thermodynamic properties for chromium metal and its aqueous ions, hydrolysis species, oxides, and hydroxides: Journal of Chemical and Engineering Data, v. 43, p. 895–918.

Baranov, V., 1957, A new method for interpretation of aeromagnetic maps; pseudo-gravimetric anomalies: Geophysics, v. 22, no. 2, p. 359–382.

Barbosa, J.S.F., Sabaté, P., and Dominguez, J.M.L., 1996, O Estado da Bahia na Plataforma Sul-americana, suas subdivisões, critérios de empilhamento estratigráfico das coberturas plataformais e ciclose geotectônicos, *in* Barbosa, J.S.F. and Dominguez, J.M.L., eds., Geologia da Bahia: Texto Explicativo para o Mapa Geológico ao Milionésimo: Salvador, Secretaria de Indústria Comércio e Minas/Superintendência de Geologia e Recursos Minerais, v. 2, p. 39–61.

Barnes, S.J., 1989, Are Bushveld U-type parental magmas boninites or contaminated komatiites?: Contributions to Mineralogy and Petrology, v. 101, p. 447–457.

Barnes, S.-J., and Francis, D., 1995, The distribution of platinum-group elements, nickel, copper, and gold in the Muskox Layered intrusion, Northwest Territories, Canada: Economic Geology, v. 90, p. 135–154.

Barnes, S.J., and Roeder, P.L., 2001, The range of spinel compositions in terrestrial mafic and ultramafic rocks: Journal of Petrology, v. 42, n. 12, p. 2279–2302.

Becker, D.S., Long, E.R., Proctor, D.M., and Ginn, T.C., 2006, Evaluation of potential toxicity and bioavailability of chromium in sediments associated with chromite ore processing residue: Environmental Toxicology and Chemistry, v. 25, p. 2576–2583.

Bédard, J.H., Sparks, R.S.J., Renner, R., Cheadle, M.J., and Hallworth, M.A., 1988, Peridotite sills and metasomatic gabbros in the Eastern Layered Series of the Rhum complex: Journal of the Geological Society of London, v. 145, p. 207–224.

Berry, W.J., Boothman, W.S., Serbst, J.R., and Edwards, P.A., 2004, Predicting toxicity of chromium in sediments: Environmental Toxicology and Chemistry, v. 23, p. 2981–2992.

Besser, J.M., Brumbaugh, W.G., Kemble, N.E., May, T.W., and Ingersoll, C.G., 2004, Effects of sediment characteristics on the toxicity of chromium (III) and chromium (VI) to the amphipod, *Hyallela azteca*: Environmental Science and Technology, v. 38, p. 6210–6216.

Bewley, R.J.F., Jeffries, R., Watson, S., and Granger, D., 2001, An overview of chromium contamination issues in the south-east of Glasgow and the potential for remediation: Environmental Geochemistry and Health, v. 23, no. 3, p. 267–271.

Black, L.P., Moorbath, S., Pankhurst, R.J., and Windley, B.F., 1973, $^{207}Pb/^{206}Pb$ whole rock age of the Archaean granulite facies metamorphic event in West Greenland: Nature Physical Science, v. 244, p. 50–53.

Blakely, R.J., and Simpson, R.W., 1986, Approximating edges of source bodies from magnetic or gravity anomalies: Geophysics, v. 51, no. 7, p. 1494–1498.

Blakely, R.J., and Zientek, M.L., 1985, Magnetic anomalies over a mafic intrusion—The Stillwater Complex: Montana Bureau of Mines and Geology Special Publication, v. 92, p. 39–45.

Boorman, S., Boudreau, A., and Kruger, F.J., 2004, The Lower Zone-Critical Zone transition of the Bushveld Complex—A Quantitative Textural Study: Journal of Petrology, v. 45, no. 6, p. 1209–1235.

Borradaile, G.J., Keeler, W., Alford, C., and Sarvas, P., 1987, Anisotrophy of magnetic susceptibility of some metamorphic minerals: Physics of the Earth and Planetary Interiors, v. 48, no. 1–2 , p. 161–166.

Boudreau, A.E., 1994, Mineral segregation during crystal aging in two-crystal, two-component systems: South African Journal of Geology, v. 97, no. 4, p. 473–485.

Boukili, H., Novikoff, A., and França, J., 1984, Mineralogie et géochimie des chlorites et hydroxycarbonates chromitifères de Campo Formoso, Bahia, Brésil: Cahiers ORSTOM, Série Géologie, v. 14, no. 2, p. 141–152.

Boyle, E.H., Jr., Shields, D.J., and Wagner, L.A., 1993, Chromium availability in market economy countries and network flow model analysis of world chromium supply: U.S. Bureau of Mines Information Circular 9337, 131 p.

Brandeis, G., 1992, Constraints on the formation of cyclic units in ultramafic zones of large basaltic chambers: Contributions to Mineralogy and Petrology, v. 112, no. 2–3, p. 312–328.

Breeze, V.G., 1973, Land reclamation and river pollution problems in the Croal Valley caused by waste from chromate manufacture: Journal of Applied Ecology, v. 10, no. 2, p. 513–525.

Brown, G.M., 1956, The layered ultrabasic rocks of Rhum, Inner Hebrides: Philosophical Transactions of the Royal Society of London, Series B, Biological Sciences, v. 240, no. 668, p. 1–54.

Brozdowski, R.A., 1985, Cumulate xenoliths in the Lodgepole, Enos Mountain and Susie Peak intrusions—A guide: Montana Bureau of Mines and Geology Special Publication, v. 92, p. 368–372.

Brozdowski, R.A., Ulmer, G., Bonini, W.E., and Gold, D.P., 1982, The Stillwater stratiform complex—New evidence for its northern extent: Geological Society of America, Abstracts with Programs, v. 14, p. 453.

Buchanan, D.L., Nolan, J., Suddaby, P., Rouse, J.E., Viljoen, M.J., and Davenport, W.J., 1981, The genesis of sulfide mineraliztion in a portion of the Potgietersrus Limb of the Bushveld Complex: Economic Geology and the Bulletin of the Society of Economic Geologists, v. 76, p. 568–579.

Burke, T., Fagliano, J., Goldoft, M., Hazen, R.E., Iglewicz, R., and McKee, T., 1991, Chromite ore processing residue in Hudson County, New Jersey: Environmental Health Perspectives, v. 92, p. 131–137.

Butcher, A.R., Pirrie, D., Prichard, H.M., and Fisher, P., 1999, Platinum-group mineralization in the Rum layered intrusion, Scottish Hebrides, UK: Journal of the Geological Society of London, v. 156, p. 213–216.

Calas, G., Manceau, A., Novikoff, A., and Boukili, H., 1984, Chromium behavior in alteration minerals of the Campo Formoso chromite deposit, Bahia, Brazil: Bulletin de Mineralogie, v. 107, no. 6, p. 755–766.

Cameron, E.N., 1964, Chrome deposits of the eastern part of the Bushveld Complex, *in* Haughton, S.H., ed., The Geology of Some Ore Deposits in Southern Africa: Geological Society of South Africa Special Publication, v. 2, p. 131–168.

Cameron, E.N., 1977, Chromite in the central sector of the Eastern Bushveld Complex, South Africa: American Mineralogist, v. 62, p. 1082–1096.

Cameron, E.N., 1978, The Lower Zone of the Eastern Bushveld Complex in the Olifants River Trough: Journal of Petrology, v. 19, p. 140–150.

Cameron, E.N., 1980, Evolution of the Lower Critical Zone, central sector, eastern Bushveld Complex, and its chromite deposits: Economic Geology, v. 75, p. 845–871.

Cameron, E.N., 1982, The Upper Critical Zone of the Eastern Bushveld Complex—Precursor of the Merensky Reef: Economic Geology, v. 77, p. 1307–1327.

Cameron, E.N., and Desborough, G.A., 1969, Occurrence and characteristics of chromite deposits in the eastern Bushveld Complex: Economic Geology Monograph, v. 4, p. 23–40.

Cameron, E.N., and Emerson, M.E., 1959, The origin of certain chromite deposits of the Eastern part of the Bushveld Complex: Economic Geology, v. 54, p. 1151–1213.

Campbell, I.H., and Murck, B.W., 1993, Petrology of the G and H chromitite zones in the Mountain View area of the Stillwater Complex, Montana: Journal of Petrology, v. 34, part 2, p. 291–316.

Canadian Council of Ministries of the Environment (CCME), 1999a, Canadian Soil Quality Guidelines for the Protection of Environmental and Human Health—Chromium: CCME Factsheet, 9 p. (Also available at *http://ceqg-rcqe.ccme.ca/.*)

Canadian Council of Ministries of the Environment (CCME), 1999b, Canadian water quality guidelines for the protection of aquatic life—Chromium: CCME Factsheet, 4 p. (Also available at *http://ceqg-rcqe.ccme.ca/.*)

Canadian Council of Ministries of the Environment (CCME), 1999c, Canadian sediment quality guidelines for the protection of aquatic life – chromium: CCME Factsheet, 4 p., available online at *http://ceqg-rcqe.ccme.ca/.*

Canadian Council of Ministries of the Environment (CCME), 2008, Guidelines for Canadian drinking water quality summary table, prepared by the Federal-Provincial-Territorial Committee on Drinking Water: Ottawa, Health Canada, 14 p. (Also available at *http://ceqg-rcqe.ccme.ca/.*)

Cawthorn, R.G., 1995, A re-evaluation of magma compositions and processes in the Upper Critical Zone of the Bushveld Complex: University of Witwatersrand Information Circular, Economic Geology Research Unit, v. 286, 22 p.

Cawthorn, R.G., 1999, Geological models for platinum-group metal mineralization in the Bushveld Complex: South African Journal of Science, v. 95, no. 11–12, p. 490–498.

Cawthorn, R.G., 2002, Delayed accumulation of plagioclase in the Bushveld Complex: Mineralogical Magazine, v. 66, p. 881–893.

Cawthorn, R.G., 2005, Stratiform Platinum-Group Element deposits in layered intrusions, *in* Raeside, R., ed., Exploration for Platinum-Group Elements: Mineralogical Society of Canada, Short Course Series, v. 35, p. 57–73.

Cawthorn, R.G., 2007, Cr and Sr: Keys to parental magmas and processes in the Bushveld Complex, South Africa: Lithos, v. 95, p. 381–398.

Cawthorn, R.G., Barnes, S.J., Ballhaus, C., and Malitch, K.N., 2005, Platinum Group Element, Chromium, and Vanadium deposits in mafic and ultramafic rocks, *in* Raeside, R., ed., Exploration for Platinum-Group Elements: Mineralogical Society of Canada, Short Course Series, v. 35, p. 215–249.

Cawthorn, R.G., and Barry, S., 1992, The role of intercumulus residua in the formation of pegmatoid associated with the UG2 chromitite, Bushveld Complex: Australian Journal of Earth Science, v. 39, p. 263–276.

Cawthorn, R.G., and Davies, G., 1983, Experimental data at 3 kbars pressure on parental magma to the Bushveld Complex: Contributions to Mineralogy and Petrology, v. 83, p. 128–135.

Cawthorn, R.G., Grant, R., Meyer, P.S., and Kruger, F.J., 1991, Major addition of magma at the Pyroxenite Marker in the Western Bushveld Complex, South Africa: Journal of Petrology, v. 32, no. 4, p. 739–763.

Cawthorn, R.G., and Walraven, F., 1998, Emplacement and crystallization time for the Bushveld Complex: Journal of Petrology, v. 39, no. 9, p. 1669–1687.

Cawthorn, R.G., and Webb, S.J., 2001, Connectivity between the western and eastern limbs of the Bushveld Complex: Tectonophysics, v. 330, p. 195–209.

Chamberlain, J.A., 1967, Sulfides in the Muskox intrusion: Canadian Journal of Earth Sciences, v. 4, p. 105–153.

Chaumba, J.B., and Wilson, A.H., 1997, An oxygen isotope study of the Lower Mafic Succession of the Darwendale Subchamber of the Great Dyke, Zimbabwe: Chemical Geology, v. 135, p. 293–305.

Clark, D.A., 1997, Magnetic petrophysics and magnetic petrography: aides to geological interpretation of magnetic surveys: Journal of Australian Geology and Geophysics, v. 17, no. 2, p. 83–103.

Coats, C.J.A., Stockford, H.R., and Buchan, R., 1979, Geology of the Maskwa West Nickel deposit, Manitoba: Canadian Mineralogist, v. 17, p. 309–318.

Coghill, B.M., and Wilson, A.H., 1993, Platinum-group minerals in the Selukwe Subchamber, Great Dyke, Zimbabwe; implications for PGE collection mechanisms and post-formational redistribution: Mineralogical Magazine, v. 57, no. 4, p. 613–633.

Cooper, G.R.C., 2002, Oxidation and toxicity of chromium in ultramafic soils in Zimbabwe: Applied Geochemistry, v. 17, p. 981–986.

Cordell, Lindrith, and Grauch, V.J.S., 1982, Reconciliation of the discrete and integral Fourier transforms: Geophysics, v. 47, no. 2, p. 237–243.

Crocker, I.T., Eales, H.V., and Ehlers, D.L., 2001, The fluorite, cassiterite and sulphide deposits associated with the acid rocks of the Bushveld Complex: Pretoria, South African Council for Geosciences, Memoir 90, 151 p.

Cousins, C.A., 1959, The structure of the mafic portion of the Bushveld Igneous Complex: Transactions of the Geological Society of South Africa, v. 62, p. 174–189.

Cousins, C.A., 1964, Additional notes on the chromite deposits of the eastern part of the Bushveld Complex, *in* Haughton, S.H., ed. The Geology of Some Ore Deposits in Southern Africa: Geological Society of South Africa Special Publication, v. 2, p. 169–182.

Cousins, C.A., and Feringa, G., 1964, The chromite deposits of the western belt of the Bushveld Complex, *in* Haughton, S.H., ed., The Geology of Some Ore Deposits in Southern Africa: Geological Society of South Africa Special Publication, v. 2, p. 235–239.

Czamanske, G.K., and Zientek, M.L., eds., 1985, The Still-water Complex, Montana—Geology and guide: Montana Bureau of Mines and Geology Special Publication 92, 396 p.

Dale, C.W., Pearson, D.G., Starkey, N.A., Stuart, F.M., Ellam, R.M., Larsen, L.M., Fitton, J.G., and Macpherson, C.G., 2009, Osmium isotopes in Baffin Island and West Greenland picrites—Implications for the 187Os/188Os composition of the convecting mantle and the nature of high ^{3}He/^{4}He mantle: Earth and Planetary Science Letters, v. 278, p. 267–277.

Danni, J.C.M., Fuck, R.A. and Leonardos Jr., O.H., 1982, Archean and Lower Proterozoic units in Central Brazil: Geologische Rundschau, v. 71, no. 1, p. 291–317.

Darrie, R.G., 2001, Commercial extraction technology and process waste disposal in the manufacture of chromium chemicals form ore: Environmental Geochemistry and Health, v. 23, p. 187–193

Davies, G., and Cawthorn, R.G., 1984, Mineralogical data on a multiple intrusion in the Rustenburg Layered Suite of the Bushveld Complex: Mineralogical Magazine, v. 48, p. 469–480.

Davison, G.E., and Chunnett, G.K., 1999, Seismic exploration for Merensky Reef—The way ahead: South African Journal of Geology, v. 102, p. 261–267.

Day, J.M.D., Pearson, D.G., and Hulbert, L.J., 2008, Rhenium-osmium isotope and platinum-group element constraints on the origin and evolution of the 1.27 Ga Muskox layered intrusion: Journal of Petrology, v. 49, p. 1255–1295.

Deakin, D., West, L.J., Stewart, D.I., and Yardley, B.W.D., 2001, The leaching characteristics of chromite ore processing residue: Environmental Geochemistry and Health, v. 23, no. 3, p.201–206.

De Beer, J.H., Meyer, R., and Hattingh, P.J., 1987, Geoelectrical and palaeomagnetic studies on the Bushveld Complex, *in* Kröner, A., ed., Proterozoic Lithospheric Evolution, Geodynamics Series: Washington, DC, American Geophysical Union, v. 17, p. 191–205.

de Deus, P.B., d'El Rey, L.J.H., Hasui, Y., Lima e Silva, F., Mandetta, P., de Oliveira, J.G., Franke, N.D., Carvalho, P.R., de Moraes, J.A.C., Miola, W., Vianna, J.S., Duarte, P.M., and Qeiroz, W.A., 1982, Caraíba, Pedrinhas and Andorinhas minas, Bahia State—Copper and chrome in Archean and (or) Proterozoic rocks: International Symposium on Archean and Early Proterozoic geological evolution and metallogenesis, Salvador, Brazil—Abstracts and Excursions, p. 89–117.

Dekkers, M.J., 1990, Magnetic monitoring of pyrrhotite alteration during thermal demagnetization: Geophysical Research Letters, v. 17, p. 779–782.

DePaolo, D.J., and Wasserburg, G.J., 1979, Sm-Nd age of the Stillwater Complex and the mantle evolution curve for neodymium: Geochimica et Cosmochimica Acta, v. 43, n. 7, p. 999–1008.

Dermatas, D., Bonaparte, R., Chrysochoou, M., and Moon, D.H., 2006a, Chromite ore processing residue (COPR)—Hazardous contaminated soil or solid waste?: Journal of ASTM International, v. 3, no. 7, 10 p.

Dermatas, D., Chrysochoou, M., Moon, D.H., Grubb, D.G., Wazne, M., and Christodoulatos, C., 2006b, Ettringite-induced heave in chromite ore processing residue (COPR) upon ferrous sulfate treatment: Environmental Science and Technology, v. 40, no. 18, p. 5786–5792.

Dick, H.J.B., and Bullen, T., 1984, Chromian spinel as a petrogenetic indicator in abyssal and alpine-type peridotites and spatially associated lavas: Contributions to Mineralogy and Petrology, v. 86, p. 54–76.

Dickey, J.S., Jr., Yoder, H.S., and Schairer, J.F., 1971, Chromium in silicate-oxide systems: Carnegie Institute of Washington Year Book, v. 70, p. 1530–1533.

Donaldson, C.H., 1977, Laboratory duplication of comb layering in the Rhum pluton: Mineralogical Magazine, v. 41, p. 323–336.

Duke, J.M., 1995, Stratiform Chromite, *in* Eckstrand, O.R., Sinclair, W.D., and Thorpe, R.I., eds., Geology of Canadian Mineral Deposit Types: Geological Survey of Canada, p. 617–620.

Dunham, A.C., and Wadsworth, W.J., 1978, Cryptic variation in the Rhum layered intrusion: Mineralogical Magazine and Journal of the Mineralogical Society, v. 42, no. 323, p. 347–356.

Dunn, T., 1986, An investigation of the oxygen isotope geochemistry of the Stillwater Complex: Journal of Petrology, v. 27, p. 987–997.

Du Plessis, A., and Kleywegt, R.J., 1987, A dipping sheet model for the mafic lobes of the Bushveld Complex: Transactions of the Geological Society of South Africa, v. 90, p. 1–6.

Eales, H.V., 1987, Upper Critical Zone chromitite layers at R.P.M. Union Section Mine, western Bushveld Complex, *in* Stowe, C.W., and Walker, W., eds., Evolution of Chromium Ore Fields: New York, Van Nostrand Reinhold Company, p. 144–168.

Eales, H.V., 2000, Implications of the chromium budget of the western limb of the Bushveld Complex: South African Journal of Geology, v. 103, no. 2, p. 141–150.

Eales, H.V., Botha, W.J., Hattingh, P.J., De Klerk, W.J., Maier, W.D., and Odgers, A.T.R., 1993, The mafic rocks of the Bushveld Complex—A review of emplacement and crystallization history, and mineralization, in light of recent data: Journal of African Earth Sciences, v. 16, p. 121–142.

Eales, H.V., and Cawthorn, R.G., 1996, The Bushveld Complex, *in* Cawthorn, R.G., ed., Layered intrusions: Amsterdam, Elsevier, p. 181–229.

Eales, H.V., de Klerk, W.J., and Teigler, B., 1990, Evidence for magma mixing processes within the Critical and Lower Zones of the northwestern Bushveld Complex, South Africa: Chemical Geology, v. 88, p. 261–278.

Eales, H.V., and Marsh, J.S., 1983, Al/Cr ratios of coexisting pyroxenes and spinellids in some ultramafic rocks: Chemical Geology, v. 38, no. 1–2, p. 57–74.

Eales, H.V., and Reynolds, I.M., 1986, Cryptic variations within chromitites of the Upper Critical Zone, Northwestern Bushveld Complex: Economic Geology, v. 81, p. 1056–1066.

Emeleus, C.H., Cheadle, M.J., Hunter, R.H., Upton, B.G.J., and Wadsworth, W.J., 1996, The Rum Layered Suite, *in* Cawthorn, R.G., ed., Layered intrusions: Amsterdam, Elsevier, p. 403–439.

Engelbrecht, J.P., 1987, The chromites of the Bushveld Complex in the Nietverdiend area: Economic Geology, v. 80, p. 896–910.

Fahrig, W.F., 1987, The tectonic settings of continental mafic dyke swarms – failed arm and early passive margin, *in* Halls, H.C., and Fahrig, W.F., eds., Geological Association of Canada Special Paper, v. 34, p. 331–348.

Fahrig, W.F., and Jones, D.L., 1969, Paleomagnetic evidence for the extent of Mackenzie igneous events: Canadian Journal of Earth Sciences, v. 6, p. 679–688.

Faithfull, J.W., 1985, The lower Eastern Layered Series of Rhum: Geological Magazine, v. 122, p. 459–468.

Fantoni, D., Brozzo, G., Canepa, M., Cipolli, F., Marini, L., Ottonello, G., and Zuccolini, M.V., 2002, Natural hexavalent chromium in groundwaters interacting with ophiolitic rocks: Environmental Geology, v. 42, p. 871–882.

Farmer, J.G, Graham, M.C., Thomas, R.P., Licona Manzur, C., Paterson, E., Campbell, C.D., Geelhoed, J.S., Lumsdon, D.G., Meeussen, J.C.L., Roe, M.J., Conner, A., Fallick, A.E., and Bewley, R.J.F., 1999, Assessment and modeling of the environmental chemistry and potential for remediative treatment of chromium-contaminated land: Environmental Geochemistry and Health, v. 21, p. 331–337.

Farmer, J. G., Thomas, R. P., Graham, M. C., Geelhoed, J. S., Lumsdon, D. G., and Paterson, E., 2002, Chromium speciation and fractionation in ground and surface waters in the vicinity of chromite ore processing residue disposal sites: Journal Environmental Monitoring v. 4, p. 235–243.

Fendorf, S.E., 1995, Surface reactions of chromium in soils and waters: Geoderma, v. 67, p. 55–71.

Fenton, M.D., and Faure, G., 1969, The age of igneous rocks of the Stillwater Complex of Montana: Geological Society of America Bulletin, v. 80, n. 8, p. 1599–1604.

Fernandes, T.R.C., 1999, Significance of ferrimagnetism in chromitites from the Great Dyke, Zimbabwe: Journal of African Earth Sciences, v. 28, no. 2, p. 337–348.

Ferrario, A., and Garuti, G., 1988, Platinum-group minerals in chromite-rich horizons of the Niquelândia Complex (central Goiás, Brazil), *in* Prichard, H.M., and others, eds., Geo-Platinum '87: London and New York, Elsevier Applied Sciences, p. 261–272.

Ferré, E.C., Maes, S.M., and Butak, K.C., 2009, The magnetic stratification of layered mafic intrusions—Natural examples and numerical models: Lithos, v. 111, p. 83–94.

Ferreira-Filho, C.F., and Garuti, G., 1988, Platinum-group minerals in chromite-rich horizons of the Niquelândia Complex (central Goiás, Brazil), *in* Prichard, H.M. and others, eds., Geo-Platinum '87: London and New York, Elsevier Applied Sciences, p. 261–272.

Ferreira-Filho, C.F., Kamo, S.L., Fuck, R.A., Krogh, T.E., and Naldrett, A.J., 1994, Zircon and rutile U-Pb geochronology of the Niquelândia layered mafic and ultramafic intrusion, Brazil—Constraints for the timing of magmatism and high grade metamorphism: Precambrian Research, v. 68, p. 241–255.

Ferreira Filho, C.F., Naldrett, A.J., and Asif, M., 1995, Distribution of platinum-group elements in the Niquelândia layered mafic-ultramafic intrusion, Brazil—Implications with respect to exploration: The Canadian Mineralogist, v. 33, p. 165–184.

Ferreira-Filho, C.F., Nilson, A.A., and Naldrett, A.J., 1992, The Niquelândia mafic-ultramafic complex, Goiás, Brazil—A contribution to the ophiolite x stratiform controversy based on new geological and structural data: Precambrian Research, v. 59, p. 125–143.

Foose, M.P., 1991, Deposits containing nickel, cobalt, chromium, and platinum-group elements in the United States, *in* Gluskoter, J.J., Rice, D.D., and Taylor, R.B., eds., Economic Geology, U.S.: Geological Society of America, The Geology of North America, v. P–2, p. 87–102.

Foose, R.M., Wise, D.U., and Garbarini, G.S., 1961, Structural geology of the Beartooth Mountains, Montana and Wyoming: Bulletin of the Geological Society of America, v. 72, no. 8, p. 1143–1172.

Forester, R.W., and Harmon, R.S., 1983, Stable isotope evidence for deep meteoric-hydrothermal circulation—Isle of Rhum, Inner Hebrides, Scotland: Extended Abstracts, Proceedings of the 3rd International Conference on Water-Rock Interactions, p. 135–136.

Fourie, G.P., 1959, The chromite deposits in the Rustenburg area: South African Geological Survey Bulletin, v. 27, p. 1–45.

Francis, D., 1994, Chemical interaction between picritic magmas and upper crust along the margins of the Muskox intrusion, Northwest Territories: Geological Survey of Canada Paper 92–12, 94 p.

French, J.E., Heaman, L.M., and Chacko, T., 2002, Feasibility of chemical U-Th-total Pb baddeleyite dating by electron microprobe: Chemical Geology, v. 188, p. 85–104.

Gain, S.B., 1985, The geologic setting of the platiniferous UG-2 chromitite layer on the Farm Maandagshoek, Eastern Bushveld Complex: Economic Geology, v. 80, p. 925–943.

Garnier, J., Quantin, C., Guimarães, E., and Becquer, T., 2008, Can chromite weathering be a source of Cr in soils?: Mineralogical Magazine, v. 72, p. 49–53.

Garnier, J., Quantin, C., Guimarães, E., Garg, V.K., Martins, E.S., and Becquer, T., 2009, Understanding the genesis of ultramafic soils and catena dynamics in Niquelândia, Brazil: Geoderma, v. 151, p. 204–214.

Garnier, J., Quantin, C., Martins, E.S., and Becquer, T., 2006, Solid speciation and availability of chromium in ultramafic soils from Niquelândia, Brazil: Journal of Geochemical Exploration, v. 88, p. 206–209.

Garuti, G., Proenza, J.A., and Zaccarini, F., 2005, Platinum-group element distribution and mineralogy in altered chromitite of the Campo Formoso layered intrusion (Bahia state, Brazil), *in* Tormanen, T.O., and Alapieti, T.T., eds., 10th International Platinum Symposium, Extended Abstracts: Finland, University of Oulu, p. 82–85.

Garuti, G., Proenza, J.A., and Zaccarini, F., 2007, Distribution and mineralogy of platinum-group elements in altered chromitites of the Campo Formoso layered intrusion (Bahia State, Brazil)—Control by magmatic and hydrothermal processes: Mineralogy and Petrology, v. 89, p. 159–188.

Geelhoed, J.S., Meeussen, J.C.L., Hillier, S., Lumsdon, D.G., Thomas, R.P., Farmer, J.G., and Paterson, E., 2002, Identification and geochemical modeling of processes controlling leaching of Cr(VI) and other major elements from chromite ore processing residue: Geochimica et Cosmochimica Acta, v.66, no. 22, p. 3927–3942.

Geelhoed, J.S., Meeussen, J.C.L., Lumsdon, D.G., Hillier, S.J., Roe, M.J., Thomas, R.P., Bewley, R.J.F., Farmer, J.G., and Paterson, E., 2001, Modeling of chromium behaviour and transport at sites contaminated with chromite ore processing residue—Implications for remediation methods: Environmental Geochemistry and Health, v. 23, no. 3, p.261–265.

Geissman, J.W., and Harlan, S.S., 1986, Stillwater Complex (Montana) paleomagnetism—Results from altered banded series units and younger intrusions: Eos, Transactions of the American Geophysical Union, v. 67, no. 16, p. 268.

Ghisler, M., 1966, The chromite deposits at Fiskenaesset: Grønlands Geologiske Undersøgelse Rapport, v. 11, p. 31–31.

Ghisler, M., 1970, Pre-metamorphic folded chromite deposits of stratiform type in the early Precambrian of West Greenland: Mineralium Deposita, v. 5, p. 223–236.

Ghisler, M., 1976, The geology, mineralogy and geochemistry of the pre-orogenic Archean stratiform chromite deposits at Fiskenæsset, West Greenland: Monograph Series Mineral Deposits, v. 14, 156 p.

Girardi, V.A.V., Rivalenti, G., and Sinigoi, S., 1986, The petrogenesis of the Niquelândia layered basic-ultrabasic complex, Central Goias, Brazil: Journal of Petrology, v. 27, no. 3, p. 715–744.

Girardi, V.A.V., Ferrario, A., Correia, C.T., and Diella, V., 2006, A comparison of selected Precambrian Brazilian chromitites—Chromite, PGE-PGM, and Re/Os as parental source indicators: Journal of South American Earth Sciences, v. 20, p. 303–313.

Giuliani, G., Zimmerman, J.L., and Montigny, R., 1994, K-Ar and ^{40}Ar/^{39}Ar evidence for a Transamazonian age (2030–1970 Ma) for the granites and emerald-bearing K-meatsomatites from Campo Formoso and Carnaíba (Bahia, Brazil): Journal of South American Earth Sciences, v. 7, p. 149–165.

Godgul, G., and Sahu, K.C., 1995, Chromium contamination from chromite mine: Environmental Geology (Berlin), v. 25, no. 4, p. 251–257.

Greenwood, R.C., Donaldson, C.H., and Emeleus, C.H., 1990, The contact zone of the Rhum ultrabasic intrusion—Evidence of peridotite formation form magnesian magmas: Journal of the Geological Society of London, v. 147, p. 209–212.

Greenwood, R.C., Fallick, A.E., and Donaldson, C.H., 1992, Oxygen isotope evidence for major fluid flow along the contact zone of the Rum ultrabasic intrusion: Geological Magazine, v. 129, p. 243–246.

Grishaenko, V.P., 2007, Independent Report on the Shalozerskoe (Burakovsky), Lukkulaisvaara and Tsipringa Platinum, Palladium, Copper, Nickel Deposits in the Autonomous Republic of Karelia Russian Federation: London, Behre Dolbear International Ltd., 58 p.

Hall, A.L., 1932, The Bushveld Igneous Complex of the Central Transvaal: Geological Survey of South Africa Memoirs, v. 28, p. 560.

Hamilton, J., 1977, Strontium isotope and trace element studies on the Great Dyke and Bushveld mafic phase and their relation to early Proterozoic magma genesis in southern Africa: Journal of Petrology, v. 18, p. 24–52.

Hammarstrom, J.M., Seal, R.R., II, Ouimette, A.P., and Foster, S.A., 2001, Sources of metals and acidity at the Elizabeth and Ely mines—Geochemistry and mineralogy of solid mine waste and the role of secondary minerals in metal recycling, *in* Hammarstrom, J.M., and Seal, R.R., II, eds., Environmental geochemistry and mining history of massive sulfide deposits in the Vermont copper belt: Society of Economic Geologists Field Trip Guidebook Series, v. 35, pt. II, p. 213–248.

Harmer, R.E., 2000, New precise dates on the acid phase of the Bushveld and their implications: Abstracts of the Workshop on the Bushveld Complex, 18th–21st November 2000, University of Wiwatersrand, Johannesburg, South Africa, p.11–12.

Harmer, R.E., and Sharpe, M.R., 1985, Field relations and strontiuim isotope systematics of the marginal rocks of the eastern Bushveld Complex: Economic Geology, v. 80, no. 4, p. 813–837.

Harris, C., Pronost, J.J.M., Ashwal, L.D., and Cawthorn, R.G., 2005, Oxygen and hydrogen isotope stratigraphy of the Rustenberg Layered Suite, Bushveld Complex—Constraints on crustal contamination: Journal of Petrology, v. 46, p. 579–601.

Hart, S.R., and Kinloch, E.D., 1989, Osmium isotope systematics in Witwatersrand and Bushveld ore deposits: Economic Geology and the Bulletin of the Society of Economic Geologists, v. 84, no. 6, p. 1651–1655.

Hattingh, P.J., 1980, The structure of the Bushveld Complex in the Groblersdal-Lydenbrug-Belfast area of the Eastern Transvaal as interpreted from a regional gravity survey: Transactions of the Geological Society of South Africa, v. 83, p. 125–134.

Hatton, C.J., Harmer, R.E., and Sharpe, M.R., 1986, Petrogenesis of the middle group of chromitite layers, Doornvlei, eastern Bushveld Complex, *in* Gallagher, M.J., ed., Metallogeny of basic and ultrabasic rocks: London, Institute of Mineralogy and Metallurgy, p. 241–247.

Hatton, C.J., and Sharpe, M.R., 1989, Significance and origin of boninite-like rocks associated with the Bushveld Complex, *in* Crawford, A.J., ed., Boninites: London, Unwin Hyman, p. 174–207.

Hatton, C.J., and Von Gruenewaldt, G., 1990, Early Precambrian layered intrusions, *in* Hall, R.P., and Hughes, D.J., eds., Early Precambrian basic magmatism: New York, Chapman and Hall, p. 56–82.

Heider, F., Zitzelsberger, A., and Fabian, K., 1996, Magnetic susceptibility and remanence coercive force in grown magnetite crystals from 0.1 mm to 6 mm: Physics of the Earth and Planetary Interiors, v. 93, p. 239–256.

Hess, H.H., 1960, Stillwater igneous complex, Montana—A quantitative mineralogical study: Geological Society of America Memoir, 230 p.

Higgins, S.J., Snyder, G.A., Mitchell, J.N., Taylor, L.A., Sharkov, E.V., Bogatikov, O.A., Grokhovskaya, T.L., Chistyakov, T.L., Ganin, V.A., and Grinevich, N.G., 1997, Petrology of the early Proterozoic Burakovsky layered intrusion, southern Karelia, Russia—Mineral and whole-rock majorelement chemistry: Canadian Journal of Earth Sciences, v. 34, no. 4, p. 390–406.

Hillier, S., Roe, M.J., Geelhoed, J.S., Fraser, A.R., Farmer, J.G., and Paterson, E., 2003, Role of quantitative mineralogical analysis in the investigation of sites contaminated by chromite ore processing residue: Science of the Total Environment, v. 308, p. 195–210.

Hoffman, P.F., 1984, Geology, northern internides of Wopmay Orogen, District of MacKenzie, Northwest Territories: Geological Survey of Canada Map 1576A.

Hofmann, A.W., 1988, Chemical differentiation of the Earth: the relationship between mantle, continental crust, and oceanic crust: Earth and Planetary Science Letters, v. 90, no. 3, p. 297–314.

Holwell, D.A., Boyce, A.J., and McDonald, I., 2007, Sulfur isotope variations within the Platreef Ni-Cu-PGE deposit—Genetic implications for the origin of sulfide mineralization: Economic Geology and the Bulletin of the Society of Economic Geologists, v. 102, p. 1091–1110.

Horan, M.F., Morgan, J.W., Walker, R.J., and Cooper, R.W., 2001, Re-Os isotopic constraints on magma mixing in the peridotite zone of the Stillwater Complex, Montana, USA: Contributions to Mineralogy and Petrology, v. 141, p. 446–457.

Hoyle, P., 1993, Chemical and modal variations at the top of the Upper Zone in the Northwestern Bushveld Complex, *in* Symposium on Layering in Igneous Complexes, Abstracts Volume: Johannesburg, University of Witwatersrand.

Hulbert, L., and Von Gruenewaldt, G., 1985, Textural and compositional features of chromite in the lower and critical zones of the Bushveld Complex south of Potgietersrus: Economic Geology and the Bulletin of the Society of Economic Geologists, v. 80, no. 4, p. 872–895.

Huppert, H.E., and Sparks, R.S.J., 1980, The fluid dynamics of a basaltic magma chamber replenished by influx of hot dense ultrabasic magma: Contributions to Mineralogy and Petrology, v. 75, p. 278–289.

International Chromium Development Association (ICDA), 2010, Ore Processing: Discover Chromium, 3 p.,accessed March 1, 2010, at *http://www.icdachromium.com/home.php*.

Irvine, T.N., 1967, Chromian spinel as a petrogenetic indicator—Part 2. Petrologic applications: Canadian Journal of Earth Sciences, v. 4, no. 1, p. 71–103.

Irvine, T.N., 1970, Crystallization sequences in the Muskox intrusion and other layered intrusions—I. Olivine-pyroxene-plagioclase relations: Geological Society of South Africa Special Publication, v. 1, p. 441–476.

Irvine, T.N., 1975, Crystallization sequences in the Muskox intrusion and other layered intrusions—II. Origin of chromitite layers and similar deposits of other magmatic ores: Geochimica et Cosmochimica Acta, v. 39, p. 991–1020.

Irvine, T.N., 1977, Origin of chromitite layers in the Muskox intrusion and other stratiform intrusions; a new interpretation: Geology, v. 5, p. 273–277.

Irvine, T.N., 1979, The ultramafic rocks of the Muskox intrusion, Northwest Territories, Canada, *in* Wylie, P.J., ed., Ultramafic and Related Rocks: Chicago, University of Chicago, p. 38–49.

Irvine, T.N., 1980, Magmatic infiltration metasomatism, double-diffusive fractional crystallization, and adcumulus growth in the Muskox intrusion and other layered intrusions, *in* Hargraves, R.B., ed., Physics of Magmatic Processes: Princeton University, p. 325–384.

Irvine, T.N., and Baragar, W.R.A., 1972, Muskox and Coppermine River lavas, Northwest Territories, Canada: International Geologic Congress (Montreal), Excursion A29, 70 p.

Irvine, T.N., Keith, D.W., and Todd, S.G., 1983, The J-M platinum-palladium reef of the Stillwater Complex, Montana—II. Origin by double-diffusive convection magma mixing and implications for the Bushveld Complex: Economic Geology, v. 78, p. 1287–1334.

Irvine, T.N., and Sharpe, M.R., 1982, Source-rock compositions and depths of origin of Bushveld and Stillwater magmas: Carnegie Institution of Washington Year Book, v. 81, p. 294–303.

Irvine, T.N., and Smith, C.H., 1967, The ultramafic rocks of the Muskox intrusion, Northwest Territories, Canada, *in* Wyllie, P.J., ed., Ultramafic and Related Rocks: New York and London, John Wiley and Sons, p. 38–49.

Irvine, T.N., and Smith, C.H., 1969, Primary oxide minerals in the layered series of the Muskox intrusion, Economic Geology Monograph 4, *in* H.D.B. Wilson, ed., 1969, Magmatic Ore Deposits, A Symposium: Society of Economic Geologists, p. 76–94.

Jackson, E.D., 1961, Primary textures and mineral associations in the Ultramafic Zone of the Stillwater Complex, Montana: U.S. Geological Survey Professional Paper 358, 106 p.

Jackson, E.D., 1968, The chromite deposits of the Stillwater Complex, Montana, *in* Ridge, J.D., ed., Ore deposits of the United States, 1933–1967—The Graton-Sales volume: New York, The American Institute of Mining, Metallurgical, and Petroleum Engineers, Inc., v. 2, p. 1495–1510.

Jackson, E.D., 1969, Chemical variation in coexisting chromite and olivine in chromitite zones of the Stillwater Complex, *in* Wyllie, P.J., ed., 1969, Magmatic ore deposits—A symposium: Economic Geology Monograph, v. 4, p. 41–75.

Jackson, E.D., 1970, The cyclic unit in layered intrusions – a comparison of the repetitive stratigraphy in the ultramafic parts of the Stillwater, Muskox, Great Dyke, and Bushveld Complexes: Geological Society of South Africa Special Publication, v. 1, p. 391–424.

Jambor, J.L., 1994, Mineralogy of sulfide-rich tailings and their oxidation products, *in* Jambor, J.L, and Blowes, D.W., eds., Short Course Handbook on Environmental Geochemistry of Sulfide Mine-wastes: Mineralogical Association of Canada, v. 22, p. 59–102.

Jambor, J.L., 2003, Mine-waste mineralogy and mineralogical perspectives of acid-base accounting, *in* Jambor, J.L., Blowes, D.W., and Ritchie A.I.M., eds., Environmental Aspects of Mine Wastes: Mineralogical Association of Canada Short Course Series, v. 31, p. 117–146.

Jambor, J.L., Dutrizac, J.E., Groat, L.A., and Raudsepp, M., 2002, Static tests of neutralization potentials of silicate and aluminosilicate minerals: Environmental Geology, v. 43, p. 1–17.

Jambor, J.L., Dutrizac, J.E., and Raudsepp, M., 2007, Measured and computed neutralization potentials from static tests of diverse rock types: Environmental Geology, v. 52, p. 1019–1031.

James, B.R., 1994, Hexavalent chromium solubility and reduction in alkaline soils enriched with chromite ore processing residue: Journal of Environmental Quality, v. 23, no.2, p. 227–233.

James, C., H., 1957, Geochemical prospecting studies in the Great Dyke chromite district, Southern Rhodesia: London Imperial College of Science and Technology, Geochemical Prospecting Research Centre, Technical Communication, v. 13, 44 p.

Jones, W.R., Peoples, J.W., and Howland, A.L., 1960, Igneous and tectonic structures of the Stillwater Complex, Montana: U.S. Geological Survey Bulletin 1071–H, p. 281–340.

Katz, S.A., and Salem, H., 1993, The toxicity of chromium with respect to its chemical speciation; a review: Journal of Applied Toxicology, v. 13, p. 217–224.

Kinnaird, J.A., Kruger, F.J., Nex, P.A.M., and Cawthorn, R.G., 2002, Chromitite formation—A key to understanding processes of platinum enrichment: Transactions of the Institution of Mining and Metallurgy, Section B: Applied Earth Science, v. 111, p. B23–B35.

Kistler, R.W., Obradovich, J.D., and Jackson, E.D., 1969, Isotopic ages of rocks and minerals from Stillwater Complex, Montana: Journal of Geophysical Research, v. 74, no. 12, p. 3226–3237.

Kleinkopf, M.D., 1985, Regional gravity and magnetic anomalies of the Stillwater Complex area:, Montana Bureau of Mines and Geology Special Publication, v. 92, p. 33–38.

Kruger, F.J., 1990, The stratigraphy of the Bushveld Complex: a reappraisal and the relocation of the Main Zone boundaries: South African Journal of Geology, v. 93, p. 376–381.

Kruger, F.J., 1992, The origin of the Merensky cyclic unit: isotopic and mineralogical evidence for an alternative orthomagmatic model: Australian Journal of Earth Sciences, v. 39. p. 393–398.

Kruger, F.J., 1994, The Sr-isotopic stratigraphy of the Western Bushveld Complex: South African Journal of Geology, v. 97, p. 393–398.

Kruger, F.J., 1999, The Bushveld Complex unconformity related ore deposits—An isotopic perspective, *in* Stanley, C.J., Rankin, A.H., Bodnar, R.J., and others, eds., Mineral Deposits—Processes to Processing: Balkema, Rotterdam, p. 737–738.

Kruger, F.J., 2005, Filling the Bushveld Complex magma chamber—Lateral expansion, roof and floor interaction, magmatic unconformities, and the formation of giant chromitite, PGE, and Ti-V-magnetite deposits: Mineralium Deposita, v. 40, p. 451–472.

Kruger, F.J., Cawthorn, R.G., and Walsh, K.L., 1982, Strontium isotopic evidence against magma addition in the Upper Zone of the Bushveld Complex: Earth and Planetary Science Letters, v. 84, p. 51–58.

Kruger, F.J., Cawthron, R.G., and Walsh, K.L., 1987, Strontium isotopic evidence against magma addition in the Upper Zone of the Bushveld Complex: Earth Planetary Science Letters, v. 84, p. 51–58.

Kruger, F.J., and Marsh, J.S., 1982, Significane of $^{87}Sr/^{86}Sr$ ratios in the Merensky cyclic unit of the Western Bushveld Complex: Nature, v. 298, p. 53–55.

Kujanpää, J., 1989, Finland's Kemi chromite deposit: Chromium Review, v. 10, p. 5–8.

Kyser, T.K., O'Neil, J.R., and Carmichael, I.S.E., 1981, Oxygen isotope thermometry of basic lavas and mantle nodules: Contributions to Mineralogy and Petrology, v. 47, p. 631–644.

Lambert, D.D., Morgan, J.W., Walker, R.J., Shirey, S.B., Carlson, R.W., Zientek, M.L., and Koski, M.S., 1989, Rhenium-Osmium and Samarium-Neodymium Isotopic Systematics of the Stillwater Complex: Science, v. 244, no. 4909, p. 1169–1174.

Lambert, D.D., and Simmons, E.C., 1987, Magma evolution in the Stillwater Complex, Montana—I. Rare-earth element evidence for the formation of the Ultramafic Series: American Journal of Science, v. 287, no. 1, p. 1–32.

Lambert, D.D., Walker, R.J., Morgan, J.W., Shirey, S.B., Carlson, R.W., Zientek, M.L., Lipin, B.R., Koski, M.S., and Cooper, R.L., 1994, Re-Os and Sm-Nd isotope geochemistry of the Stillwater Complex, Montana—Implications for the petrogenesis of the J-M Reef: Journal of Petrology, v. 35, no. 6, p. 1717–1753.

LeCheminant, A.N., and Heaman, L.M., 1989, Mackenzie igneous events, Canada—Middle Proterozoic hotspot magmatism associated with ocean opening: Earth and Planetary Science Letters, v. 96, no. 1–2, p. 38–48.

Lee, C.A., 1981, Post-deposition structures in the Bushveld Complex mafic sequence: Journal of the Geological Society of London, v. 138, p. 327–341.

Lee, C.A., 1996, A review of mineralization in the Bushveld Complex and some other layered intrusions, *in* Cawthorn, R.G., ed., Layered intrusions: Amsterdam, Elsevier, p. 103–145.

Letts, S., Torsvik, T.H., Webb, S.J., and Ashwal, L.D., 2009, Palaeomagnetism of the 2054 Ma Bushveld Complex (South Africa)—Implications for emplacement and cooling: Geophysical Journal International, v. 179, p. 850–872.

Li, C., Ripley, E.M., Oberthür, T., Miller, Jr., J.D., and Joslin, G.D., 2008, Textural, mineralogical and stable isotope studies of hydrothermal alteration in the main sulfide zone of the Great Dyke, Zimbabwe, and the precious metals zone of the Sonju Lake intrusion, Minnesota, USA: Mineralium Deposita, v. 43, p. 97–110.

Liebenberg, L. 1970, The sulphides in the layered sequence of the Bushveld Igneous Complex: Geological Society of South Africa Special Publication, v. 1, p. 108–207.

Lioy, P.J., Freeman, N.C.G., Wainman, R., Stern, A.H., Boesch, R., Howell, T., and Shupack, S.I., 1992, Microenvironmental Analysis of Residential Exposure to Chromium-Laden Waste in and Around New Jersey Homes: Risk Analysis, v. 12, no. 2, p. 287–299.

Lipin, B.R., 1993, Pressure increases, the formation of chromite seams, and the development of the Ultramafic Series in the Stillwater Complex, Montana: Journal of Petrology, v. 34, no. 5, p. 955–976.

Loferski, P.J., Lipin, B.R., and Cooper, R.W., 1990, Petrology of chromite-bearing rocks from the lowermost cyclic units in the Stillwater Complex, Montana: U.S. Geological Survey Bulletin B1674–E, p. E1–E28.

Lord, R.A., Prichard, H.M., Sá, J.H.S., and Neary, C.R., 2004, Chromite geochemistry and PGE fractionation in the Campo Formoso Complex and Ipueira-Medrado Sill, Bahia State, Brazil: Economic Geology, v. 99, p. 339–363.

Maccelari, J.M., Kruger, F.J., and Durrheim, R.J., 1991a, The interpretation of a reflection seismic profile across the western lobe of the Bushveld Complex: South African Geophysical Association, 2nd Biennial Meeting, p. 122

Maccelari, M.J., Sutherland, R.A., and Durrheim, R.J., 1991b, The processing of a reflection seismic profile recorded across the western lobe of the Bushveld Complex: South African Geophysical Association, 2nd Biennial Meeting, p. 123–126.

MacDonald, D.D., Ingersoll, C.G., and Berger, T.A., 2000, Development and evaluation of consensus-based sediment-quality guidelines for freshwater ecosystems: Archives of Environmental Contamination and Toxicology, v. 39, p. 20–31.

Maier, W.D., Arndt, N.T., and Curl, E.A., 2000, Progressive crustal contamination of the Bushveld Complex – evidence from Nd isotopic analyses of the cumulate rocks: Contributions to Mineralogy and Petrology, v. 140, p. 316–327.

Maier, W.D., and Barnes, S.J., 1998, Concentrations of rare earth elements in silicate rocks of the Lower, Critical and Main Zones of the Bushveld Complex: Chemical Geology, v. 150, no. 1–2, p. 85–103.

Maier, W.D., Barnes, S.J., de Klerk, W.J., Teigler, B., and Mitchell, A.A., 1996, Cu/Pd and Cu/Pt of silicate rocks in the Bushveld Complex—Implications for platinum-group exploration: Economic Geology, v. 91, p. 1151–1158.

Maier, W.D., and Eales, H.V., 1994, Plagioclase inclusions in orthopyroxene and olivine of the UG2-Merensky Reef interval—Regional trends in the western Bushveld Complex: South African Journal of Geology, v. 97, no. 4, p. 408–414.

Manhès, G., Allègre, C.J., Dupré, B., and Hamelin, B., 1980, Lead isotope study of basic-ultrabasic layered complexes—Speculations about the age of the earth and primitive mantle characteristics: Earth and Planetary Science Letters, v. 47, p. 370–382.

Marathon PGM Corporation, 2008, Marathon develops two resources on the Bird River project: Marathon PGM Corporation, press release #2009–01, 3 p.

Marcantonio, F., Zindler, A., Reisberg, L., and Mathez, E.A., 1993, Re-Os isotopic systematics in chromitites from the Stillwater Complex, Montana, USA: Geochimica et Cosmochimica Acta, v. 57, p. 4029–4037.

Marques, J.C., and Ferreira-Filho, C.F., 2003, The chromite deposit of the Ipueira-Medrado Sill, São Francisco Craton, Bahia State, Brazil: Economic Geology, v. 98, p. 87–108.

Marques, J.C., Ferreira-Filho, C.F., Carlson, R.W., and Pimentel, M.M., 2003, Re-Os and Sm-Nd isotope and trace element constraints on the origin of the chromite deposit of the Ipueira-Medrado Sill, Bahia, Brazil: Journal of Petrology, v. 44, p. 659–678.

Martin, C.E., 1989, Re-Os isotopic investigation of the Stillwater Complex, Montana: Earth and Planetary Science Letters, v. 93, p. 336–344.

McBirney, A.R., and Hunter, R.H., 1995, The cumulate paradigm reconsidered: The Journal of Geology, v. 103, p. 114–122.

McBirney, A.R., and Noyes, R.M., 1979, Crystallization and layering of the Skaergaard intrusion: Journal of Petrology, v. 20, no. 3, p. 487–554.

McCallum, I.S., 1996, The Stillwater Complex, *in* Cawthorn, R.G., ed., Layered intrusions: Amsterdam, Elsevier, p. 441–483.

McCallum, I.S., Thurber, M.W., Bosch, D., and Nelson, B.K., 1992, Lead isotopic compositions of plagioclases and sulphides in the Stillwater Complex: Evidence for isotopic disequilibrium and remobilization: Lunar and Planetary Science, v. 23, p. 867–868.

McCandless, T.E., and Ruiz, J., 1991, Osmium isotopes and crustal sources for platinum-group mineralization in the Bushveld Complex, South Africa: Geology, v. 19, no. 12, p. 1225–1228.

McCandless, T.E., Ruiz, J., Adair, B.I., and Freydier, C., 1999, Re-Os isotope and Pd/Ru variations in chromitites from the Critical Zone, Bushveld Complex, South Africa: Geochimica et Cosmochimica Acta, v. 63, no. 6, p. 911–923.

McDonough, W.F., and Sun, S.-s., 1995, The composition of the Earth: Chemical Geology, v. 120, no. 3–4, p. 223–253.

Meck, M., Love, D., and Mapani, B., 2006, Zimbabwean mine dumps and their impacts on river water quality—A reconnaissance study: Physics and Chemistry of the Earth, v. 31, no. 15–16, p. 797–803.

Meyer, R., and De Beer, H., 1987, Structure of the Bushveld Complex from resistivity measurements: Nature, v. 325, p. 610–612.

Mitchell, A.A., and Scoon, R.N., 2007, The Merensky Reef at Winnaarshoek, Eastern Bushveld Complex: Economic Geology, v. 102, p. 971–1009.

Molyneux, T.G., 1974, A geological investigation of the Bushveld Complex in Sekhukhenland and part of the Steelpoort Valley: Transactions of the Geological Society of South Africa, v. 77, no. 3, p. 329–338.

Molyneux, T.G., and Klinkert, P.S., 1978, A structural interpretation of part of the eastern mafic lobe of the Bushveld Complex and its surroundings: Transactions of the Geological Society of South Africa, v. 81, p. 359–368.

Mondal, S.K., and Mathez, E. A., 2007, Origin of the UG2 chromitite layer, Bushveld Complex: Journal of Petrology, v. 48, no. 3, p. 495–510.

Moon, D.H., Dermatas, D., Chrysochoou, M., and Gang, S., 2006, An investigation of the heaving mechanism related to chromite ore processing residue: Journal of ASTM International, v. 3 no. 6.

Moon, D.H., Dermatas, D., Wazne, M., Sanchez, A.M., Chrysochoou, M., and Grubb, D.G., 2007a, Swelling related to ettringite crystal formation in chromite ore processing residue: Environmental Geochemistry and Health, v. 29, no. 4, p. 289–294.

Moon, D.H., Wazne, M., Dermatas, D., Christodoulatos, C., Sanchez, A.M., Grubb, D.G., Chrysochoou, M., and Kim, M.G., 2007b, Long-term treatment issues with chromite ore processing residue (COPR) – Cr6+ reduction and heave: Journal of Hazardous Materials, v. 143, no. 3, p. 629–635.

Moon, D.H., Wazne, M., Jagupilla, S.C., Christodoulatos, C., Kim, M.G., and Koutsospyros, A., 2008, Particle size and pH effects on remediation of chromite ore processing residue using calcium polysulfide (CaS5): Science of the Total Environment, v.. 399, no. 1–3, p. 2–10.

Mukasa, S.B., Wilson, A.H., and Carlson, R.W., 1998, A multielement geochronological study of the Great Dyke, Zimbabwe—Significance of the robust and reset ages: Earth and Planetary Science Letters, v. 164, p. 353–369.

Myers, J.S., 1976, Channel deposits of peridotite, gabbro and chromitite from turbidity currents in the stratiform Fiskenæsset anorthosite complex, southwest Greenland: Lithos, v. 9, p. 281–291.

Myers, J.S., 1985, Stratigraphy and structure of the Fiskenæsset Complex, southern West Greenland: Bulletin—Gronlands Geologiske Undersogelse, v. 150, 72 p.

Myers, J.S., and Platt, R.G., 1977, Mineral chemistry of layered Archaean anorthosite at Majorqap qâva, near Fiskenæsset, southwest Greenland: Lithos, v. 10, p. 59–72.

Naldrett, A.J., 1989, Sulfide melts – crystallization temperatures, solubilities in silicate melts, and Fe, Ni, and Cu partitioning between basaltic magmas and olivine: Reviews in Economic Geology, v. 4, p. 5–20.

Naldrett, A.J., 2004, Magmatic sulfide deposits; geology, geochemistry and exploration: Berlin, Springer-Verlag, p. 137–277.

Naldrett, A.J., Bruegmann, G.E., and Wilson, A.H., 1990, Models for the concentration of PGE in layered intrusions: The Canadian Mineralogist, v. 28, no. 3, p. 389–408.

Naldrett, A.J., Cameron, G., Von Gruenewaldt, G., and Sharpe, M.R., 1987, The formation of stratiform PGE deposits in layered intrusions, *in* Parsons, I., ed., Origins of Igneous Layering: NATO Advanced Science Institute Series, Series C—Mathematical and Physical Sciences, v. 196, p. 313–397.

VNaldrett, A.J., Kinnaird, J., Wilson, A., Yudovskaya, M., McQuade, S., Chunnett, G., and Stanley, C., 2009, Chromite composition and PGE content of Bushveld chromitites, Part 1—The Lower and Middle Groups: Transactions of the Institution of Minerals and Metallurgy, Section B—Applied Earth Science, v. 118, no. 3–4, p. 131–161.

Naslund, H.R., and McBirney, A.R., 1996, Mechanisms of formation of igneous layering, *in* Cawthorn, R.G., ed., Layered intrusions: Amsterdam, Elsevier, p. 1–43.

Nigbor, M.T., Iverson, S.R., and Hyndman, P.O., 1985, Environmental issues related to mineral development in the Stillwater Complex, Montana: Bureau of Mines Information Circular, v. 9040, 33 p.

Oberthür, T., 2002, Platinum-group element mineralization of the Great Dyke, Zimbabwe, *in* Calibri, L.J., ed., The geology, geochemistry, mineralogy and mineral benefication of platinum-group elements: Canadian Institute of Mining, Metallurgy, and Petroleum, Special Volume 54, p. 483–506.

Odgers, A.T.R., and Du Plessis, A., 1993, Interpretation of a regional reflection seismic survey in the north-eastern Bushveld Complex: South African Geophysical Association Third Biennial Meeting, p. 125–129.

O'Driscoll, B., Day, J.M.D., Daly, J.S. Daly, Walker, R.J., and McDonough, W.F., 2009b, Rhenium-osmium isotopes and platinum-group elements in the Rum Layered Suite, Scotland—Implications for Cr-spinel seam formation and the composition of the Iceland mantle anomaly: Earth and Planetary Science Letters, v. 286, p. 41–51.

O'Driscoll, B., Donaldson, C.H., Daly, J.S., and Emeleus, C.H., 2009a, The roles of melt infiltration and cumulate assimilation in the formation of anorthosite and a Cr-spinel seam in the Rum Eastern Layered intrusion, NW Scotland: Lithos, v. 111, p. 6–20.

O'Driscoll, B., Donaldson, C.H., Troll, V.R., Jerran, D.A., and Emeleus, C.H., 2007, An origin for harrisitic and granular olivine in the Rum Layered Suite, NW Scotland: a crystal size distribution study: Journal of Petrology, v. 48, no. 2, p. 253–270.

O'Driscoll, O'Driscoll, B., Emeleus, C.H., Donaldson, C.H., and Daly, J.S., 2010, Cr-spinel seam petrogenesis in the Rum layered suite, NW Scotland—Cumulate assimilation and in situ crystallization in a deforming crystal mush: Journal of Petrology, v. 51, no. 6, p. 1171–1201.

Ohnenstetter, C., Wakinson, D.H., Jones, P.C., and Talkington, R., 1986, Cryptic compositional variation in laurite and enclosing chromite from the Bird River Sill, Manitoba: Economic Geology, v. 81, p. 1159–1168.

Oliveira, E.P., and Lafon, J.M., 1995, Idade dos Complexos máficoultramáficos mineralizados de Caraíba e Medrado, Bahia, por evaporação de Pb em zircão: Congresso Brasileiro de Geoquímica, 5th, Niterói, 1995, 2 p.

Oze, C., Bird, D.K., and Fendorf, S., 2007, Genesis of hexavalent chromium from natural sources in soil and groundwater: Proceedings of the National Academy of Sciences, v. 104, p. 6544–6549.

Oze, C., Fendorf, S., Bird, D.K., and Coleman, R.G., 2004a, Chromium geochemistry in serpentinized ultramafic rocks and serpentine soils from the Franciscan complex of California: American Journal of Science, v. 304, p. 67–101.

Oze, C., Fendorf, S., Bird, D.K., and Coleman, R.G., 2004b, Chromium geochemistry of serpentine soils: International Geology Review, v. 46, p. 97–126.

Page, N.J., 1971, Comments on the role of oxygen fugacity in the formation of immiscible sulfide liquids in the H Chromitite zone of the Stillwater Complex, Montana: Economic Geology, v. 66, p. 607–610.

Page, N.J., 1972, Pentlandite and pyrrhotite from the Stillwater Complex, Montana—Iron-nickel ratios as function of associated minerals: Economic Geology, v. 67, p. 814–820.

Page, N.J., Rowe, J.J., and Haffty, J., 1976, Platinum metals in the Stillwater Complex, Montana: Economic Geology, v. 71, p. 1352–1363.

Palacz, Z.A., 1984, Isotopic and geochemical evidence for the evolution of a cyclic unit in the Rhum intrusion, north-west Scotland: Nature (London), v. 207, p. 618–620.

Palacz, Z.A., 1985, Sr-Nd-Pb isotopic evidence for crustal contamination in the Rhum intrusion: Earth and Planetary Science Letters, v. 74, p. 35–44.

Palacz, Z.A., and Tait, S.R., 1985, Isotopic and geochemical investigation of Unit 10 from Eastern Layered Series of the Rhum intrusion, Northwest Scotland: Geological Magazine, v. 122, p. 485–490.

Papike, J.J., Spilde, M.N., Fowler, G.W., and McCallum, I.S., 1995, SIMS studies of planetary cumulates—Orthopyroxene from the Stillwater Complex, Montana: American Mineralogist, v. 80, no. 11–12, p. 1208–1221.

Papp, J.F., 2007, Chromium – a national mineral commodity perspective: U.S. Geological Survey Open-File Report 2007–1167, 48 p.

Papp, J.F., 2009, Chromium, *in* Metals and minerals: U.S. Geological Survey Minerals Yearbook 2007, v. I, p. 7.1–17.28.

Papp, J.F., and Lipin, B.R., 2001, Chromium: U.S. Geological Survey Open-File Report 01–381, 161 p.

Patchett, P., Kouvo, O., Hedge, C.E., and Tatsumoto, M., 1981, Evolution of continental crust and mantle heterogeneity—Evidence from Hf isotopes: Contributions to Mineralogy and Petrology, v. 78, p. 279–297.

Penniston-Dorland, S.C., Wing, B.A., Nex, P.A.M., Kinnaird, J.A., Farquhar, J., Brown, M., and Sharman, E.R., 2008, Multiple sulfur isotopes reveal a magmatic origin for the Platreef platinum group element deposit, Bushveld Complex, South Africa: Geology, v. 36, p. 979–982.

Perron, L., 1995, Chromium: Canadian Minerals Yearbook, 1995, Geological Survey of Canada, 19 p.

Pickering, R.G.B., 2004, The optimization of mining method and equipment: International Platinum Conference 'Platinum Adding Value', The South African Institute of Mining and Metallurgy, p. 111–115.

Pidgeon, R.T., Aftalion, M., and Kalsbeek, F., 1976, The age of the Ilivertalik granite in the Fiskenæsset area: Rapport—Gronlands Geolgiske Undersogelse, v. 73, p. 31–33.

Pimentel, M.M., Ferreira-Filho, C.F., and Armstrong, R.A., 2004, SHRIMP U-Pb and Sm-Nd ages of the Niquelandia layered complex—Meso- (1.25 Ga) and Neoproterozoic (0.79 Ga) extensional events in central Brazil: Precambrian Research, v. 132, p. 133–153.

Podmore, F., 1982, The first Bouguer anomaly map of Zimbabwe: Transactions of the Geological Society of South Africa, v. 85, p. 127–133.

Podmore, F., 1985, A gravity study of the Great Dyke, Zimbabwe: Ph.D. dissertation, University of London, London, 439 p.

Podmore, F., and Wilson, A.H., 1987, A reappraisal of the structure, geology and emplacement of the Great Dyke, Zimbabwe, *in* Halls, H.C., and Fahrig, W.F., eds., Mafic Dyke Swarms: Geological Association of Canada Special Paper, v. 34, p. 317–330.

Polat, A., Appel, P.W.U., Fryer, B., Windley, B., Frei, R., Samson, I.M., and Huang, H., 2009, Trace element systematics of the Neoarchean Fiskenæsset anorthosite complex and associated meta-volcanic rocks, southwest Greenland – Evidence for a magmatic arc origin: Precambrian Research, v. 175, p. 87–115.

Power, M.R., Pirrie, D., Andersen, J.C.Ø., and Wheeler, P.D., 2000, Testing the validity of chrome spinel chemistry as a provenance and petrogenetic indicator: Geology, v. 28, no. 11, p. 1027–1030.

Prendergast, M.D., 1990, Platinum-group minerals and hydro-silicate "alteration" in Wedza-Mimosa platinum deposit, Great Dyke, Zimbabwe; genetic and metallurgical implications: Transactions of the Institution of Mining and Metallurgy, v. B99, p. 91–105.

Prendergast, M.D., and Wilson, A.H., 1989, The Great Dyke of Zimbabwe II: mineralization and mineral deposits, *in* Prendergast, M.D., and Jones, M.J., eds., Magmatic Sulfides—The Zimbabwe Volume: London, Institute of Mineralogy and Metallurgy, p. 21–42.

Price, P.M., 1963, Mining methods and costs, Mouat mine, American Chrome Company, Stillwater Complex, Montana. U.S. Bureau of Mines Information Circular 8204, 59 p.

Poikolainen, J., Kubin, E., Piispanen, J., and Karhu, J., 2004, Atmospheric heavy metal deposition in Finland during 1985–2000 using mosses as bioindicators: Science of the Total Environment, v. 318, p. 171–185.

Raedeke, L.D., and McCallum, I.S., 1984, Investigations in the Stillwater Complex—Part II. Petrology and Petrogenesis of the Ultramafic Series: Journal of Petrology, v. 25, no. 2, p. 395–420.

Rai, D., Eary, L.E., and Zachara, J.M., 1989, Environmental geochemistry of chromium: Science of the Total Environment, v. 86, p. 15–23.

Renner, R., and Palacz, Z.A., 1987, Basaltic replenishment of the Rhum magma chamber—Evidence from unit 14: Journal of the Geological Society, v. 144, p. 961–970.

Ripley, E.M., 1999, Systematics of sulfur and oxygen isotopes in mafic igneous rocks and related Cu-Ni-PGE mineralization, *in* Keays, R.R., Lesher, C.M., Lightfoot, P.C., and Farrow, C.E.G., eds., Dynamic processes in magmatic ore deposits and their application in mineral exploration: Geological Association of Canada Short Course Notes, v. 13, p. 133–158.

Ripley, E.M., and Li, C., 2003, Sulfur isotope exchange and metal enrichment in the formation of magmatic Ni-Cu-(PGE) deposits: Economic Geology, v. 98, p. 635–641.

Rivalenti, G., Correia, C.T., Girardi, V.A.V., Mazzucchelli, M., Tassinari, C.C.G., and Bertotto, G.W., 2008, Sr-Nd isotopic evidence for crustal contamination in the Niquelândia Complex, Goiás, Central Brazil: Journal of South American Earth Sciences, v. 25, p. 298–312.

Roach, T.S., Roeder, P.L., and Hulbert, L.J., 1998, Composition of chromite in the Upper Chromitite, Muskox Layered intrusion, Northwest Territories: Canadian Mineralogist, v. 36, no. 1, p. 117–135.

Roberts, A.E., 1994, Current research into mechanized mining on the Great Dyke: Minerals and Energy—Raw Materials Report, v. 10, no. 3, p. 26–27.

Roberts, A., E., 1996, The environmental impact of chromite mining, *in* Lipalile, M.S., ed., Twenty seventh annual report for the year 1995: University of Zimbabwe, Institute of Mining Research, v. 159, p. 38–39.

Rodushkin, I., Engstrom, E., Sorlin, D., Ponter, C., and Baxter, D.C., 2007, Osmium in environmental samples from Northeast Sweden—Part II. Identification of anthropogenic sources: Science of the Total Environment, v. 386, no. 1–3, p. 159–168.

Roedder, P.L., and Reynolds, I., 1991, Crystallization of chromite and chromium solubility in basaltic melts: Journal of Petrology, v. 32, p. 909–934.

Ropbles-Camacho, J., and Armienta, M.A., 2000, Natural chromium contamination at LeóValley, Mexico: Journal of Geochemical Exploration, v. 68, p. 167–181.

Rudashevsky, N.S., Garuti, G., Anderson, J.C.Ø., Kretser, Y.L., Rudashevsky, V.N., and Zaccarini, F., 2002, Separation of accessory minerals from rocks and ores by hydro-separation (HS) technology-method and application to CHR-2 chromitite, Niquelândia intrusion, Brazil: Applied Earth Science—Transactions of the Institution of Mining and Metallurgy, Section B, v. 111, p. 87–94.

Rütschlin, M., Cloete, J.H., Mason, I.M., and Palmer, K.D., 2007, The radio frequency dielectric properties of the stratified UG1-UG2 geological unit in the Bushveld Complex: Journal of Applied Geophysics, v. 62, p. 354–360.

Ryder, G.. 1984, Olivine in lunar dunite 72415, a rather shallow-origin cumulate: Lunar and Planetary Science Abstract, v. 14, p. 709–710.

Sakko, M., 1971, Radiometric zircon ages on the early Karelian metadiabases, Finland: Geologi, v. 23, no. 9–10, p. 117–119.

Saleh, F.Y., Parkerton, T.F., Lewis, R.V., Huang, J.H., and Dickson, K.L., 1989, Kinetics of chromium transformations in the environment: Science of the Total Environment, v. 86, p. 25–41.

Saxton, J., and Geissman, J.W., 1985, Paleomagnetic constraints on the age of serpentinization of plagioclase-olivine cumulate rocks, Banded Series, Stillwater Complex, Montana: Eos, Transactions of the American Geophysical Union, v. 66, n. 10, p. 113.

Schoenberg, R., Kruger, F.J., Nägler, T.F., Meisel, T., and Kramers, J.D., 1999, PGE enrichment in chromitite layers and the Merensky Reef of the western Bushveld Complex—A Re-Os and Rb-Sr isotope study: Earth and Planetary Science Letters, v. 172, p. 49–64.

Schoenberg, R., Nagler, T.F., Gnos, E., Kramers, J.D., and Kamber, B.S., 2003, The source of the Great Dyke, Zimbabwe, and its tectonic significance—Evidence from Re-Os isotopes: Journal of Geology, v. 111, p. 565–578.

Schiano, P., Birck, J.-L., and Allègre, C.J., 1997, Osmium-strontium-neodymium-lead isotopic covariations in mid-ocean ridge basalt glasses and the heterogeneity of the upper mantle: Earth and Planetary Science Letters, v. 150, no. 3–4, p. 363–379.

Scoates, R.F.J., Williamson, B.L., Eckstrand, O.R., and Duke, J.M., 1989, Stratigraphy of the Bird River Sill and its chromitiferous zone, and preliminary geochemistry of the chromitite layers and PGE-bearing units, Chrome property, Manitoba, in Galley, A.G., ed., Investigations by the Geological Society of Canada in Manitoba and Saskatchewan during the 1984–1989 Mineral Development Agreements: Geological Survey of Canada Open File Report 2133, p. 69–82.

Scoon, R.N., and Mitchell, A.A., 1994, Discordant iron-rich ultramafic pegmatites in the Bushveld Complex and their relationship to iron-rich intercumulus and residual liquids: Journal of Petrology, v. 35, p. 881–917.

Scoon, R.N., and Teigler, B., 1994, Platinum-group element mineralization in the Critical Zone of the Western Bushveld Complex—I. Sulfide-poor chromitites below the UG2: Economic Geology, v.89, p.1094–1121.

Scott, S.D., and Gasparrini, E., 1973, Argentinian pentlandite $(Fe, Ni)_8AgS_8$, from Bird River, Manitoba: The Canadian Mineralogist, v. 12, p. 165–168.

Seabrook, C.L., Cawthorn, R.G., and Kruger, F.J., 2005, The Merensky Reef, Bushveld Complex: Mixing of minerals not mixing of magmas: Economic Geology, v. 100, p. 1191–1206.

Sharkov, E.V., Bogatikov, O.A., Grokhovskaya, T.L., Chistyakov, A.V., Ganin, V.A., Grinevich, N.G., Snyder, G.A., and Taylor, L.A., 1995, Petrology and Ni-Cu-Cr-PGE mineralization of the largest mafic pluton in Europe-the Early Proterozoic Burakovsky Layered intrusion, Karelia, Russia: International Geology Review, v. 37, p. 509–525.

Sharpe, M.R., 1981, The chronology of magma influxes to the eastern compartment of the Bushveld Complex as exemplified by its marginal border groups: Journal of Geological Society, v. 138, no. 3, p. 307–326.

Sharpe, M.R., 1985, Strontium isotope evidence for preserved density stratification in the main zone of the Bushveld Complex: Nature, v. 298, p. 53–55.

Sharpe, M.R., and Hulbert, L.J., 1985, Ultramafic sills beneath the eastern Bushveld Complex: Economic Geology, v. 80, p. 849–871.

Shirey, S.B., and Walker, R.J., 1998, The Re-Os isotope system in cosmochemistry and high-temperature geochemistry: Annual Reviews of Earth and Planetary Sciences, v. 26, p. 423–500.

Shürmann, L.W., Grabe, P-J., and Steenkamp, C.J., 1998, Chromium, in Wilson, M.G.C., and Anhaeusser, C.R., eds., The Mineral Resources of South Africa: Handbook, Council for Geoscience, v. 16, p. 90–105.

Simmons, E.C., and Lambert, D.D., 1982, Magma evolution in the Stillwater Complex, Montana—A preliminary evaluation using REE data for whole-rocks and cumulate feldspars: Montana Bureau of Mines Special Publication, v. 84, p. 91–106.

Singer, P.C., and Stumm, W., 1970, Acidic mine drainage—The rate-determining step: Science, v. 167, no. 3921, p. 1121–1123.

Skovgaard, A.C., Storey, M., Baker, J., Blusztajn, J., and Hart, S.R., 2001, Osmium-oxygen isotope evidence for a recycled and strongly depleted component in the Iceland mantle plume: Earth and Planetary Science Letters, v. 194, p. 259–275.

Smit, P.J., Hales, A., and Gough, D.I., 1962, The gravity survey of the Republic of South Africa—Handbook of the Geological Society of South Africa, v. 3, 484 p.

Smoliar, M.I., Walker, R.J., and Morgan, J.W., 1996, Re-Os ages of Group IIA, IIA, IVA, and IVB iron meteorites: Science, v. 271, p. 1099–1102.

Snyder, G.A., Higgins, S.J., Taylor, L.A., Jain, J., Neal, C.R., and Sharkov, E., 1996, Archean enriched mantle beneath the Baltic Shield—Rare-earth-element evidence from the Burakovsky Layered intrusion, Southern Karelia, Russia: International Geology Review, v. 38, p. 389–404.

Spandler, C., Mavrogenes, J.A., and Arculus, R., 2005, Origin of chromitites in layered intrusions—Evidence from chromite-hosted melt inclusions from the Stillwater Complex: Geology, v. 33, no. 11, p. 893–896.

Stewart, B.M., and DePaolo, D.J., 1987, Sr isotopic stratigraphy of the Stillwater Complex, Montana: Evidence for multiple magma injections: Eos, Transactions of the American Geophysical Union, v. 68, p. 429.

Stowe, C.W., 1994, Compositions and tectonic settings of chromite deposits through time: Economic Geology, v. 89, p. 528–546.

Stubbs, H.M., Hall, R.P., Hughes, D.J., and Nesbitt, R.W., 1999, Evidence for a high Mg andesitic parental magma to the east and west satellite dykes of the Great Dyke, Zimbabwe—A comparison with the continental tholeiitic Mashonaland sills: Journal of African Earth Sciences, v. 28, p. 325–336.

Sun, S.-s. and McDonough, W.F., 1989, Chemical and isotopic systematics of oceanic basalts—Implications for mantle composition and processes: Geological Society Special Publication, v. 42, no. 1, p. 313–345.

Tait, S.R., 1985, Fluid dynamic and geochemical evolution of cyclic unit 10, Rhum, Eastern Layered Series: Geological Magazine, v. 122, no. 5, p. 469–484.

Talkington, W., Watkinson, D.H., Whittaker, P.J., and Jones, P.C., 1983, Platinum-group-mineral inclusions of chromite from the Bird River Sill, Manitoba: Mineraluim Deposita, v. 18, p. 245–255.

Taylor, H.P., Jr., 1968, The oxygen isotope geochemistry of igneous rocks: Contributions to Mineralogy and Petrology, v. 19, p. 1–71.

Teigler, B., 1990, Platinum group element distribution in the Lower and Middle Group Chromitites in the Western Bushveld Complex.: Mineralogy and Petrology, v. 42, p. 165–179.

Teigler, B., 1999, Chromite chemistry and platinum-group element distribution of the LG6 chromitite, northwestern Bushveld Complex: South African Journal of Geology, v. 102, p. 282–285.

Teigler, B., and Eales, H.V., 1993, Correlation between chromite composition and PGE mineralization in the Critical Zone of the western Bushveld Complex: Mineralium Deposita, v. 28, p. 291–302.

Teigler, B., and Eales, H.V., 1996, The Lower and Critical Zones of the Western Limb of the Bushveld Complex as intersected by the Nooitgedacht boreholes: Geological Survey of South Africa Bulletin, v. 111, 126 p.

Tepley, F.J., and Davidson, J.P., 2003, Mineral-scale Sr-isotope constraints on magma evolution and chamber dynamics in the Rum layered intrusion, Scotland: Contributions to Mineralogy and Petrology, v. 145, p. 628–641.

Theyer, P., 1991, Petrography, chemistry, and distribution of platinum and palladium in ultramafic rocks of the Bird River Sill, south-eastern Manitoba, Canada: Mineralium Deposita, v. 26, no. 3, p. 165–174.

Theyer, P., Bruni, E., and Sundell, C., 2001, Stratigraphy, geology and mineralization of selected parts of the Page property, Bird River Sill (part of NTS 52L/5): Report of Activities 2001, Manitoba Geological Survey, p. 126–132.

Thomas, R.P., Hillier, S.J., Roe, M.J., Geelhoed, J.S., Graham, M.C., Paterson, E. and Farmer, J.G., 2001, Analytical characterization of solid- and solution-phase chromium species at COPR-contaminated sites: Environmental Geochemistry and Health v. 23, p. 195–199.

Timmins, E.A., Turek, A., Symons, D.T.A., and Smith, P.E., 1985, U-Pb zircon geochronology and paleomagnetism of the Bird River greenstone belt, Manitoba, *in* Mineralogical Association of Canada Joint Annual Meeting, 1985, Program with Abstracts: Geological Association of Canada, v. 10, p. A62.

Tinjum, J.M., Benson, C.H., and Edil, T.B., 2008, Mobilization of Cr(VI) from chromite ore processing residue through acid treatment: Science of the Total Environment, v. 391, no. 1, p. 13–25.

Tiwary, R.K., Dhakate, R., Rao, A.V., and Singh, V.S., 2005, Assessment and prediction of contaminant migration in ground water from chromite waste dump: Environmental Geology (Berlin), v. 48, no. 4–5, p. 420–429.

Todd, S.G., Keith, D.W., LeRoy, L.W., Schissel, D.J., Mann, E.L., and Irvine, T.N., 1982, The J-M platinum-palladium reef of the Stillwater Complex, Montana—I. Stratigraphy and petrology: Economic Geology, v. 77, p. 1454–1480.

Trueman, D.L., 1971, Petrological, structural and magnetic studies of a layered basic intrusion—Bird River Sill, Manitoba: M.S. thesis, University of Manitoba, 150 p.

Tsuru, A., Walker, R.J., Kontinen, A., Peltonen, P., and Hanski, E., 2000, Re-Os isotopic systematics of the Jormua Ophiolite Complex, northwest Finland: Chemical Geology, v. 164, p. 123–141.

Ulmer, G.C., 1969, Experimental investigations of chromite spinels, *in* Wilson, H.D.B., ed., Magmatic ore deposits: Economic Geology Mongraph 4, p. 114–131.

United States Environmental Protection Agency (USEPA), 2009a, Regional Screening Level Summary Table, 11 p., accessed March 1, 2010, at *http://www.epa.gov/region09/superfund/prg/index.html*.

United States Environmental Protection Agency (USEPA), 2009b, National Recommended Water Quality Criteria, 22 p., accessed March 1, 2010, at *http://www.epa.gov/waterscience/criteria/wqctable/*.

Van der Merwe, M.J., 1976, The layered sequence of the Potgietersrus limb of the Bushveld Complex: Economic Geology, v. 71, p. 1337–1351.

Vermaak, C.F., and Lee, C.A., 1981, Bushveld and kindred complexes, *in* Hunter, D.R., ed., The Precambrian of the Southern Hemisphere—Developments in Precambrian Geology, Volume 2: Amsterdam, Elsevier, 882 p.

Volker, J.A., 1983, The geology of the Trallval area, Rhum, Inner Hebrides: Edinburgh, Ph.D. thesis, University of Edinburgh, 120 p.

Von Gruenewaldt, G.,1972, The origin of the roof-rocks of the Bushveld Complex between Tauteshoogte and Paardekop in the eastern Transvaal: Transactions of the Geological Society of South Africa, v. 75, p. 121–134.

Von Gruenewaldt, G., Hatton, C.J., Merkle, R.K.W., and Gain, S.B., 1986, Platinum-group element chromitite associations in the Bushveld Complex: Economic Geology, v. 81, p. 1067–1079.

Von Gruenewaldt, G., Hatton, C. J., 1987, Platinum-group metals; a resource in the tailings of chromium mines in South Africa: Journal of the South African Institute of Mining and Metallurgy, v. 87, no.9, p.265–268.

Von Gruenewaldt, G., Hulbert, L.J., and Naldrett, A.J., 1989, Contrasting platinum-group element concentration patterns in cumulates of the Bushveld Complex: Mineralium Deposita, v. 24, p. 219–229.

Voordouw, R., Gutzmer, J., and Beukes, N.J., 2009, Intrusive origin for the Upper Group (UG1, UG2) stratiform chromitite seams in the Dwars River area, Bushveld Complex, South Africa: Mineralogy and Petrology, v. 97, p. 75–94.

Wager, L.R., 1953, Layered intrusions: Bulletin of the Geological Society of Denmark, v. 12, no. 3, p. 335–349.

Wager, L.R., 1959, Differing powers of crystal nucleation as a factor producing diversity in layered igneous intrusions: Geological Magazine, v. 96, p. 75–80.

Wager, L.R., and Brown, G.M., 1968, Layered igneous rocks: Edinburgh, Oliver and Boyd, 588 p.

Walker, R.J., Shirey, S.B., Hanson, G.N., and Rajamani, V., 1989, Re-Os, Rb-Sr and O isotope systematics of the Archean Kolar schist belt, Karnataka, India: Geochimica et Cosmochimica Acta, v. 53, p. 3005–3013.

Walraven, F., Armstrong, R.A., and Kruger, F.J., 1990, A chronostratigraphic framework for the north-central Kapvaal Craton, the Bushveld Complex and Vredefort structure: Tectonophysics, v. 171, p. 23–48.

Wang, T., He, M., and Pan, Q., 2007, A new method for the treatment of chromite ore processing residues: Journal of Hazardous Materials, v. 149, n. 2, p. 440–444.

Wang, X., 1993, U-Pb zircon geochronology study of the Bird River greenstone belt, southeastern Manitoba: M.S. thesis, University of Windsor, Windsor, Ontario, 96 p.

Webb, S.J., Ashwal, L.D., and Cawthorn, R.G., 2010, Continuity between eastern and western Bushveld Complex, South Africa, confirmed by xenoliths from kimberlite: Contributions to Mineralogy and Petrology, v. 162, p. 101–107.

Webb, S.J., Cawthorn, R.G., Nguuri, T., and James, D., 2004, Gravity modeling of Bushveld Complex connectivity supported by Southern African seismic experiment results: South African Journal of Geology, v. 107, p. 207–218.

Weng, C.H., Huang, C.P., Allen, H.E., Cheng, A.H.D., and Sanders, P.F., 1994, Chromium leaching behavior in soil derived from chromite ore processing waste: The Science of the Total Environment, v.154, no.1, p.71–86.

Weng, C.H., Huang, C.P., and Sanders, P.F., 2002, Transport of Cr(VI) in soils contaminated with chromite ore processing residue (COPR), *in* Ding, Y., ed., Environmental multimedia transport: Practice Periodical of Hazardous, Toxic, and Radioactive Waste Management, v.6, no.1, p.6–13.

Whalley, C., Hursthouse, A., Rowlatt, S., Iqbal-Zahid, P., Vaughan, H., and Durant, R., 1999, Chromium speciation in natural waters draining contaminated land, Glasgow, U.K.: Water, Air, Soil Pollution, v. 112, p. 389–405.

Wilhelm, H.J., Zhang, H., Chen, F.L., Elsenbroek, J.H., Lombard, M., and de Bruin, D., 1997, Geochemical exploration for platinum-group elements in the Bushveld Complex, South Africa: Mineralium Deposita, v. 32, p. 349–361.

Williamson, M.A., Kirby, C.S., and Rimstidt, J.D., 2006, Iron dynamics in acid mine drainage, *in* Barnhisel, R.I., ed., The 7th International Conference on Acid Rock Drainage, St. Louis, Missouri, p. 2411–2423.

Wilson, A.H., 1982, The geology of the Great "Dyke", Zimbabwe; the ultramafic rocks: Journal of Petrology, v. 23, p. 240–292.

Wilson, J.F., 1987, The tectonic setting of the Great Dyke of Zimbabwe and the Mashonaland Igneous Event: 14th Colloqium of African Geology, CIFEG Occasional Publication, v. 12, p. 140–141.

Wilson, A.H., 1996, The Great Dyke of Zimbabwe, *in* Cawthorn, R.G., ed., Layered intrusions: Amsterdam, Elsevier, p. 365–402.

Wilson, A.H., and Prendergast, M.D., 1987, The Great Dyke of Zimbabwe—An overview: Guidebook for the 5th Magmatic Sulphides Field Conference, Harare, Zimbabwe, p. 23–55.

Wilson, A.H., and Prendergast, M.D. 2001. Platinum-group element mineralisation in the Great Dyke, Zimbabwe, and its relationship to magma evolution and magma chamber structure. South African Journal of Geology, v. 104, no. 4, p. 319–342.

Wilson, A.H., and Tredoux, M., 1990, Lateral and vertical distribution of Platinum-Group Elements and petrogenetic controls on the sulfide mineralization in the P1 Pyroxenite Layer of the Darwendale Subchamber of the Great Dyke, Zimbabwe: Economic Geology, v. 85, p. 556–584.

Wooden, J.L., Czamanske, G.K., and Zientek, M.L., 1991, A lead isotopic study of the Stillwater Complex, Montana—Constraints on crustal contamination and source regions: Contributions to Mineralogy and Petrology, v. 107, p. 80–93.

Wooden, J.L., and Mueller, P.A., 1988, Pb, Sr, and Nd isotopic compositions of a suite of late Archean igneous rocks, eastern Beartooth Mountains—Implications for crust-mantle evolution: Earth and Planetary Science Letters, v. 87, p. 59–72.

World Health Organization, 2008, Guidelines for drinking-water quality—3rd Electronic version for the web: Geneva, Switzerland, WHO Press, accessed March 1, 2010, at *http://www.who.int/water_sanitation_health/dwq/gdwq3rev/en/index.html*.

Zientek, M.L., and Ripley, E.M., 1990, Sulfur isotope studies of the Stillwater Complex and associated rocks, Montana: Economic Geology, v. 85, p. 376–391.

Zientek, M.L., Czamanske, G.K., and Irvine, T.N., 1985, Stratigraphy and nomenclature for the Stillwater Complex, *in* Czamanske, G.K., and Zientek, M.L., eds., 1985, The Stillwater Complex, Montana—Geology and guide: Montana Bureau of Mines and Geology Special Publication 92, p. 21–32.

Zonenshain, L.P., Kuzmin, M.I., and Natapov, L.M., 1990, Geology of the United Soviet Socialist Republic—A plate tectonic synthesis: Geodynamics Series, v. 21, 242 p.